[redacted]

X67-10045

Copy 575

NASA TM X-669

[redacted]

NASA TM X-669

GPO PRICE $ ______

OTS PRICE(S) $ ______

Hard copy (HC) 5.00

Microfiche (MF) 1.00

TECHNICAL MEMORANDUM

X-669

DECLASSIFIED BY AUTHORITY OF NASA
CLASSFICATION CHANGE NOTICES NO. 19
DATED 5-26-65 ITEM NO. 11

LONGITUDINAL AERODYNAMIC CHARACTERISTICS OF A 1/30-SCALE SUBSONIC CANARD-AIRPLANE MODEL HAVING A WING WITH AN ASPECT RATIO OF 3.6 AT MACH NUMBERS FROM 0.30 TO 0.98

By William B. Igoe, Richard J. Re, and Francis J. Capone

Langley Research Center
Langley Station, Hampton, Va.

DECLASSIFIED: EFFECTIVE 4-29-65
AUTHORITY F.G. DROBKA (ATSS*A)
memo dated 5-13-65:AFSDO 5439

[redacted]

NATIONAL AERONAUTICS AND SPACE ADMINISTRATION

WASHINGTON June 1962

[redacted]

DECL[redacted]SIFIED

NATIONAL AERONAUTICS AND SPACE ADMINISTRATION

TECHNICAL MEMORANDUM X-669

LONGITUDINAL AERODYNAMIC CHARACTERISTICS OF A 1/30-SCALE SUBSONIC CANARD-AIRPLANE MODEL HAVING A WING WITH AN ASPECT RATIO OF 3.6 AT MACH NUMBERS FROM 0.30 TO 0.98*

By William B. Igoe, Richard J. Re, and Francis J. Capone

SUMMARY

26637

An investigation of the longitudinal aerodynamic characteristics of a 1/30-scale model of a proposed subsonic nuclear powered canard airplane was made at Mach numbers from 0.30 to 0.98, at angles of attack primarily from -1.5° to 17.5°, and at Reynolds numbers per foot from 2.0×10^{6} to 4.5×10^{6}. The model tested had a wing with an aspect ratio of 3.6, a leading-edge sweepback angle of 51°, and a taper ratio of 0.4. End plates were mounted on the wing tips as vertical tails. The test objectives were to determine the canard-surface loads and effectiveness and the longitudinal stability and performance effects of model components such as deflection of outboard leading-edge chord-extensions, inboard leading-edge camber, wing fences, end plates, and a body filler which increased the maximum cross-sectional area.

The test results indicated that the maximum lift-drag ratio of the model was increased by the addition of the end plates at the wing tips. A deflection of the leading-edge chord-extension of 15° was the best chord-extension deflection for high lift stability and for maximum lift-drag ratio. Inboard thickened leading edges, inboard leading-edge camber, and wing fences did not significantly reduce abrupt high lift instability. The maximum lift-drag ratio was no lower for the longitudinally trimmed model with the canard surface and end plates than for the untrimmed model without the canard surface and end plates.

Author

---

*Title, Unclassified.

[redacted]

INTRODUCTION

The aerodynamic performance, static longitudinal stability, and control characteristics of a proposed nuclear powered airplane were investigated in the Langley 16-foot transonic tunnel. The proposed nuclear airplane was a subsonic bomber, missile carrier, and airborne alert vehicle with long-range and long-duration capabilities. It possessed several unusual aerodynamic features, such as large nacelles to house nuclear powered jet engines and control surfaces placed to avoid the nuclear-engine nacelle structure. The longitudinal trim control was accomplished with a free-floating canard control surface, and end plates were mounted on the wing tips acting as vertical tails (lateral stabilizing and control surfaces).

Tests were conducted with a 1/30-scale model. The model canard surface was fixed rather than free floating. This report contains the results on an investigation of the model with a wing having an aspect ratio of 3.6. Similar results of an investigation for the model with a wing having an aspect ratio of 6.0 are contained in reference 1. The fuselage, engine duct, and canard-surface geometry were identical for both investigations.

The test objectives included determination of the canard-surface loads and effectiveness and the effects on the airplane stability and performance of outboard leading-edge chord-extensions, inboard leading-edge camber, wing-tip end plates, and wing fences. For most of the tests, the Mach number was varied from 0.70 to 0.98 at wing angles of attack from -1.5° to 17.5°. Some tests to evaluate take-off characteristics were made at a Mach number of 0.30 at angles of attack up to about 26.5°. The test Reynolds number per foot varied from about 2.0×10^{6} to 4.5×10^{6}.

SYMBOLS

a — lift-curve slope per deg

A — cross-sectional area

$A_{t,\infty}$ — free-stream cross-sectional area of stream tube which enters nacelle duct

$\bar{c}$ — mean aerodynamic chord of basic wing (15.029 in.)

$\bar{c}_c$ — mean aerodynamic chord of exposed canard planform (6.494 in.)

$\bar{c}_{tab}$ mean aerodynamic chord of canard tab (0.943 in.)

C_D drag coefficient, $\frac{\text{Drag}}{qS}$

$C_{D,i}$ nacelle duct internal-drag coefficient,

$$\frac{2A_i}{S}\left\{\frac{A_{t,\infty}}{A_i} + \frac{1}{\gamma M^2}\frac{A_e}{A_i}\left[1 - \frac{p_e}{p_\infty}\left(1 + \gamma M_e{}^2\right)\right]\cos(\alpha - 3.5^\circ)\cos 5^\circ\right\}$$

$C_{h,c}$ canard-surface hinge-moment coefficient, $\frac{\text{Canard-surface hinge moment (one side)}}{qS_c\bar{c}_c}$

$C_{h,tab}$ tab hinge-moment coefficient, $\frac{\text{Tab hinge moment}}{qS_{tab}\bar{c}_{tab}}$

C_L lift coefficient, $\frac{\text{Lift}}{qS}$

$C_{L,c}$ canard-surface lift coefficient, $C_{N,c}\cos(\alpha + \delta_c)$

C_m pitching-moment coefficient about quarter-chord point of $\bar{c}$, $\frac{\text{Pitching moment}}{qS\bar{c}}$

$C_{m_{C_L}}$ static longitudinal stability parameter, $\frac{\partial C_m}{\partial C_L}$ at $C_L = 0$

$C_{m,o}$ pitching-moment coefficient at $C_L = 0$

$C_{m_{\delta_c}}$ canard effectiveness parameter, $\frac{\partial C_m}{\partial \delta_c}$ at $\alpha = 0$

$C_{N,c}$ canard-surface normal-force coefficient, $\frac{\text{Canard-surface normal force (one side)}}{qS_c}$

$C_{p,b}$ base pressure coefficient, $\frac{p_b - p_\infty}{q}$

L/D lift-drag ratio

[redacted]

[redacted]

M free-stream Mach number

M_e Mach number at nacelle duct exit

p static pressure, lb/sq ft

q free-stream dynamic pressure, lb/sq ft

S planform area of basic wing, includes area covered by fuselage and nacelles (5.2778 sq ft)

S_c canard-surface exposed planform area (one side) (0.21144 sq ft)

S_{tab} canard-surface tab planform area (one side) (0.012874 sq ft)

α angle of attack of wing chord plane, positive leading edge up, deg

α_o angle of attack at $C_L = 0$

γ ratio of specific heats (1.4 for air)

δ_c canard-surface deflection angle from wing chord plane measured normal to hinge line, positive leading edge up, deg

δ_{le} outboard leading-edge chord-extension deflection angle from wing chord plane measured normal to hinge line, positive leading edge down, deg

δ_{te} trailing-edge flap deflection angle from wing chord plane measured normal to hinge line, positive trailing edge down, deg

δ_{tr} trailing-edge trim-flap deflection angle from wing chord plane measured normal to hinge line, positive trailing edge up, deg

δ_{tab} canard-surface tab deflection angle from canard-surface chord plane measured normal to hinge line, positive trailing edge down, deg

Subscripts:

b base

c canard surface

[redacted]

e nacelle duct exit

i nacelle duct inlet

∞ free stream

max maximum

min minimum

MODEL COMPONENT DESIGNATIONS AND ABBREVIATIONS

The following designations are used in the present paper to identify the various components of the model:

B fuselage and nacelles with modified rear end

B_1 B with filler

C canard

E wing end plate

F_1 wing fence at SS 12.667

F_2 wing fence at SS 16.408

W wing with outboard leading-edge chord-extension

W_1 W with inboard leading edge cambered

W_2 W with inboard thickened leading edge

The following abbreviations are used in the present paper to identify various distances measured on the model:

BL buttock lines, in.

WL water lines, in.

FS fuselage station, measured positive rearward from a reference point 1/2 in. ahead of actual fuselage nose, in.

WS wing station, measured positive rearward from leading-edge apex, in.

SS span station, measured positive outboard from plane of symmetry in wing or canard-surface chord plane, in.

MODEL, APPARATUS, AND PROCEDURE

Model

The 1/30-scale model consisted of a wing with an aspect ratio of 3.6 and with end plates, a fuselage, a canard surface, and flow-through nacelles. Figure 1 is a photograph of the model without canard surface sting mounted in the wind tunnel. A sketch of the complete model with overall dimensions is shown in figure 2.

Wing.- The wing details are given in table I and the planform geometry is shown in figure 3. The basic wing planform had an aspect ratio of 3.789 but this was decreased to 3.600 by the addition of an outboard leading-edge chord-extension. A take-off configuration was represented by deflection of plain trailing-edge flaps and trailing-edge trim flaps. When the trailing-edge flaps were deflected down, the trailing-edge trim flaps were deflected up to trim out the pitching moment caused by the flaps. In addition, the wing had provision for inboard leading-edge camber which increased linearly from 0 at SS 6.333 to a maximum at SS 16.833 as shown in figure 3. Also shown in this figure is a sketch of an alternate, thickened inboard leading edge.

A wing fence, shown in figure 4, could be attached to the wing in two possible locations, at SS 12.667 and at SS 16.408, as indicated on the wing sketch of figure 3.

End plates.- The wing-tip end plates served as vertical tails. They had sweptback planforms with about 75 percent of the surface area above the wing chord plane and the remainder beneath. The end-plate geometry is shown in figure 4 and details are given in table I.

Fuselage.- The fuselage, shown in figure 5, had an overall length of 59.333 inches, a maximum height including the ducts of 5.937 inches, and a maximum width including ducts of 13.706 inches. There was a simulated canopy shape near the nose, and the sides of the fuselage were flat in the vicinity of the canard. The rear end of the fuselage differed from the proposed airplane shape so that the model could be sting mounted in the wind tunnel. In order to allow for the presence of the sting cavity, the nacelle inboard duct exits were also deformed. These differences between the model and the proposed airplane are shown in figure 6 which also shows that some external duct-exit shroud geometry was not duplicated.

Nacelles.- Two nacelles were mounted side by side near the rear of the fuselage. The elliptical inlets were located at the side of the fuselage just forward and below the wing leading edge. The external geometry of the nacelles may be seen in figure 5 and the nacelle internal ducting is illustrated in figure 7. Each duct had two exits, with the area of the inboard exits for each duct decreased (see fig. 6) because of the presence of the model sting cavity as has already been indicated.

The duct internal cross-sectional area distribution is given in figure 8. Internal blockage was provided in the ducts by a screen, of about 70 percent porosity, installed just forward of the duct splitter plate for the inboard and outboard exits. The external geometry of the nacelles was varied with the use of a filler, as shown in figure 5, to simulate an alternate powerplant configuration.

Canard.- The canard was located at the nose of the fuselage with the hinge line normal to the plane of symmetry, 32.460 inches forward and 2.634 inches below the model moment reference center. Although the airplane canard is free floating, the model canard was fixed, but its incidence was variable about the hinge line from -12° to 20°. A sketch of the canard-surface planform is shown in figure 9 and geometrical details are given in table I. A trailing-edge tab on the canard was used to obtain canard moment trim conditions about the hinge line. Because the sides of the fuselage were flat in the vicinity of the canard, the canard root chord fit relatively flush with the fuselage side and eliminated any canard unporting throughout the range of canard deflection angles used during the tests.

Area distribution.- Cross-sectional area distributions of the various model components are shown in figure 10. In figure 11, total area distributions for the model with and without filler are compared with the area distribution the model would have if its external geometry had not been altered due to the presence of the sting cavity. External wetted areas for the model configurations are given in table II.

Boundary-layer transition grain pattern.- For most of the tests in which the boundary-layer-transition point was fixed, No. 120 carborundum grains were sparsely distributed in a thin film of shellac in strips near the leading edges of the various model components. On the wing a 0.40-inch-wide strip was parallel to and 0.60 inch behind the leading edge. On the end plates, nacelles, and canard, a 0.25-inch-wide strip was parallel to and 0.40 inch behind the leading edge. On the fuselage, a 0.25-inch-wide circumferential strip was 0.75 inch behind the nose. All distances are measured in the streamwise direction. Configuration BWE with $\delta_{le} = 25^{\circ}$ was tested with the carborundum grain pattern extending all around the wing leading edge, thereby covering the front 1 inch of the leading edge. This same configuration was also tested with free transition.

Instrumentation

The model forces and moments were measured with a six-component internal strain-gage balance. The canard was instrumented with strain gages to measure canard normal force, hinge moment, and tab hinge moment. The model angles of attack were determined with an internal pendulum-type attitude indicator. Canard attitudes, however, were determined from deflection calibrations under load.

The nacelle-duct internal flow characteristics were determined with temporary duct-exit rakes consisting of static- and stagnation-pressure probes. Permanently installed model pressure instrumentation consisted of inlet stagnation-pressure rakes and throat- and maximum-area static-pressure orifices. This permanent instrumentation was calibrated with the exit-pressure data so that the nacelle internal flow characteristics could be determined when the temporary rakes were removed during the force tests. The duct pressure instrumentation is shown in figure 12.

Model base pressure was measured during the tests by means of three static-pressure taps distributed around the model base.

Wind Tunnel

The model was sting mounted (as shown in fig. 1) in the Langley 16-foot transonic tunnel which is described in reference 2. This is a single-return wind tunnel with a slotted octagonal throat and is operated at atmospheric stagnation pressures. The wind-tunnel model support system pivoted so that the balance moment center remained near the center of the test section throughout the angle-of-attack range.

Data Reduction

All forces and moments have been reduced to standard coefficient form with the model force data referred to the stability axis system. The nacelle internal drag has been subtracted from the model drag. Typical values of the nacelle internal-drag coefficient $C_{D,i}$ are presented in figures 13 and 14 for the model without the canard surface (BW_1E with $\delta_{le} = 15^\circ$ and $\delta_{le} = 30^\circ$) and for the model with the canard surface (BCW_1E with $\delta_{le} = 15^\circ$). In addition, model forces have been adjusted to the condition of free-stream static pressure existing at the base. Typical model base pressure coefficients (for models BW_1E and B_1WE with $\delta_{le} = 15^\circ$ and BW_1E with $\delta_{le} = 30^\circ$) are presented in figure 15. As mentioned previously, the model angle of attack was determined independently with an attitude transmitter. The canard-surface incidence settings were corrected for deflections under load. No other corrections or adjustments have been applied to the data.

Accuracy

The accuracy of the data, based on instrumentation error and repeatability, has been estimated to be:

M	± 0.01
α, deg	± 0.1
δ_c, deg	± 0.2
δ_{tab}, deg	± 0.5

At $M = 0.30$,

C_L	± 0.030
C_D at low C_L	± 0.004
C_D at high C_L	± 0.020
C_m	± 0.020

At $M = 0.60$ to $M = 0.98$,

C_L	± 0.010
C_D at low C_L	± 0.001
C_D at high C_L	± 0.005
C_m	± 0.005
$C_{N,c}$	± 0.010
$C_{h,c}$	± 0.001
$C_{h,tab}$	± 0.002

Tests

As mentioned in the introduction, most of the configurations were tested at Mach numbers from 0.70 to 0.98 for a wing angle-of-attack range from -1.5° to 17.5°. A take-off configuration (BWE with $\delta_{te} = 25^\circ$, $\delta_{tr} = 25^\circ$, and $\delta_{le} = 30^\circ$ or 45°) was tested at $M = 0.30$ at wing angles of attack from -3.5° to 26.5°. The approximate test range of Reynolds number per foot was from 2.0×10^6 to 4.5×10^6 as shown in figure 16. The test configuration variables are summarized in table III.

PRESENTATION OF RESULTS

The test results are plotted in coefficient form. The basic data, α, C_L, C_D, and C_m, for the model without the canard are presented in figures 17 to 36. Lift-curve slope, angle of zero lift, $C_{m_{C_L}}$, $C_{m,o}$, $C_{D,min}$, $(L/D)_{max}$, and C_L for $(L/D)_{max}$ for the model without the canard are compared in summary figures 37 to 64. The basic data, α, C_L, C_D, and C_m, for the model with the canard are presented in figures 65 to 71. The canard basic loads data, $C_{N,c}$ and $C_{h,c}$, are presented in figures 72 to 78 and canard trim-tab hinge-moment basic data, $C_{h,tab}$, are presented in figure 79. Trimmed drag polars for the model with the canard are presented in figure 80. Table III lists the configurations, test conditions, and the numbers of the figures in which these results are given.

DISCUSSION

Force Data for the Model Without the Canard

Effects of wing end plates.- The effects of wing end plates can be found by comparing models BW_1 and BW_1E with $\delta_{le} = 15^o$ in the basic-data figures 18 and 24 and in summary figures 37 to 40. Figures 18(c) and 24(c) show that the addition of end plates increased the model stability at low values of C_L for Mach numbers from 0.70 to 0.85. The end plates also increased the occurrence and severity of abrupt instability at high values of C_L. At all Mach numbers below 0.93, $(L/D)_{max}$ (fig. 40) was greater for the model with end plates despite an increase in $C_{D,min}$ (fig. 39). This increase in L/D was due to a reduction in the wing drag due to lift caused by the end plates.

Effects of deflection of leading-edge chord-extension.- The effects of deflection of leading-edge chord-extension can be found by comparing $\delta_{le} = 0^o$, 15^o, 25^o, and 30^o for configuration BWE and also $\delta_{le} = 0^o$, 15^o, and 30^o for configuration BW_1E in the basic-data figures 19 to 25 and in the summary figures 41 to 48. Values of δ_{le} of 15^o (figs. 20(c) and 24(c)) and 25^o (fig. 21(c)) generally improved the stability characteristics at a high value of C_L except for those at M = 0.95. Since $\delta_{le} = 15^o$ also gave the greatest value of $(L/D)_{max}$

(figs. 44 and 48), the best chord-extension deflection for cruise conditions was probably near 15°.

Effects of inboard leading-edge modifications.- The effects of inboard leading-edge modification can be found by comparing configurations BWE, BW_1E, and BW_2E for $\delta_{le} = 0^{\circ}$ in the basic-data figures 19, 23, and 26 and the summary figures 49 to 52. Detailed changes in the C_m curves of figures 19(c), 23(c), and 26(c) may be observed for these configurations but there was no significant improvement in stability characteristics. The roll-down cambered leading edge $\left(BW_1E\right)$ gave slightly higher $(L/D)_{max}$ (fig. 52) at Mach numbers up to 0.85 but the basic leading edge (BWE) was better at the higher Mach numbers.

Effects of wing fences.- The effects of wing fences can be found by comparing configurations BWE, $BWEF_1$, and $BWEF_2$ for $\delta_{le} = 15^{\circ}$ in the basic-data figures 20, 27, and 28 and in the summary figures 53 to 56. Neither fence $\left(F_1 \text{ or } F_2\right)$ improved the stability (figs. 20(c), 27(c), and 28(c)) enough to justify the loss in $(L/D)_{max}$ shown in figure 56. Both fences had about the same effect on stability, but the fence F_2 (nearest the discontinuity in the wing leading edge caused by the chord-extension) gave less increase in $C_{D,min}$ (fig. 55) and slightly greater $(L/D)_{max}$.

Effects of body filler.- The effects of body filler can be found by comparing configurations BWE and B_1WE with $\delta_{le} = 15^{\circ}$ in the basic-data figures 20 to 29, and in the summary figures 57 to 60. The instability at high C_L exhibited by model BWE (fig. 20(c)) was aggravated by the filler on model B_1WE (fig. 29(c)) especially at $M = 0.85$ and $M = 0.90$. Figure 58 shows that the filler also caused a large increase in $C_{m,o}$. An increase in $C_{D,min}$ (fig. 59) resulted in a substantial loss of $(L/D)_{max}$ (fig. 60) for the model with filler.

Effects of boundary-layer transition.- The effects of boundary-layer transition can be found by examining basic-data figures 21, 30, and 31 and summary figures 61 to 64 for configuration BWE $\left(\delta_{le} = 25^{\circ}\right)$ with free transition, standard transition strips, and transition grains distributed all around the wing leading edge. The value of $C_{D,min}$ for the standard transition strips (fig. 63) was between $C_{D,min}$ for the free transition (lowest) and $C_{D,min}$ for the distributed transition grains (highest). The effect of fixing transition was also evident in the basic data for C_L and C_m (figs. 21, 30, and 31). The configuration with free transition had more abrupt changes in C_L and C_m

associated with local flow separation on the wing than did the configurations with fixed transition.

Take-off characteristics.- Comparisons of the take-off configurations BWE and BW$_1$E with $\delta_{le} = 30^\circ$ and 45° and model BWEF$_1$ with $\delta_{le} = 45^\circ$ (all models with $\delta_{te} = 25^\circ$ and $\delta_{tr} = 25^\circ$) are shown in basic-data figures 32 to 36. The maximum lift coefficient obtained for the take-off configurations at $M = 0.30$ was about 1.15 for the leading-edge chord-extension deflected 30° (figs. 32 and 34) and about 1.07 for the chord-extension deflected 45° (figs. 33, 35, and 36). The lower chord-extension deflection was also better for stability at high lift coefficients (above $C_L = 0.6$) and therefore was better over all for a take-off configuration. The addition of fence F$_1$ did not improve the stability of configuration BWEF$_1$ for $\delta_{le} = 45^\circ$ (fig. 36) over that of configuration BWE for $\delta_{le} = 45^\circ$ (fig. 33).

Force Data for the Model With the Canard

A fixed canard is generally destabilizing; and since the tests of the configuration with the canard were conducted with the canard fixed, the model with the canard had its stability reduced with the result that it was actually unstable. However, the airplane would have the canard surface free floating so that its contribution would be essentially for trim purposes and would not affect the longitudinal stability. This characteristic of free-floating canards as longitudinal trim controls is discussed in reference 3 and should be kept in mind during the subsequent discussion of the data for the configuration with the canard. Some basic data for configuration BC are given in figures 65 and 66. The remainder of the basic data for the configuration with the canard surface (configuration BCW$_1$E with $\delta_{le} = 15^\circ$) are presented in figures 67 to 71 and may be compared for the effect of the canard with the data for configuration BW$_1$E with $\delta_{le} = 15^\circ$ in figure 24.

It is difficult to assess the effect of a free-floating canard on C_L, C_D, and C_m from the data obtained with canard fixed. The data would have to be interpolated for conditions in which both the model moments about the reference center and the canard moments about its hinge line were simultaneously trimmed. The effect of tab deflection was investigated only at $M = 0.85$. Therefore, it is only at this Mach number that sufficient data would be available for interpolation to determine canard trim conditions. This would severely limit the comparisons available. Some canard effects, however, may be seen from the untrimmed data of figures 67 to 71. The model minimum drag was not much increased by the canard at low canard deflections, nor was there a very pronounced effect of the canard on the wing stall or high lift stability characteristics. As expected, however, the fixed canard did increase the apparent lift-curve slope and gave the pitching-moment curves positive (unstable) slopes.

Trimmed drag polars.- Figure 80 contains trimmed drag polars obtained for model BCW_1E with $\delta_{le} = 15^\circ$ for $\delta_{tab} = -4^\circ$ at Mach numbers of 0.70, 0.85, and 0.90 and for $\delta_{tab} = 0^\circ$ and $\delta_{tab} = -8^\circ$ at a Mach number of 0.85. These polars were obtained for trimmed model moments but not for trimmed canard hinge-line moments. The following table lists the trimmed and untrimmed values of $(L/D)_{max}$ obtained for the model with inboard leading-edge camber and a leading-edge chord-extension deflection of 15°:

M	BCW_1E		BW_1E	BW_1
	δ_{tab}, deg	Trimmed $(L/D)_{max}$	Untrimmed $(L/D)_{max}$	Untrimmed $(L/D)_{max}$
0.70	-4	14.3	14.2	14.0
.85	-4	11.9	12.0	11.6
.90	-4	9.4	9.5	9.3
.85	0	12.2	12.0	11.6
.85	-8	11.6	12.0	11.6

The canard hinge moments were nearly trimmed at $(L/D)_{max}$ on the drag polars of figure 80 for $M = 0.85$ and $\delta_{tab} = -8^\circ$. A comparison of $(L/D)_{max}$ at this condition for models BCW_1E, BW_1E, and BW_1 shows that both the canard and the end plates were added to the configuration at no loss in maximum lift-drag ratio. The reason there was no loss is that the gain in $(L/D)_{max}$ as a result of the addition of end plates was large enough to offset the subsequent losses in $(L/D)_{max}$ caused by the addition of the canard and its associated trim loads.

Canard and tab loads.- The canard normal-force and hinge-moment coefficients are presented in figures 72 to 78 and the canard tab hinge-moment coefficients are presented in figure 79. The variation of $C_{h,c}$ with α at a fixed value of δ_c or with δ_c at a fixed value of α indicates that the canard was generally stable about its hinge line. The nonlinearities present in the $C_{h,c}$ data were apparently associated with the local angle of attack of the canard itself and were not a result of body interference. This may be seen from the data for $C_{h,c}$

of figure 76(c) in which the canard hinge moments are plotted against the canard angle of attack $\alpha + \delta_c$. A comparison of the appropriate data figures indicates that the mutual interference effects of the canard on the model components such as the body and wing, and of these components on the canard were small except for the interference of the body on the canard. This interference may be seen in the $C_{N,c}$ data of figures 72 to 78. The combinations of $\alpha + \delta_c$ for which the canard should have been alined with the free stream did not result in $C_{N,c} = 0$, probably because of an induced flow field at the body nose.

Canard effectiveness.- The canard effectiveness parameter $C_{m_{\delta_c}}$ was obtained from the C_m data of figures 65 to 71 at a constant angle of attack ($\alpha = 0^\circ$). The value of $C_{m_{\delta_c}}$ has also been calculated from the exposed panel canard loads (with no allowance for fuselage carryover or canard chord force effects) by the following equation:

$$C_{m_{\delta_c}} = 2\,\frac{S_c}{S}\left(\frac{\partial C_{L,c}}{\partial \delta_c}\,\frac{d}{\bar{c}} + \frac{\partial C_{h,c}}{\partial \delta_c}\,\frac{\bar{c}_c}{\bar{c}}\right)$$

where d is the distance from the canard hinge line to the model moment reference center. These results are compared in the following table:

Configuration	δ_{le}, deg	δ_{tab}, deg	M	$\frac{\partial C_{L,c}}{\partial \delta_c}$	$\frac{\partial C_{h,c}}{\partial \delta_c}$	Calculated $C_{m_{\delta_c}}$	Measured $C_{m_{\delta_c}}$
BC		0	0.80	0.0437	-0.0028	0.0075	0.0079
BC		0	.85	.0475	-.0035	.0081	.0080
BCW_1E	15	-4	.70	.0431	-.0030	.0074	.0079
BCW_1E	15	-4	.85	.0438	-.0034	.0075	.0079
BCW_1E	15	-4	.90	.0464	-.0029	.0079	.0074
BCW_1E	15	0	.85	.0429	-.0034	.0073	.0080
BCW_1E	15	-8	.85	.0458	-.0029	.0078	.0078

A comparison of the calculated and measured values of canard effectiveness $C_{m_{\delta_c}}$ shows that this parameter could be satisfactorily predicted from $C_{L,c}$ and $C_{h,c}$ despite the neglect of body carryover loads and canard chord force. In addition, the measured values of $C_{m_{\delta_c}}$ indicate that this parameter is not influenced appreciably by tab deflection, by Mach number variation from $M = 0.70$ to 0.90, or by the presence of the wing.

CONCLUSIONS

Wind-tunnel tests of a 1/30-scale, subsonic, nuclear-powered canard-airplane model showed that:

1. The model with end plates mounted at the wing tips as vertical tails had a slightly higher maximum lift-drag ratio than a tailless model.

2. A leading-edge chord-extension deflection of 15° was the best chord-extension deflection for stability at high lift coefficient and for maximum lift-drag ratio.

3. Neither a thickened leading edge nor roll-down camber on the wing inboard leading edge gave any significant improvement in the model aerodynamic characteristics.

4. Wing fences at two different spanwise wing positions were not significantly effective in eliminating the adverse wing longitudinal stability characteristics at high lift coefficients and also produced large losses in maximum lift-drag ratio.

5. A filler, which increased the solid cross-sectional area of the engine nacelles, adversely affected the model longitudinal stability at high lift coefficients and reduced the maximum lift-drag ratio.

6. The maximum lift-drag ratio for the model trimmed with the canard and end plates was the same as that for the untrimmed model without the canard and end plates. The reason there was no loss is that the gain in maximum lift-drag ratio as a result of the addition of end plates was large enough to offset the loss incurred by the addition of the canard and its associated trim loads.

7. Except for the effect of the body induced flow field, the canard-surface loads were relatively unaffected by the presence of the other model components; and canard effectiveness was satisfactorily predicted from measured exposed-panel canard loads.

Langley Research Center,
National Aeronautics and Space Administration,
Langley Air Force Base, Va., January 17, 1962.

REFERENCES

1. Igoe, William B., Capone, Francis J., and Re, Richard J.: Subsonic Longitudinal Aerodynamic Characteristics of a 1/30-Scale Canard-Airplane Model Having a Wing With an Aspect Ratio of 6.0. NASA TM X-668, 1962.

2. Ward, Vernon G., Whitcomb, Charles F., and Pearson, Merwin D.: Air-Flow and Power Characteristics of the Langley 16-Foot Transonic Tunnel With Slotted Test Section. NACA RM L52E01, 1952.

3. Bates, William R.: Low-Speed Static Longitudinal Stability Characteristics of a Canard Model Having a 60° Triangular Wing and Horizontal Tail. NACA RM L9H17, 1949.

TABLE I.- MODEL GEOMETRICAL CHARACTERISTICS

Wing:	
Aspect ratio -	
Basic planform	3.789
Including leading-edge chord-extension	3.6
Planform area -	
Basic planform, sq ft	[a]5.2778
Including leading-edge chord-extension, sq ft	5.5556
Mean aerodynamic chord, basic planform, in.	[a]15.029
Fuselage station of $0.25\bar{c}$, in.	40.060
Taper ratio (basic planform)	0.4
Quarter-chord sweepback angle (basic planform), deg	48.285
Root-chord incidence (relative to WL plane), deg	1.5
Dihedral angle outboard of SS 6.333, deg	4
Airfoil section (linear variation of airfoil thickness between SS) at -	
SS 0	NACA 0011.86-65 (modified)
SS 6.333	NACA 0010.7-65
SS 16.833	NACA 0007.6-65
SS 16.833	NACA 0007.6-65 (modified)
SS 26.833	NACA 0007.6-65 (modified)
End plate - upper part:	
Planform area (one side), sq ft	0.35160
Taper ratio	0.1634
Airfoil section	NACA 0008-65
End plate - lower part:	
Planform area (one side), sq ft	0.11573
Airfoil section	NACA 0007.2-65
Canard:	
Aspect ratio	2.093
Planform area, sq ft	0.72369
Exposed area (one side), sq ft	[a]0.21144
Exposed semispan, in.	5.384
Mean aerodynamic chord (of exposed area), in.	[a]6.494
Dihedral angle, deg	0
Airfoil section	NACA 0006-64
Hinge-line sweepback angle, deg	0
Tab area (one side), sq ft	[a]0.012874
Tab mean aerodynamic chord, in.	[a]0.943

[a]Data reduction constant.

TABLE II.- WETTED AREAS

Configuration	Area, sq in.
BW	2,573
BWE	2,824
B_1WE	2,891
$BWEF_1$	2,849
BCWE	2,953

TABLE III.- INDEX TO FIGURES

(a) Basic data

Configuration	Mach number	δ_{le}, deg	δ_c, deg	δ_{tab}, deg	δ_{te}, deg	δ_{tr}, deg	Boundary-layer transition	Figure
				Model forces				
B	0.60 to 0.98						Fixed	17
BW_1	.70 to .98	15			0	0	Fixed	18
BWE	.70 to .98	0			0	0	Fixed	19
BWE	.70 to .98	15			0	0	Fixed	20
BWE	.70 to .90	25			0	0	Fixed	21
BWE	.70 to .90	30			0	0	Fixed	22
BW_1E	.70 to .90	0			0	0	Fixed	23
BW_1E	.70 to .90	15			0	0	Fixed	24
BW_1E	.70 to .90	30			0	0	Fixed	25
BW_2E	.70 to .98	0			0	0	Fixed	26
$BWEF_1$	.70 to .98	15			0	0	Fixed	27
$BWEF_2$	.70 to .90	15			0	0	Fixed	28
B_1WE	.70 to .90	15			0	0	Fixed[a]	29
BWE	.70 to .90	25			0	0	Free	30
BWE	.70 to .90	25			0	0	Fixed	31
BWE	.30	30			25	25	Fixed	32
BWE	.30	45			25	25	Fixed	33
BW_1E	.30	30			25	25	Fixed	34
BW_1E	.30	45			25	25	Fixed	35
$BWEF_1$	.30	45			25	25	Fixed	36
BC	.80		-10, 2	0			Fixed	65
BC	.85		-12, 0	0			Fixed	66
BCW_1E	.85	15	-12 to 0	0	0	0	Fixed	67
BCW_1E	.70	15	-12 to 4	-4	0	0	Fixed	68
BCW_1E	.85	15	-12 to 4	-4	0	0	Fixed	69
BCW_1E	.90	15	-12 to 4	-4	0	0	Fixed	70
BCW_1E	.85	15	-8 to 8	-8	0	0	Fixed	71
				Canard loads				
BC	0.80		-10, 2	0			Fixed	72
BC	.85		-12, 0	0			Fixed	73
BCW_1E	.85	15	-12 to 0	0	0	0	Fixed	74
BCW_1E	.70	15	-12 to 4	-4	0	0	Fixed	75
BCW_1E	.85	15	-12 to 4	-4	0	0	Fixed	76
BCW_1E	.90	15	-12 to 4	-4	0	0	Fixed	77
BCW_1E	.85	15	-8 to 8	-8	0	0	Fixed	78
				Tab loads				
BCW_1E	0.70, 0.85, and 0.90	15	-12 to 8	-8, -4, 0	0	0	Fixed	79

[a]Fixed with roughness strips distributed around wing leading edge.

TABLE III.- INDEX TO FIGURES - Concluded

(b) Summary of data

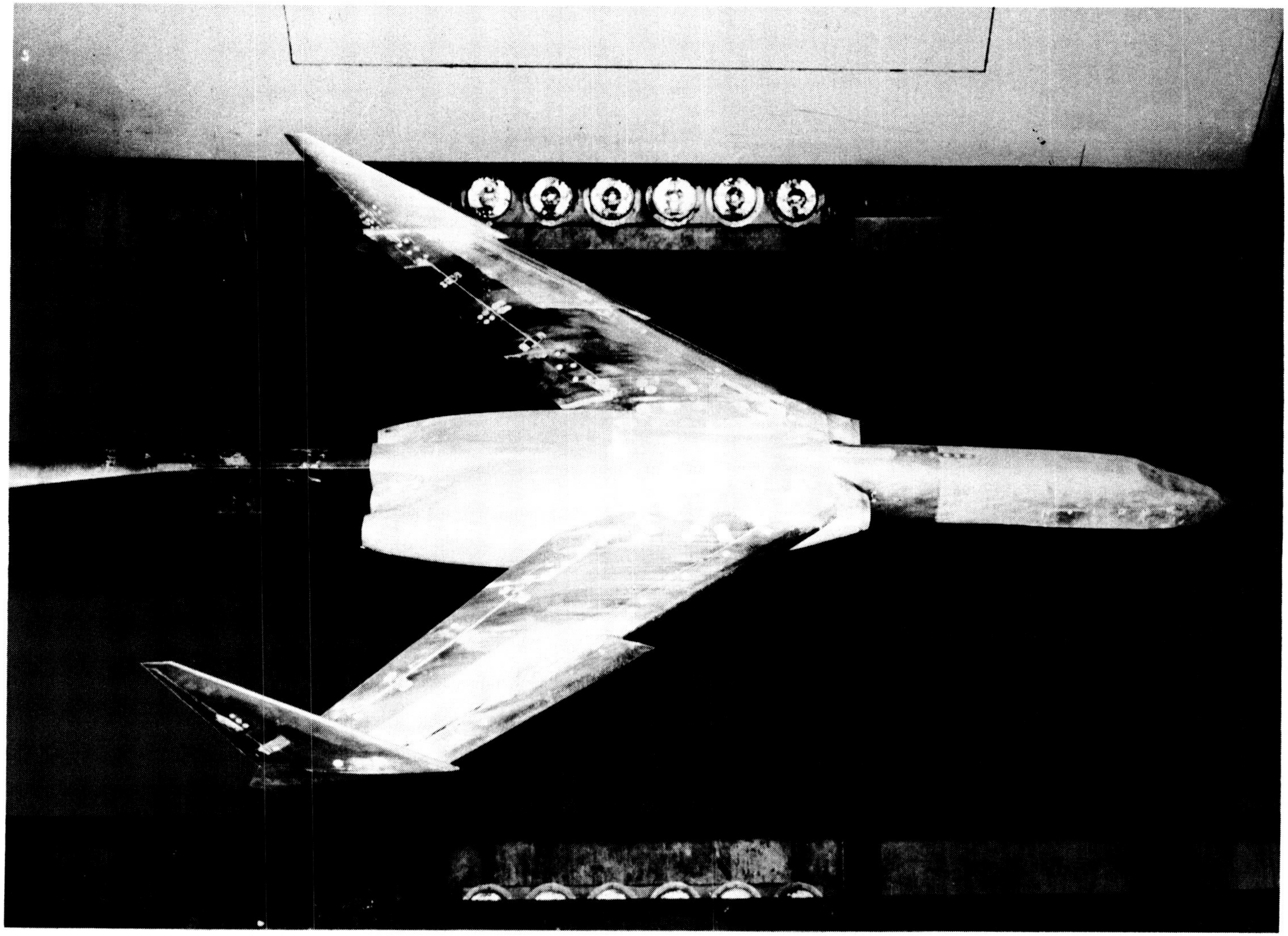

L-60-1646.1

Figure 1.- Photograph of model BWE $\left(\delta_{le} = 25^{\circ}\right)$ in Langley 16-foot transonic tunnel.

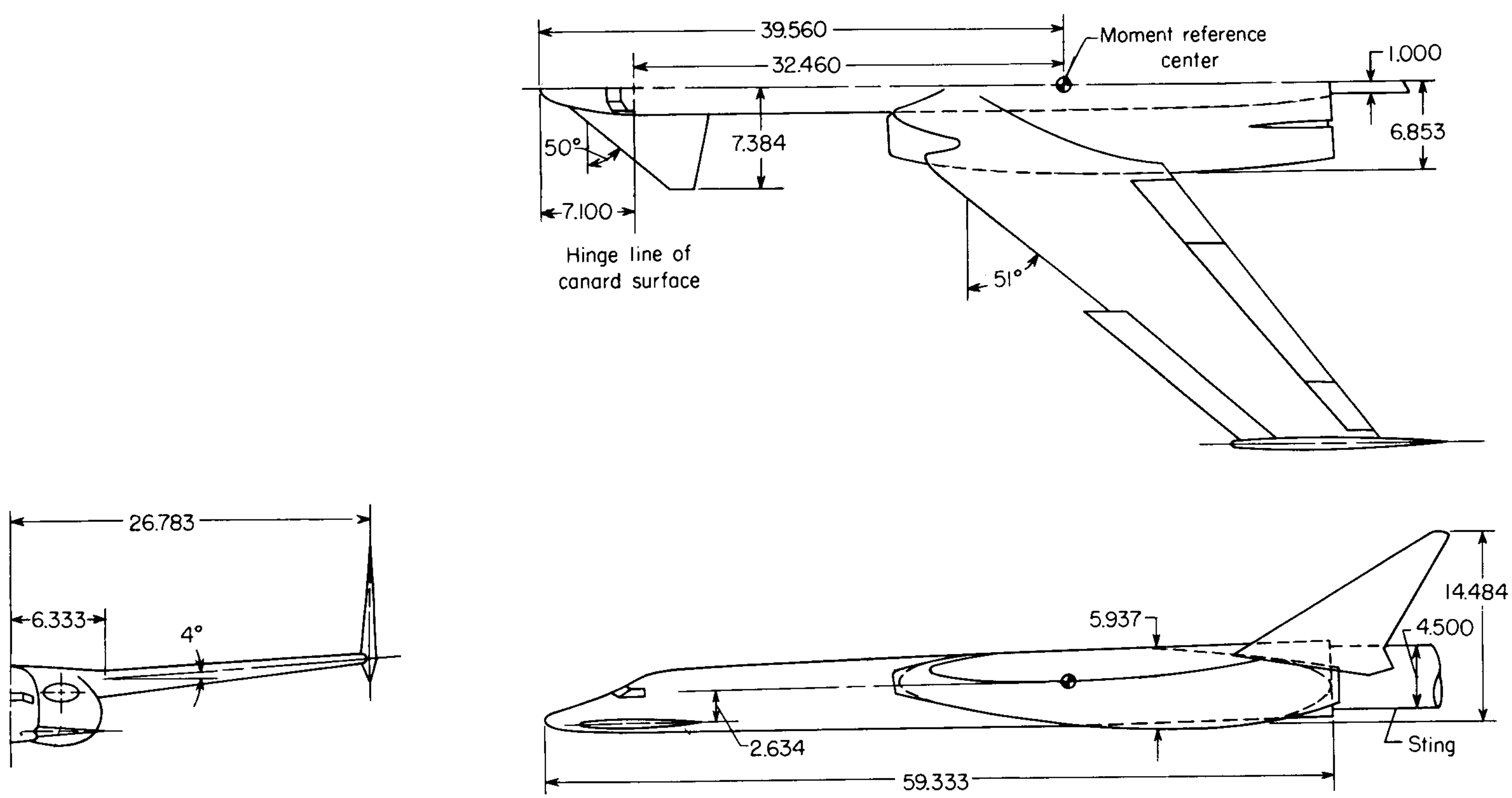

Figure 2.- General arrangement of model. All dimensions in inches unless otherwise noted.

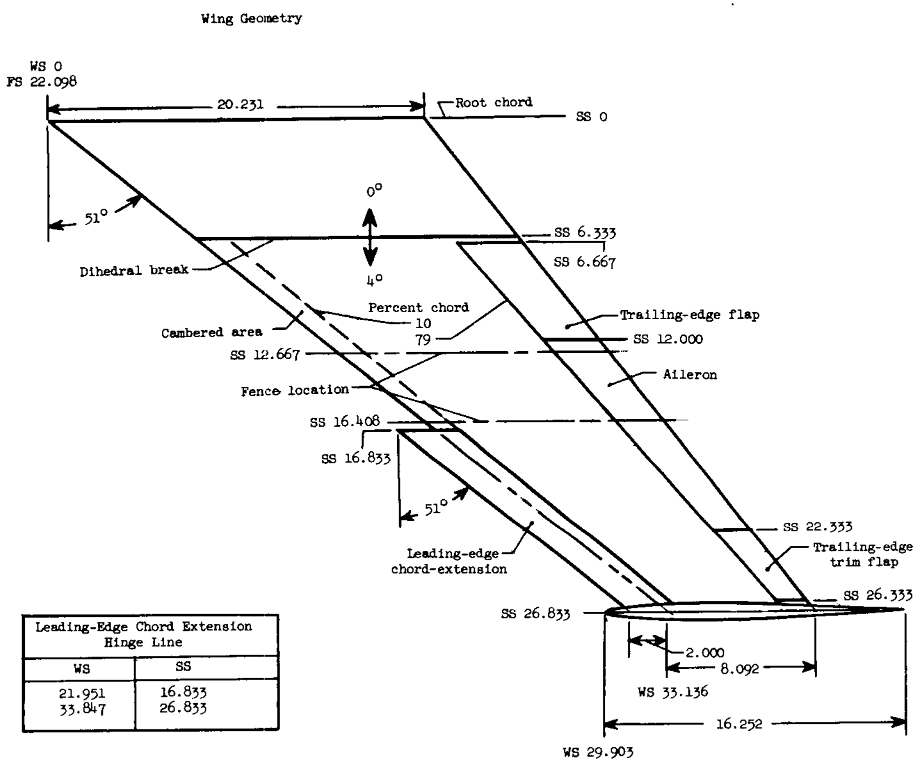

Leading-Edge Chord Extension Hinge Line	
WS	SS
21.951	16.833
33.847	26.833

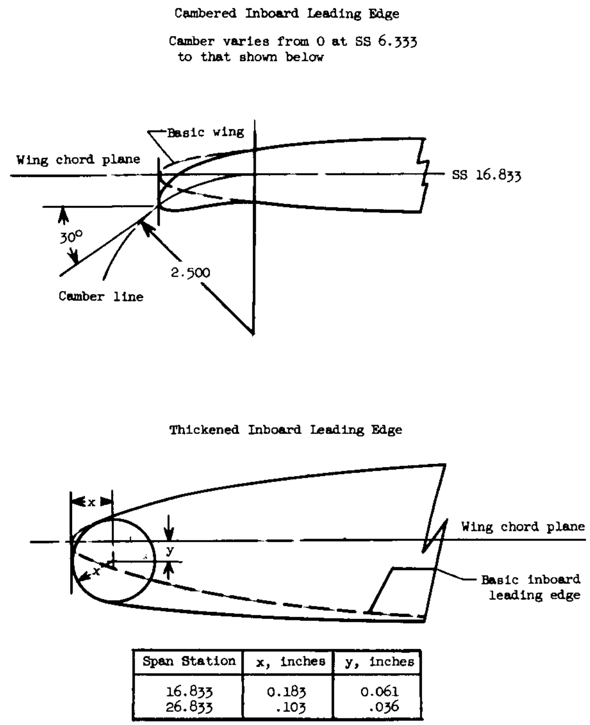

Span Station	x, inches	y, inches
16.833	0.183	0.061
26.833	.103	.036

Figure 3.- Dimensional details of wing and leading-edge variations. All dimensions in inches unless otherwise noted.

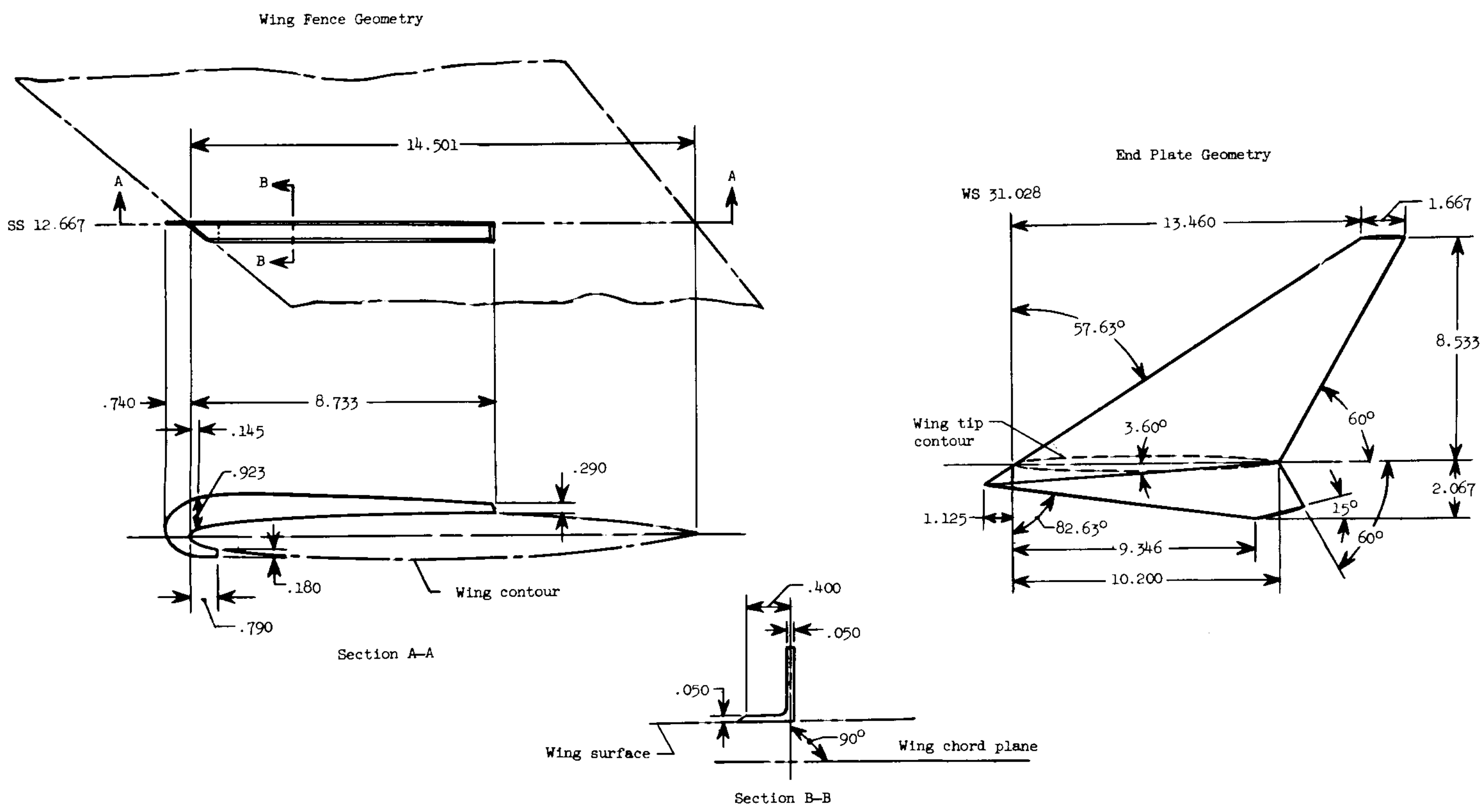

Figure 4.- Sketch showing wing fence details and end-plate geometry. All dimensions in inches unless otherwise noted.

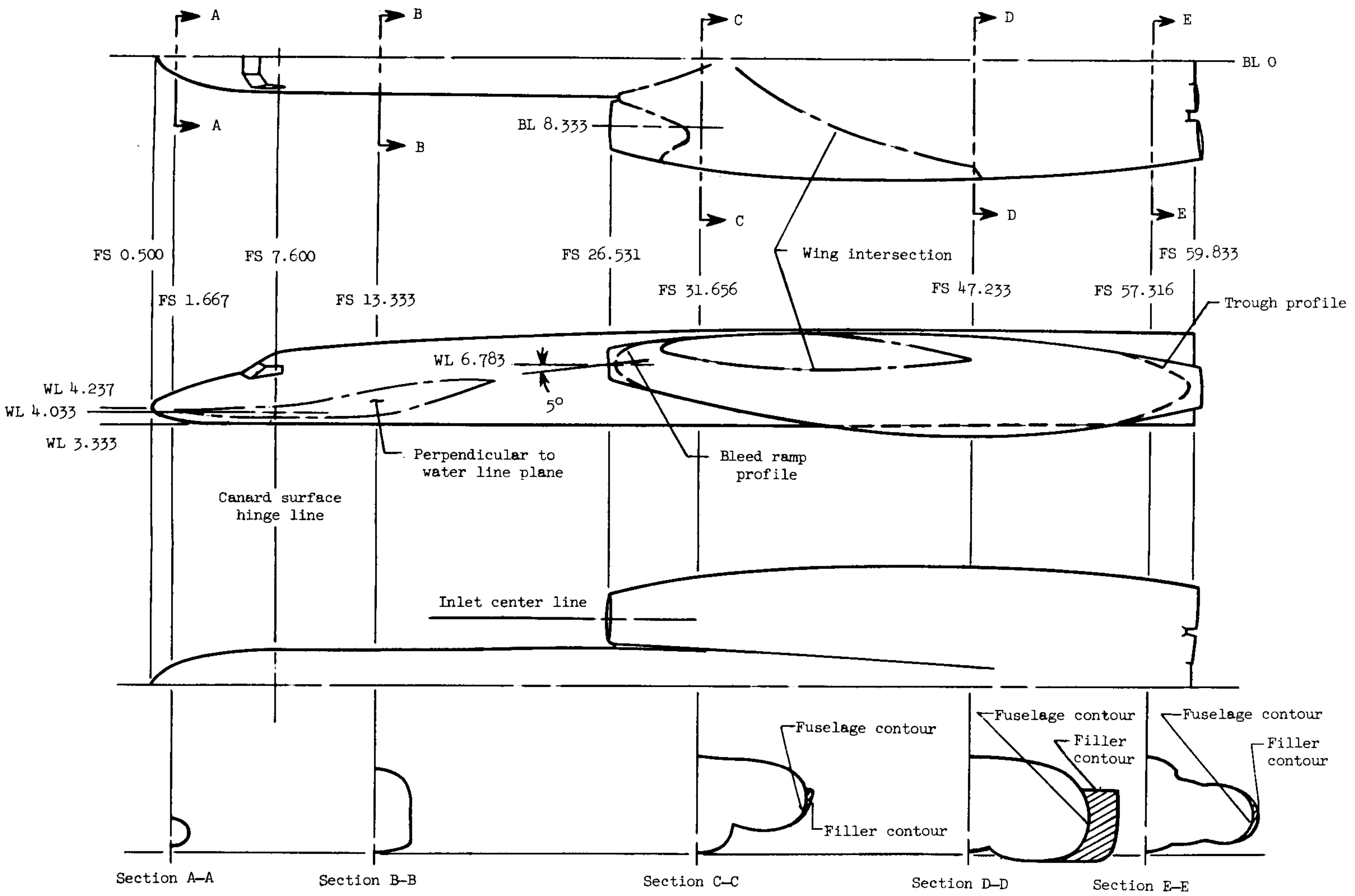

Figure 5.- External geometry of fuselage, nacelle, and filler. All dimensions in inches unless otherwise noted.

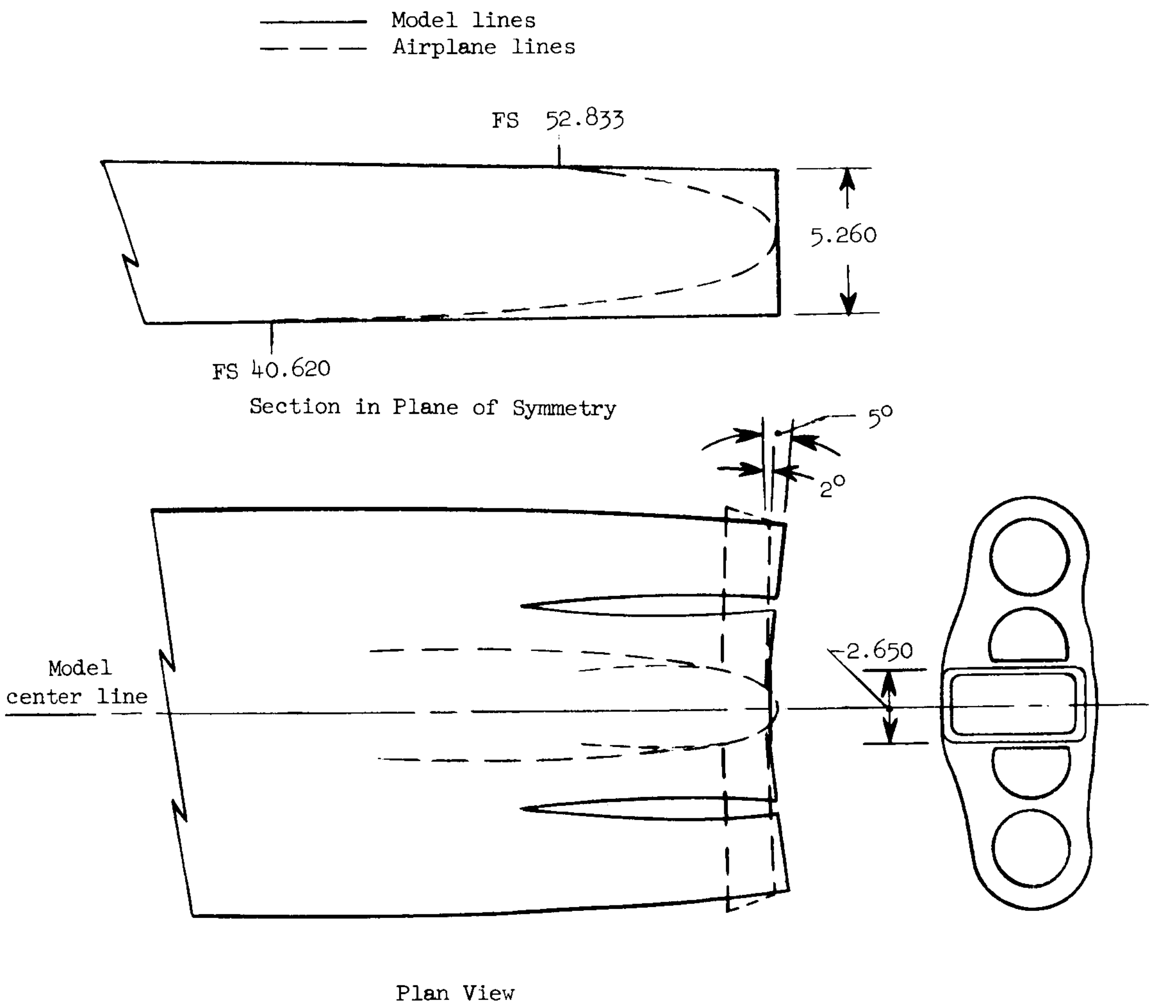

Figure 6.- Sketch showing differences between model and airplane aft ends. All dimensions in inches unless otherwise noted.

DEC[redacted]

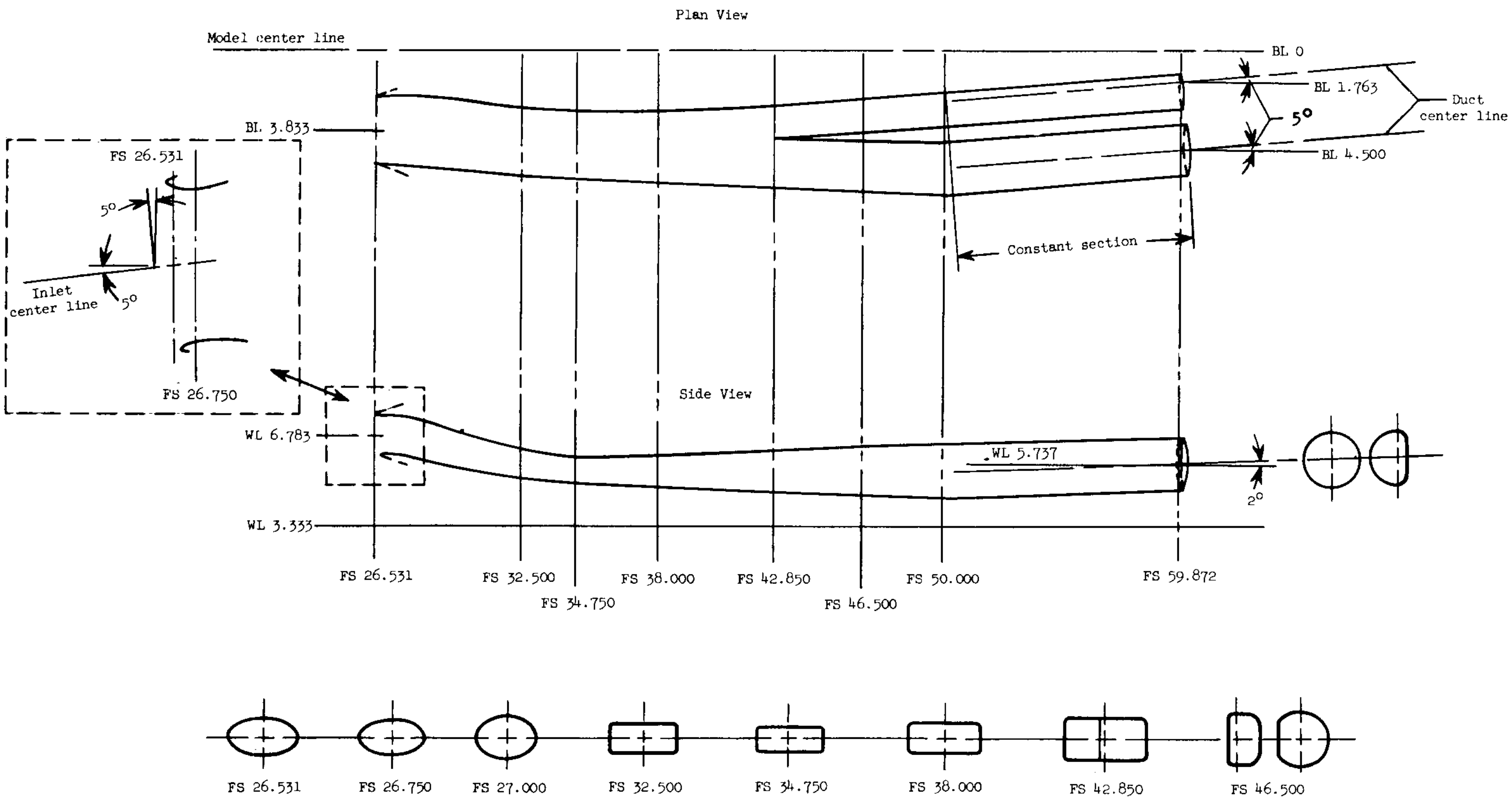

Figure 7.- Sketch of nacelle ducting. All dimensions in inches unless otherwise noted.

CON[redacted]AL

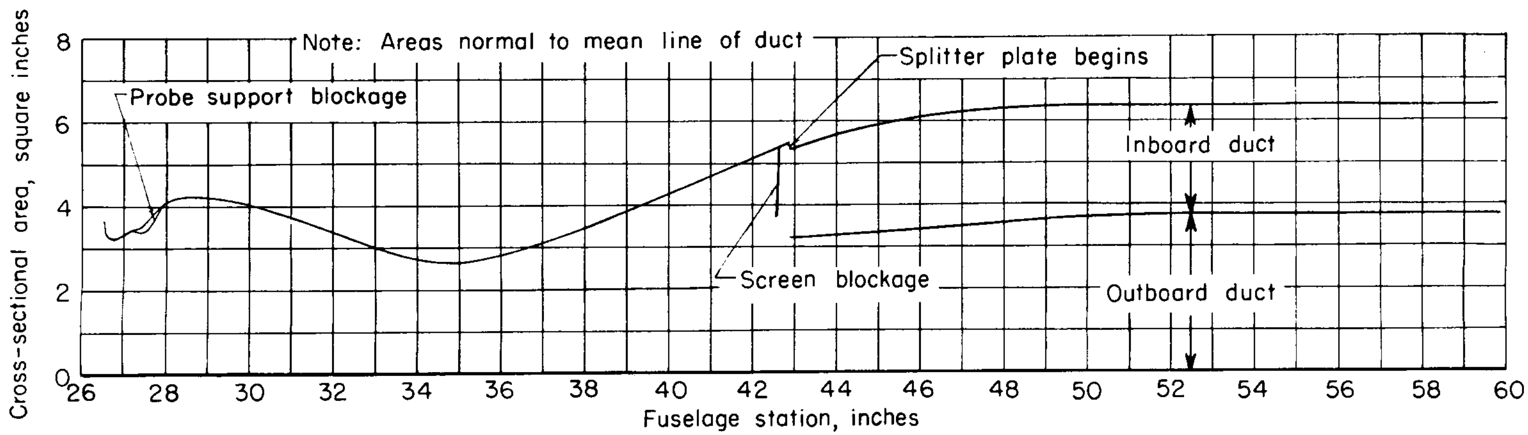

Figure 8.- Cross-sectional area distribution of nacelle ducting.

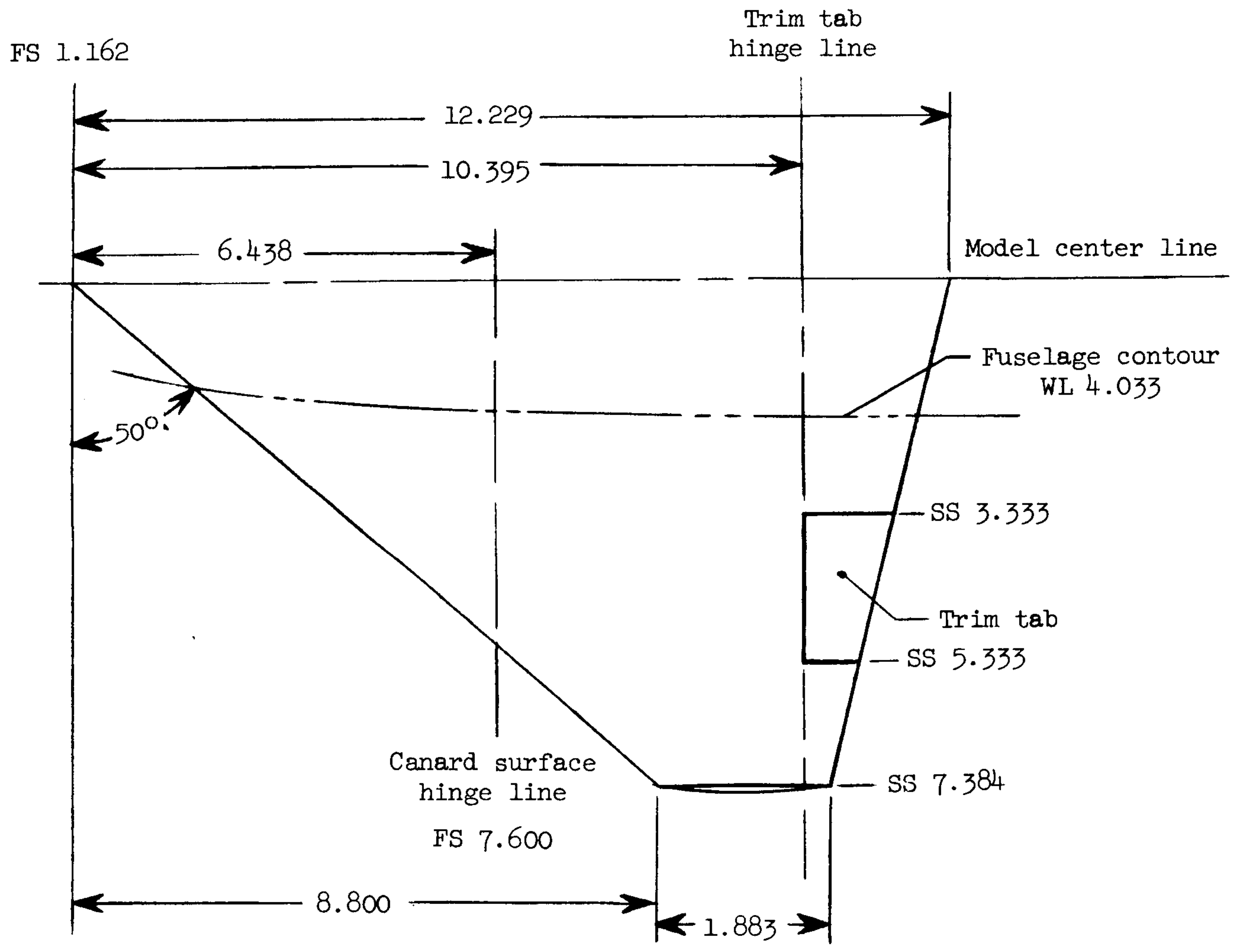

Figure 9.- Sketch of canard planform. All dimensions in inches unless otherwise noted.

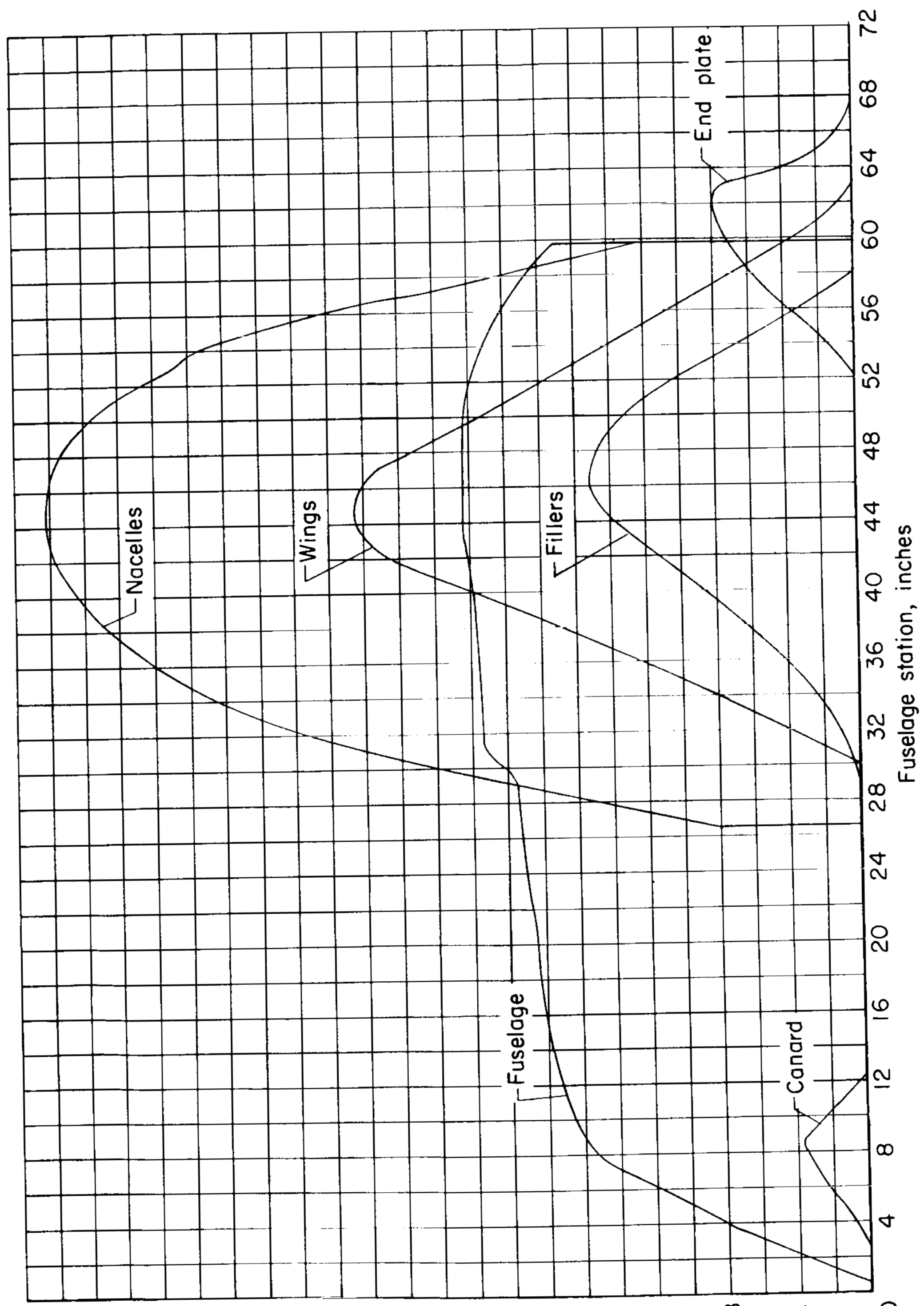

Figure 10.- Cross-sectional area distributions of model components.

L-1041

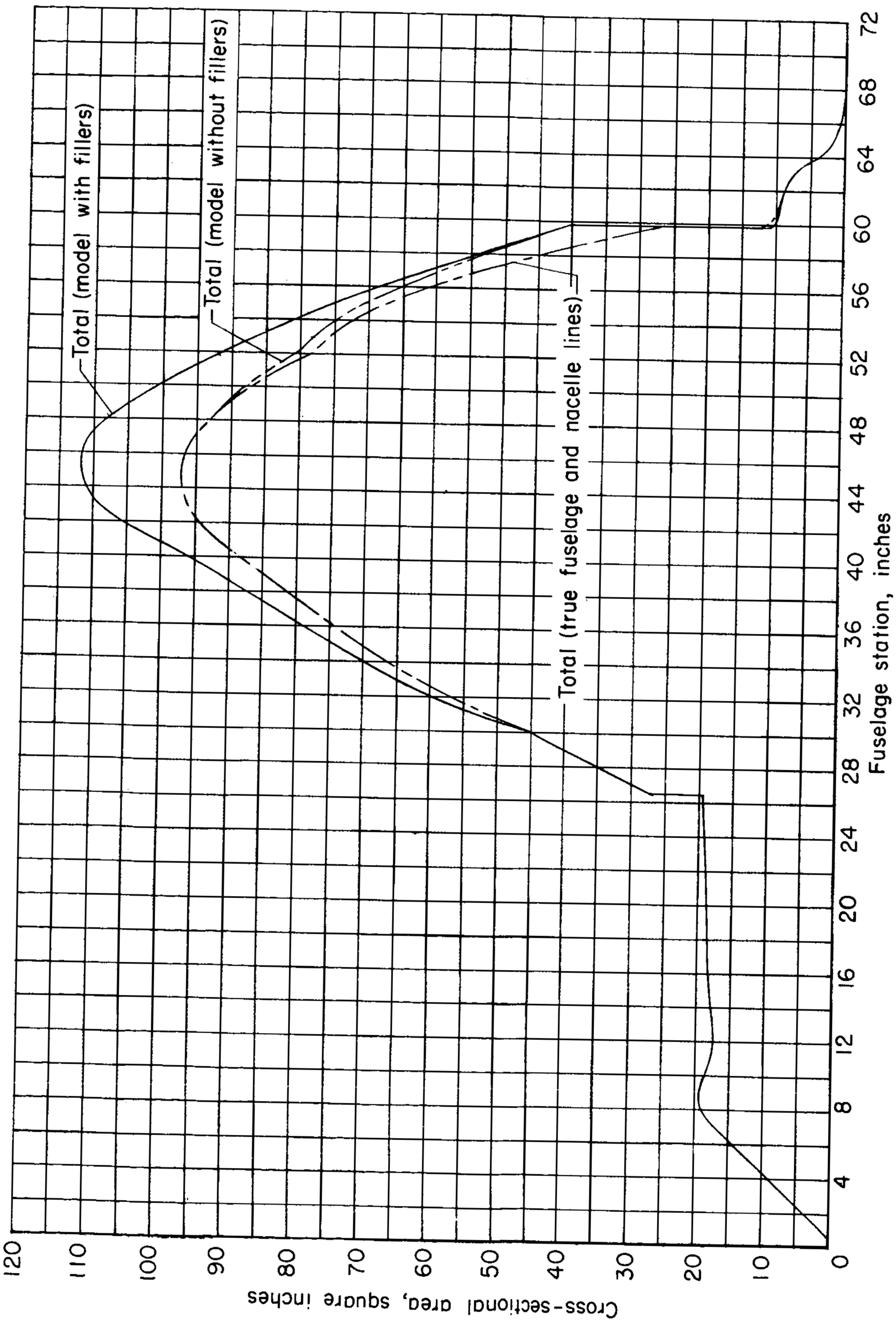

Figure 11.- Cross-sectional area distributions.

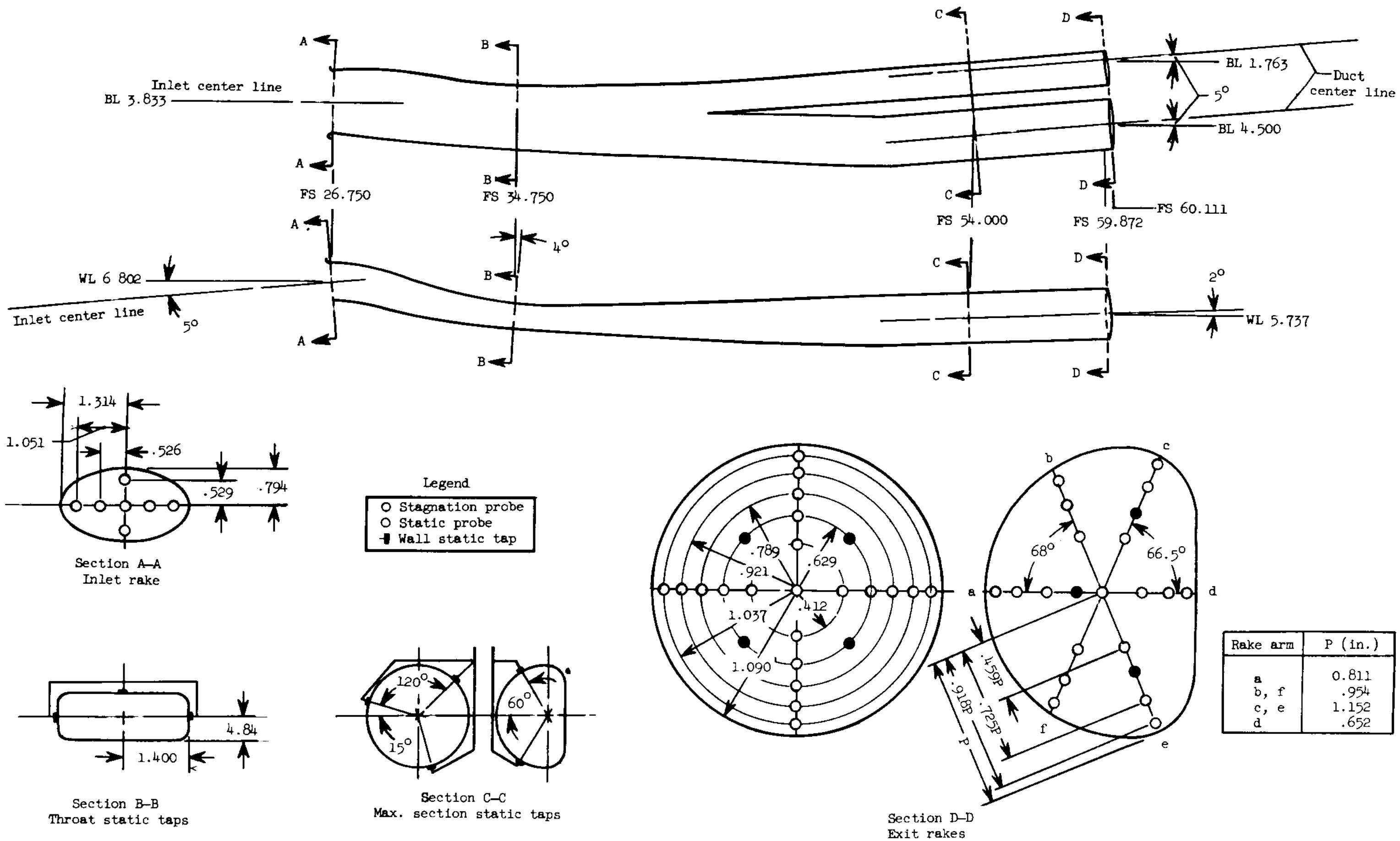

Rake arm	P (in.)
a	0.811
b, f	.954
c, e	1.152
d	.652

Figure 12.- Details of nacelle duct pressure instrumentation. All dimensions in inches unless otherwise noted.

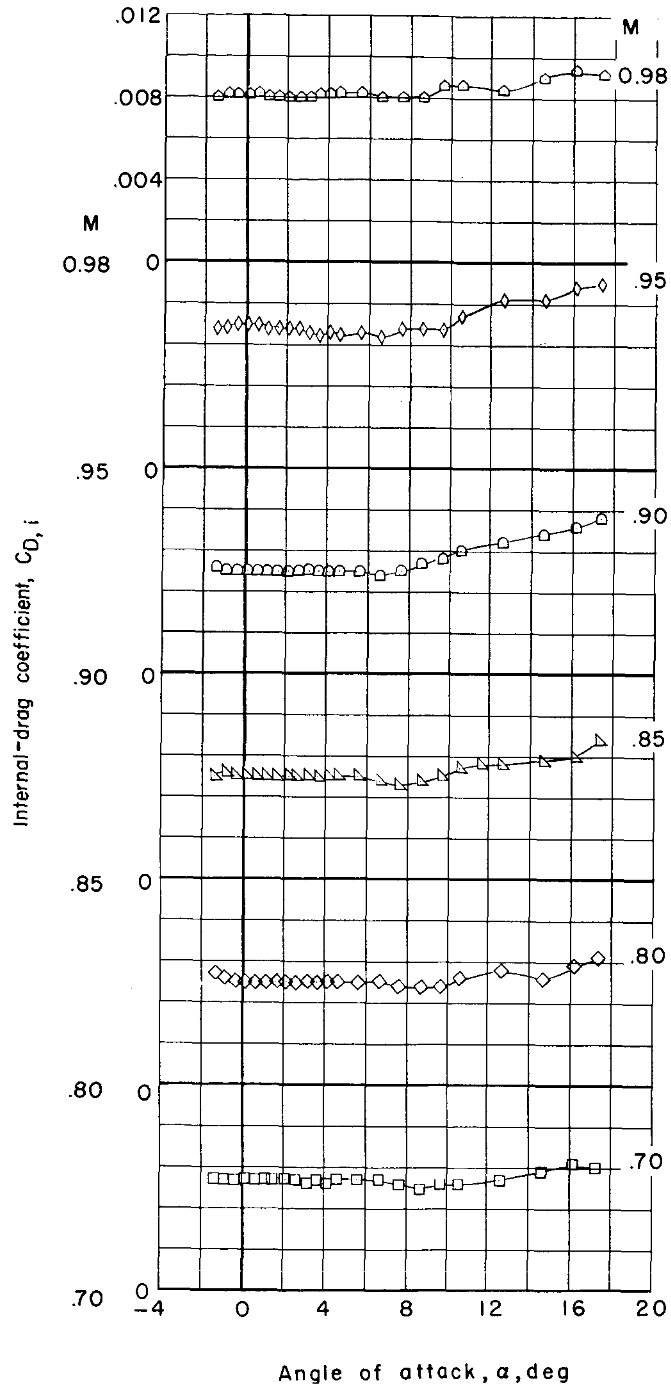

(a) Model BW_1E with $\delta_{le} = 15^{\circ}$.

Figure 13.- Variation of nacelle internal-drag coefficient with angle of attack.

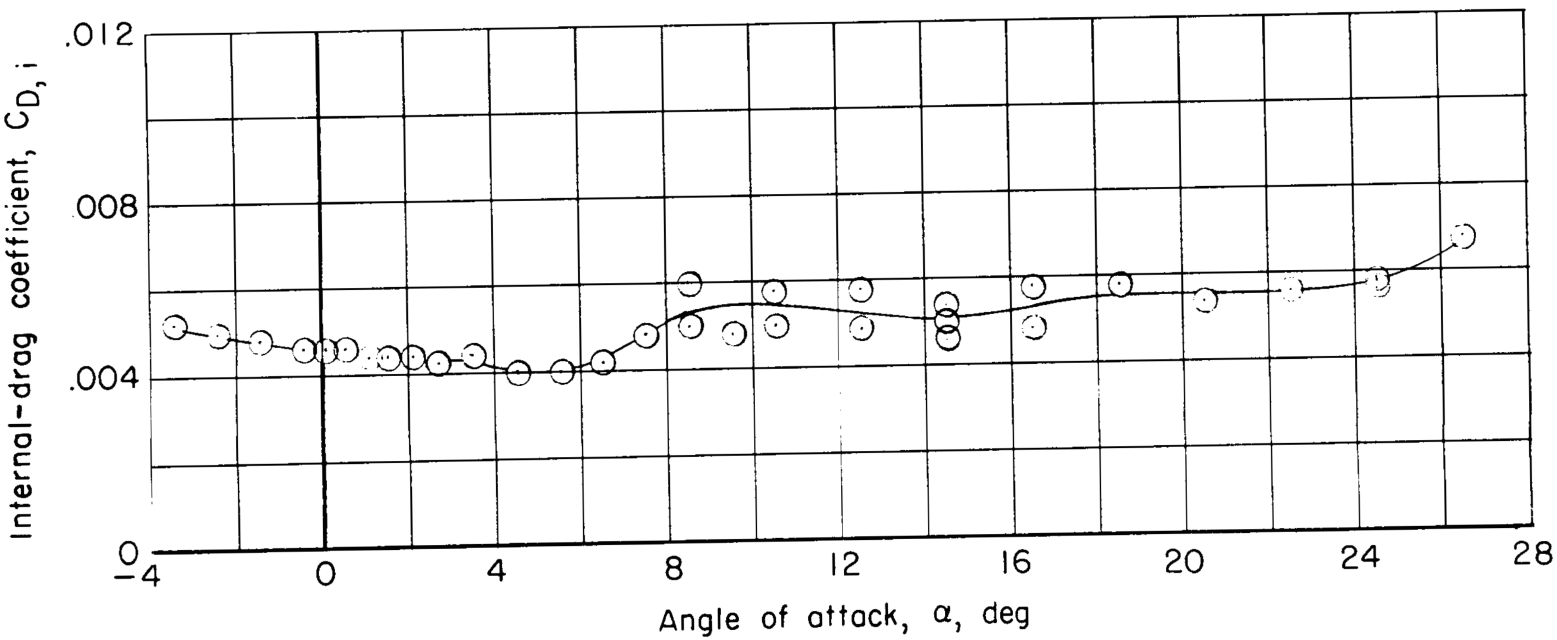

(b) Model BW_1E with $\delta_{le} = 30^\circ$ at $M = 0.30$.

Figure 13.- Concluded.

DECLASSIFIED

CON[redacted]AL

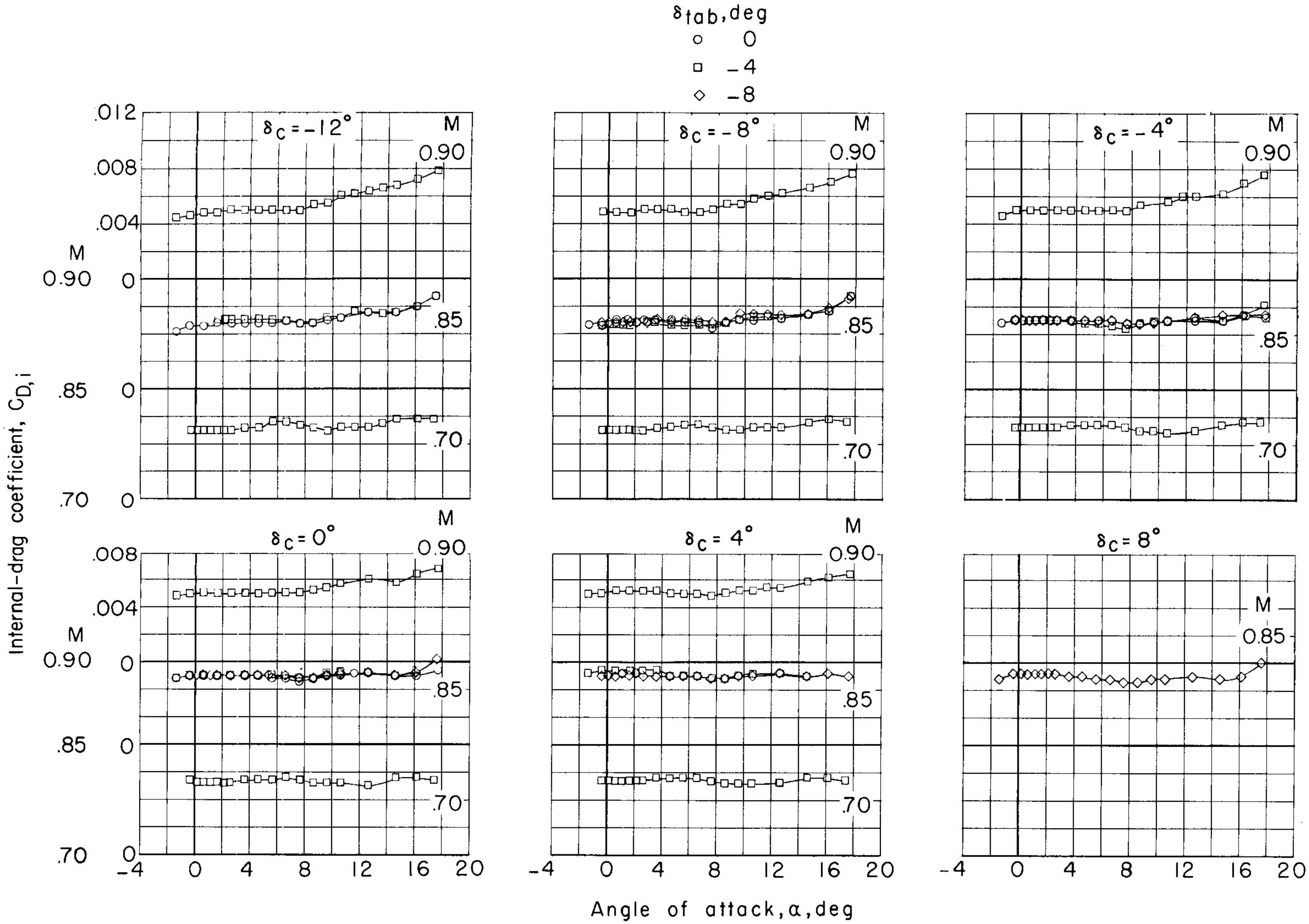

Figure 14.- Variation of internal-drag coefficient with angle of attack for model BCW_1E with $\delta_{le} = 15°$.

CO[redacted]TIAL

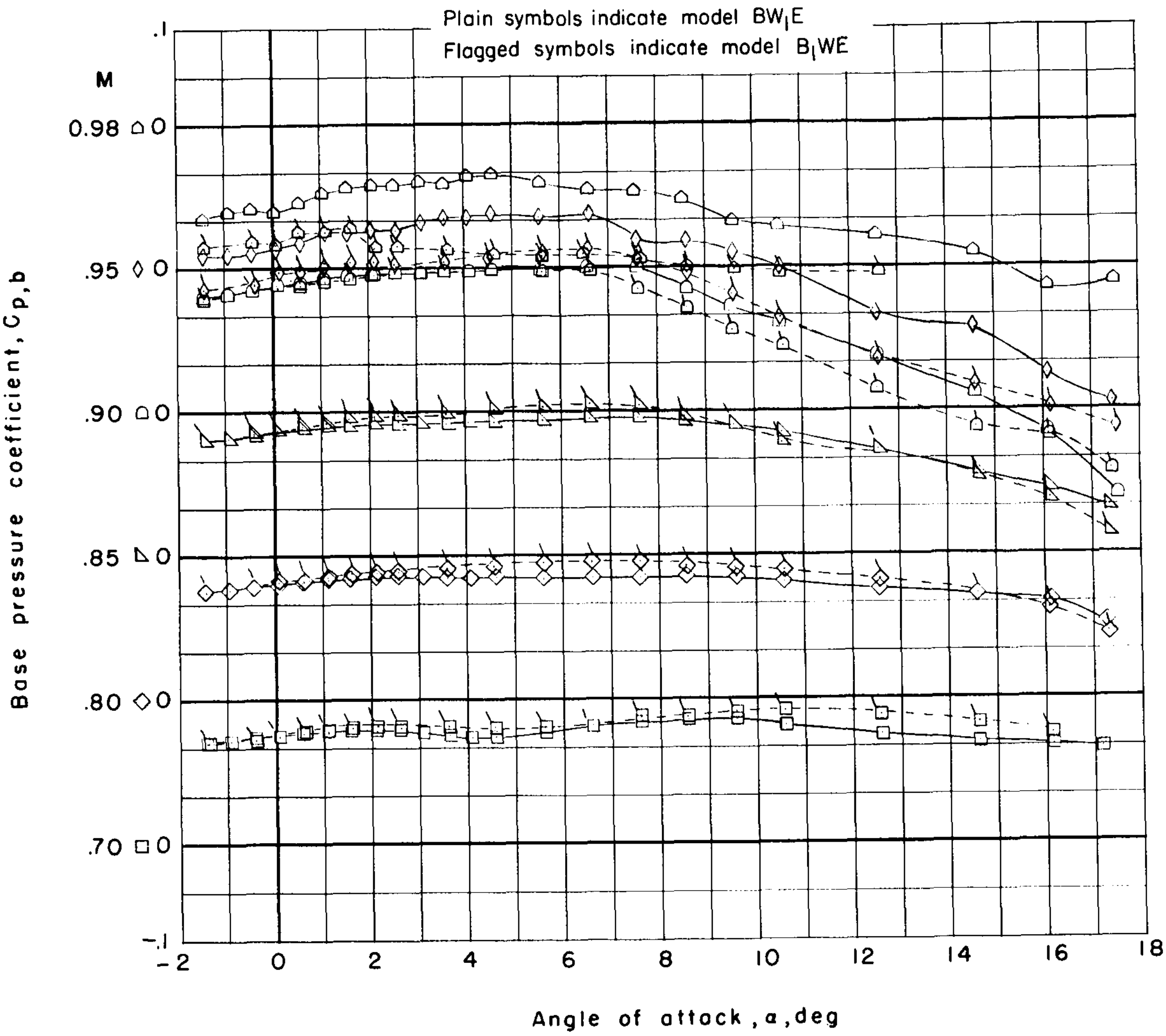

(a) Models BW_1E and B_1WE with $\delta_{le} = 15^{\circ}$.

Figure 15.- Variation of model base pressure coefficient with angle of attack.

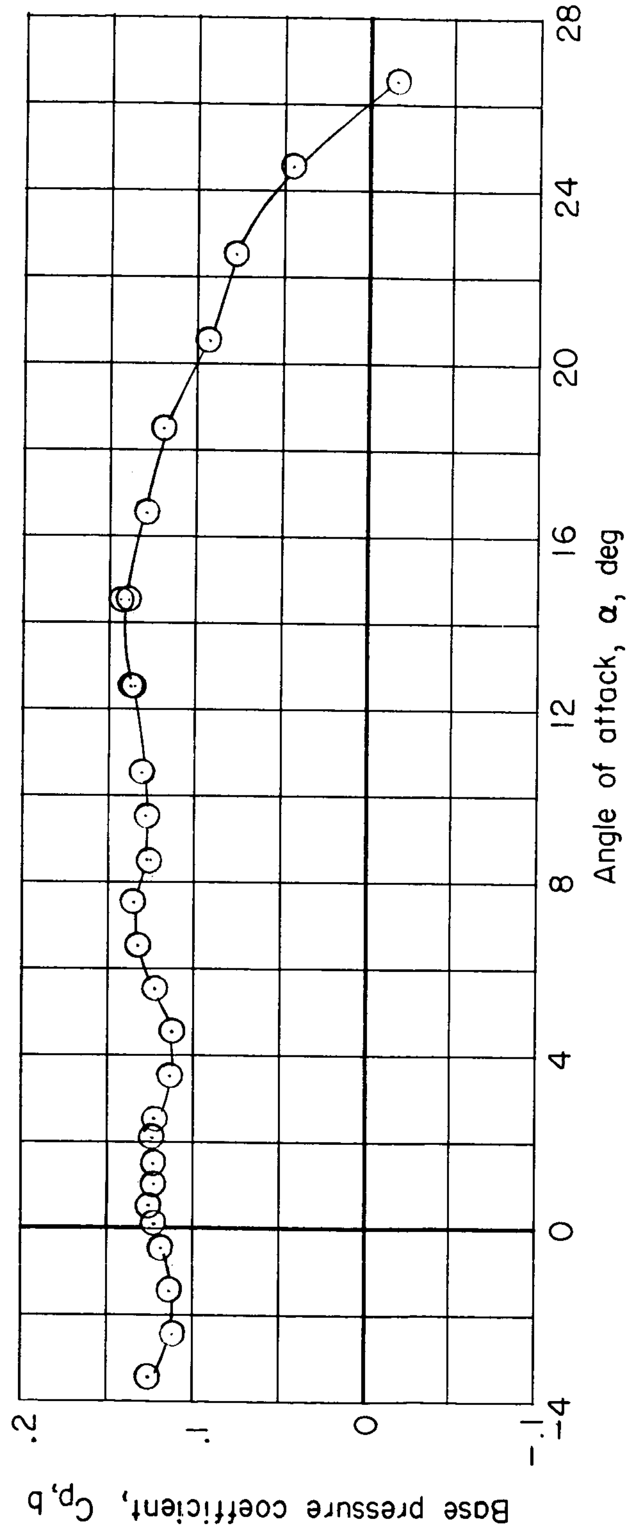

(b) Model BW_1E with $\delta_{le} = 30^{\circ}$ at M = 0.30.

Figure 15.- Concluded.

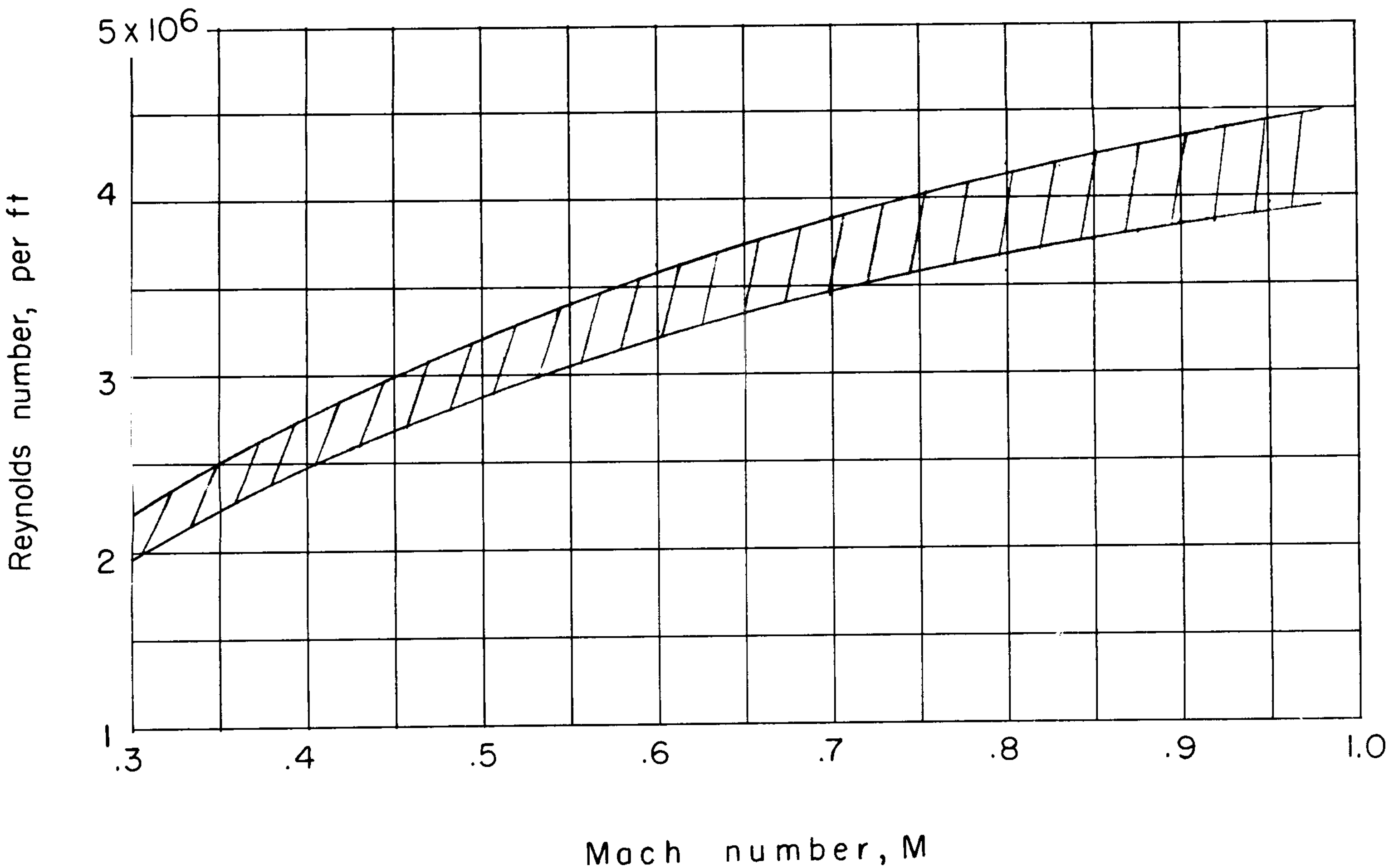

Figure 16.- Variation of Reynolds number (per foot) with Mach number for the Langley 16-foot transonic tunnel.

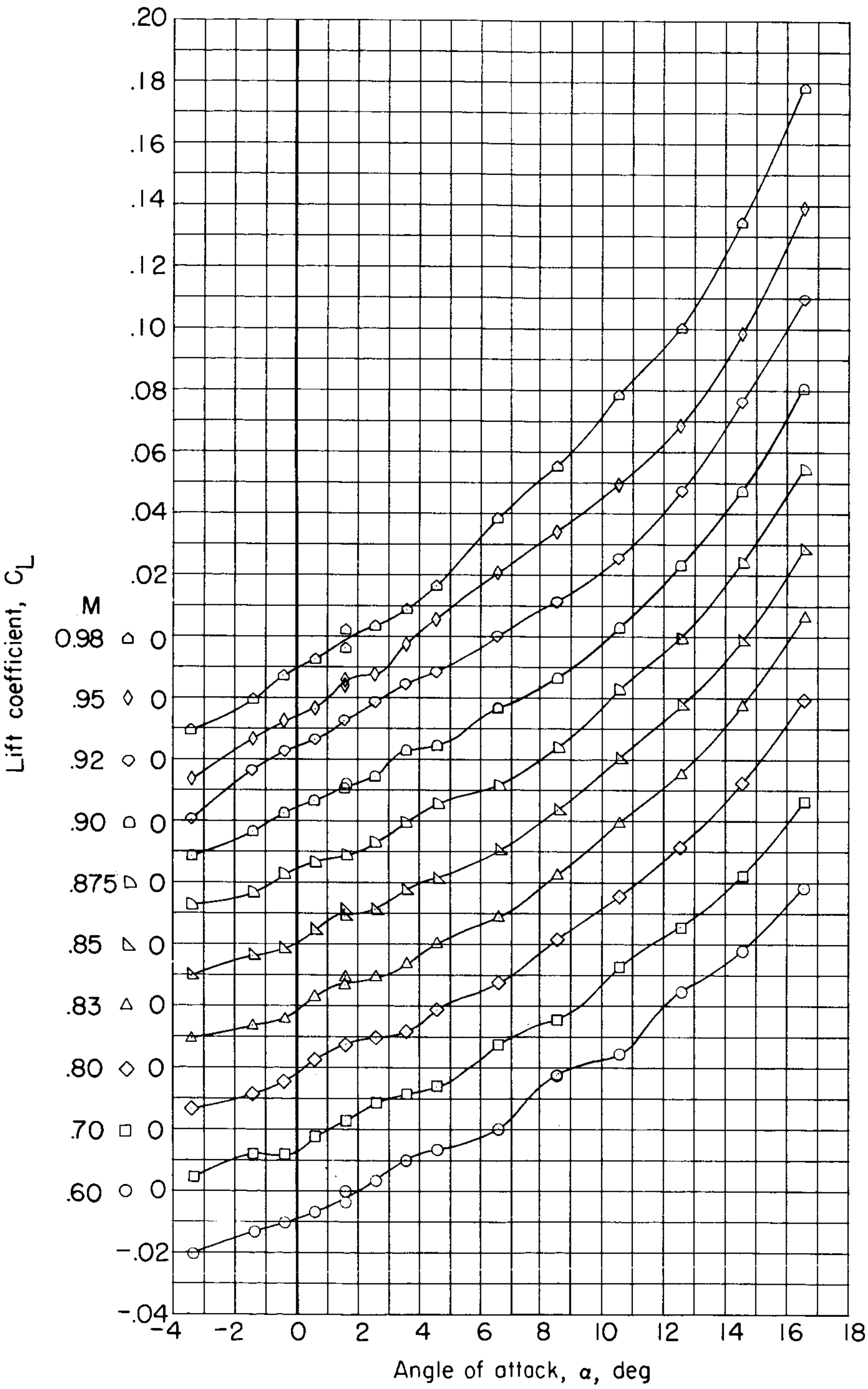

(a) Lift coefficient.

Figure 17.- Aerodynamic characteristics for model B.

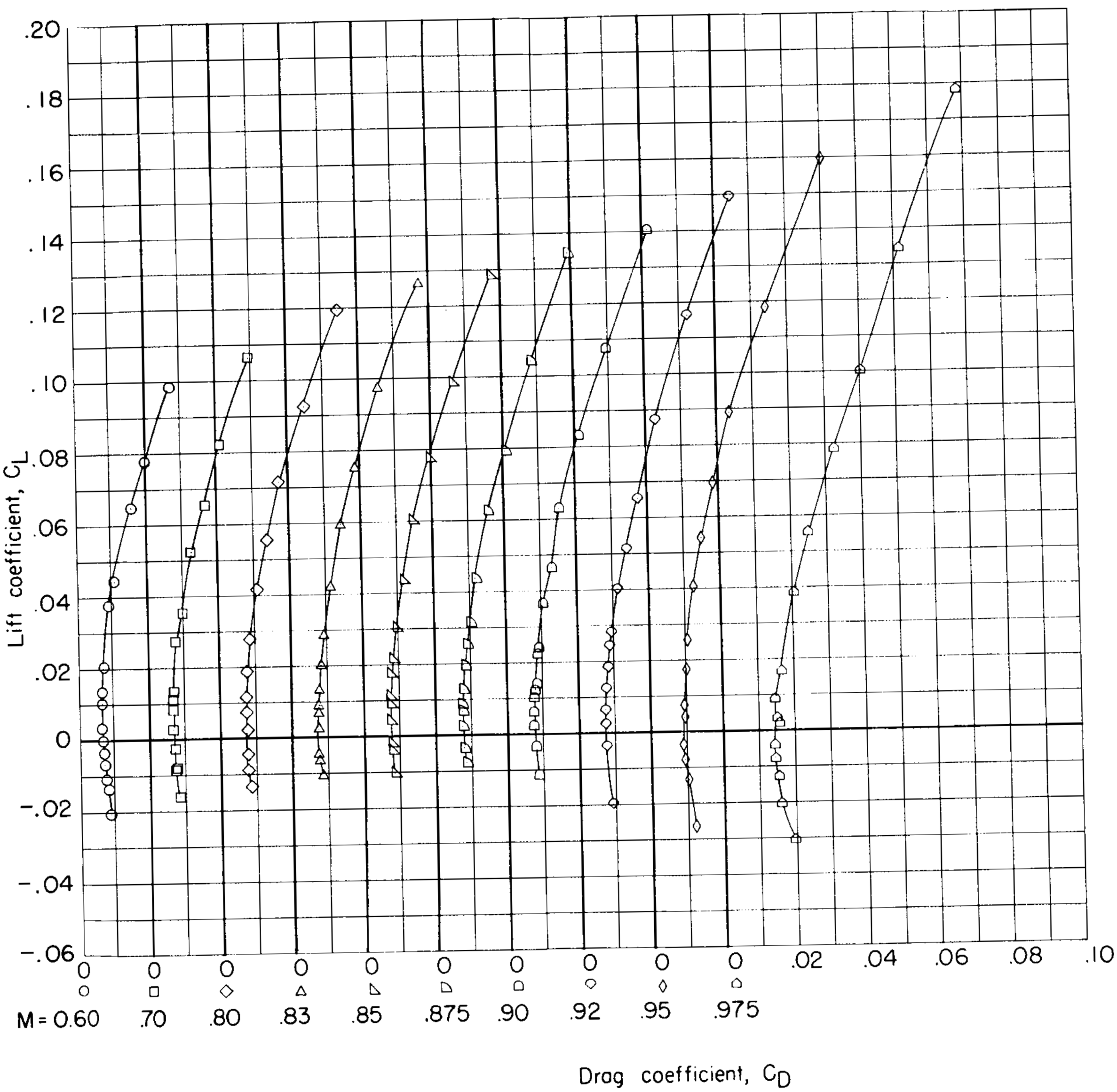

(b) Drag coefficient.

Figure 17.- Continued.

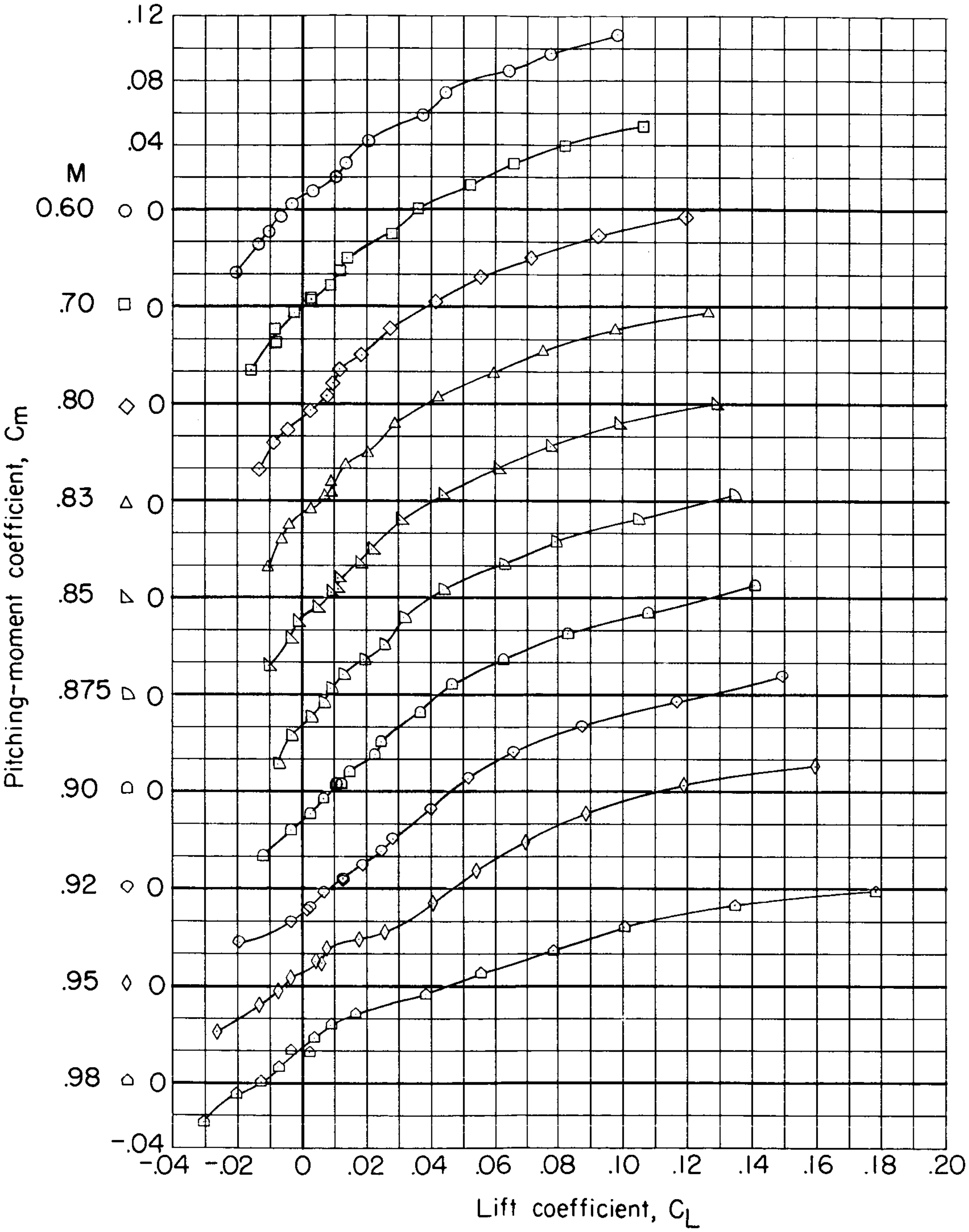

(c) Pitching-moment coefficient.

Figure 17.- Concluded.

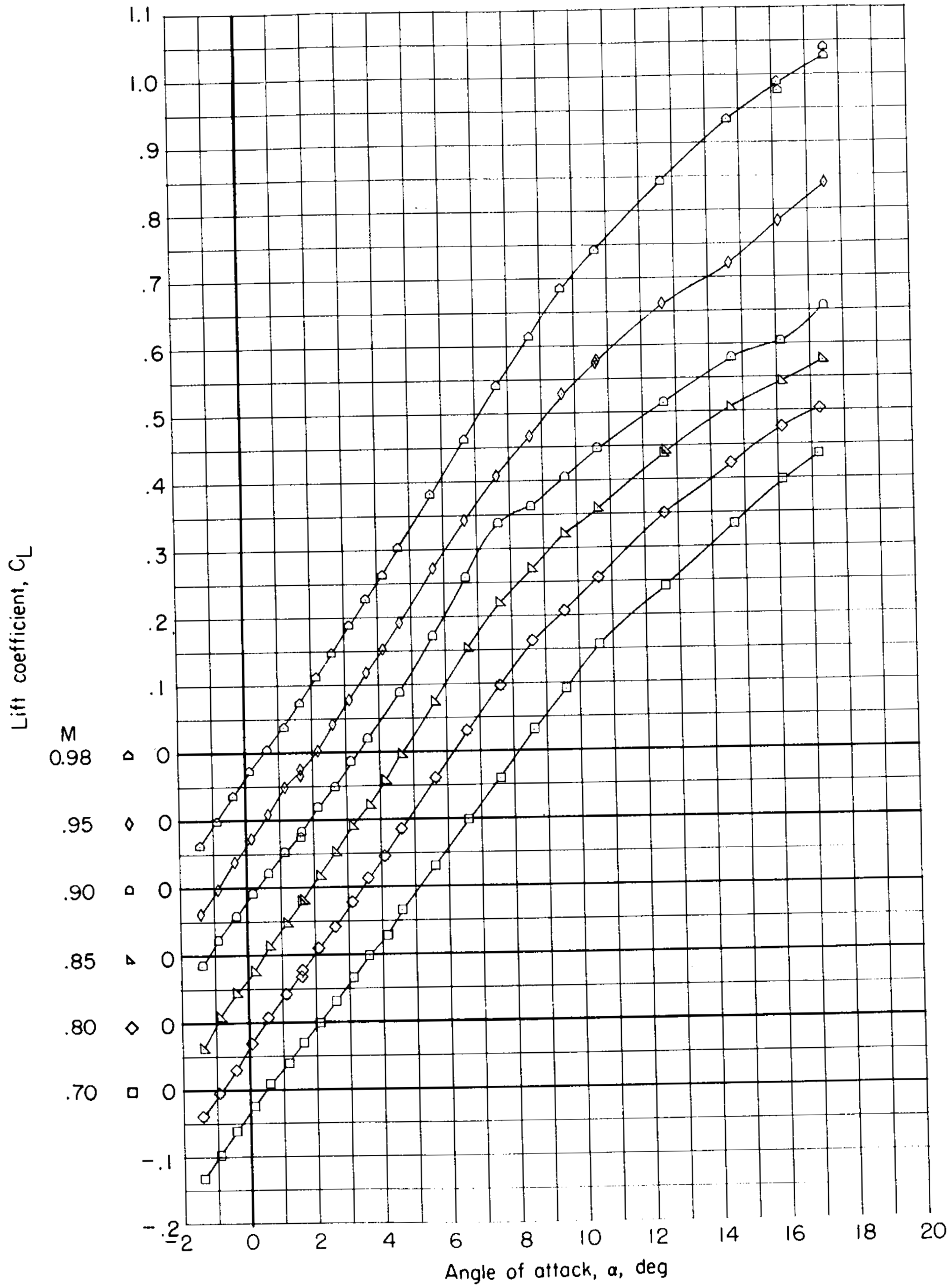

(a) Lift coefficient.

Figure 18.- Aerodynamic characteristics for model BW_1 with $\delta_{le} = 15^{o}$.

DECLASSIFIED

CONF[redacted]L

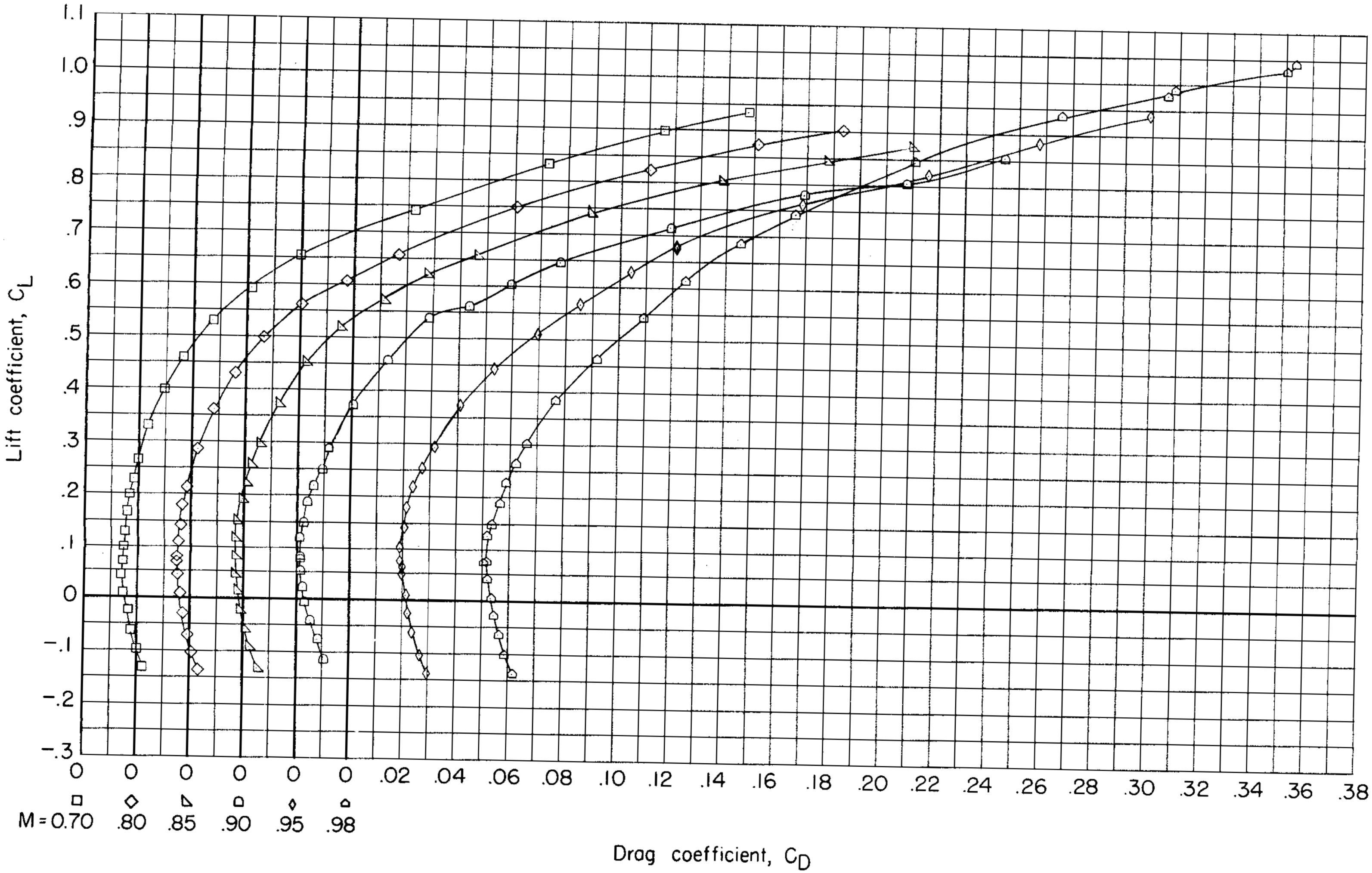

(b) Drag coefficient.

Figure 18.- Continued.

CONF[redacted]L

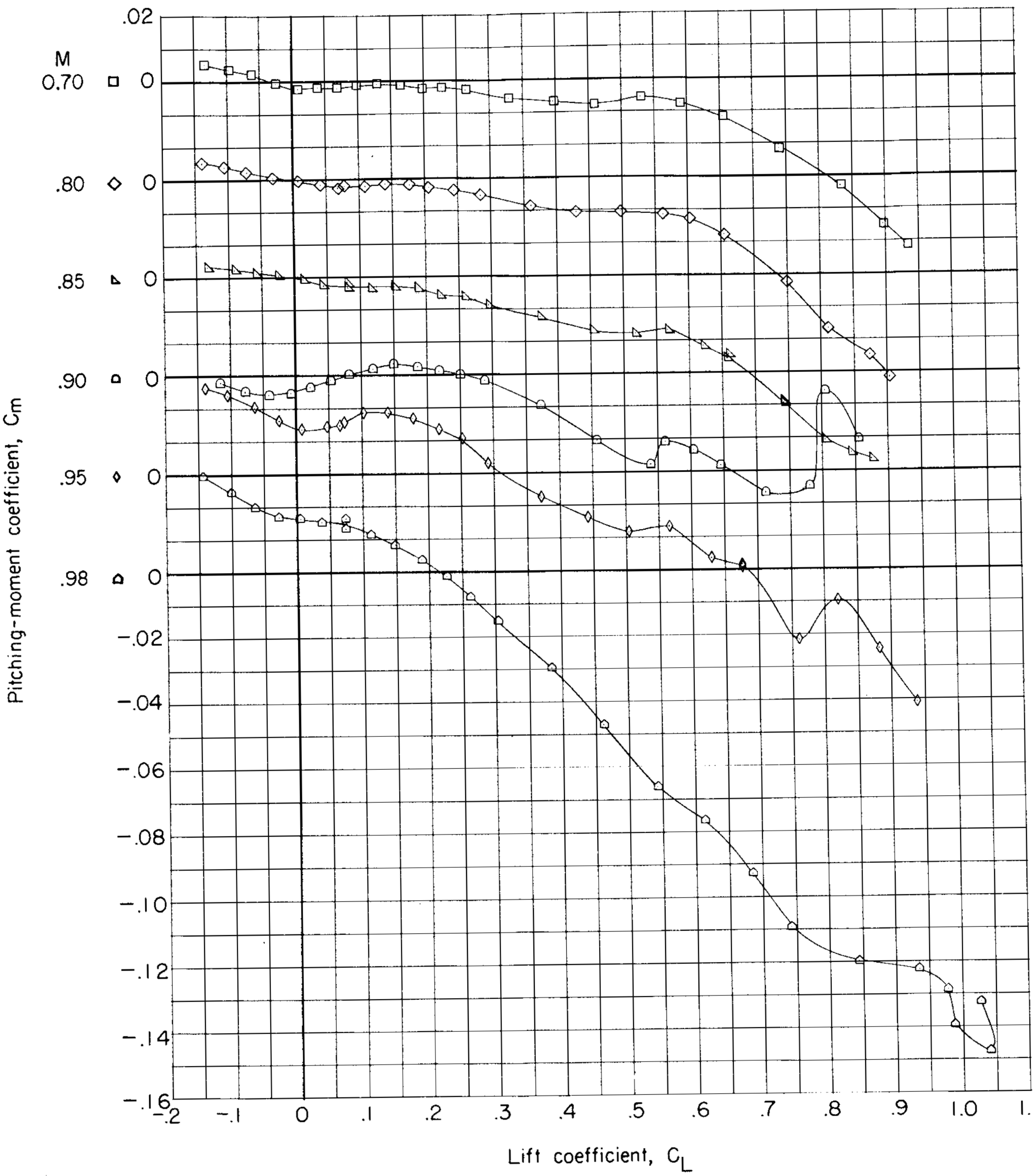

(c) Pitching-moment coefficient.

Figure 18.- Concluded.

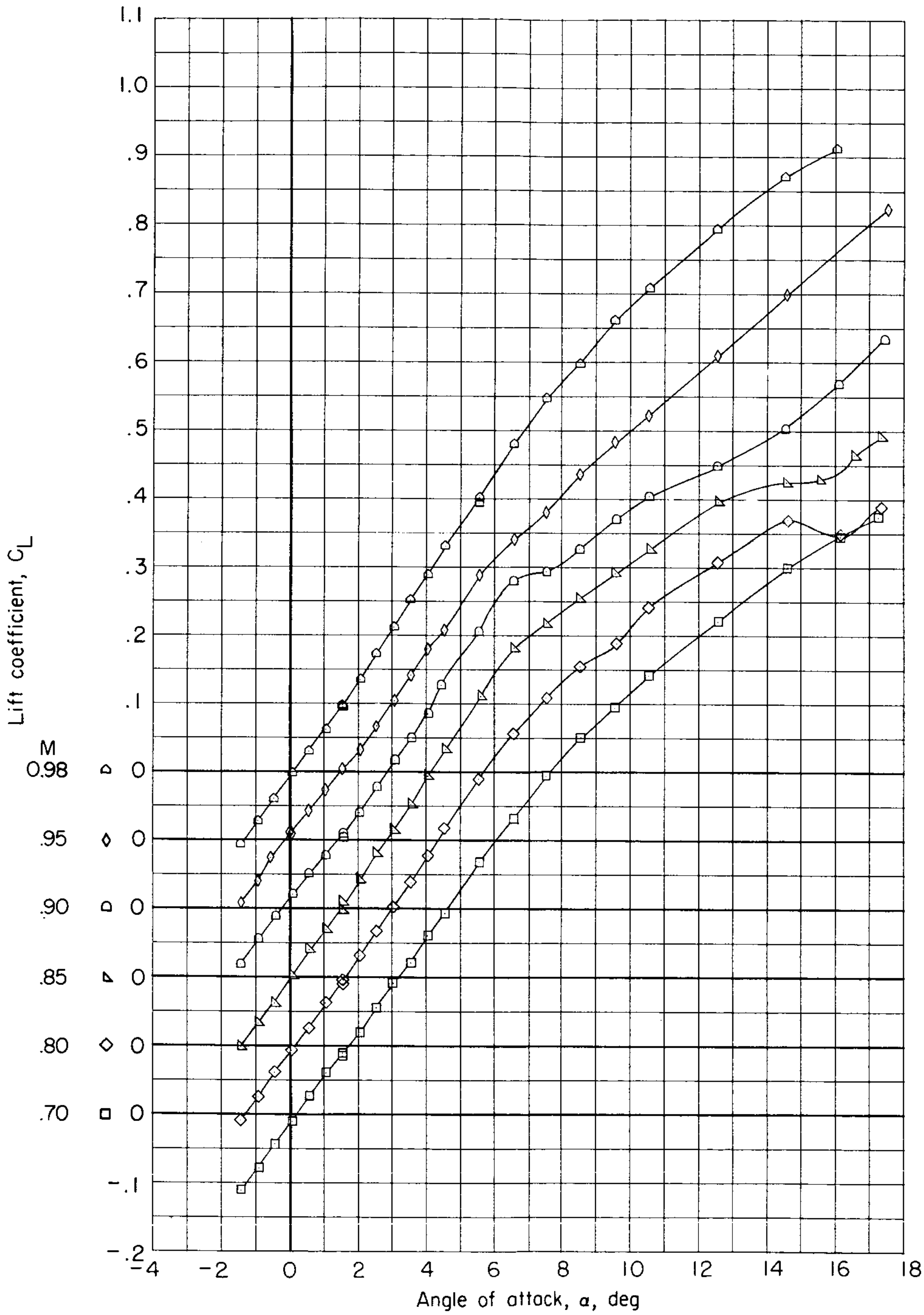

(a) Lift coefficient.

Figure 19.- Aerodynamic characteristics for model BWE with $\delta_{le} = 0^{\circ}$.

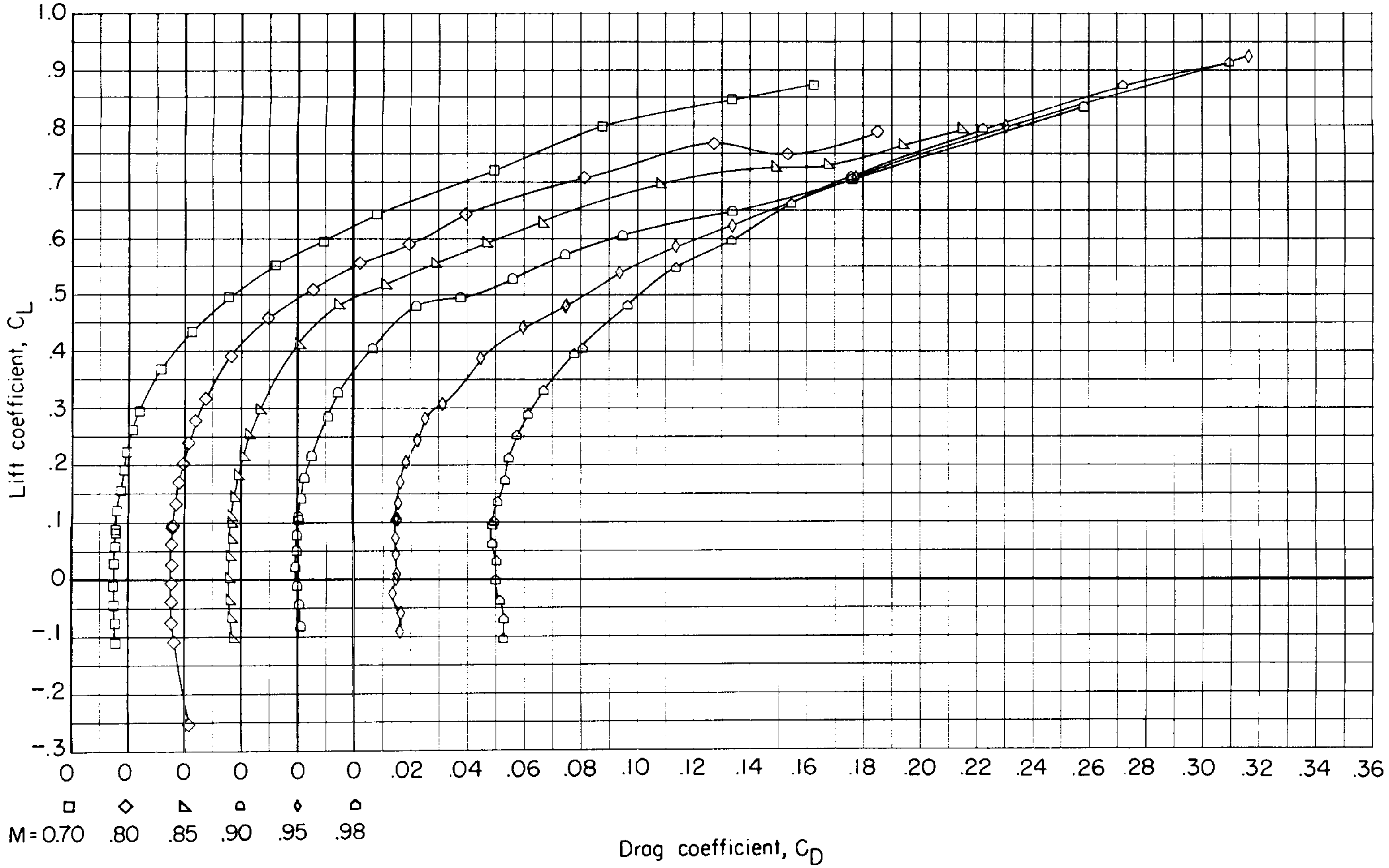

(b) Drag coefficient.

Figure 19.- Continued.

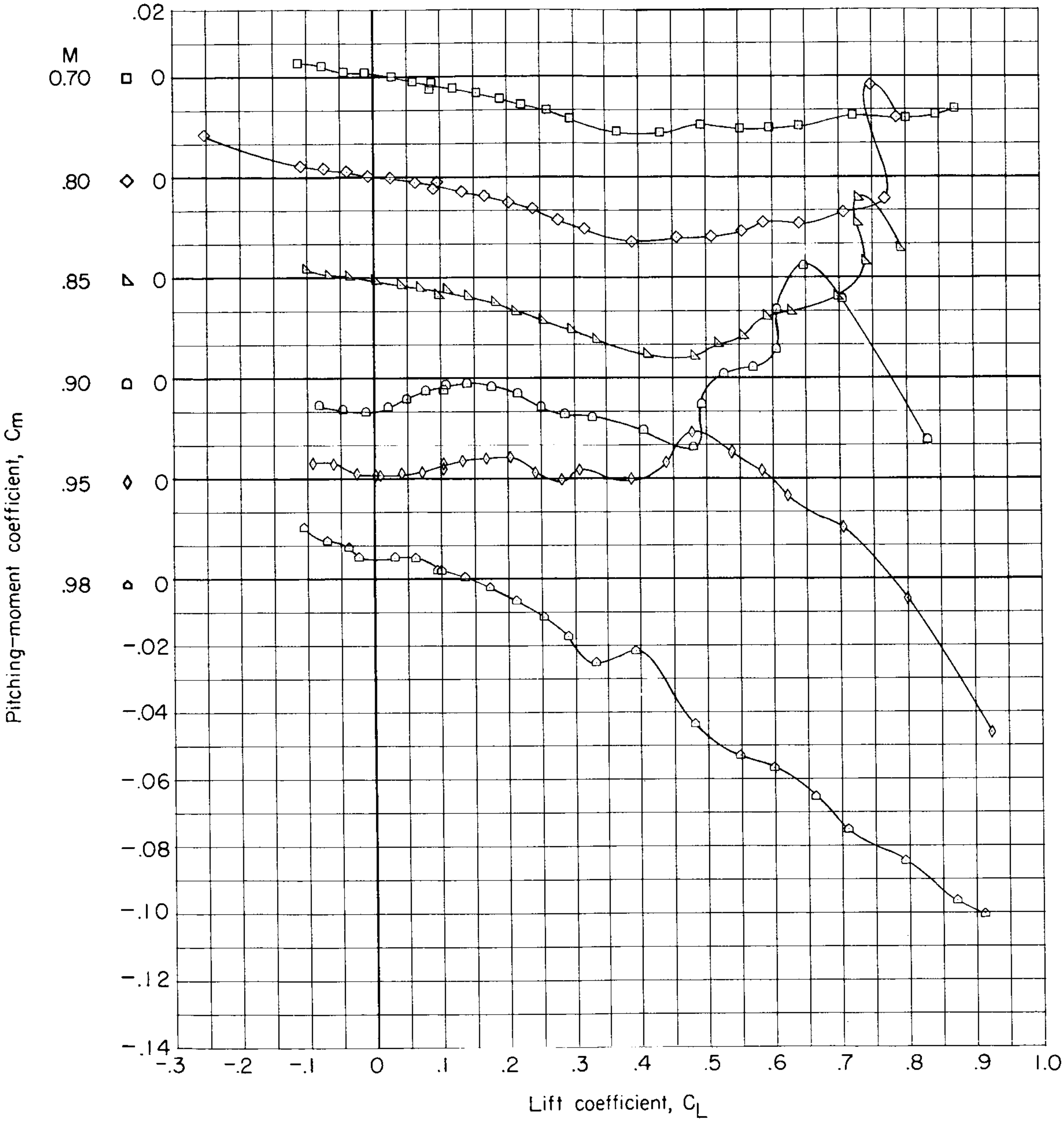

(c) Pitching-moment coefficient.

Figure 19.- Concluded.

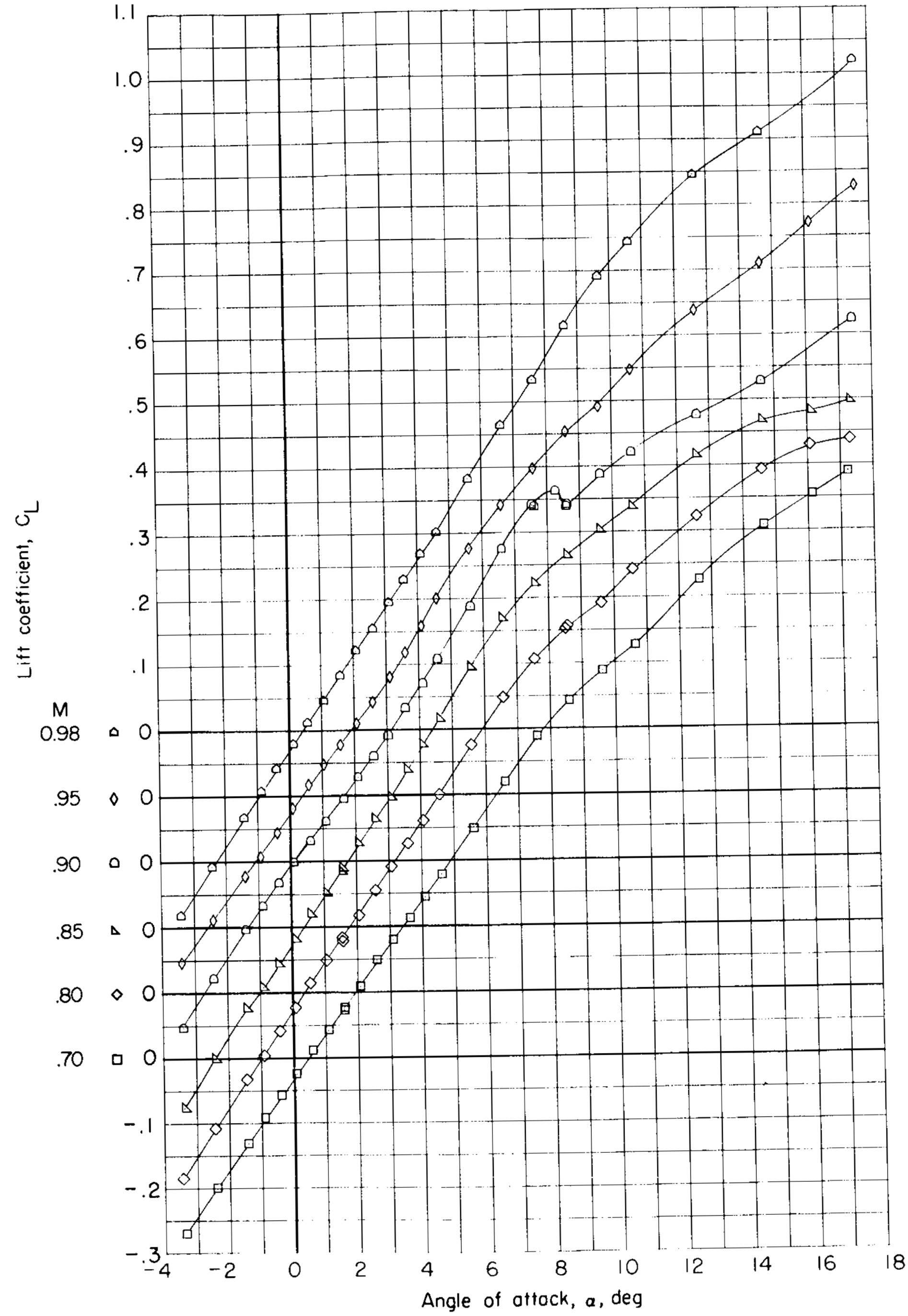

(a) Lift coefficient.

Figure 20.- Aerodynamic characteristics for model BWE with $\delta_{le} = 15^{o}$.

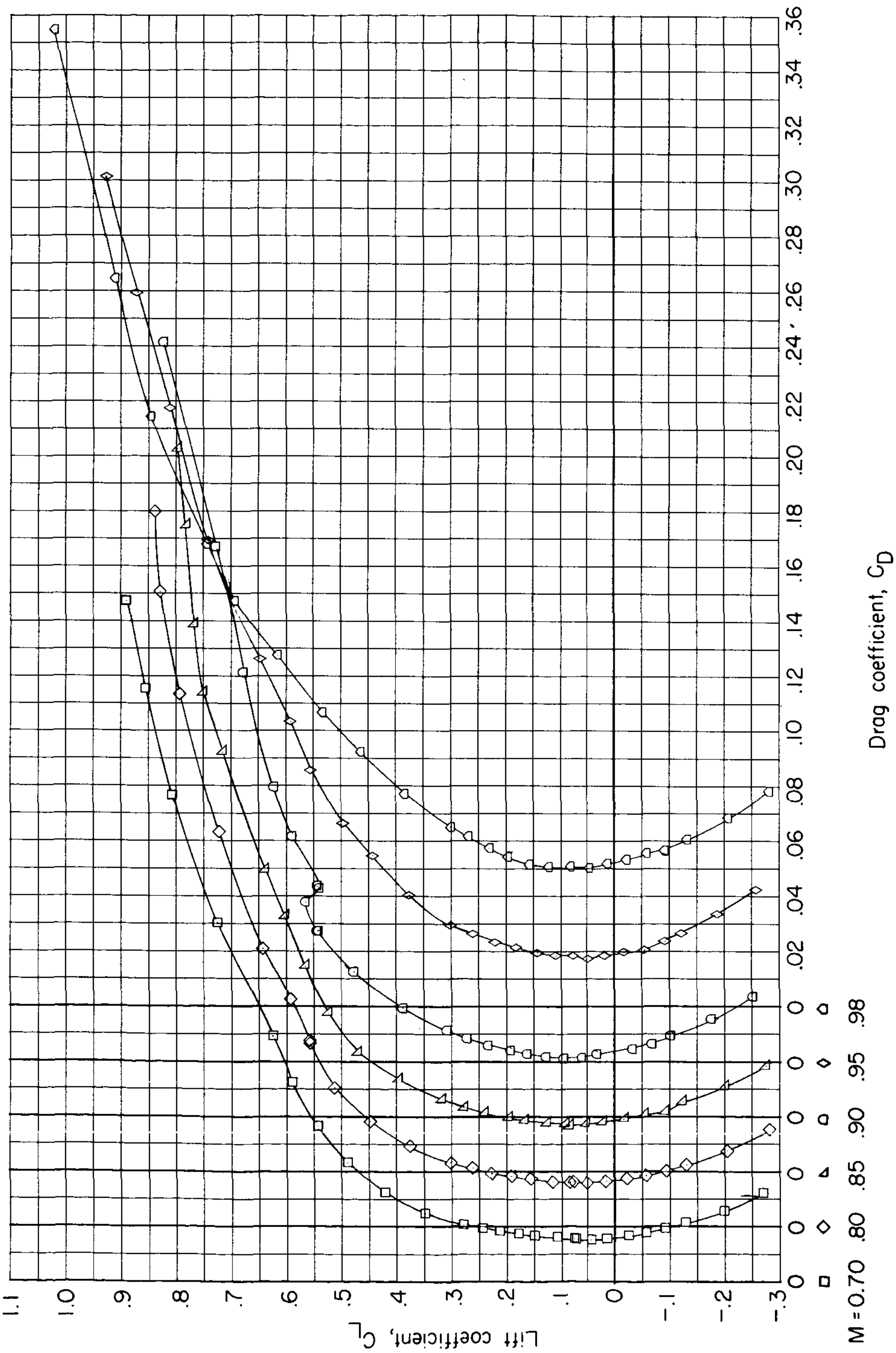

(b) Drag coefficient.

Figure 20.- Continued.

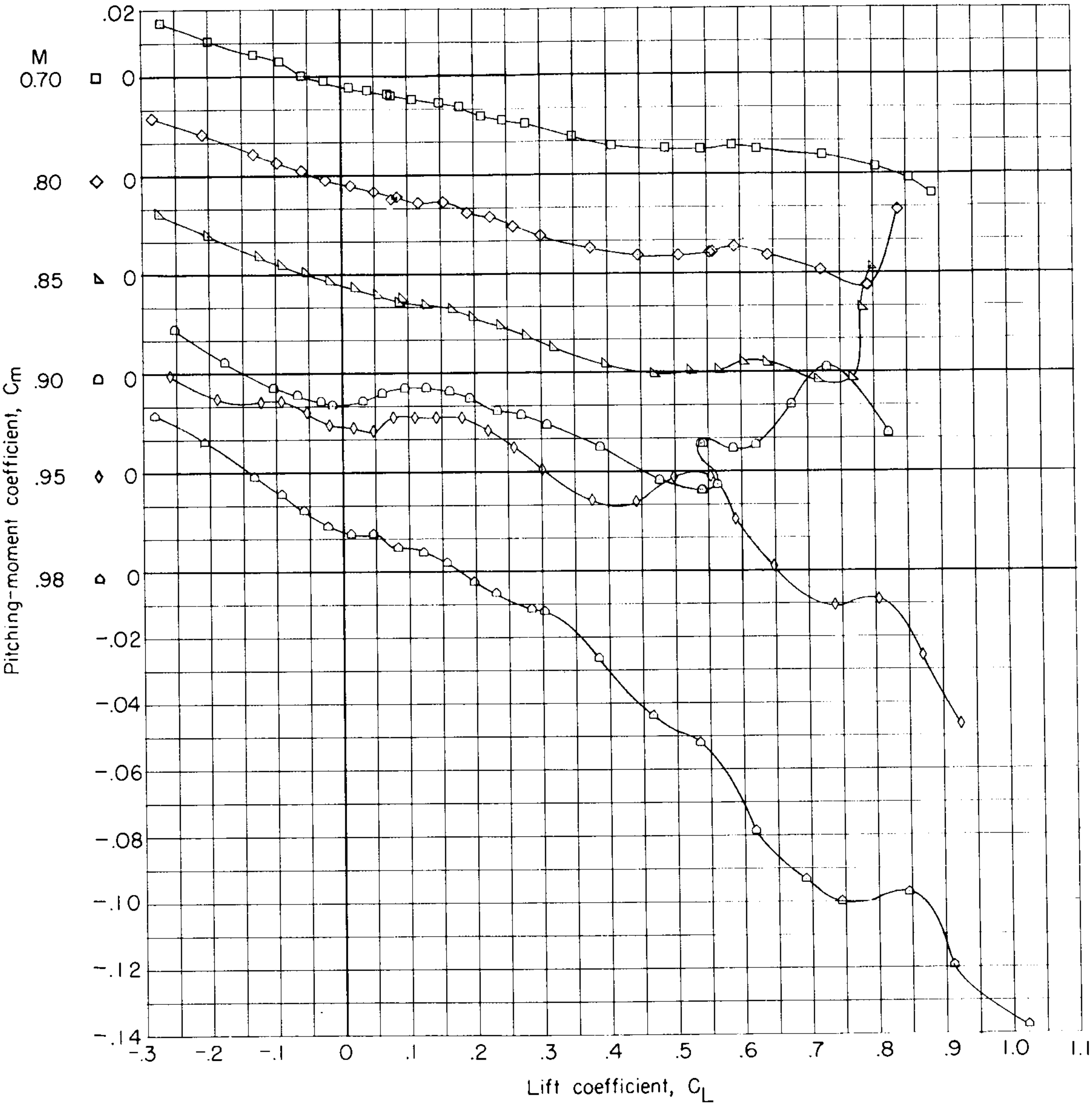

(c) Pitching-moment coefficient.

Figure 20.- Concluded.

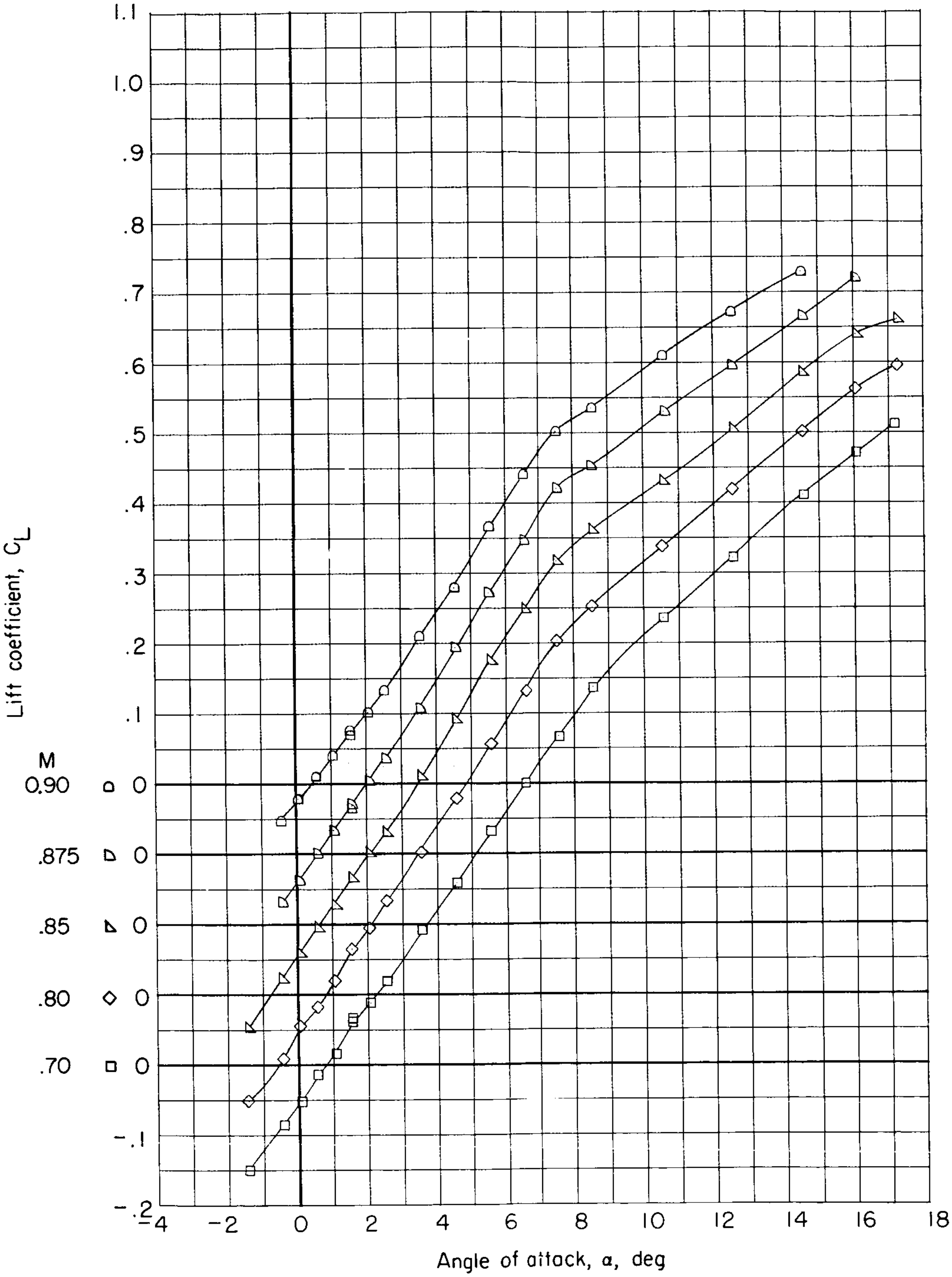

(a) Lift coefficient.

Figure 21.- Aerodynamic characteristics for model BWE with $\delta_{le} = 25^{\circ}$.

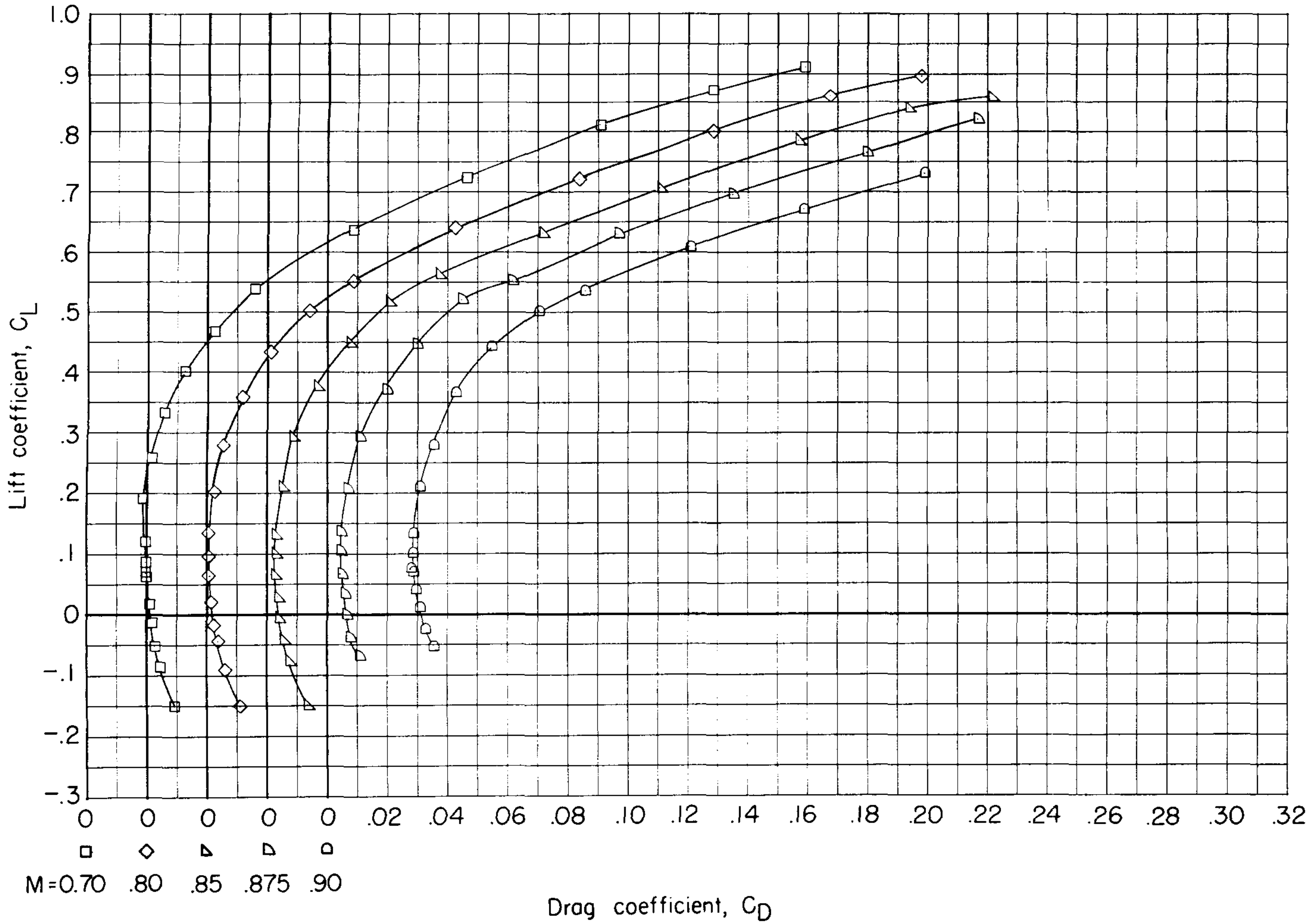

(b) Drag coefficient.

Figure 21.- Continued.

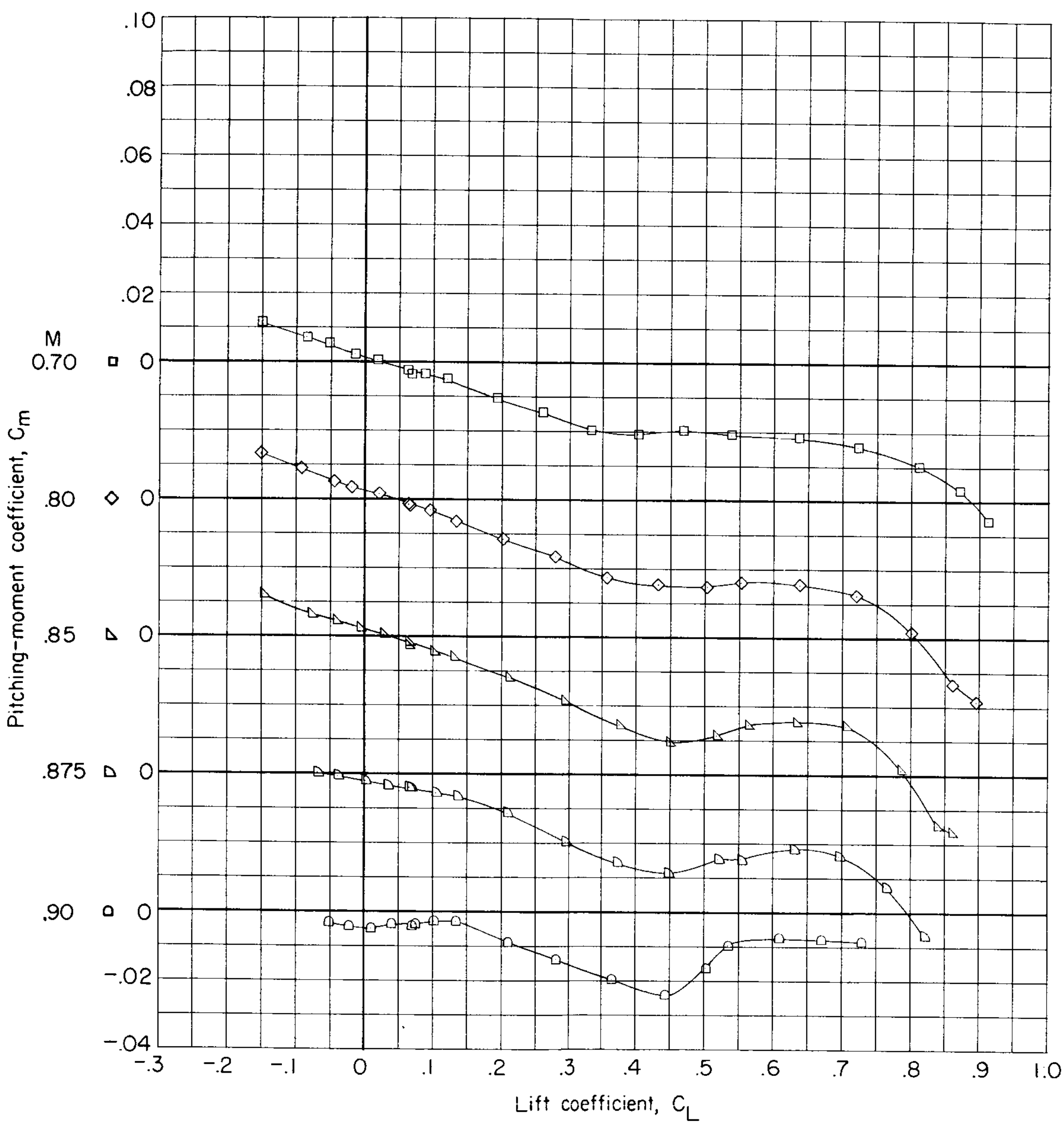

(c) Pitching-moment coefficient.

Figure 21.- Concluded.

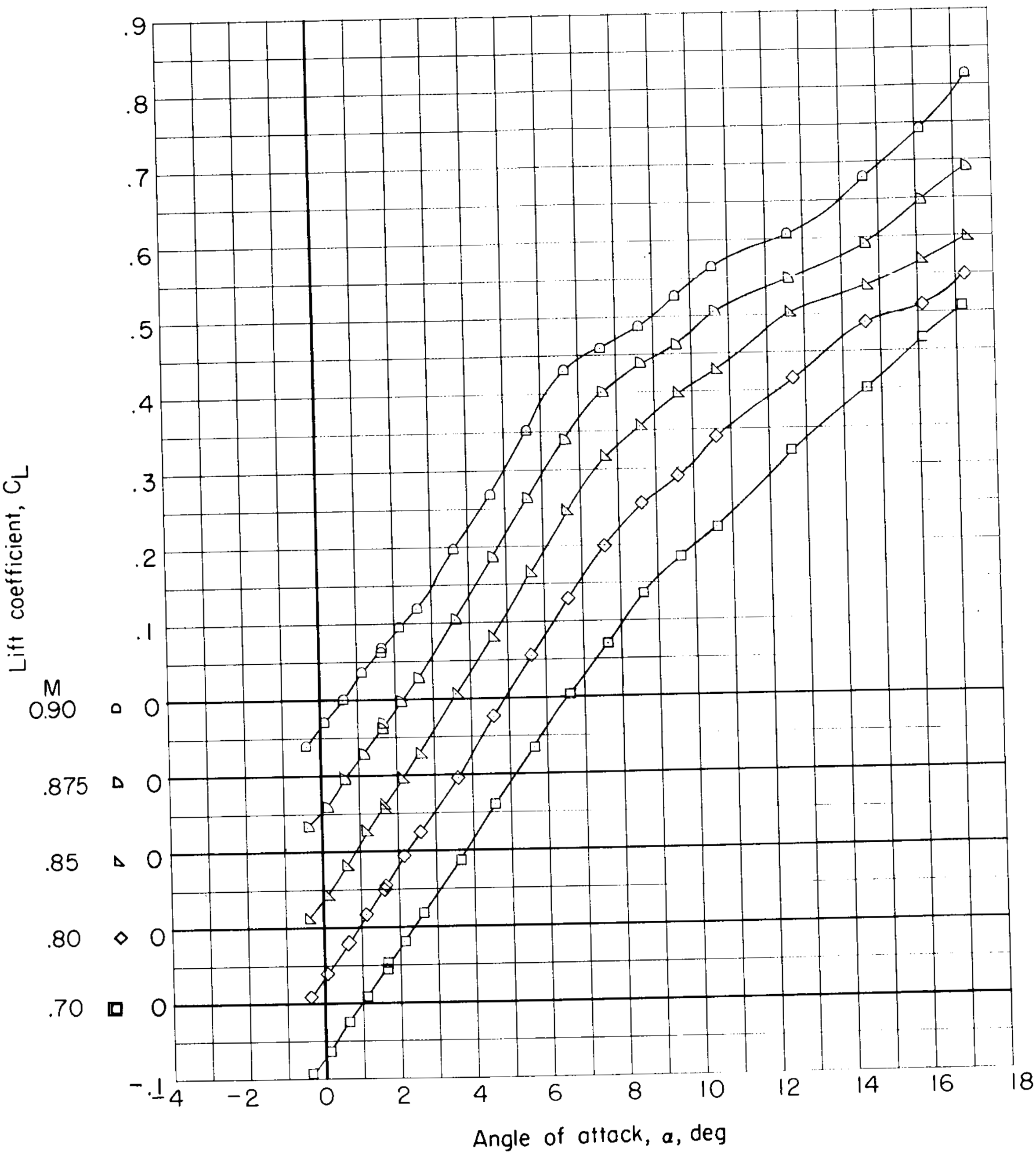

(a) Lift coefficient.

Figure 22.- Aerodynamic characteristics for model BWE with $\delta_{le} = 30^{\circ}$.

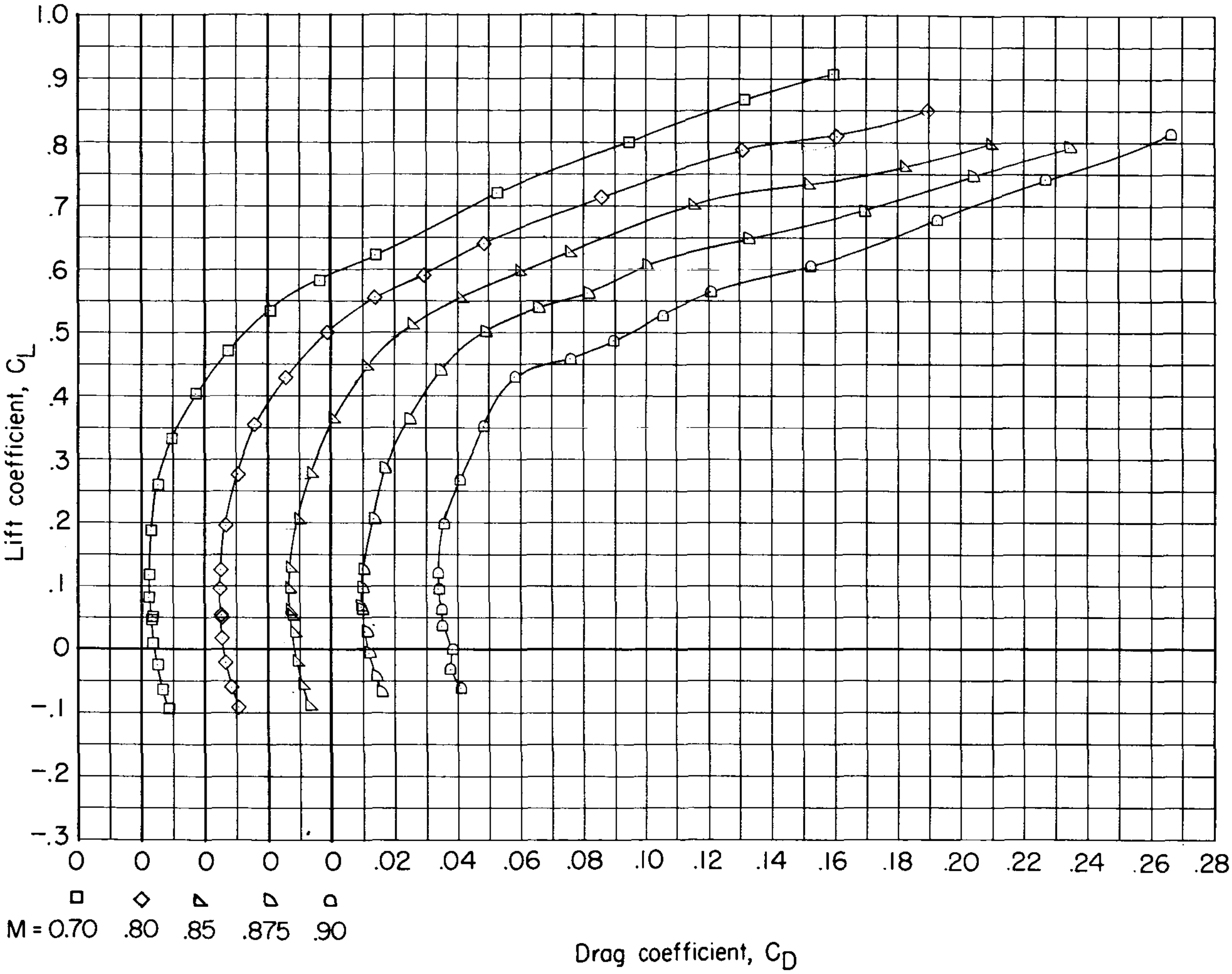

(b) Drag coefficient.

Figure 22.- Continued.

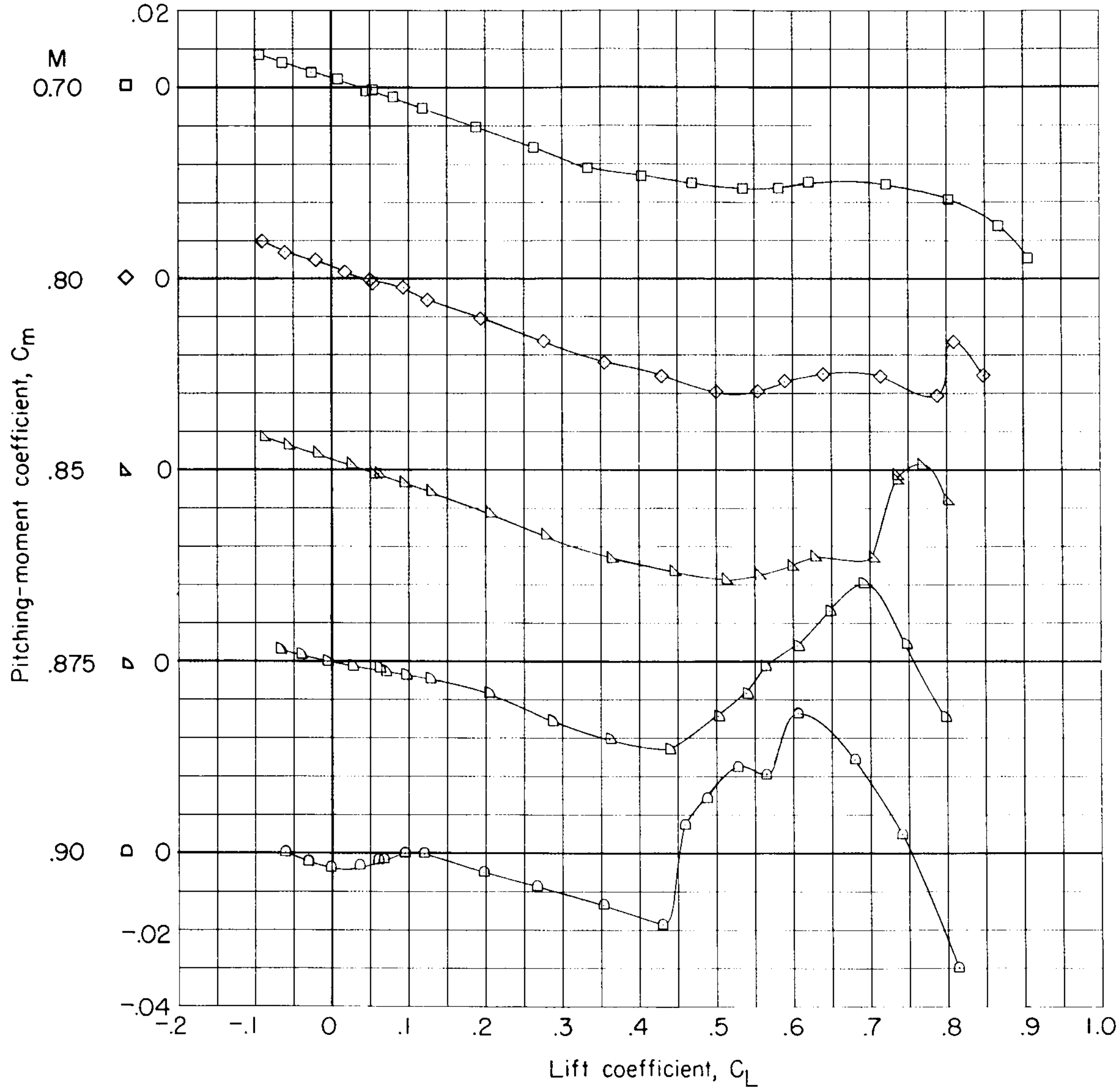

(c) Pitching-moment coefficient.

Figure 22.- Concluded.

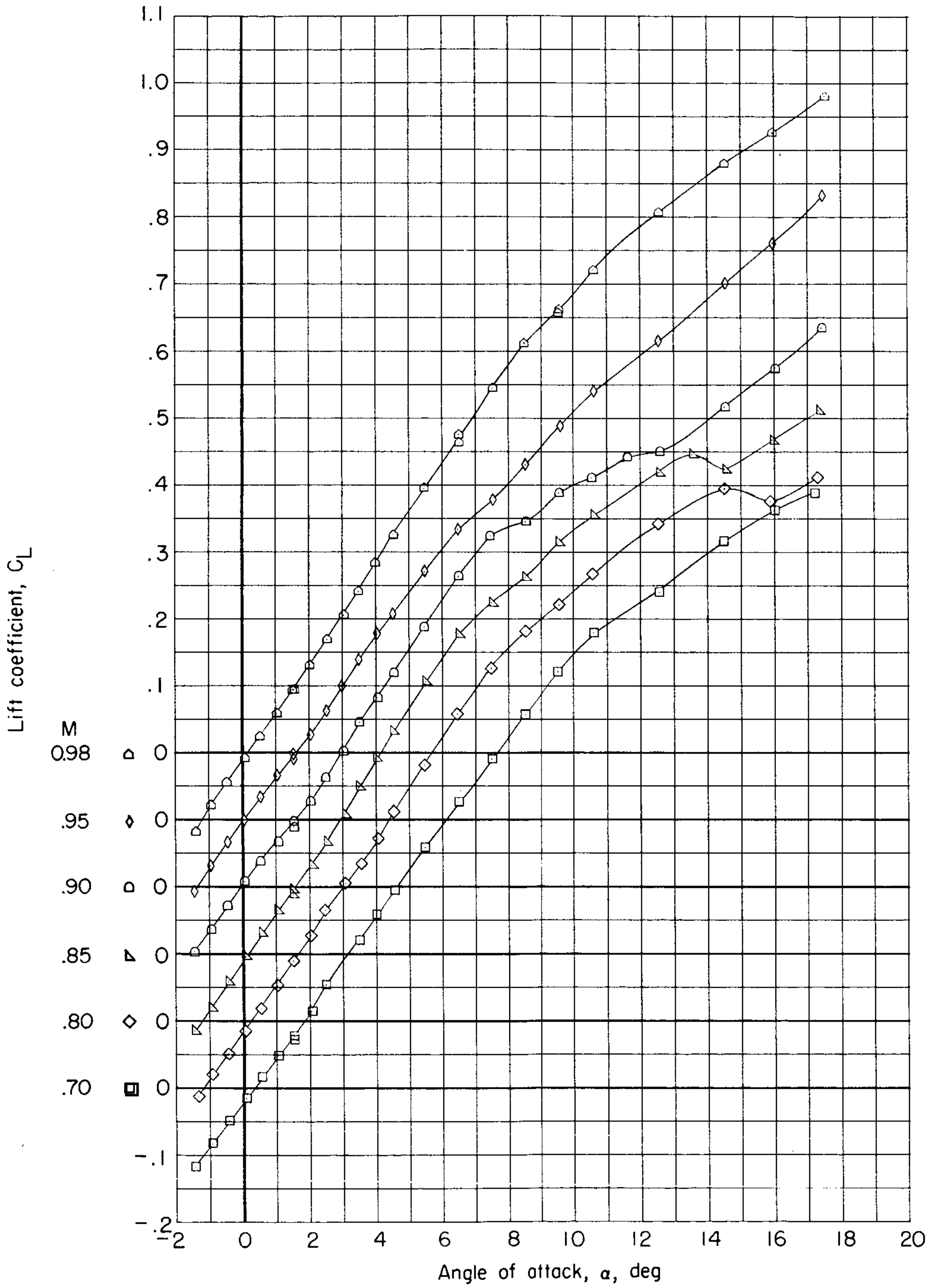

(a) Lift coefficient.

Figure 23.- Aerodynamic characteristics for model BW_1E with $\delta_{le} = 0^{\circ}$.

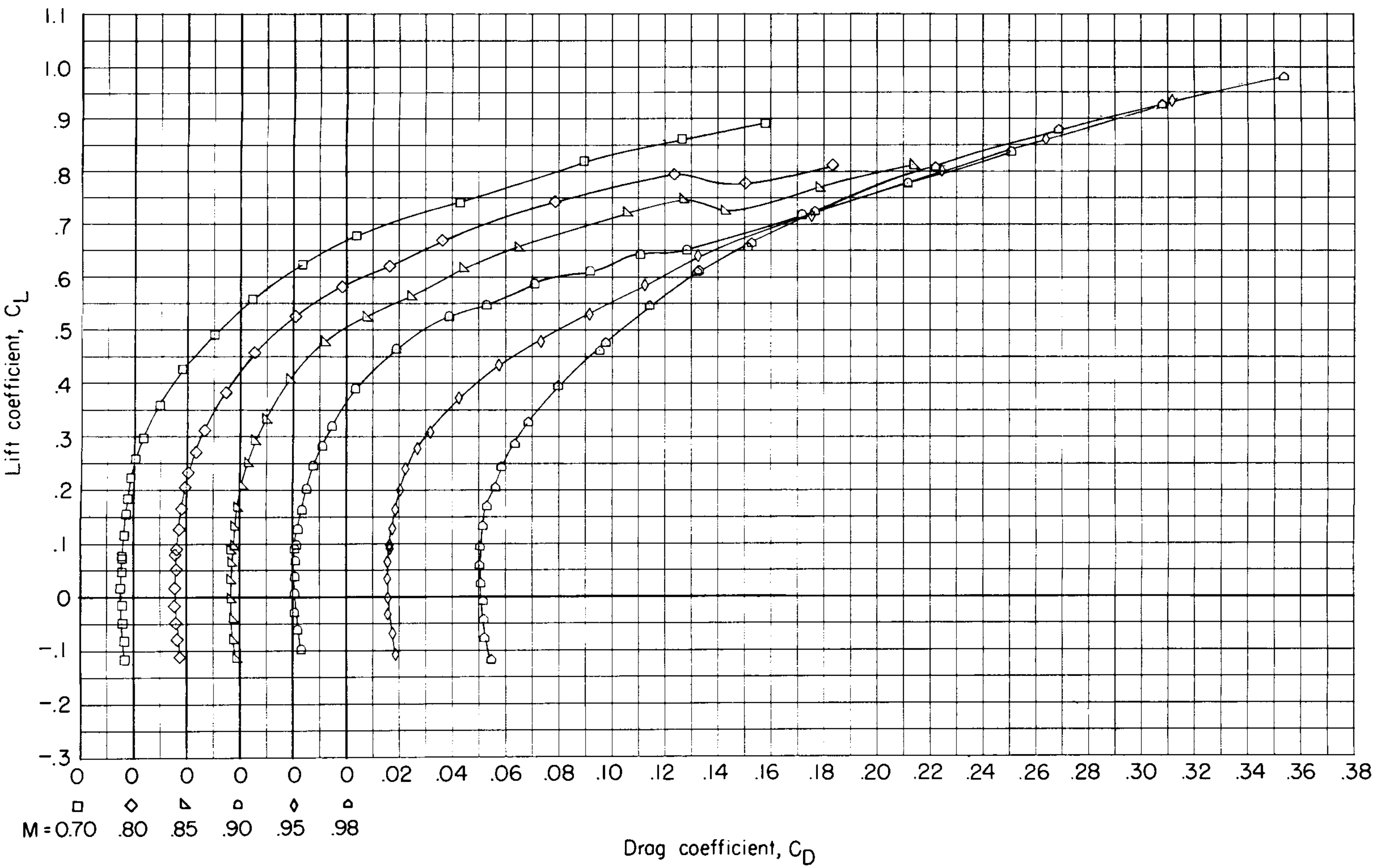

(b) Drag coefficient.

Figure 23.- Continued.

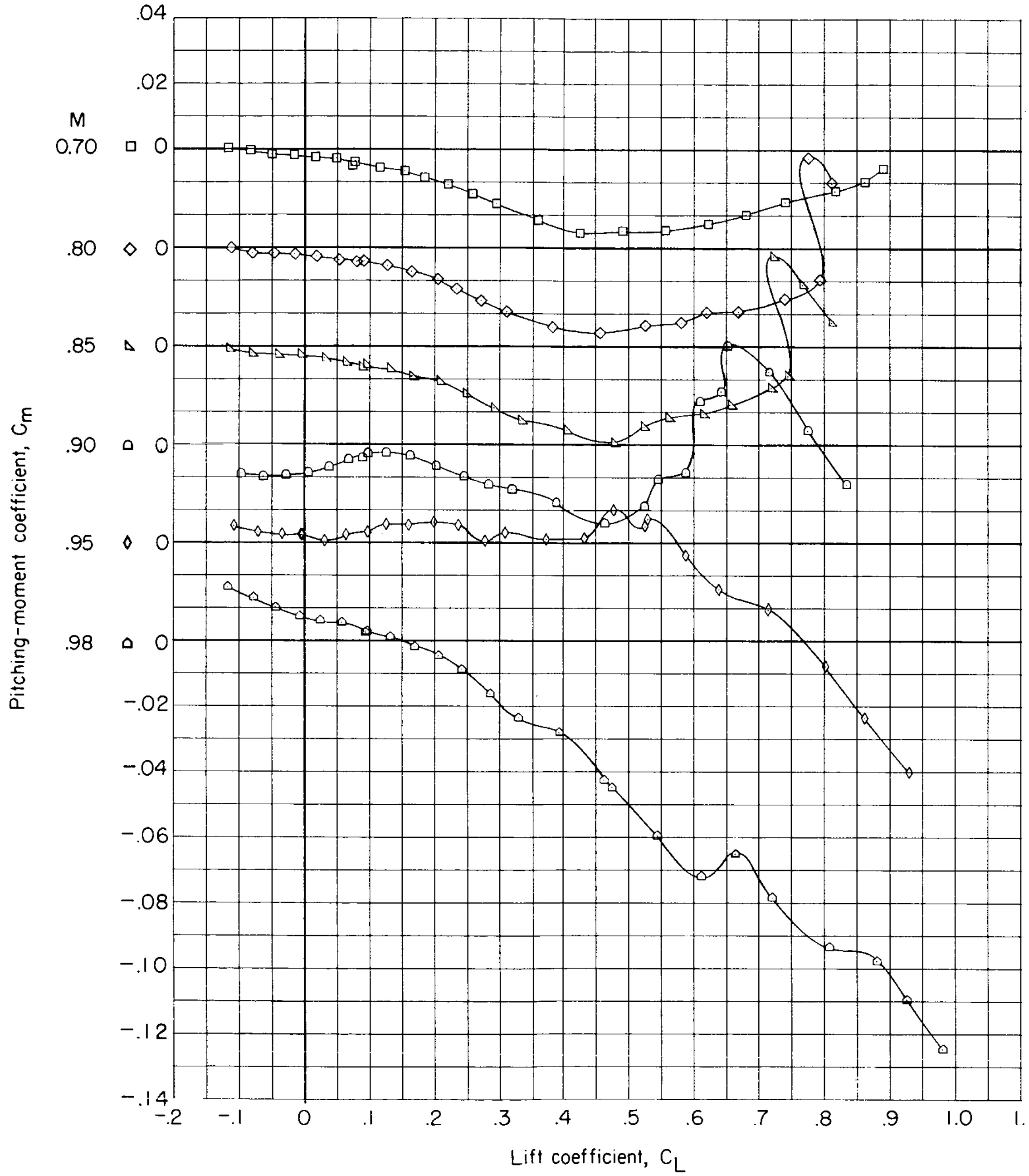

(c) Pitching-moment coefficient.

Figure 23.- Concluded.

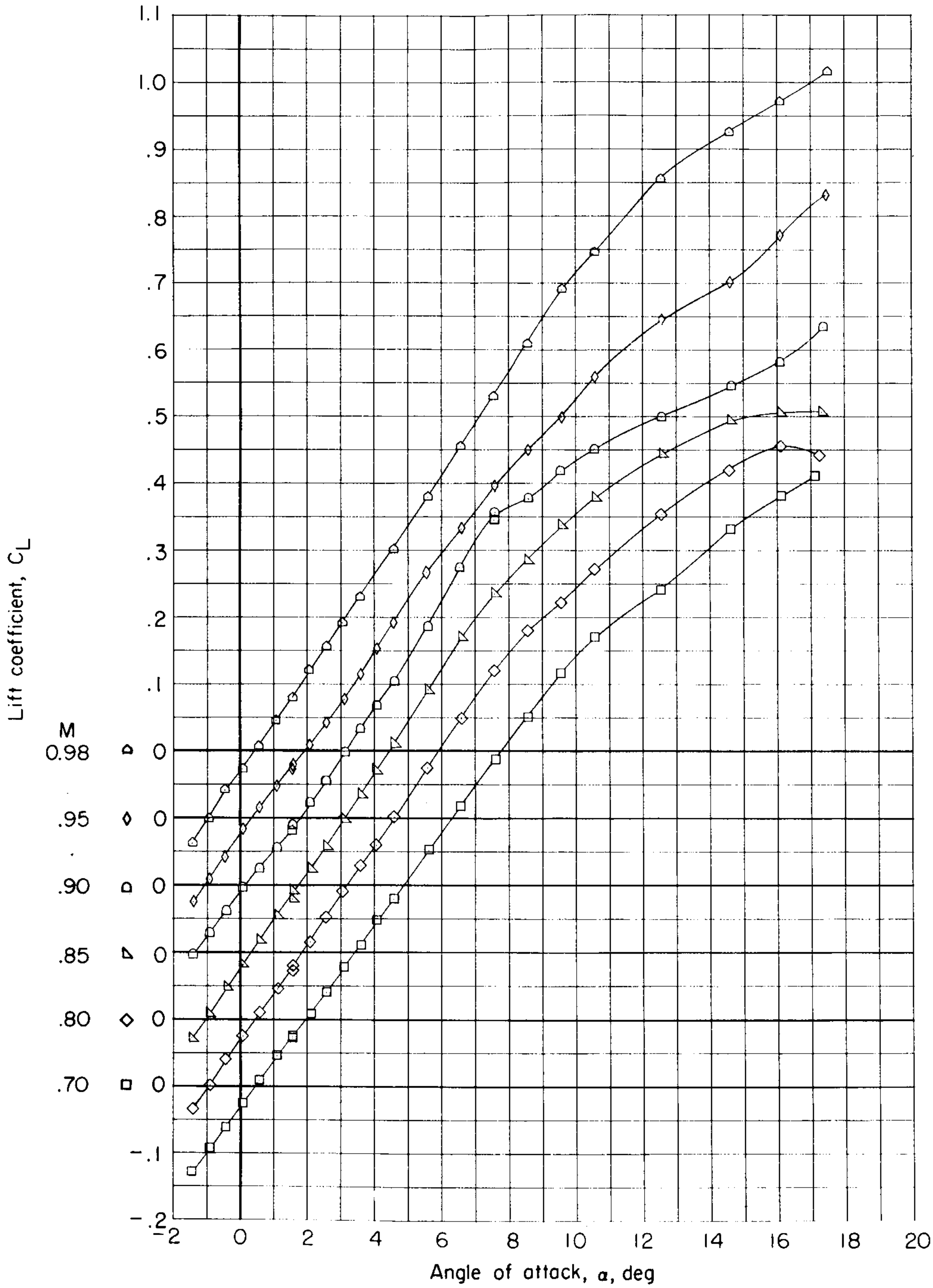

(a) Lift coefficient.

Figure 24.- Aerodynamic characteristics for model BW_1E with $\delta_{le} = 15^\circ$.

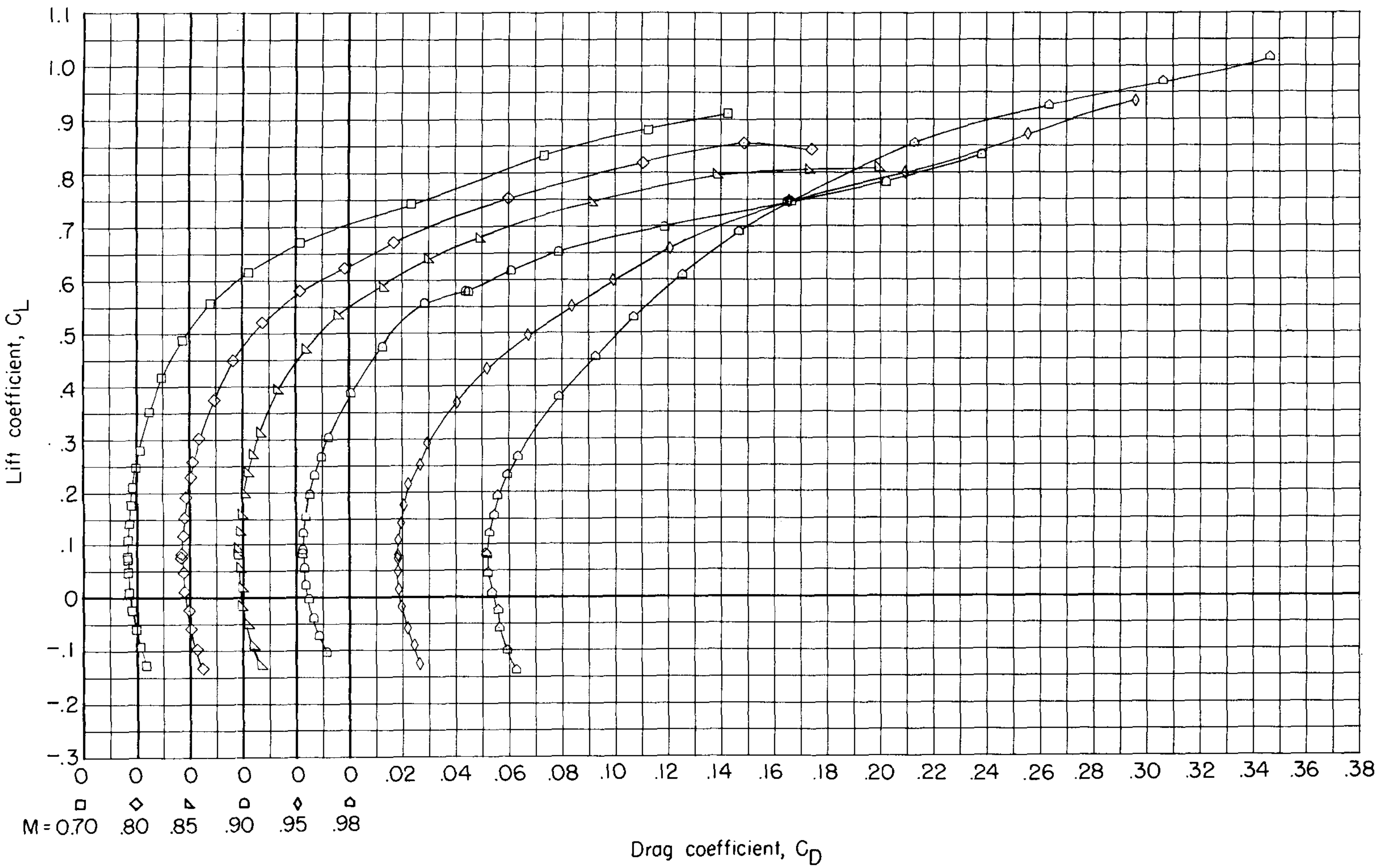

(b) Drag coefficient.

Figure 24.- Continued.

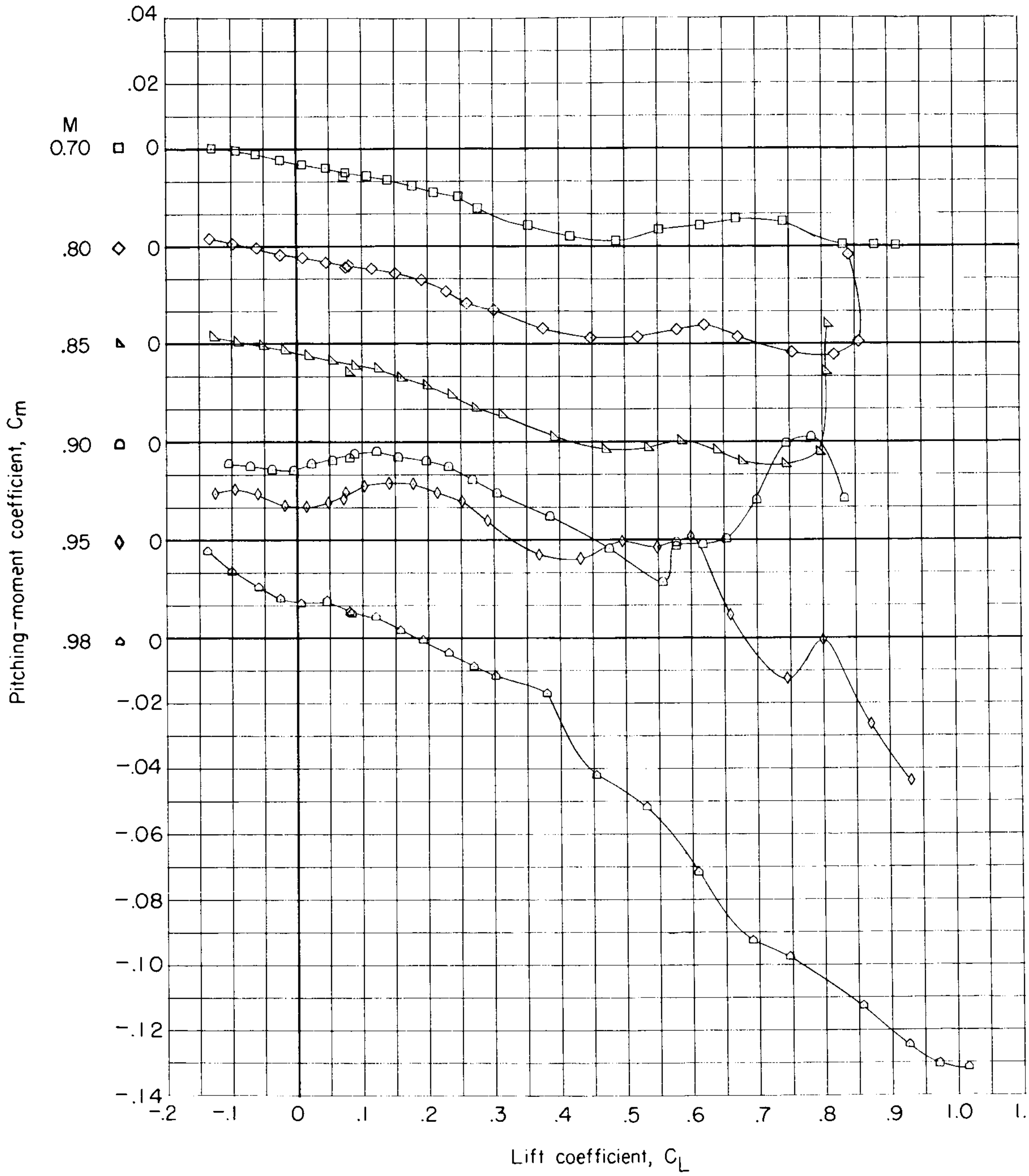

(c) Pitching-moment coefficient.

Figure 24.- Concluded.

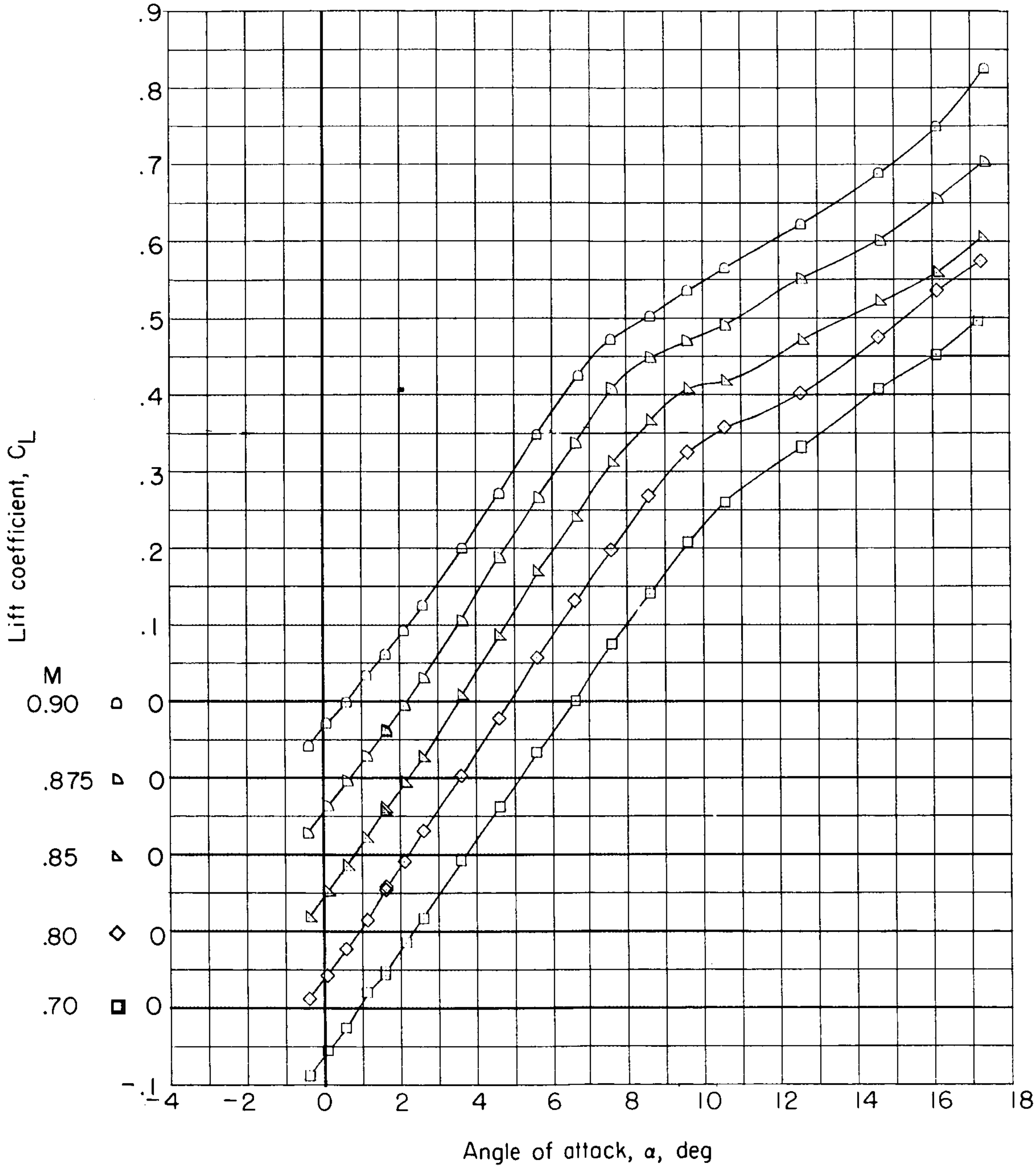

(a) Lift coefficient.

Figure 25.- Aerodynamic characteristics for model BW_1E with $\delta_{le} = 30^{\circ}$.

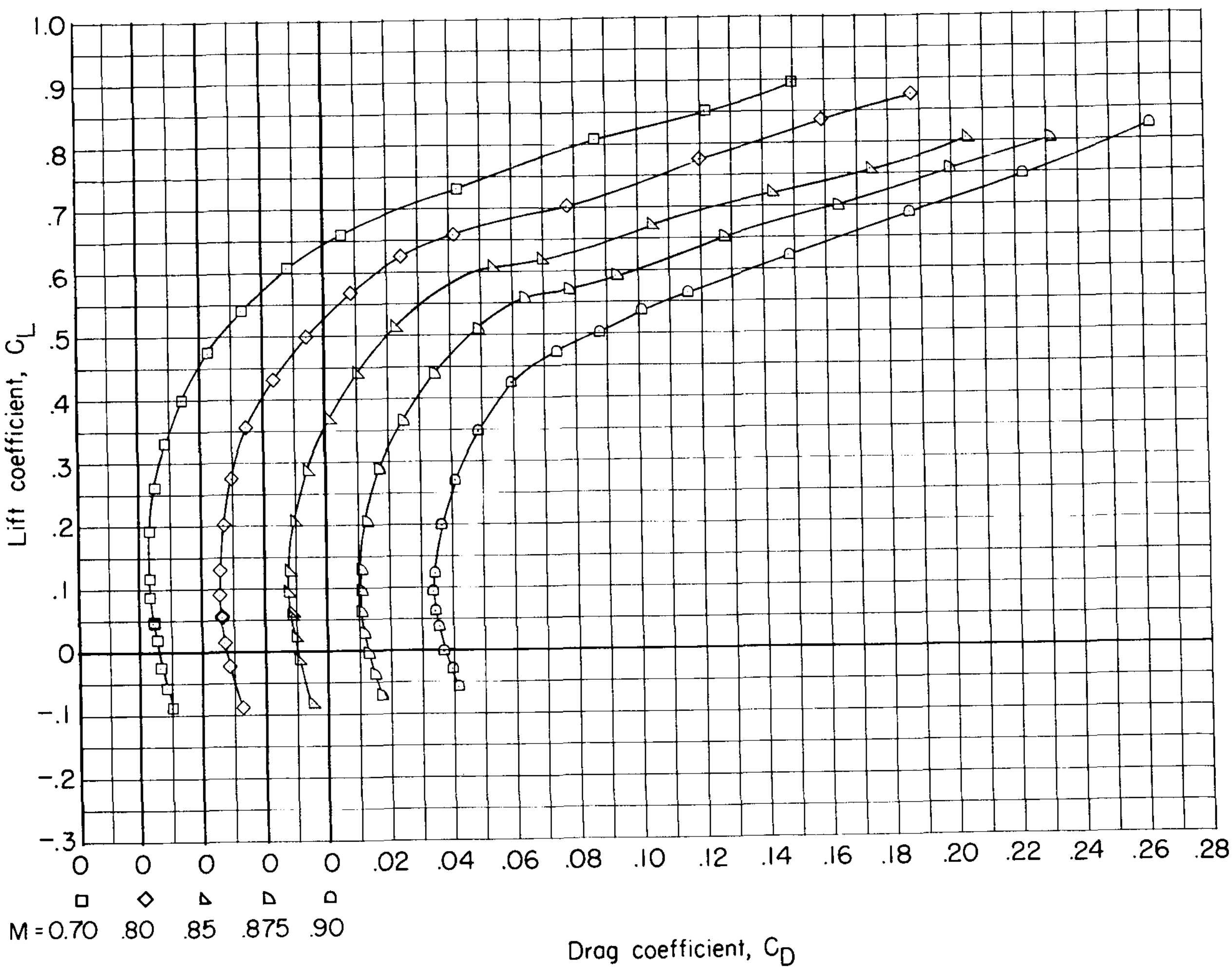

(b) Drag coefficient.

Figure 25.- Continued.

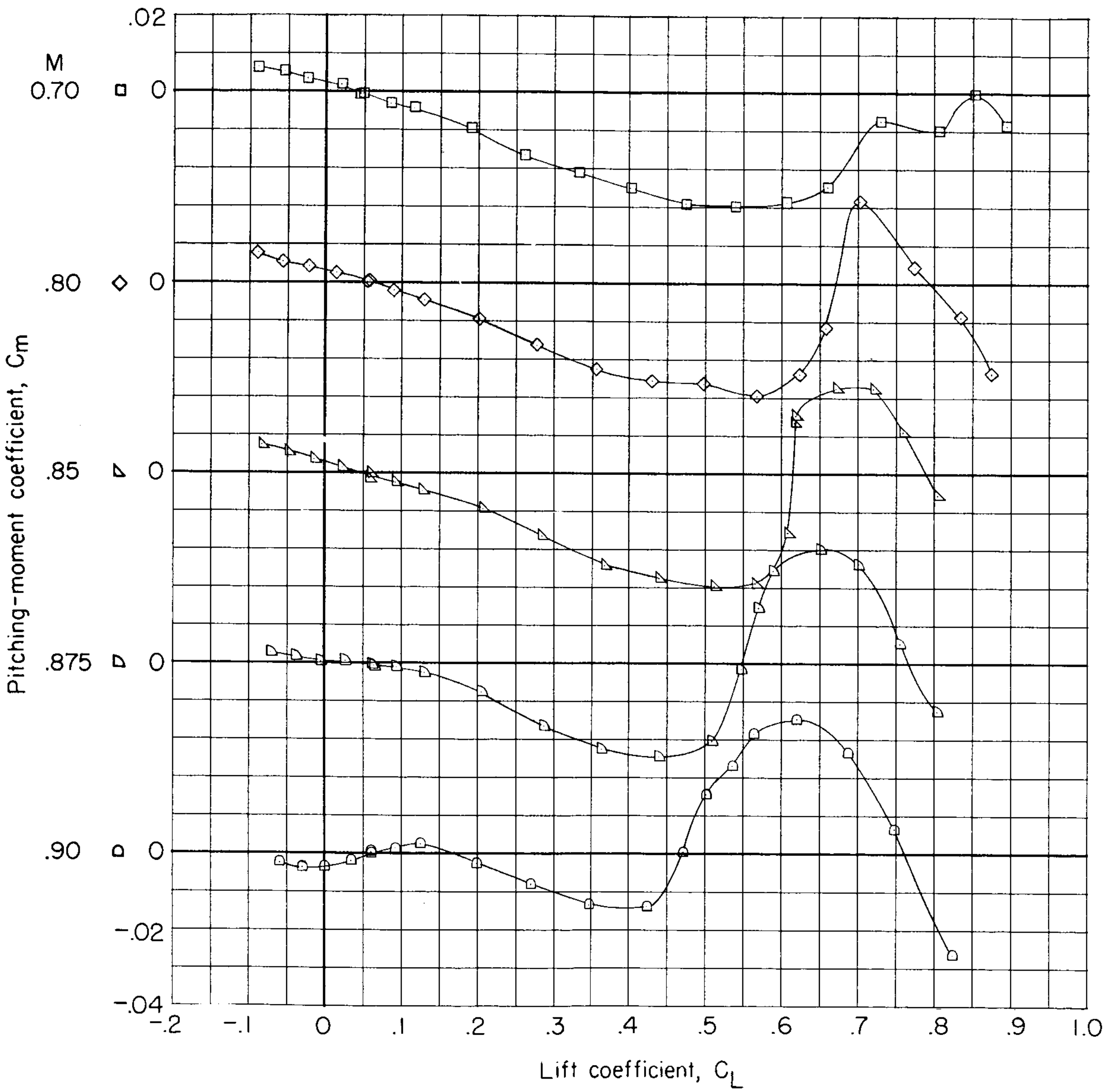

(c) Pitching-moment coefficient.

Figure 25.- Concluded.

C[redacted]IAL

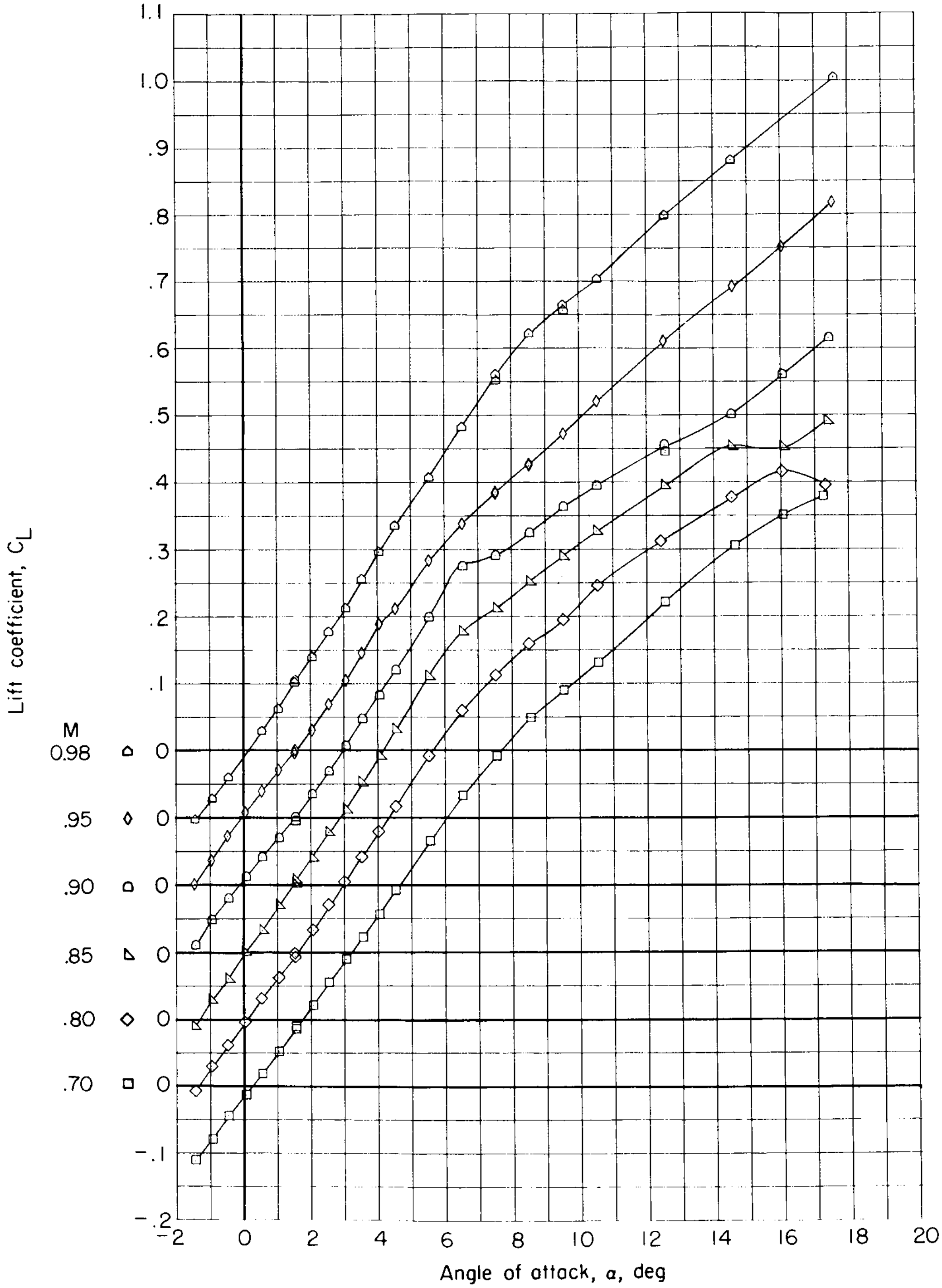

(a) Lift coefficient.

Figure 26.- Aerodynamic characteristics for model BW_2E with $\delta_{le} = 0^{\circ}$.

C[redacted]TIAL

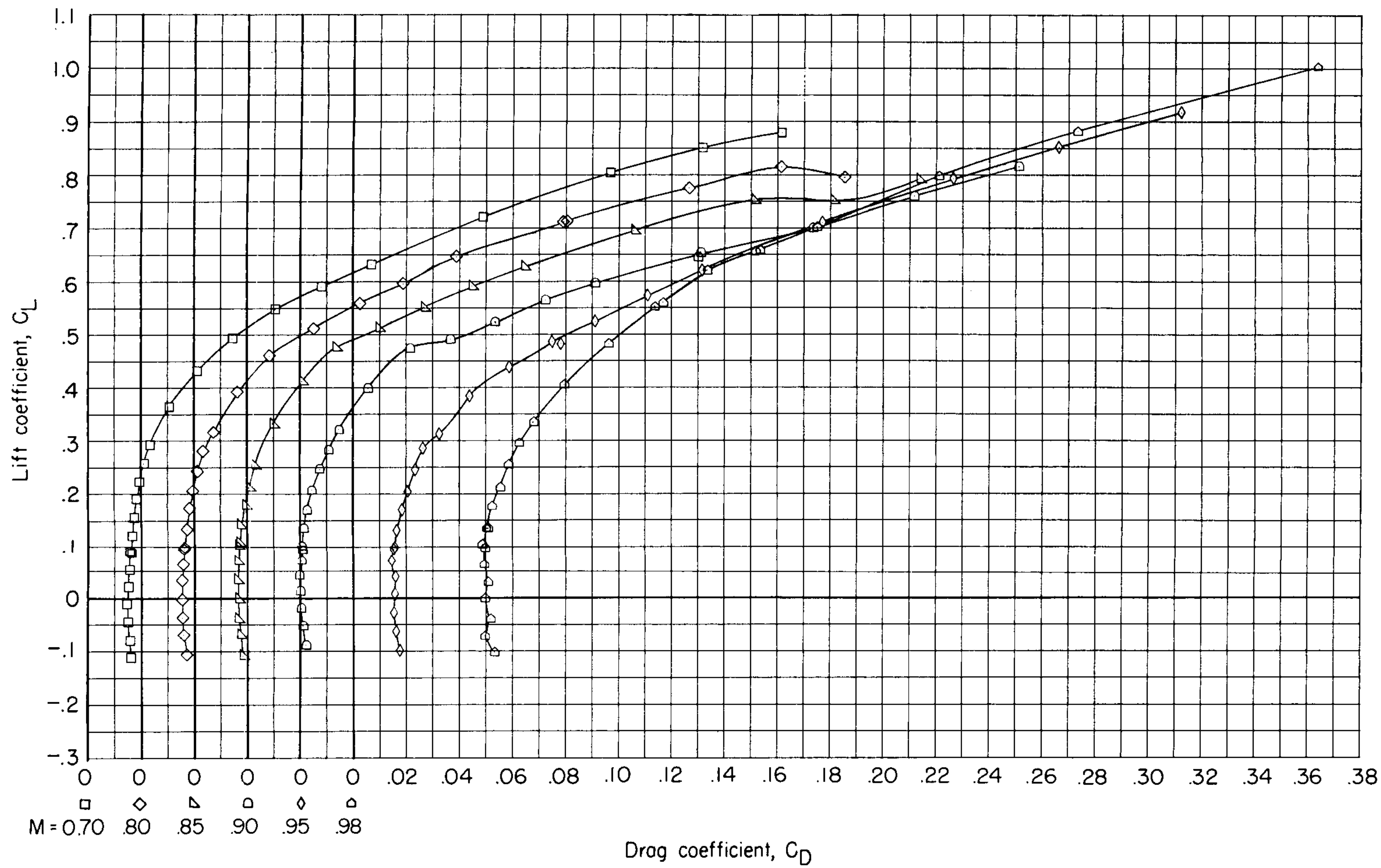

(b) Drag coefficient.

Figure 26.- Continued.

CONF[redacted]AL

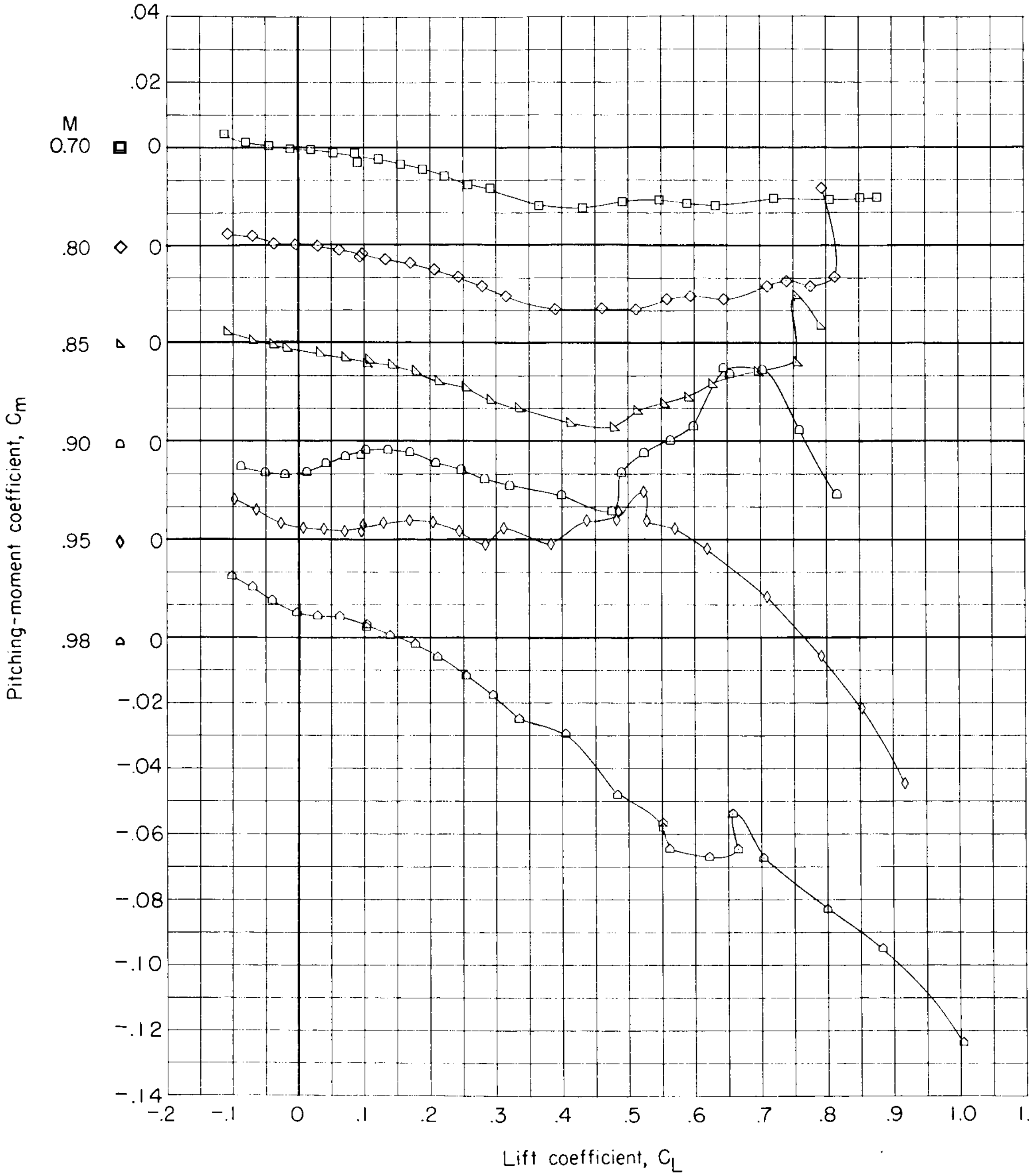

(c) Pitching-moment coefficient.

Figure 26.- Concluded.

C[redacted]IAL

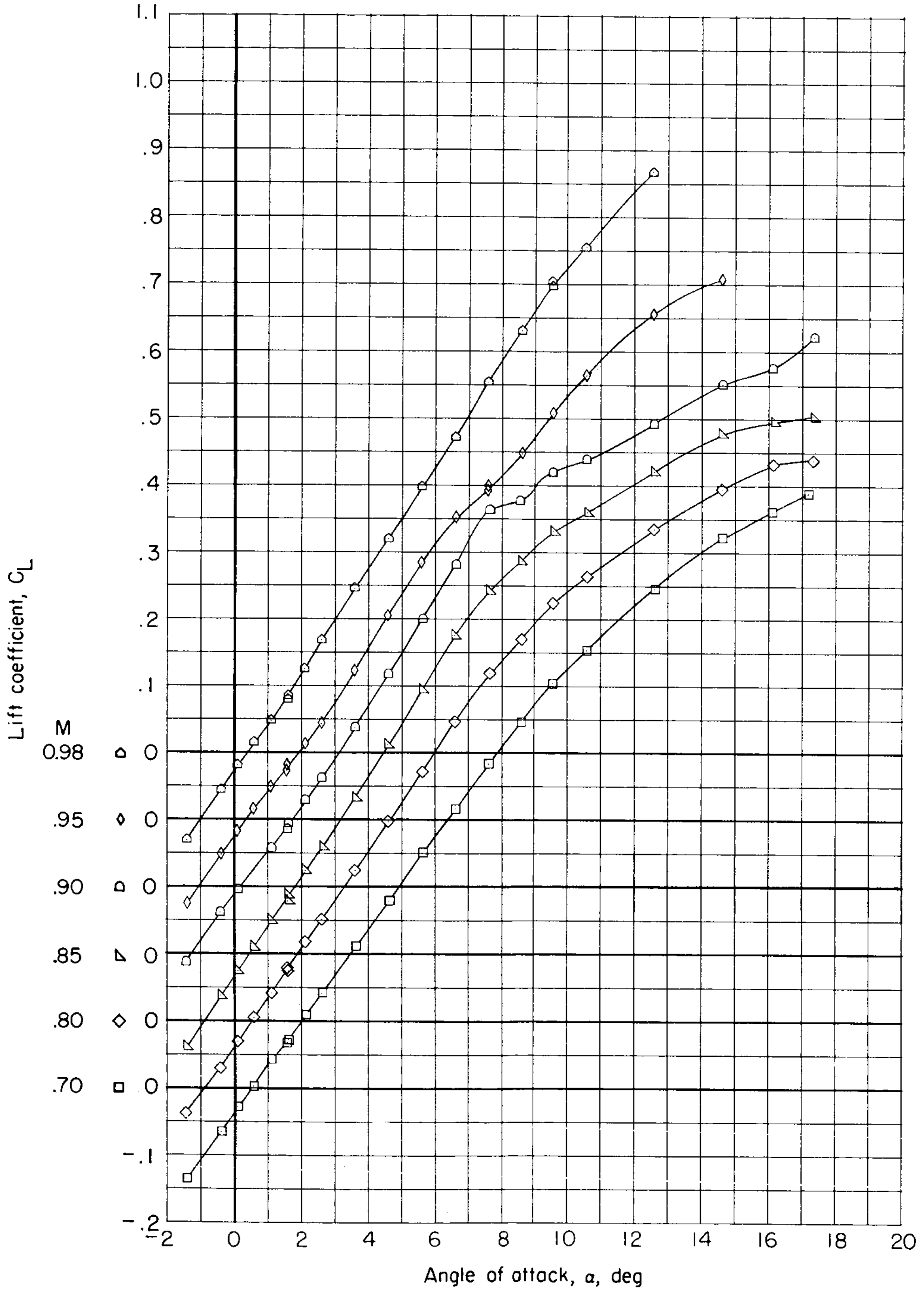

(a) Lift coefficient.

Figure 27.- Aerodynamic characteristics for model $BWEF_1$ with $\delta_{le} = 15^\circ$.

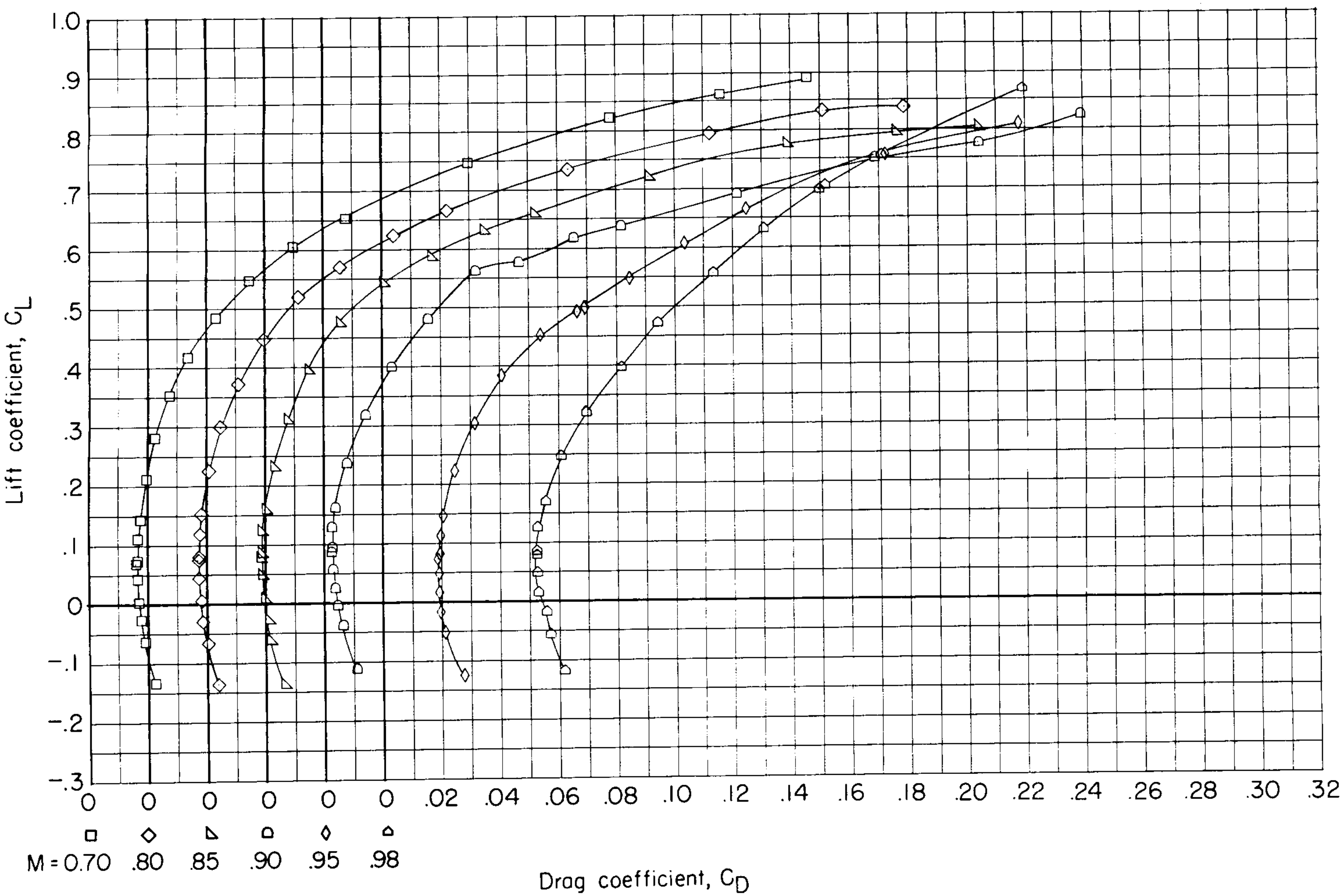

(b) Drag coefficient.

Figure 27.- Continued.

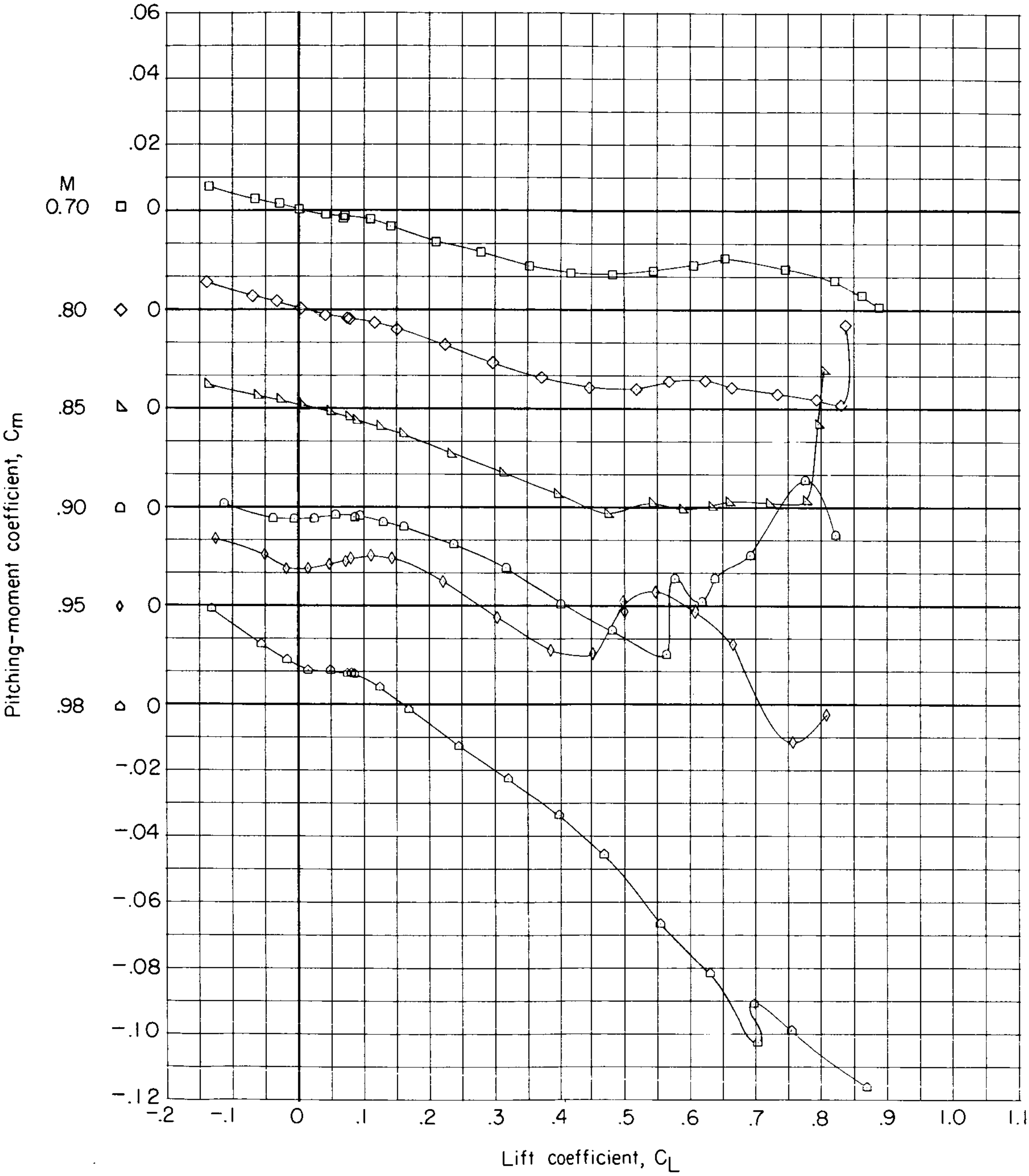

(c) Pitching-moment coefficient.

Figure 27.- Concluded.

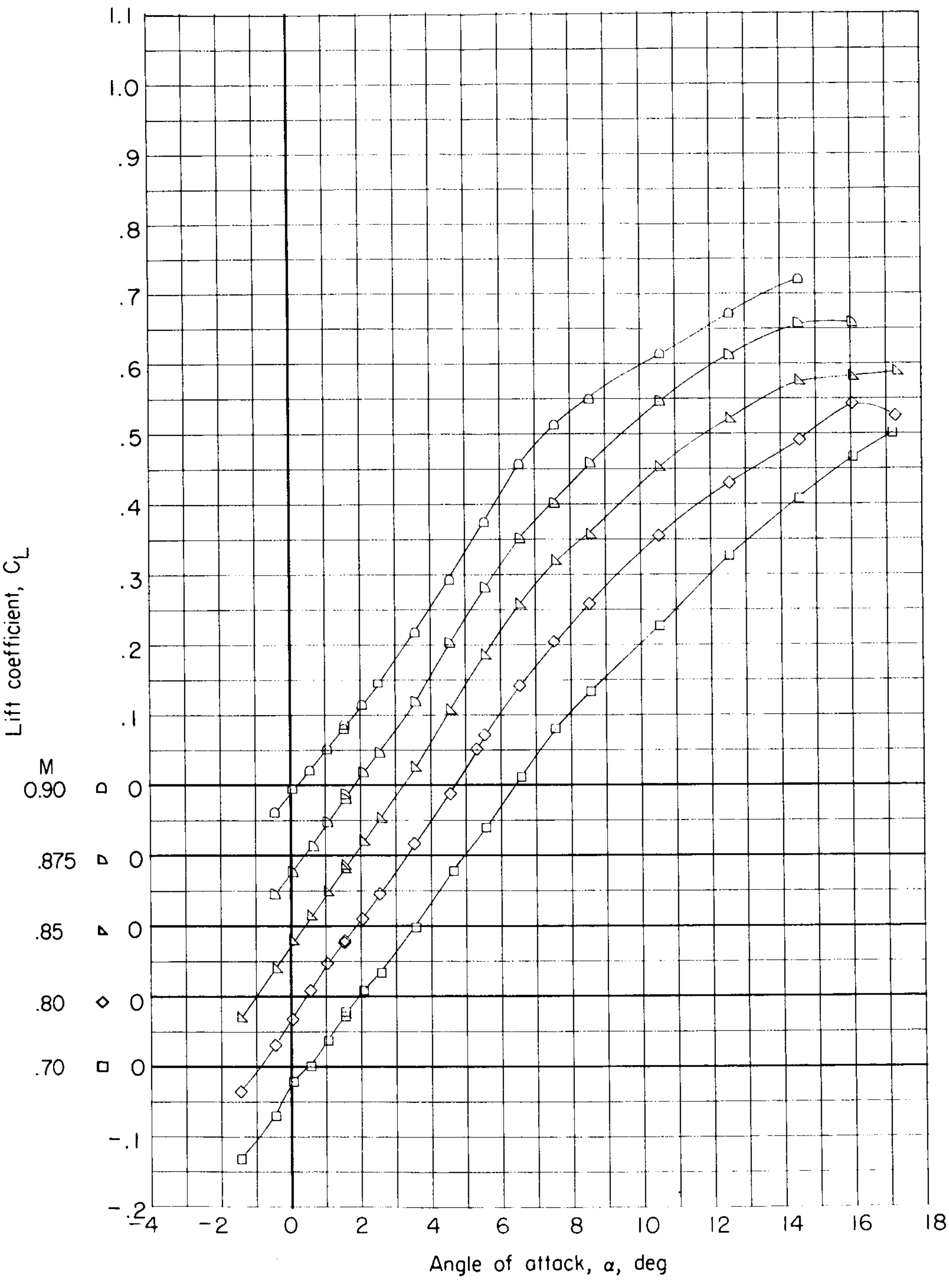

(a) Lift coefficient.

Figure 28.- Aerodynamic characteristics for model $BWEF_2$ with $\delta_{le} = 15^{\circ}$.

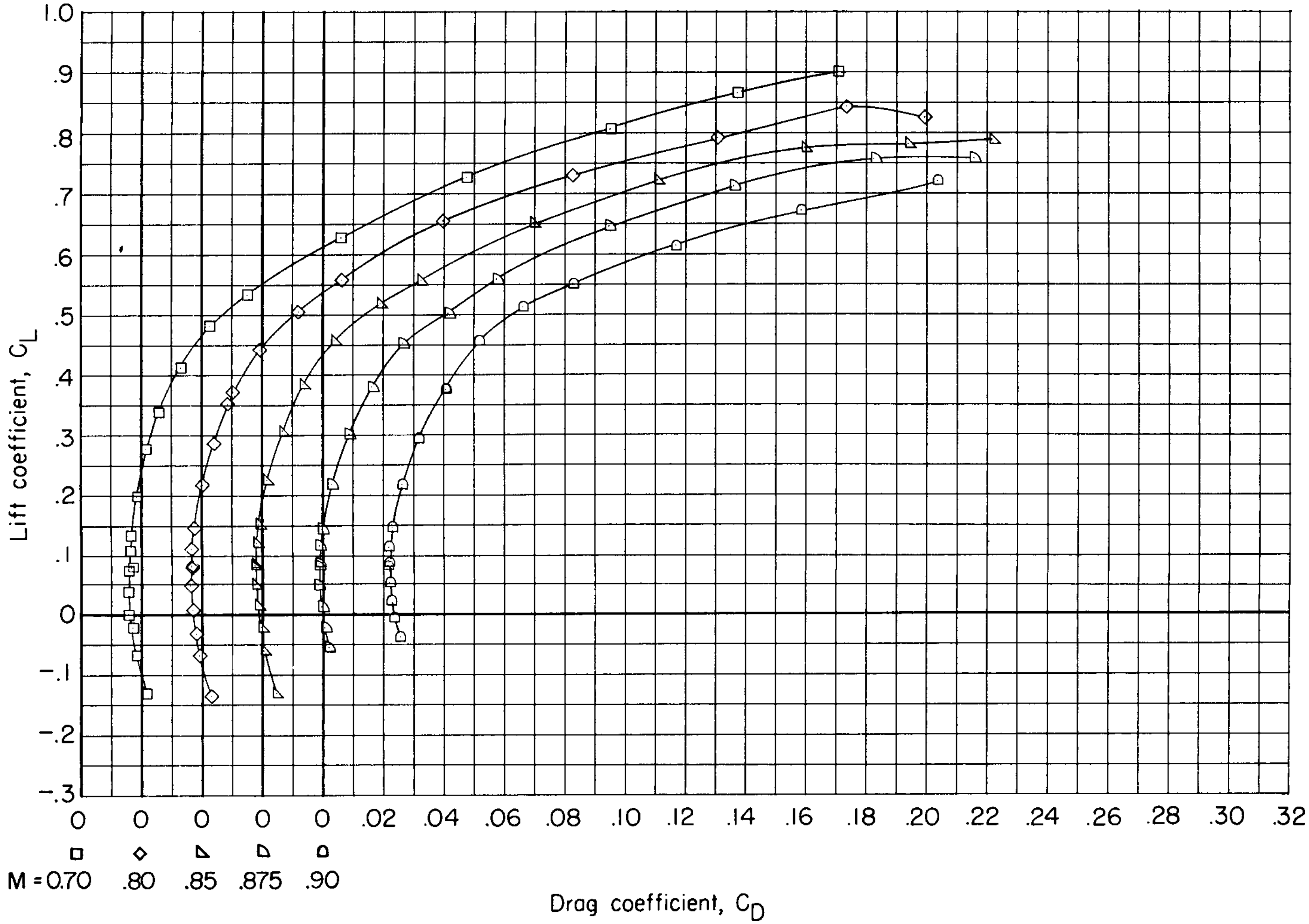

(b) Drag coefficient.

Figure 28.- Continued.

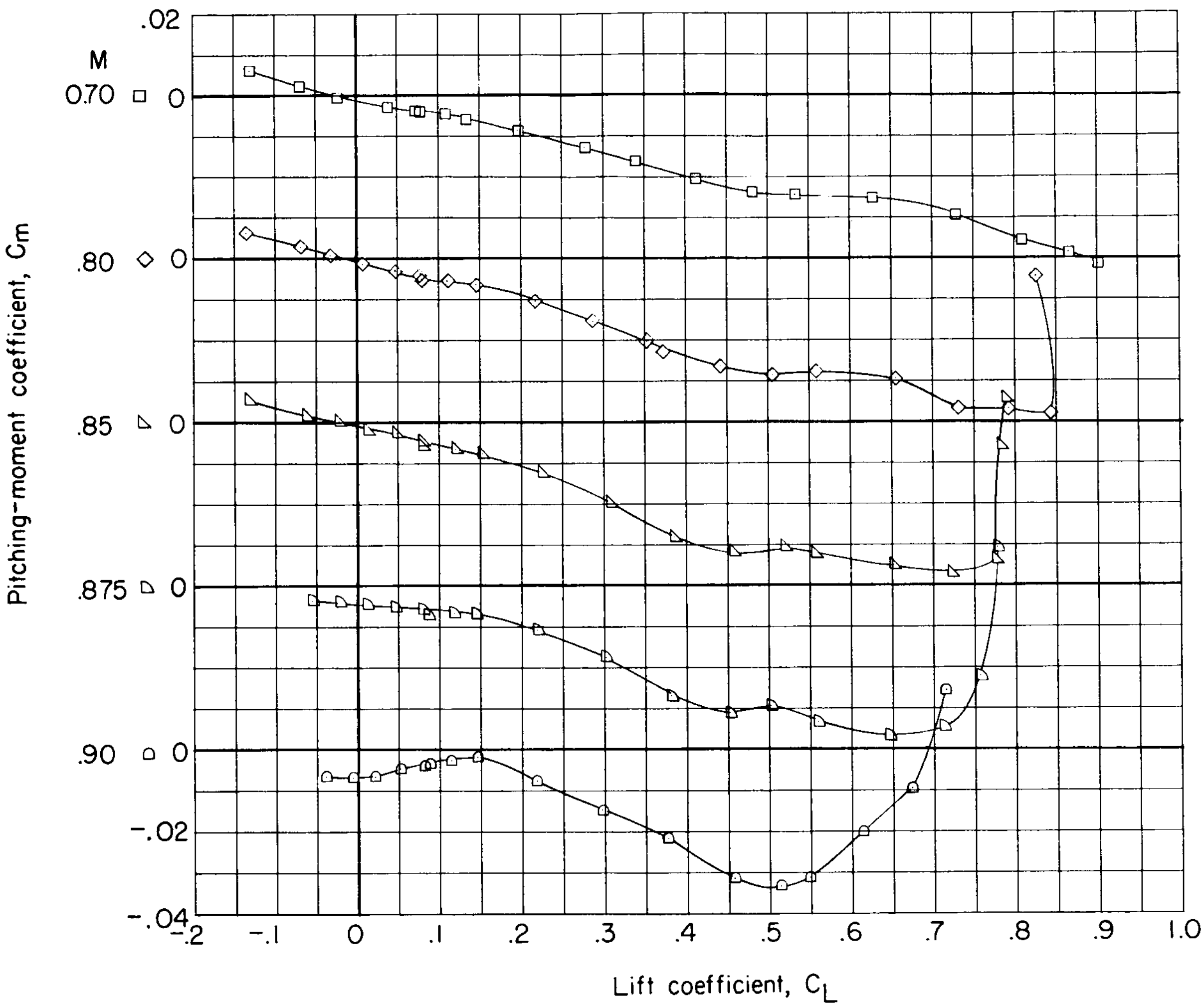

(c) Pitching-moment coefficient.

Figure 28.- Concluded.

L-1841

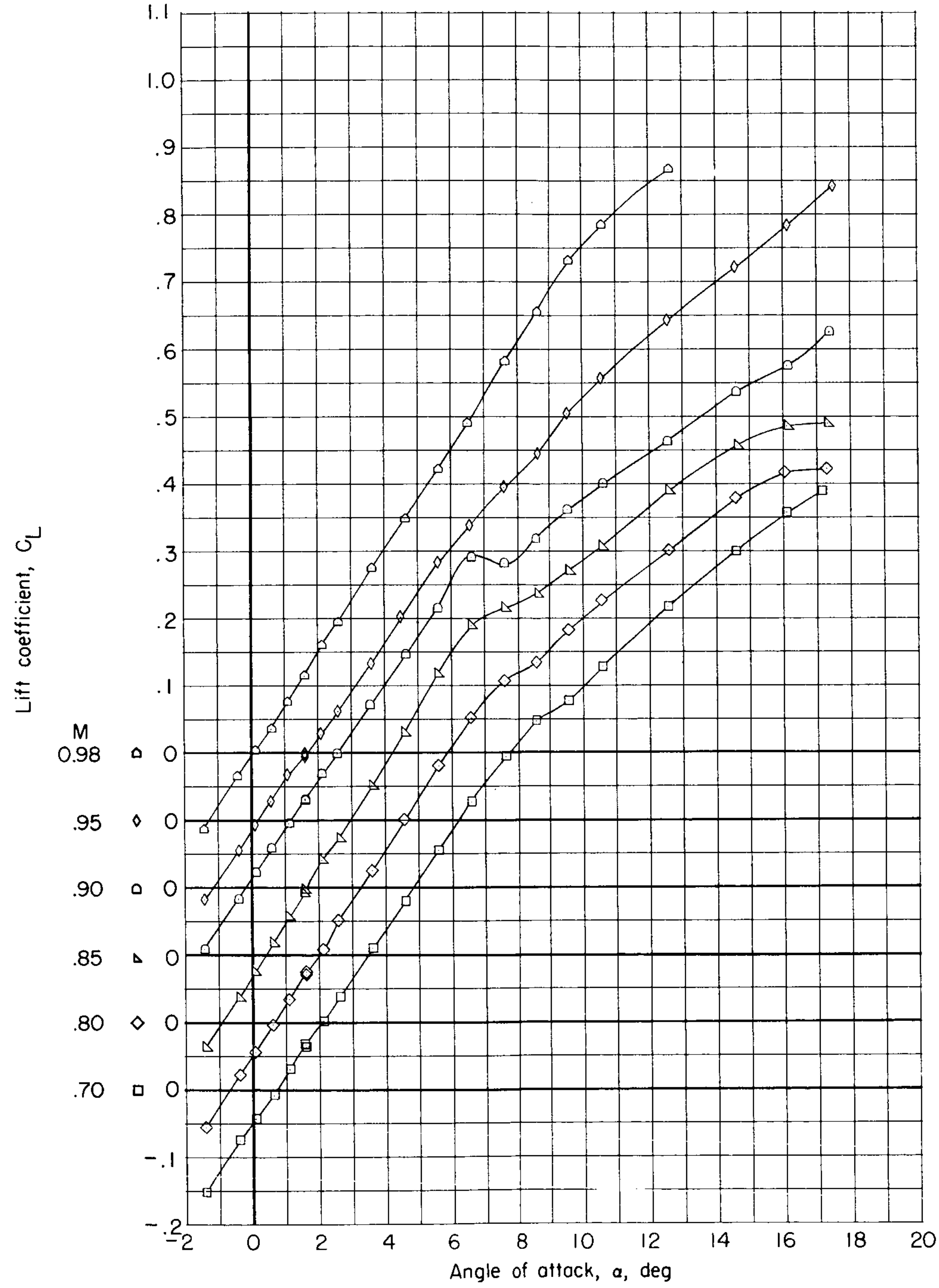

(a) Lift coefficient.

Figure 29.- Aerodynamic characteristics for model B_1WE with $\delta_{le} = 15^{\circ}$.

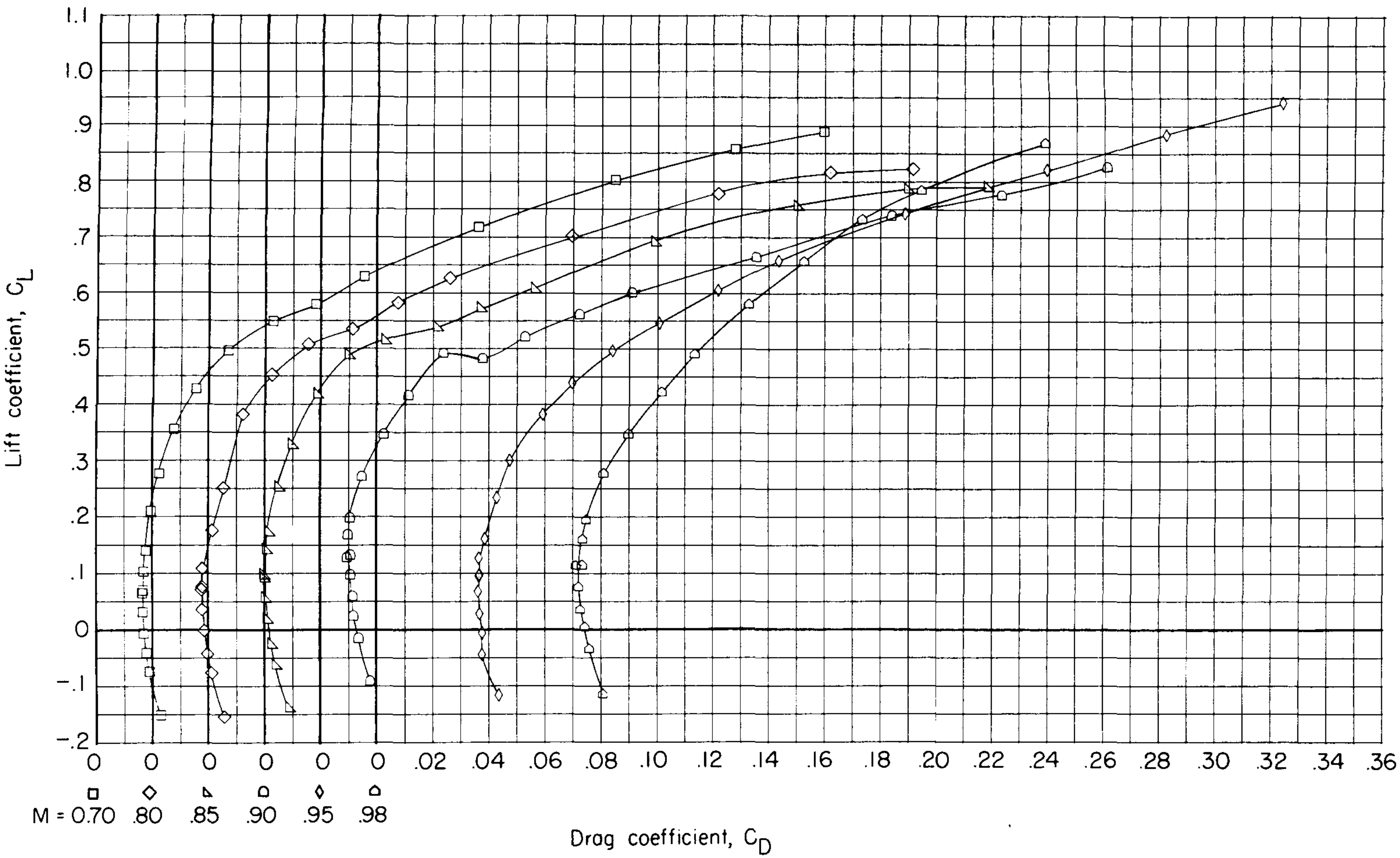

(b) Drag coefficient.

Figure 29.- Continued.

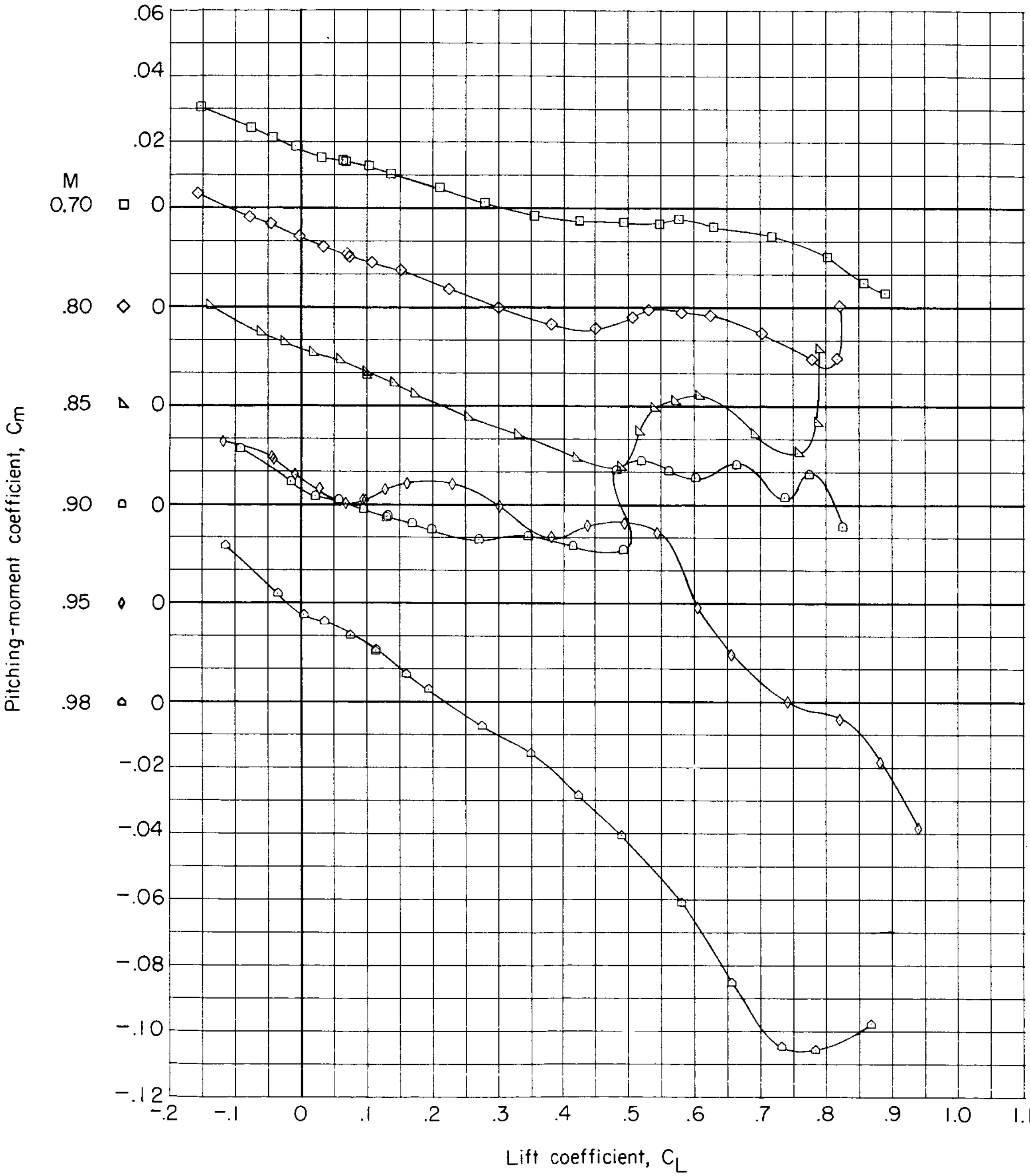

(c) Pitching-moment coefficient.

Figure 29.- Concluded.

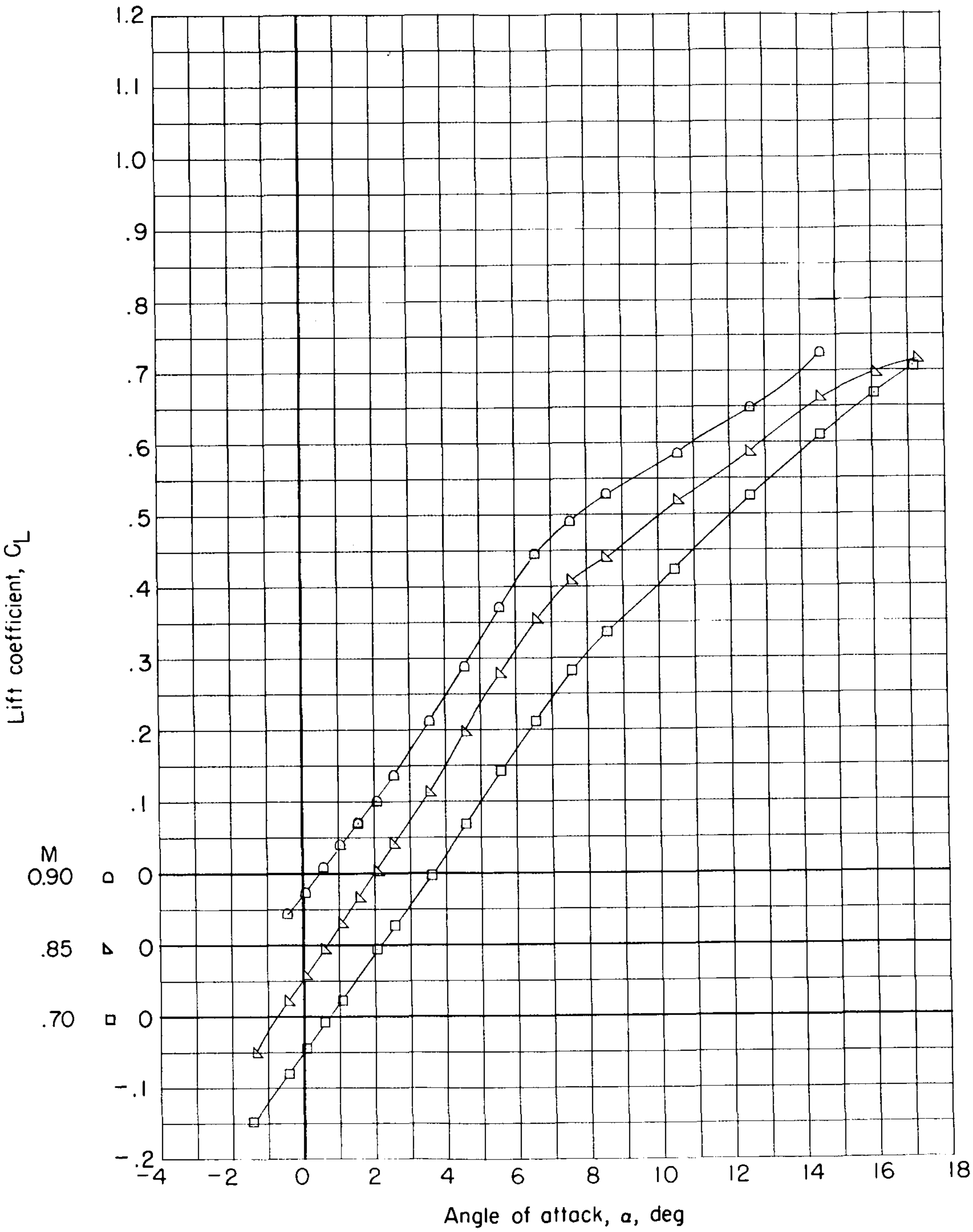

(a) Lift coefficient.

Figure 30.- Aerodynamic characteristics with transition distributed around wing leading edge for model BWE with $\delta_{le} = 25^{\circ}$.

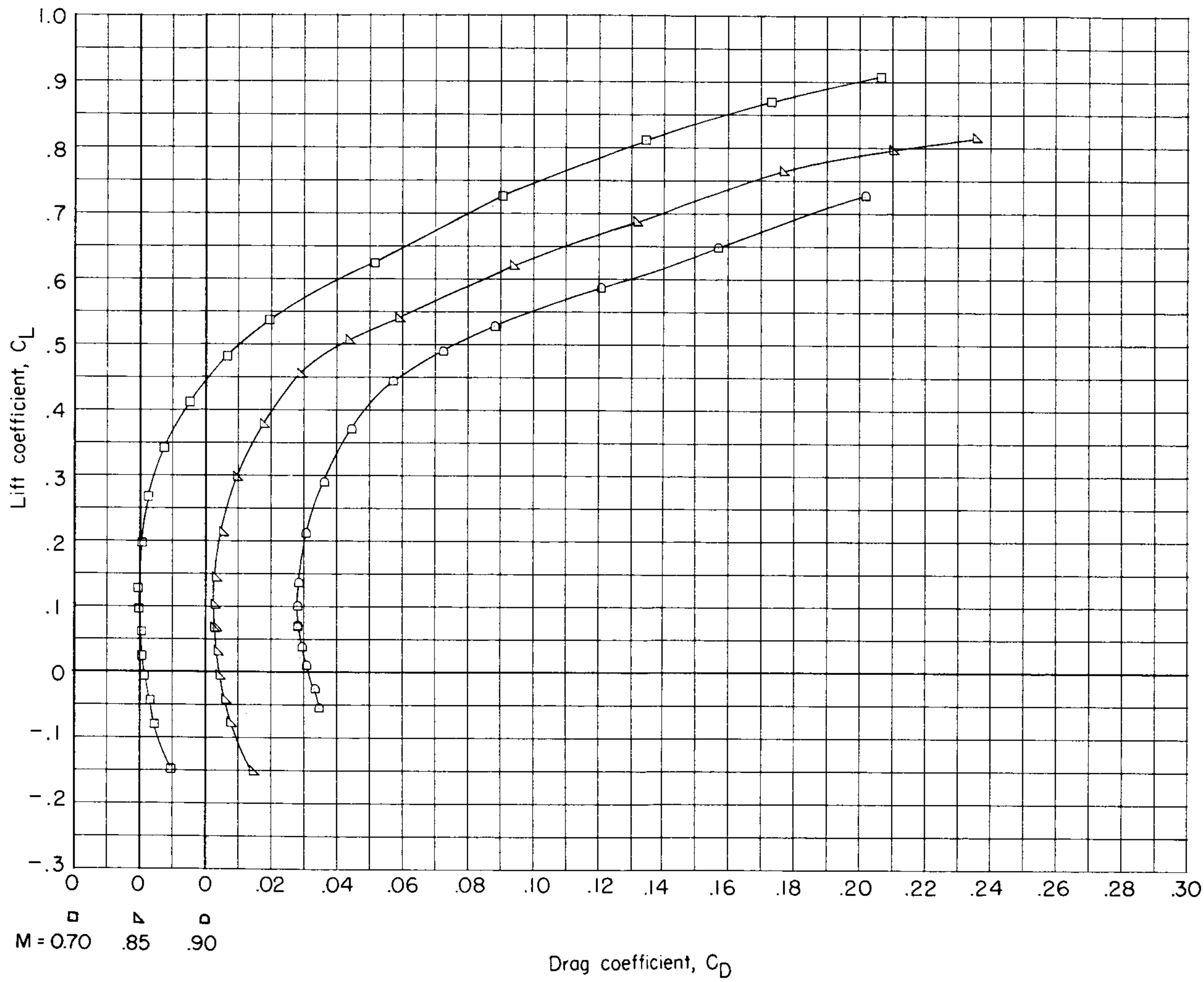

(b) Drag coefficient.

Figure 30.- Continued.

[redacted]

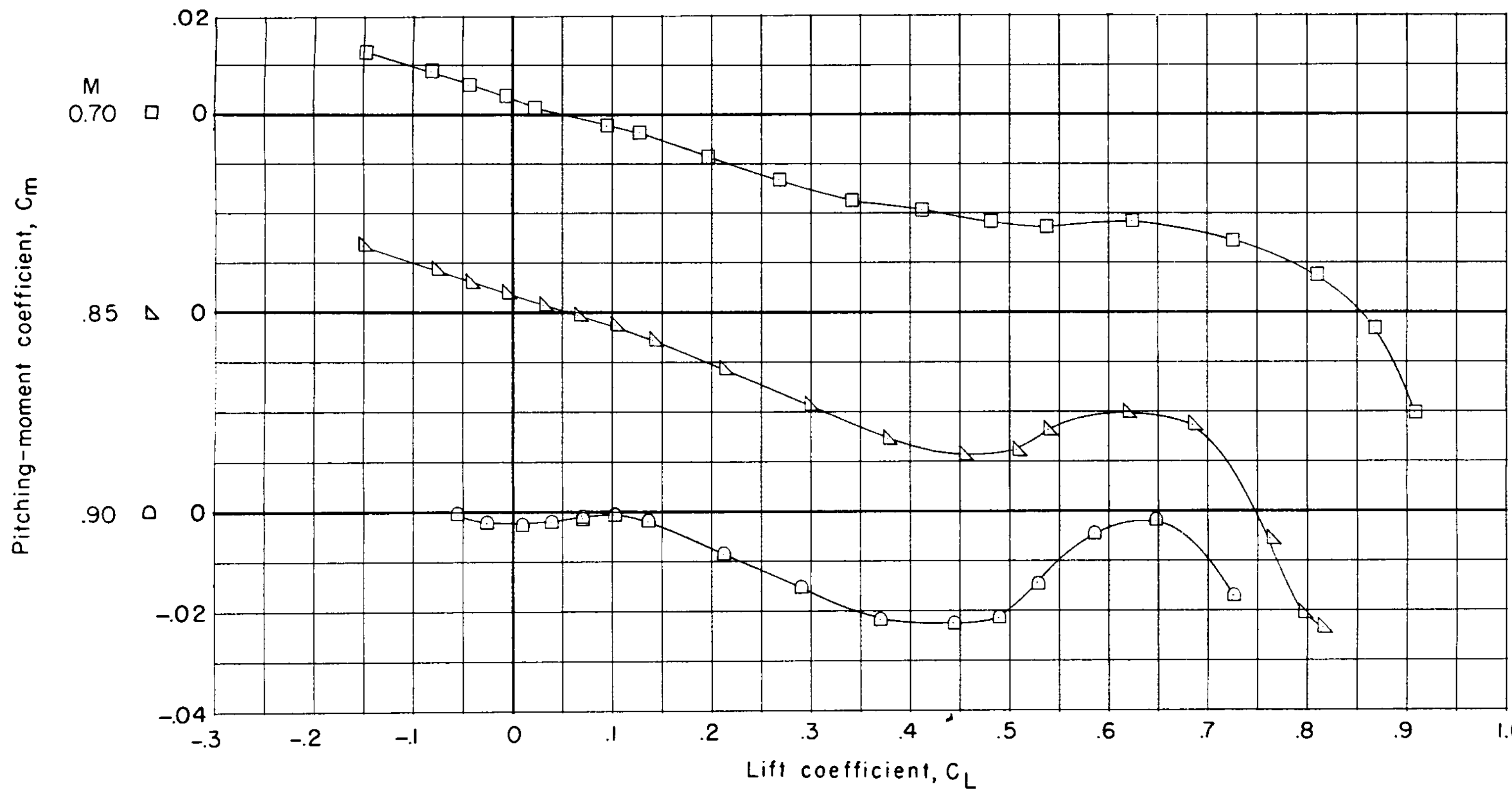

(c) Pitching-moment coefficient.

Figure 30.- Concluded.

[redacted]

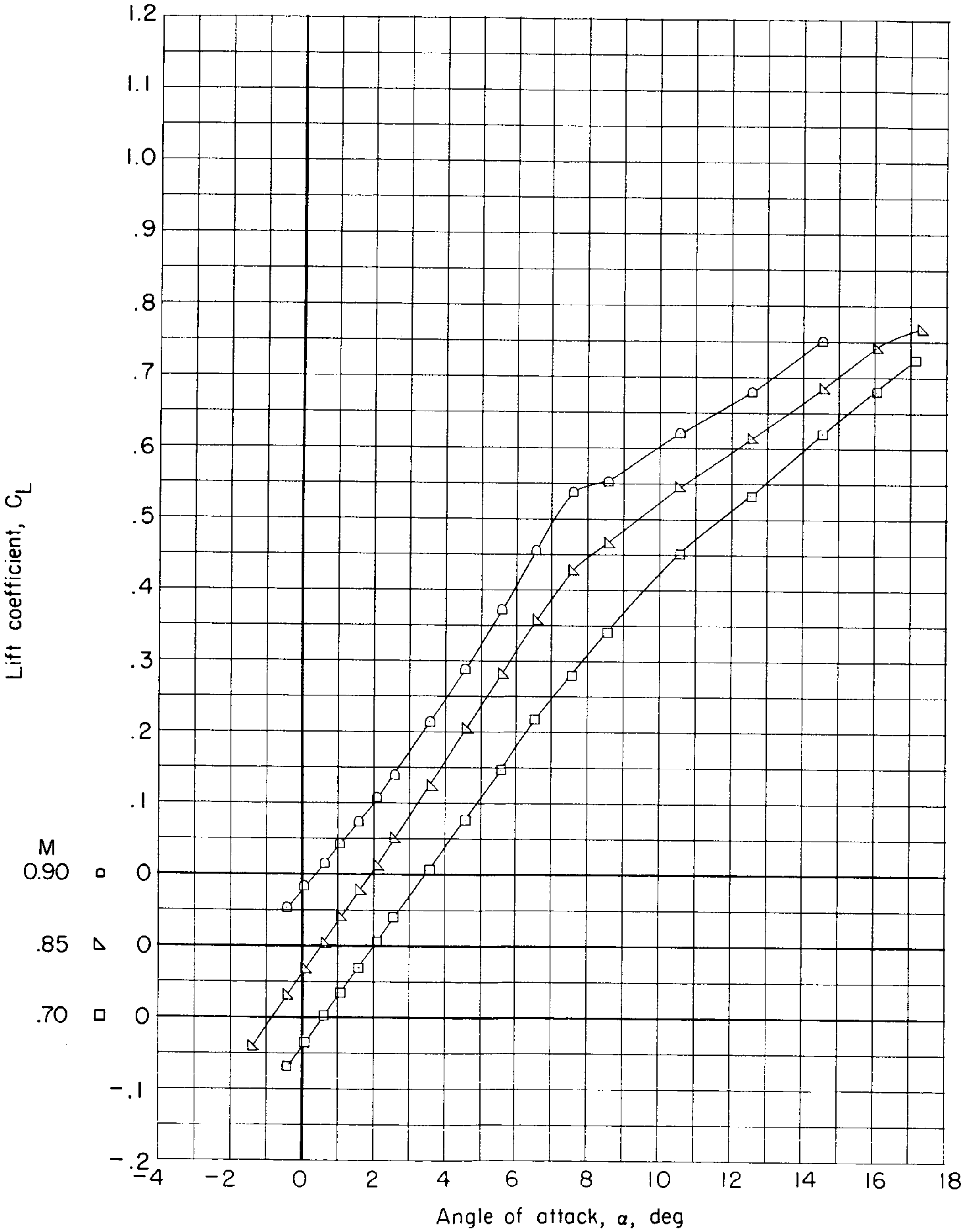

(a) Lift coefficient.

Figure 31.- Aerodynamic characteristics with free transition for model BWE with $\delta_{le} = 25^{\circ}$.

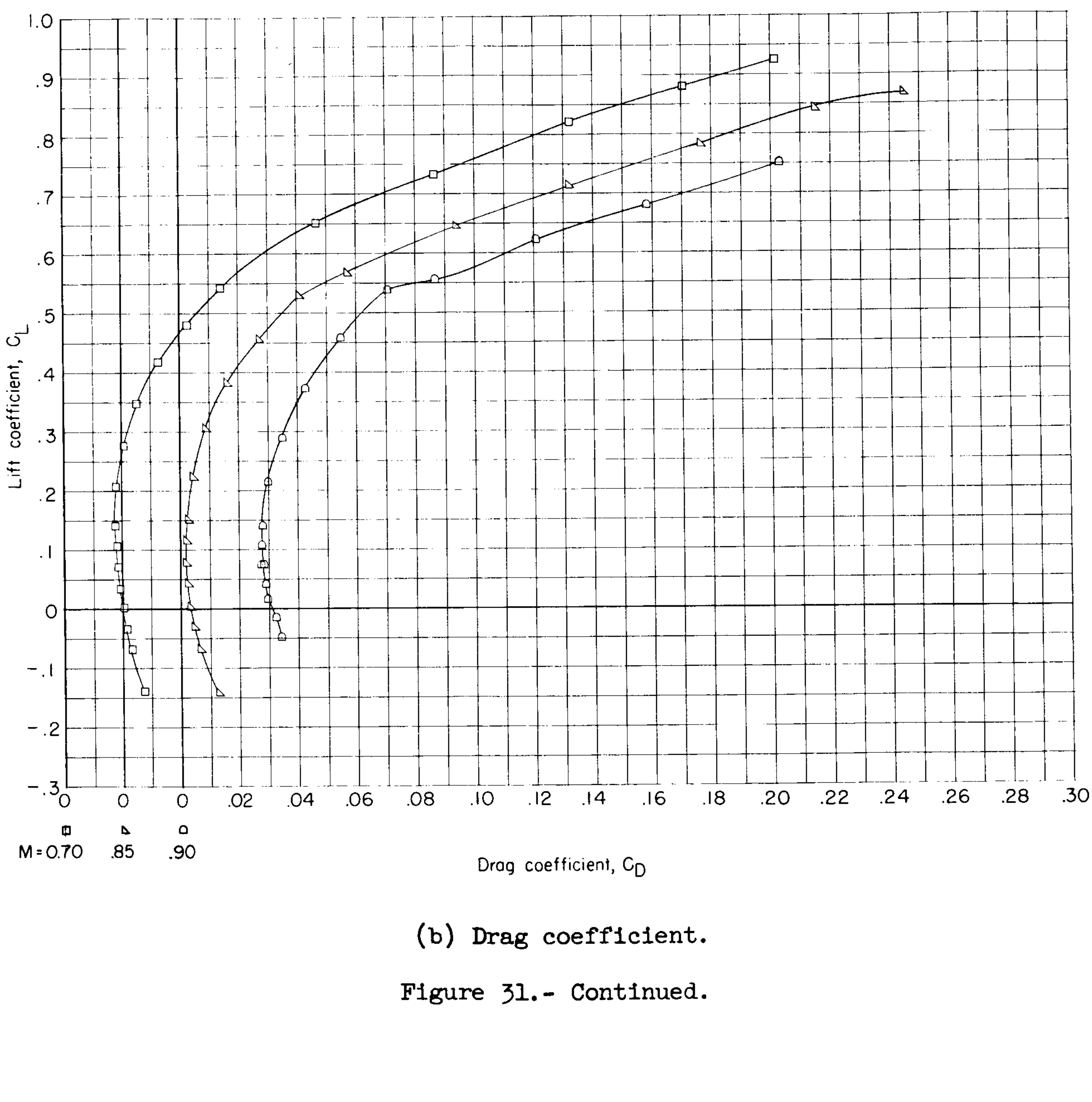

(b) Drag coefficient.

Figure 31.- Continued.

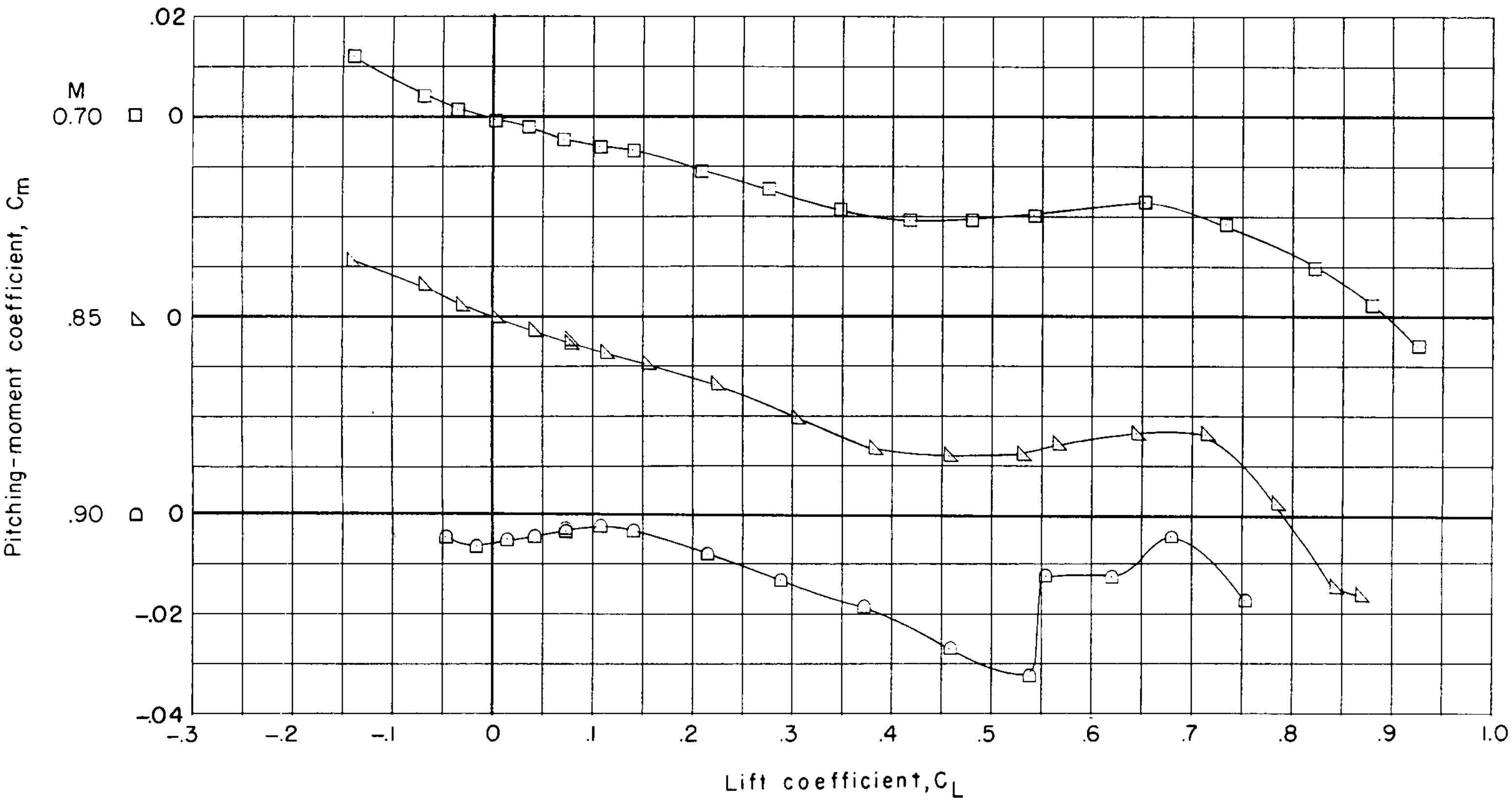

(c) Pitching-moment coefficient.

Figure 31.- Concluded.

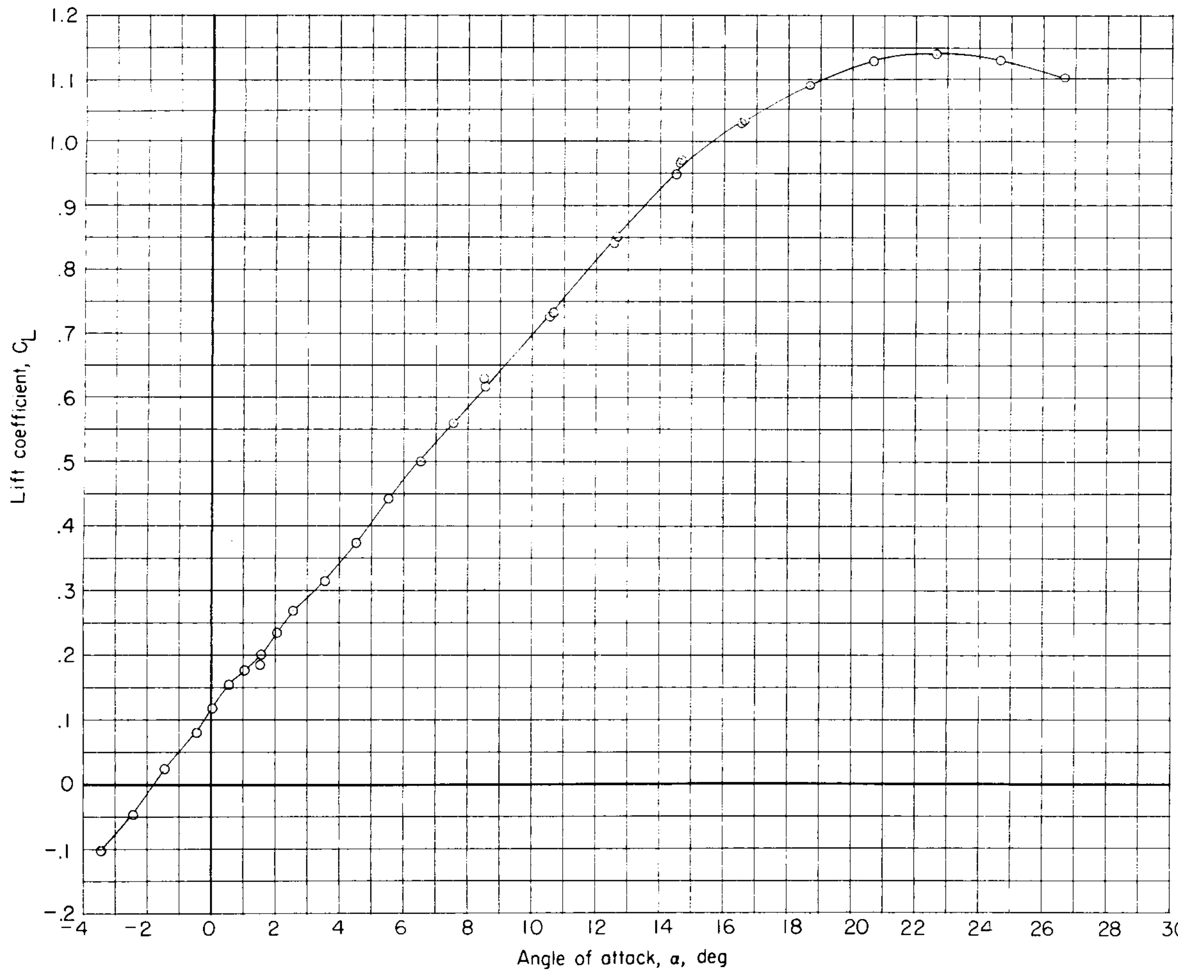

(a) Lift coefficient.

Figure 32.- Aerodynamic characteristics for model BWE with $\delta_{le} = 30^{\circ}$, $\delta_{te} = 25^{\circ}$, and $\delta_{tr} = 25^{\circ}$ at $M = 0.30$.

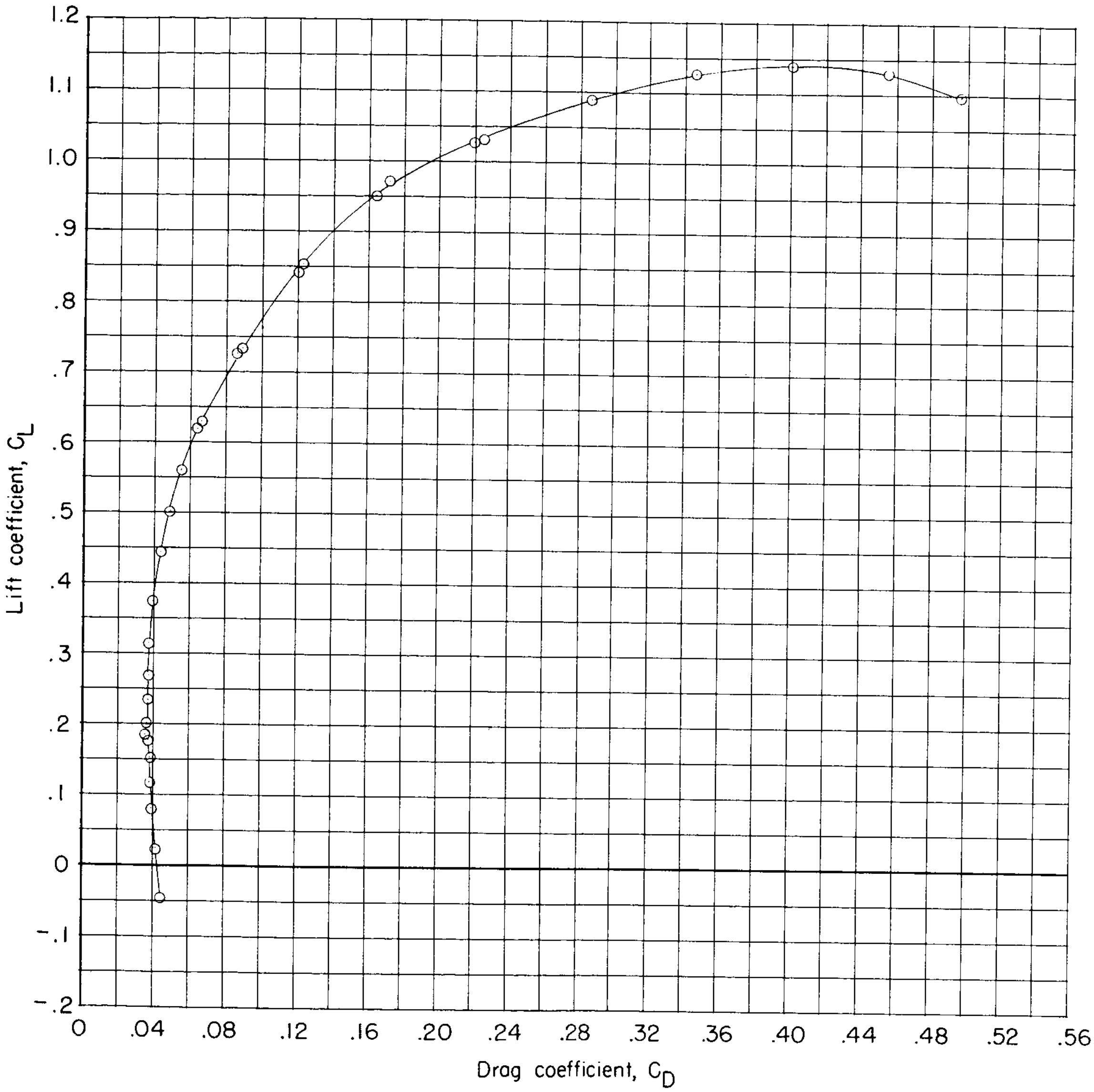

(b) Drag coefficient.

Figure 32.- Continued.

[redacted]

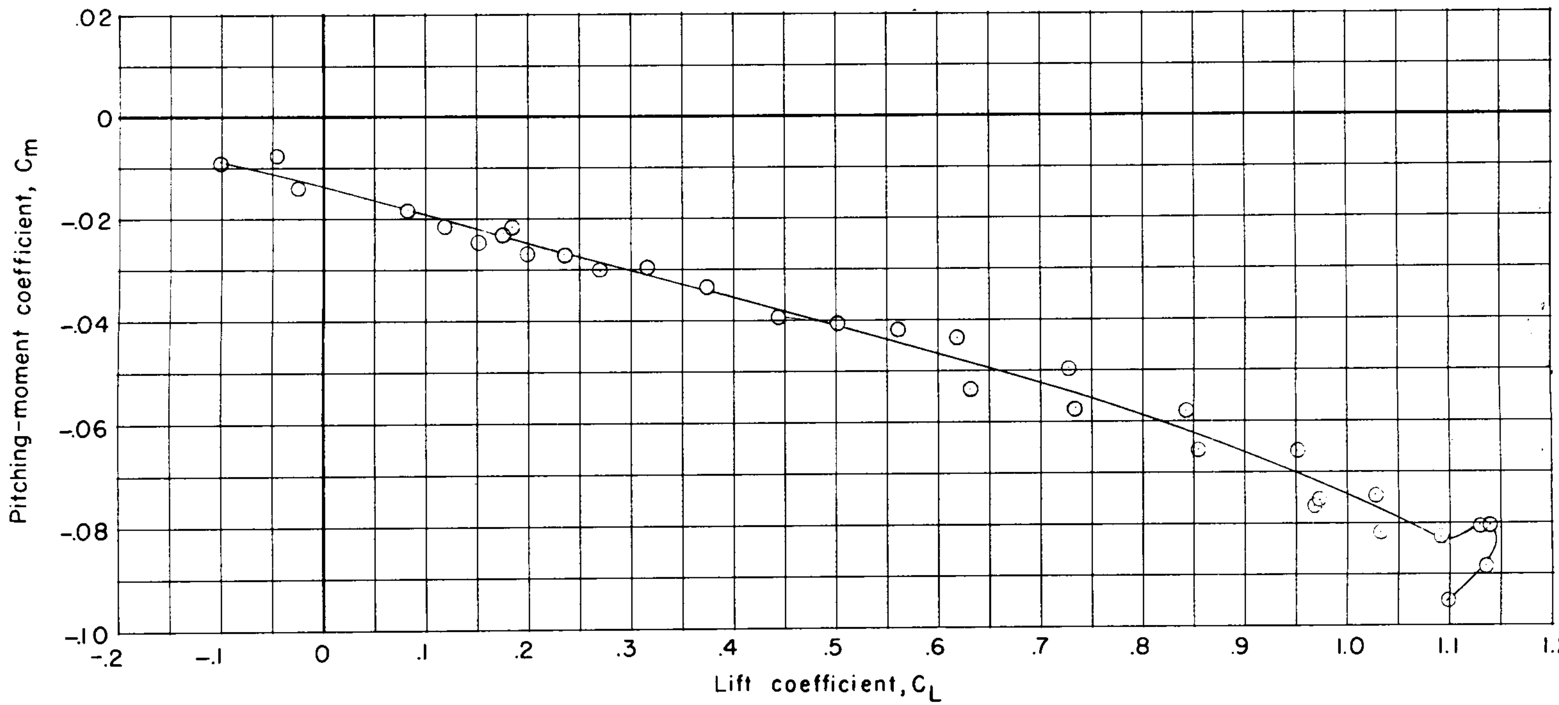

(c) Pitching-moment coefficient.

Figure 32.- Concluded.

C[redacted]TIAL

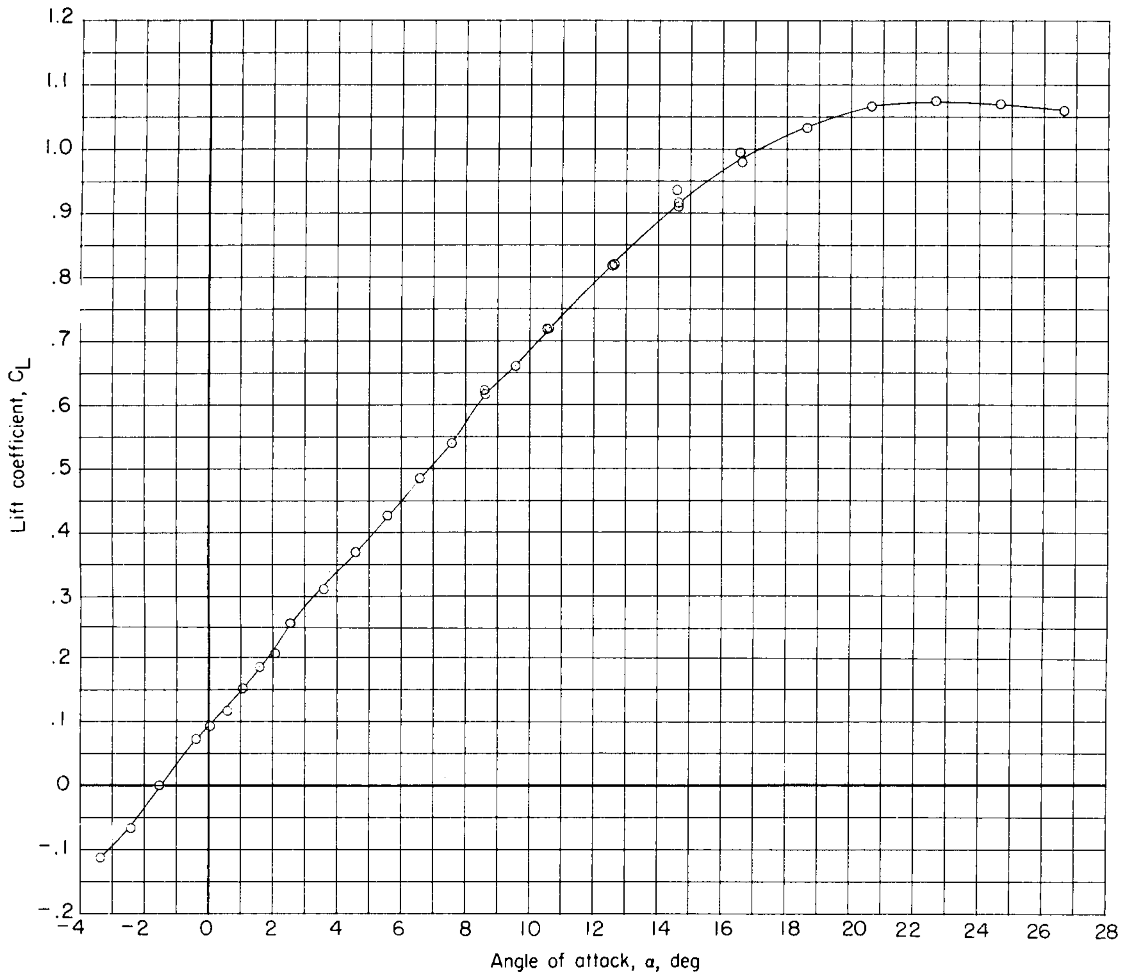

(a) Lift coefficient.

Figure 33.- Aerodynamic characteristics for model BWE with $\delta_{le} = 45^o$, $\delta_{te} = 25^o$, and $\delta_{tr} = 25^o$ at $M = 0.30$.

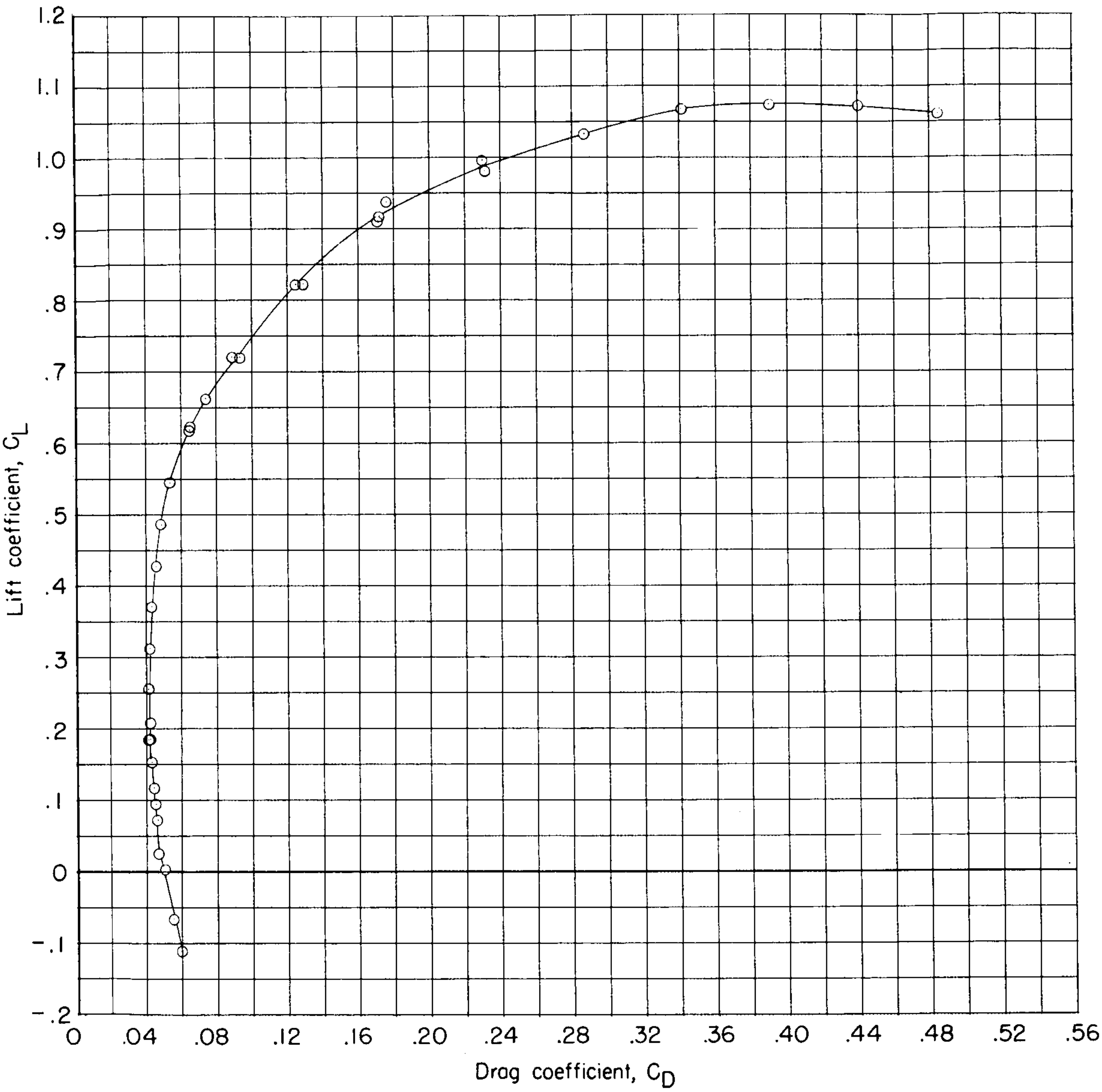

(b) Drag coefficient.

Figure 33.- Continued.

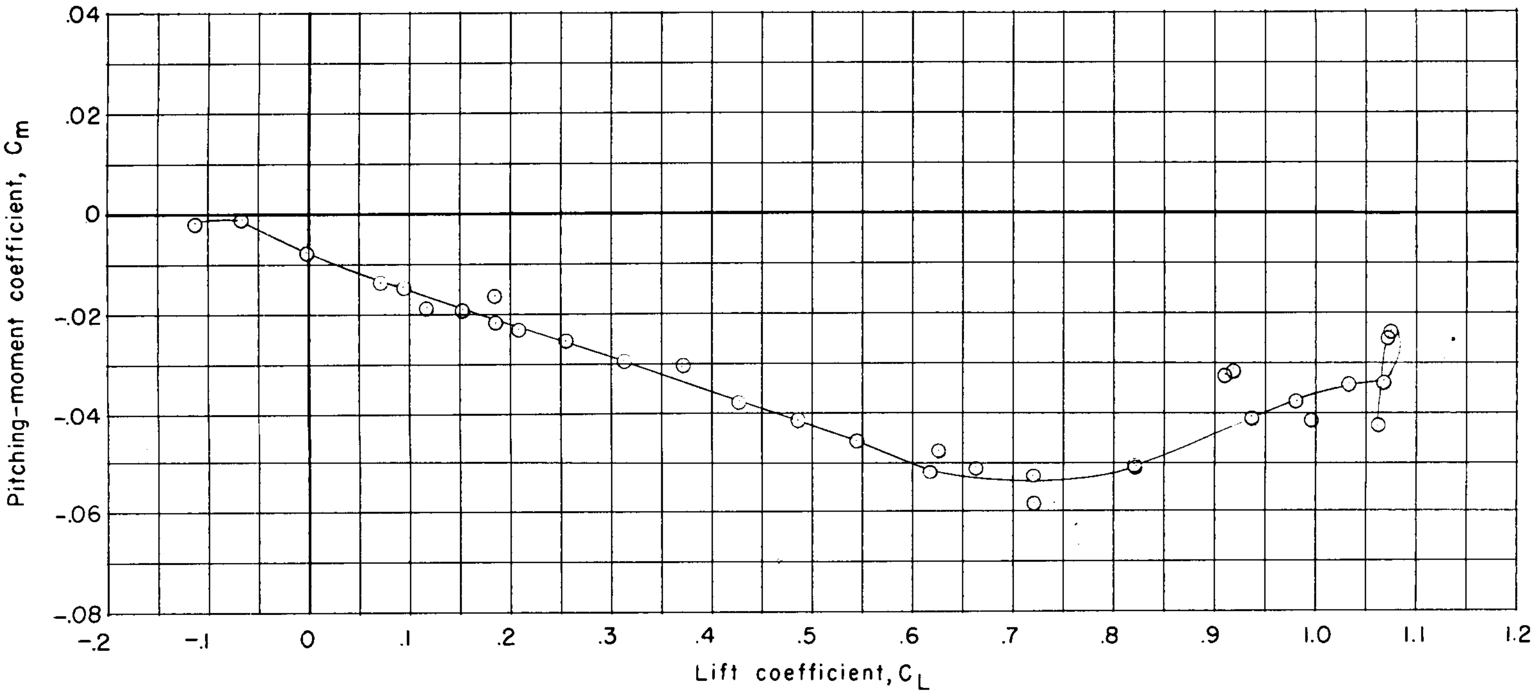

(c) Pitching-moment coefficient.

Figure 33.- Concluded.

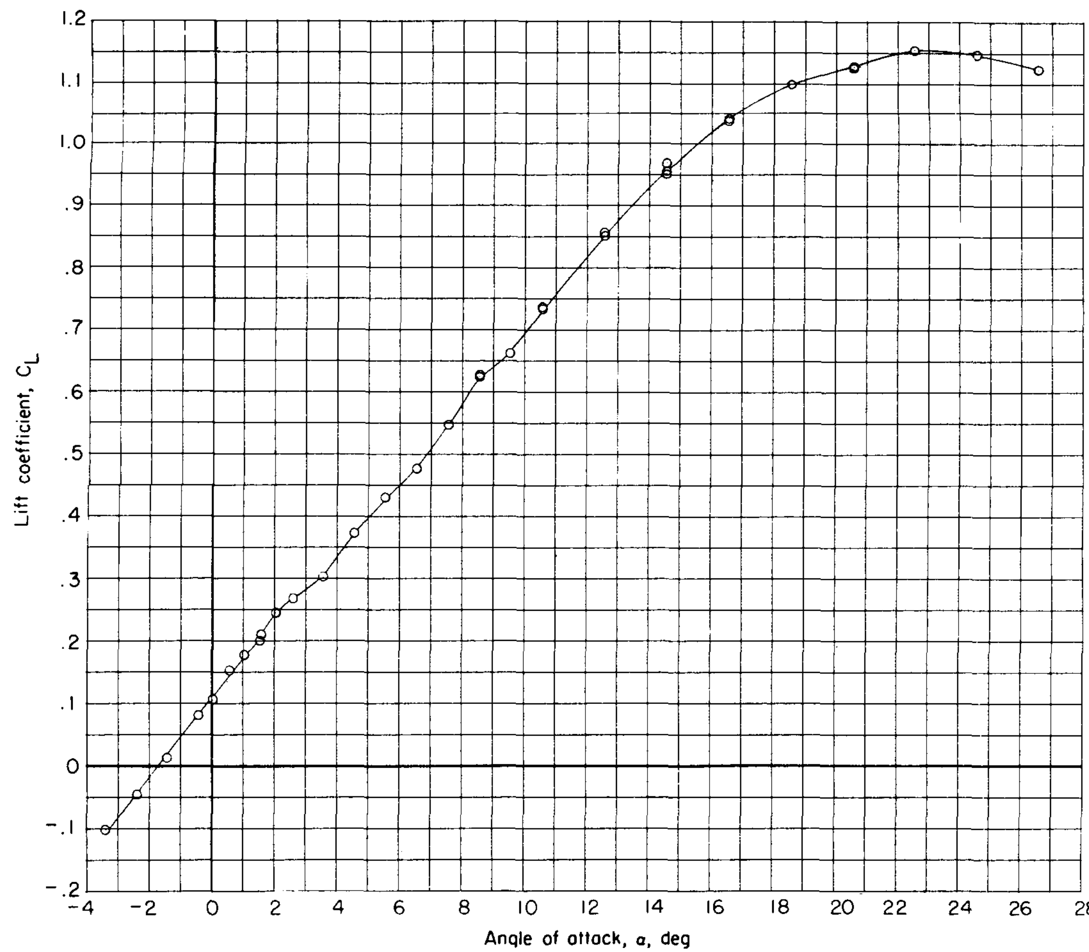

(a) Lift coefficient.

Figure 34.- Aerodynamic characteristics for model BW_1E with $\delta_{le} = 30^o$, $\delta_{te} = 25^o$, and $\delta_{tr} = 25^o$ at $M = 0.30$.

L-1841

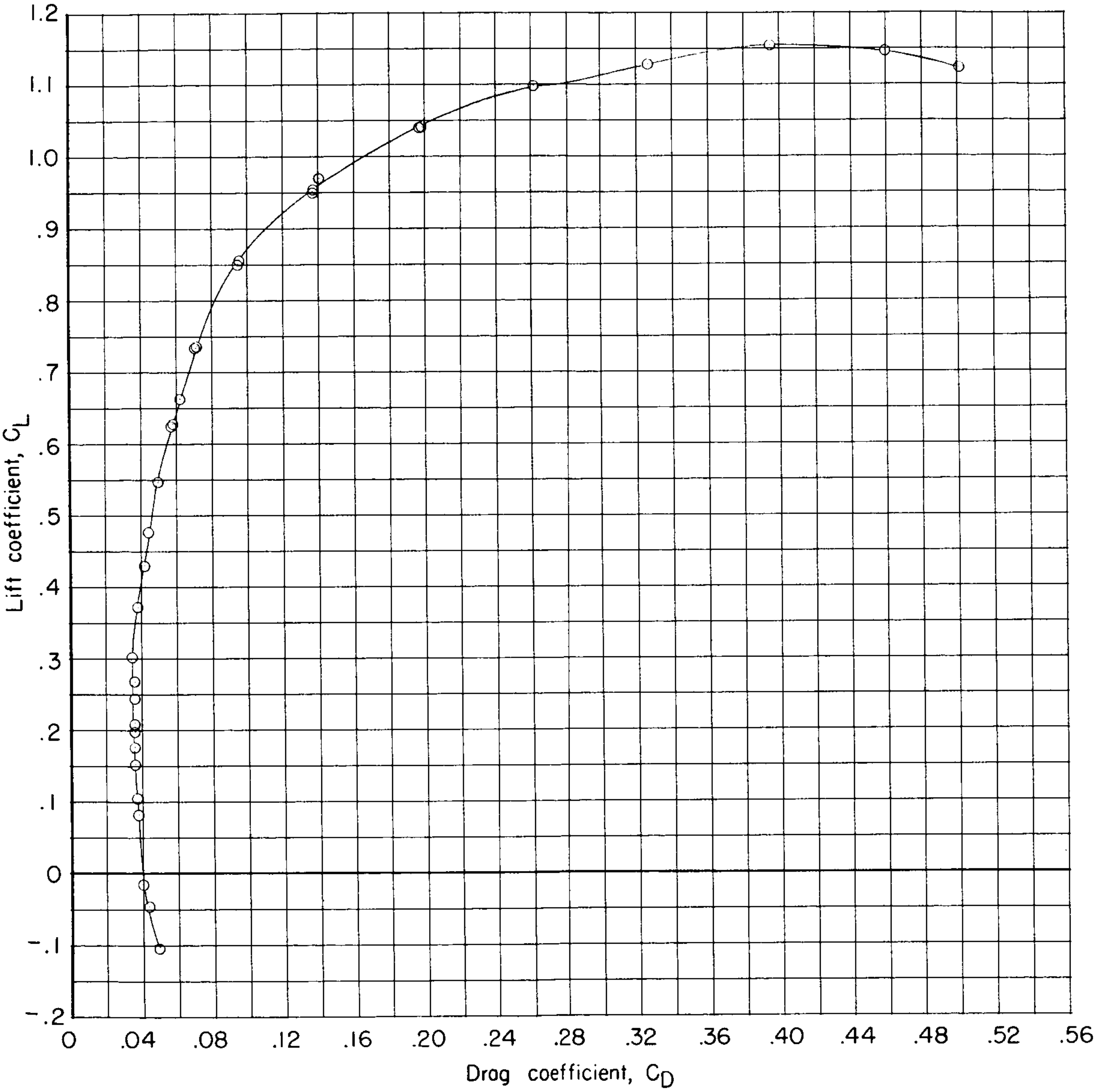

(b) Drag coefficient.

Figure 34.- Continued.

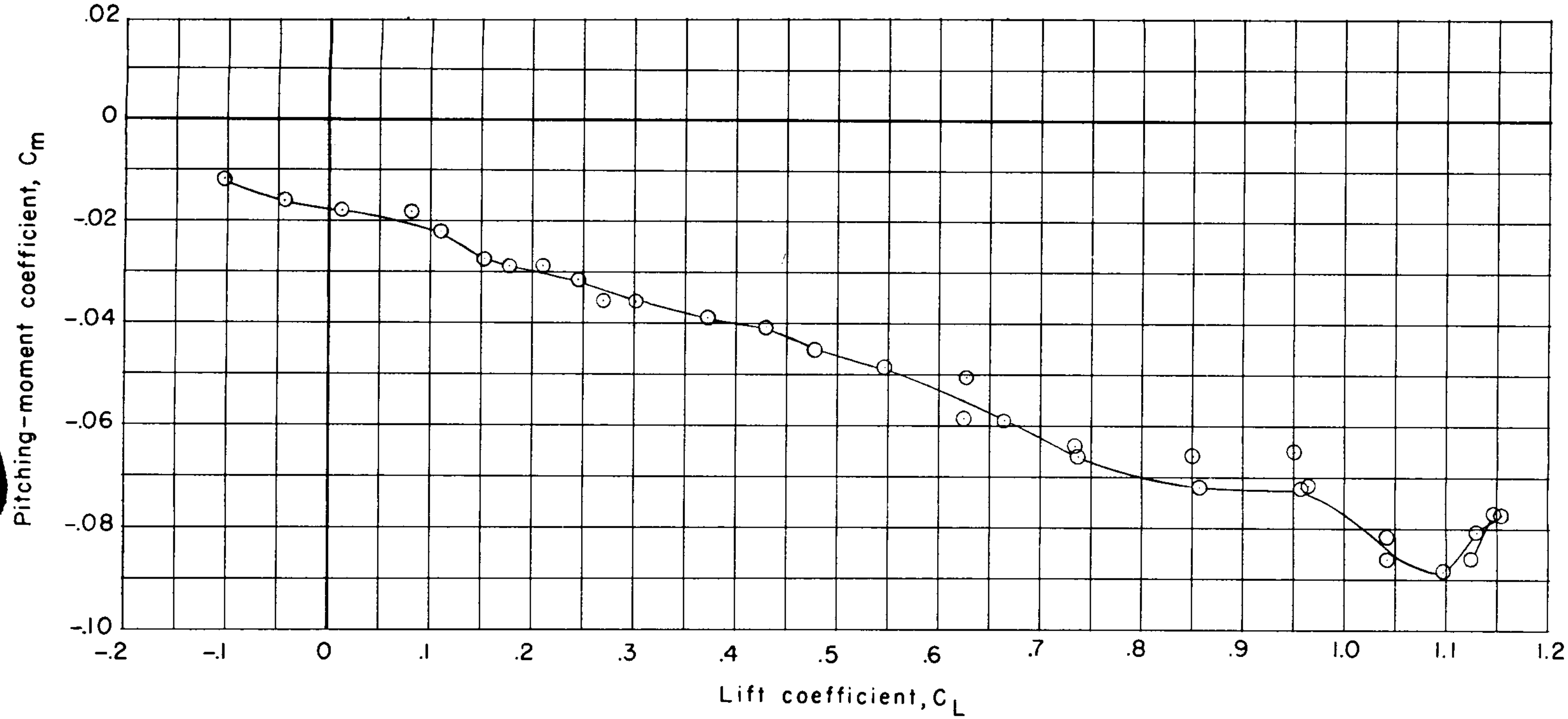

(c) Pitching-moment coefficient.

Figure 34.- Concluded.

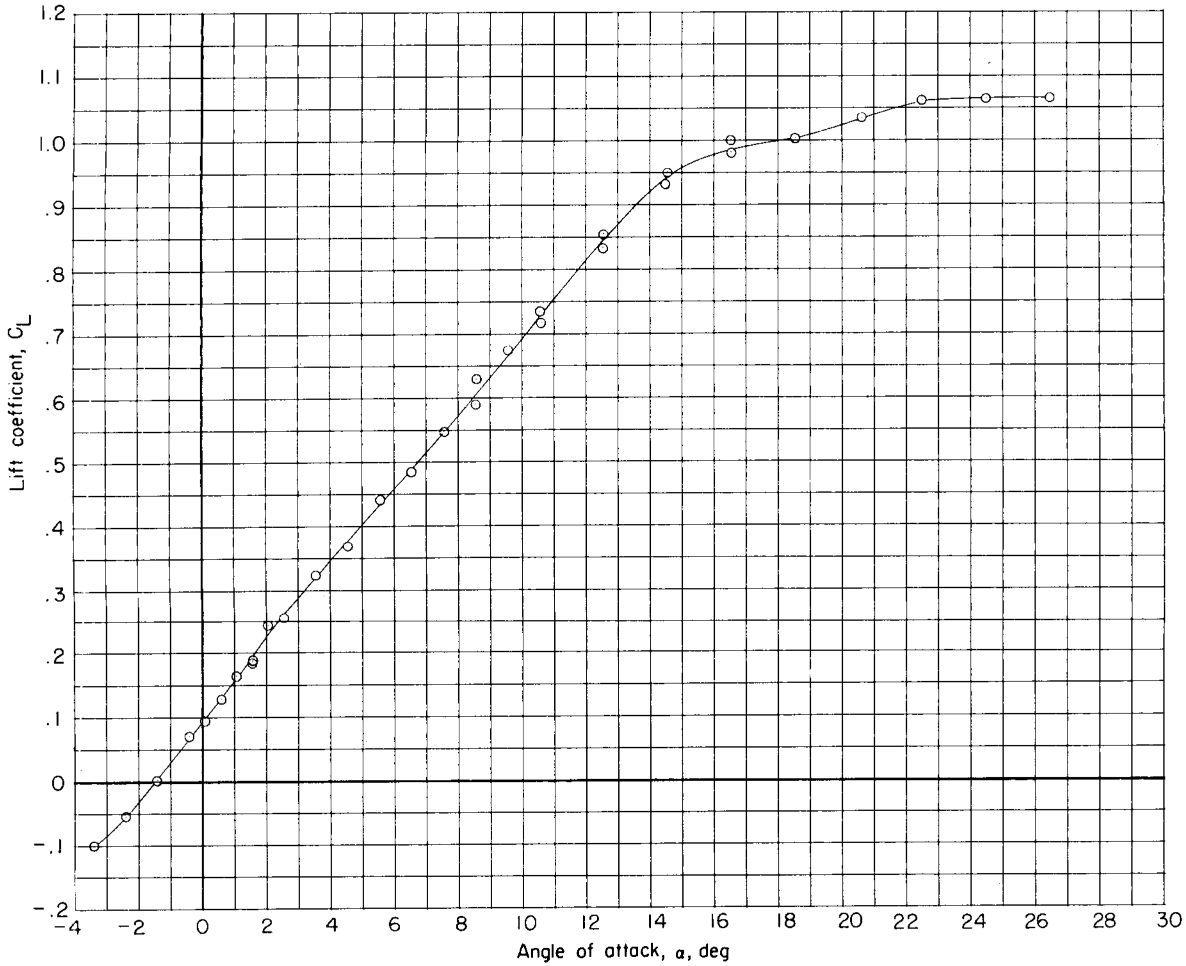

(a) Lift coefficient.

Figure 35.- Aerodynamic characteristics for model BW_1E with $\delta_{le} = 45^{\circ}$, $\delta_{te} = 25^{\circ}$, and $\delta_{tr} = 25^{\circ}$ at $M = 0.30$.

[redacted]

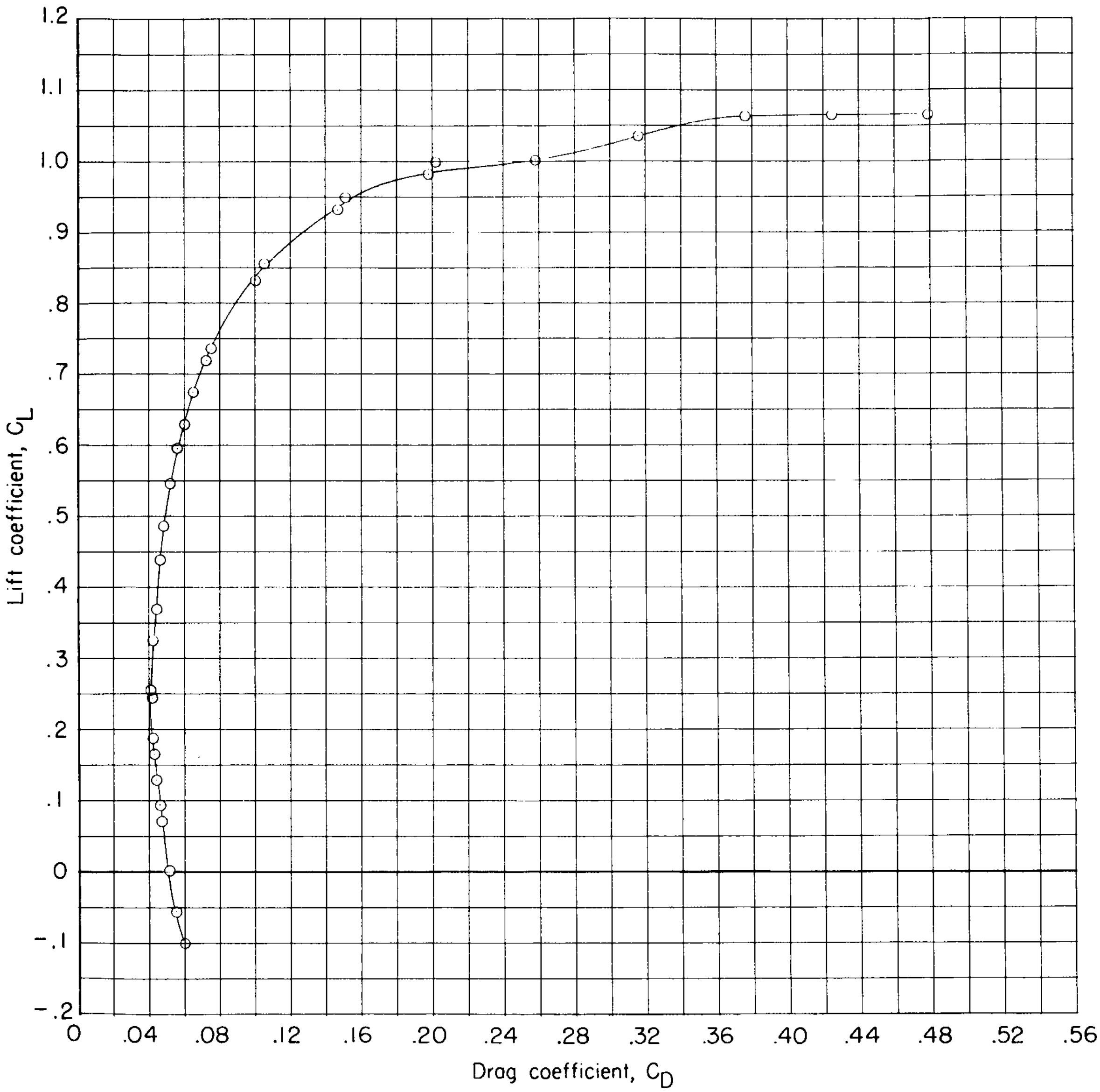

(b) Drag coefficient.

Figure 35.- Continued.

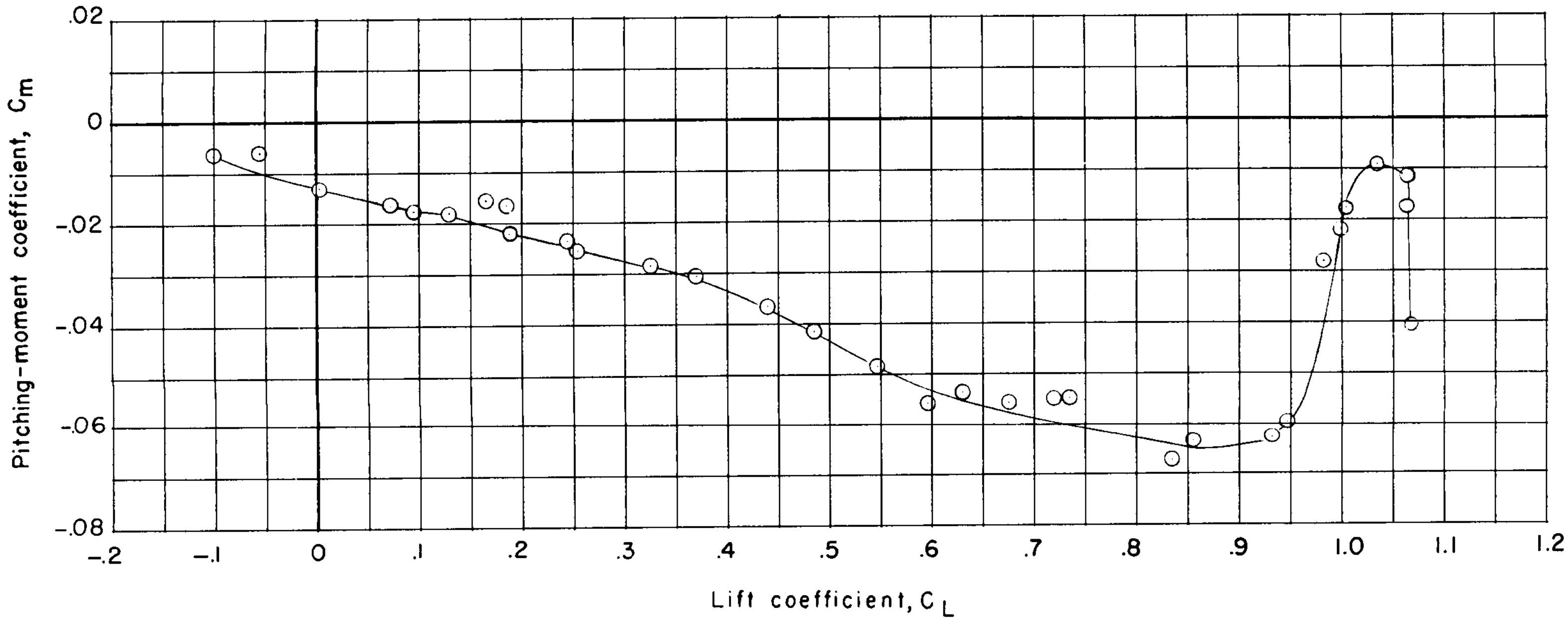

(c) Pitching-moment coefficient.

Figure 35.- Concluded.

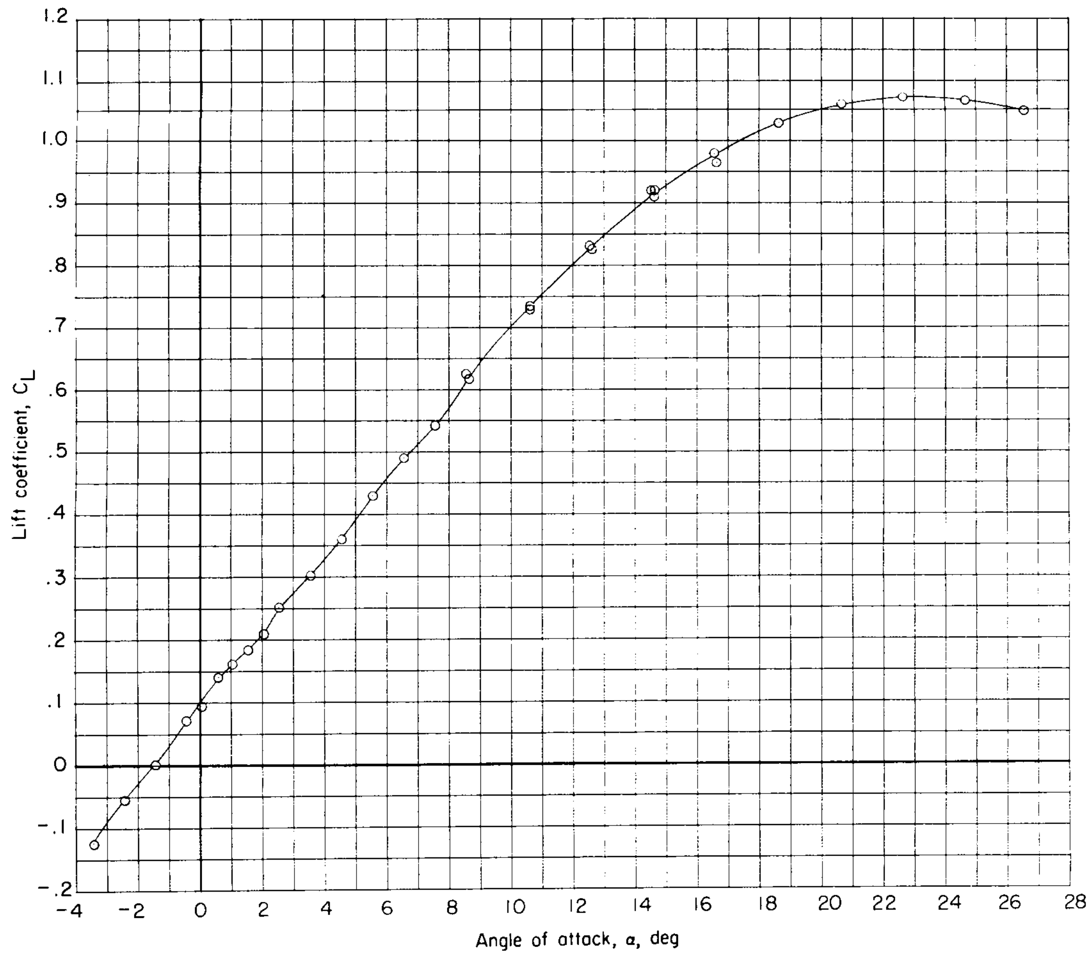

(a) Lift coefficient.

Figure 36.- Aerodynamic characteristics for model $BWEF_1$ with $\delta_{le} = 45^\circ$, $\delta_{te} = 25^\circ$, and $\delta_{tr} = 25^\circ$ at $M = 0.30$.

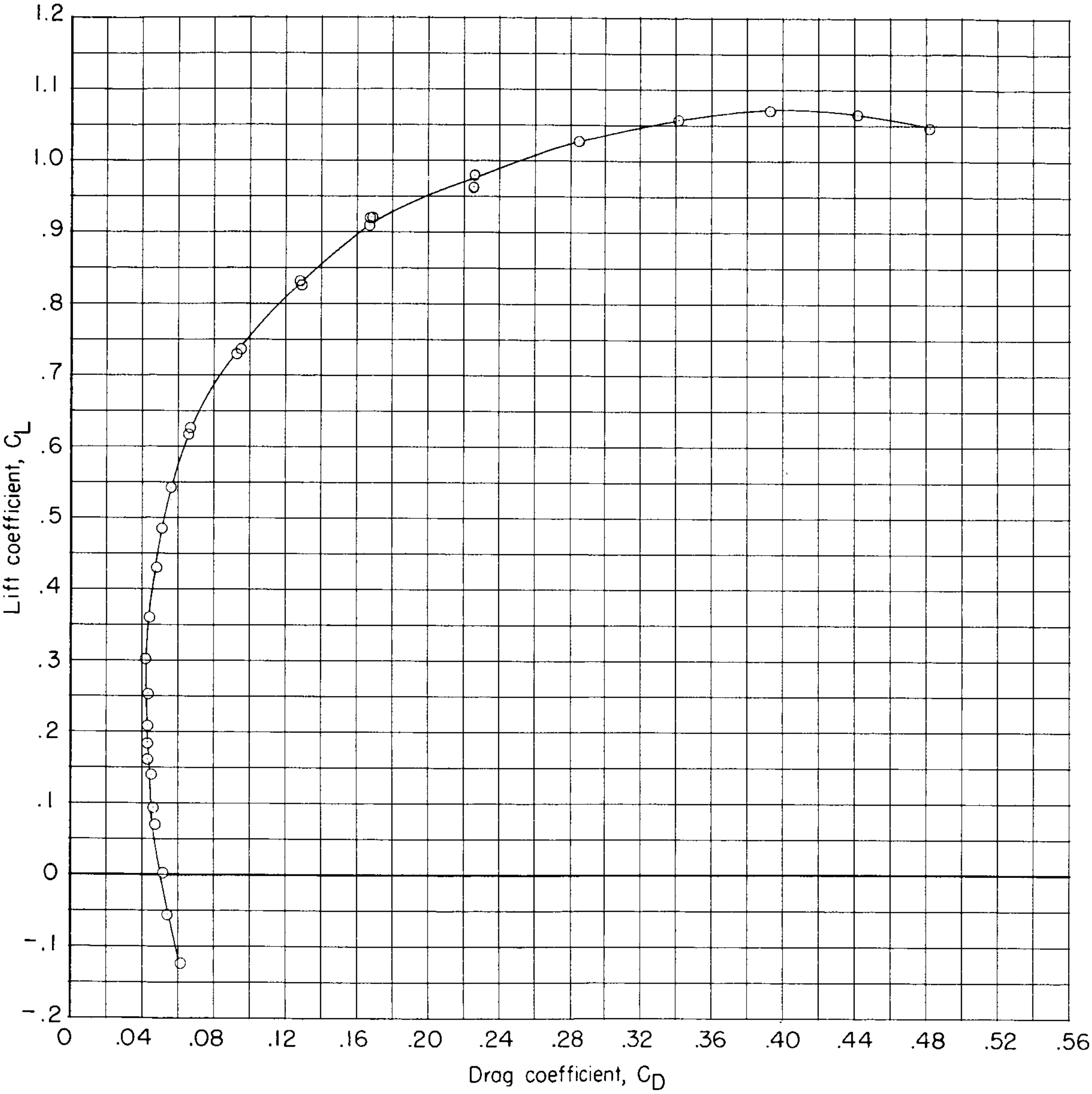

(b) Drag coefficient.

Figure 36.- Continued.

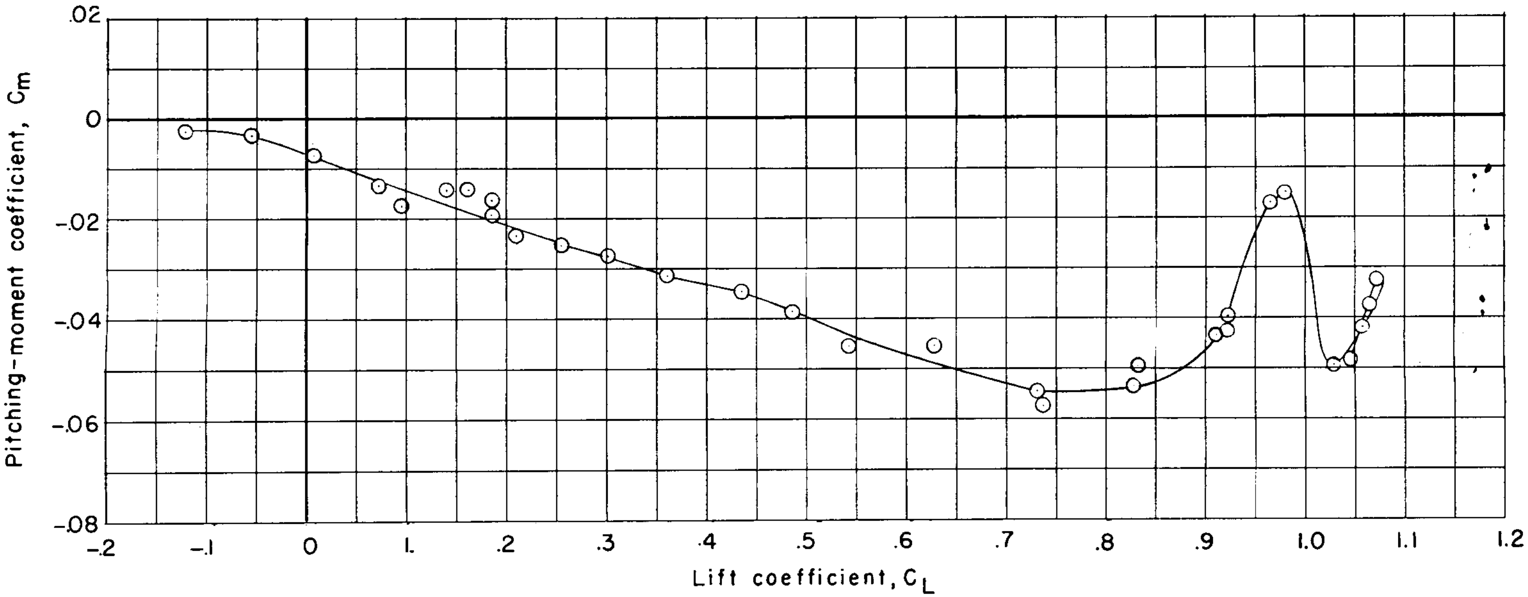

(c) Pitching-moment coefficient.

Figure 36.- Concluded.

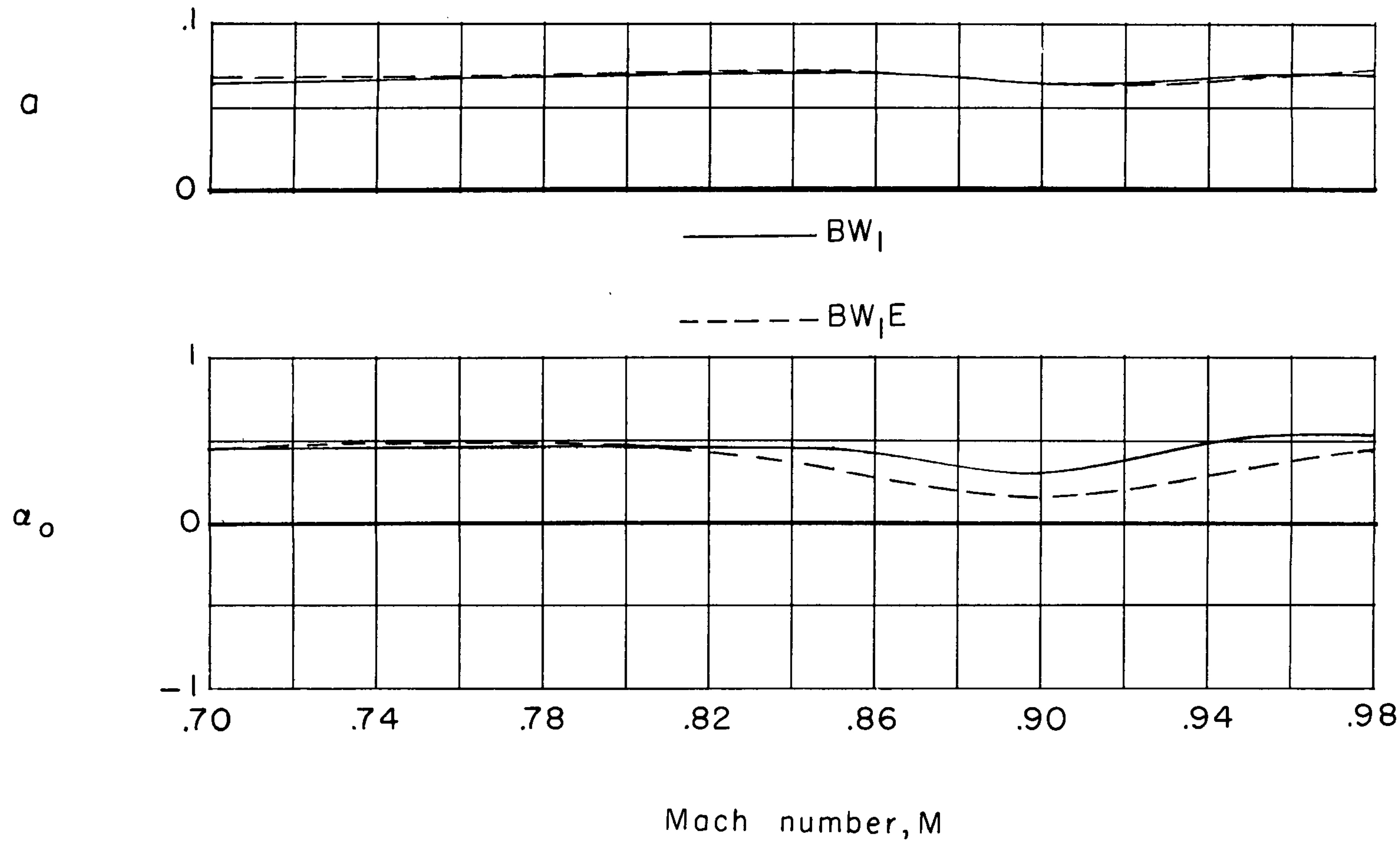

Figure 37.- Effect of end plates on the variation of lift-curve slope and angle of zero lift with Mach number. $\delta_{le} = 15^o$.

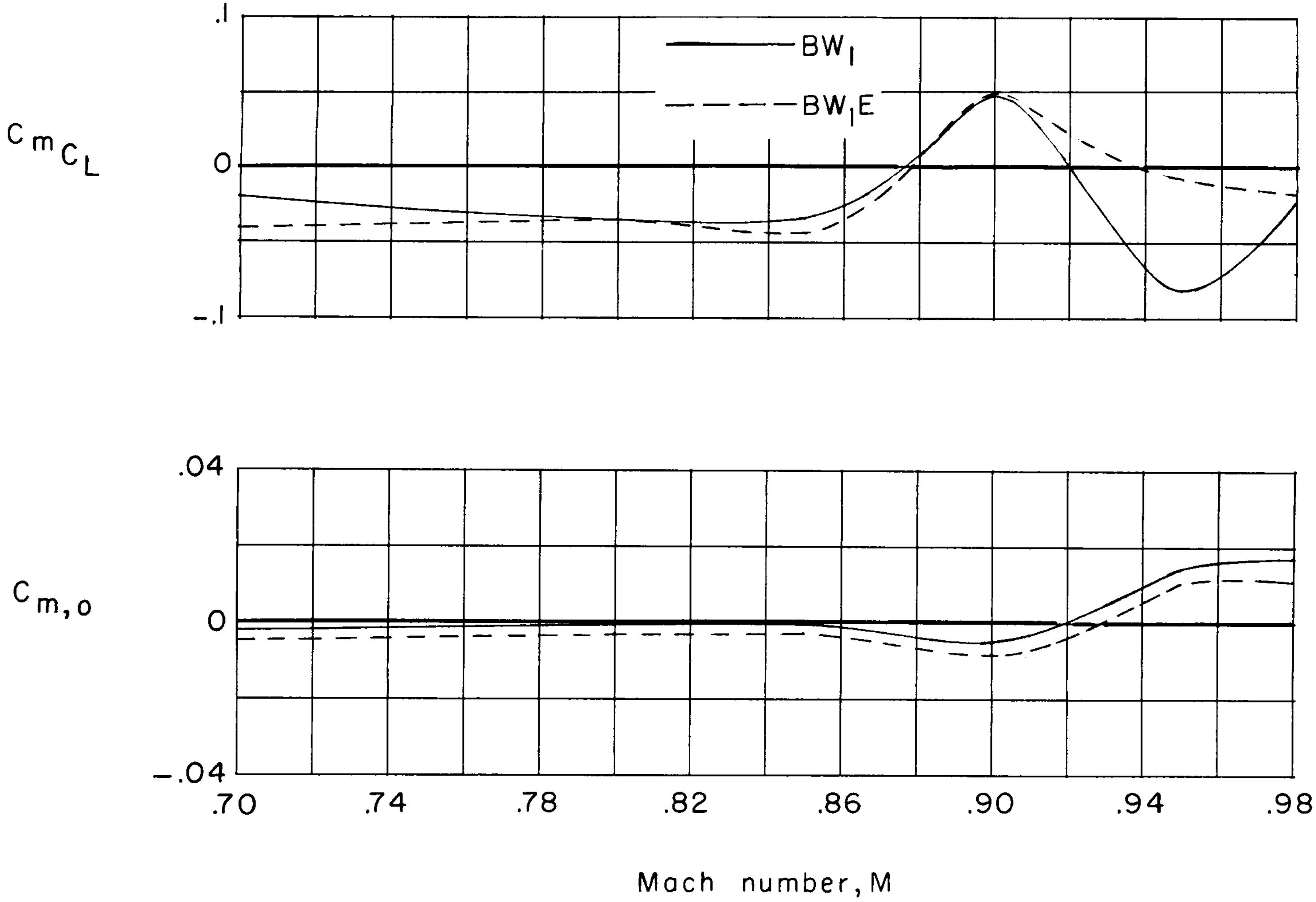

Figure 38.- Effect of end plates on the variation of $C_{m_{C_L}}$ and $C_{m,o}$ with Mach number. $\delta_{le} = 15^{\circ}$.

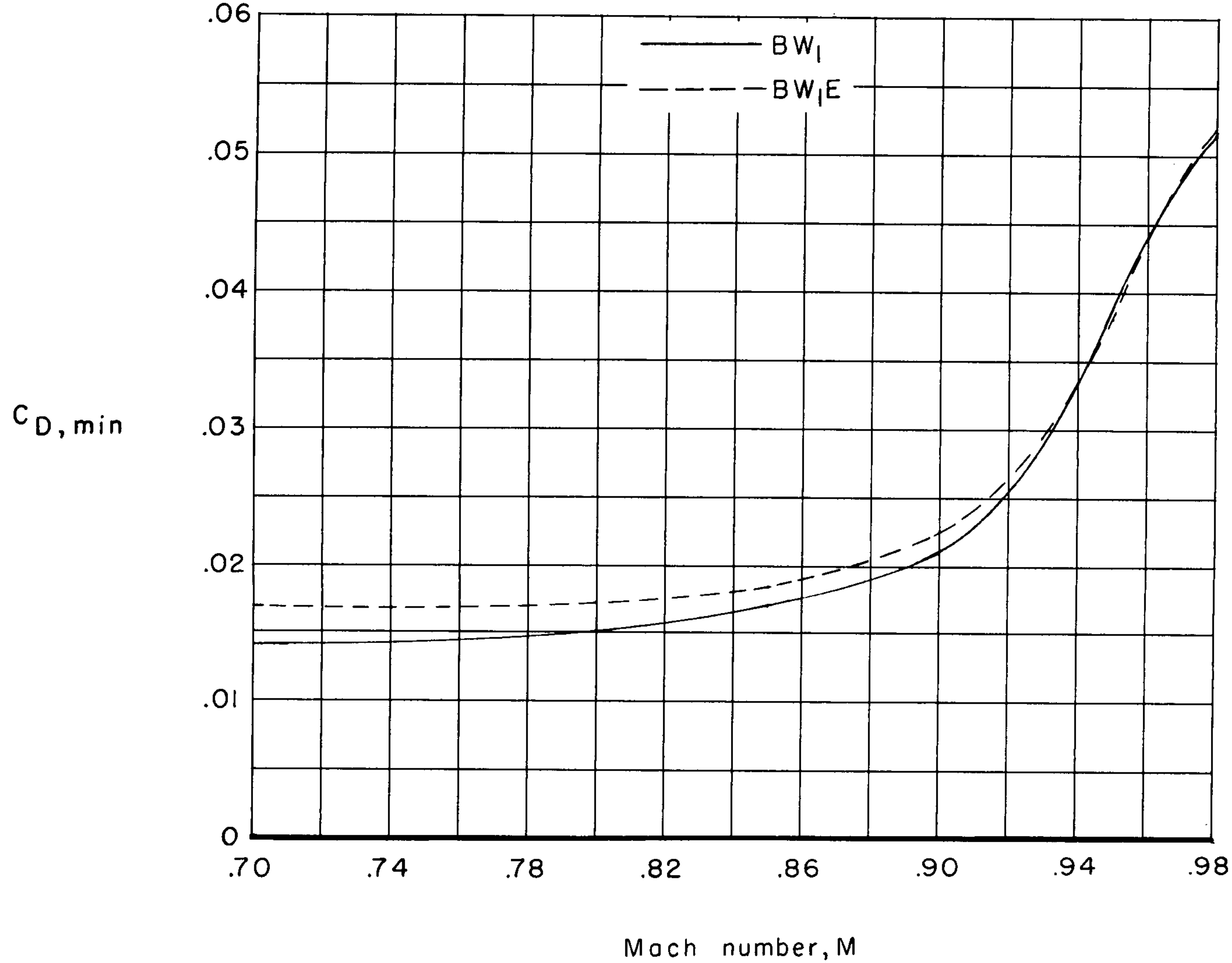

Figure 39.- Effect of end plates on the variation of $C_{D,min}$ with Mach number. $\delta_{le} = 15^{\circ}$.

[redacted]

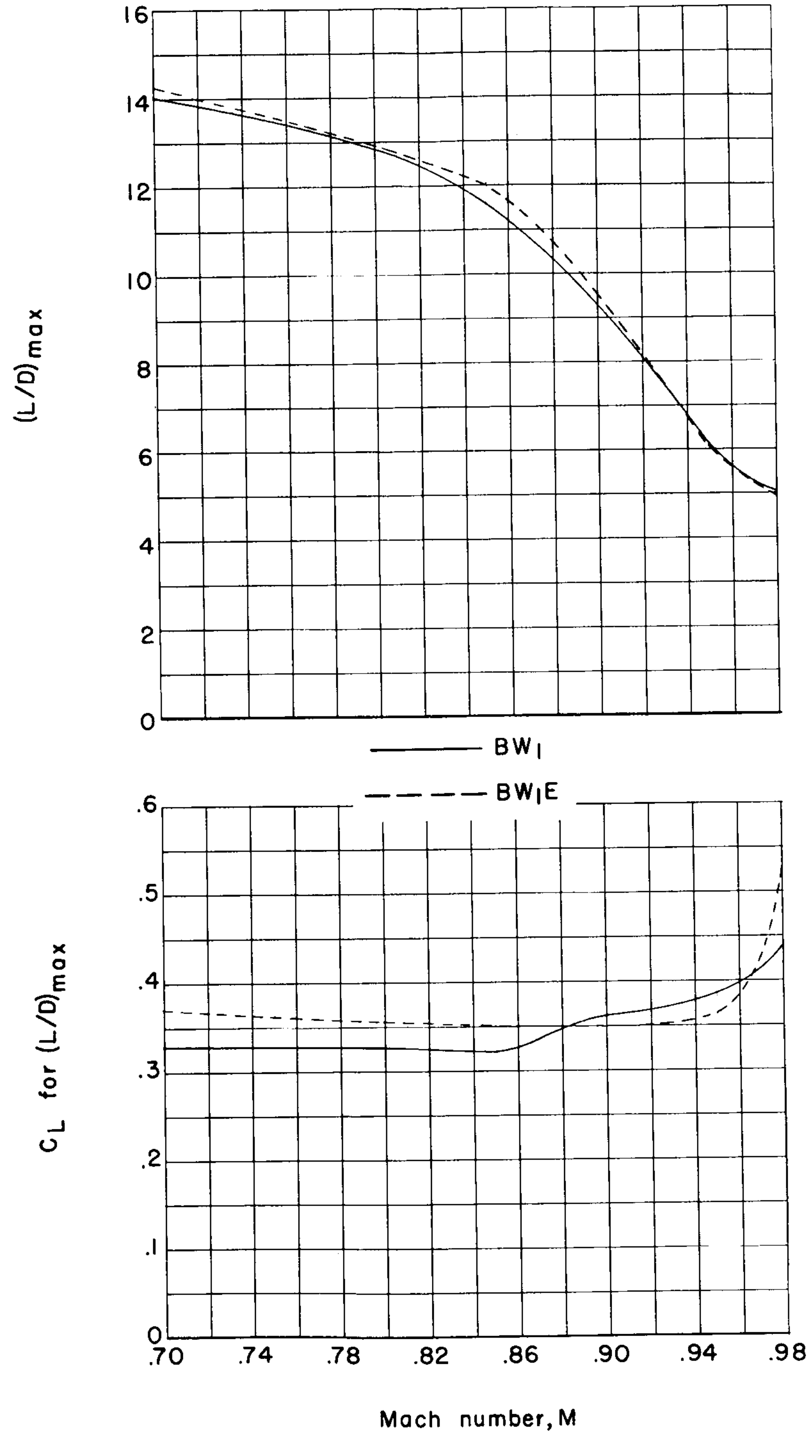

Figure 40.- Effect of end plates on the variation of $(L/D)_{max}$ and C_L for $(L/D)_{max}$ with Mach number. $\delta_{le} = 15^\circ$.

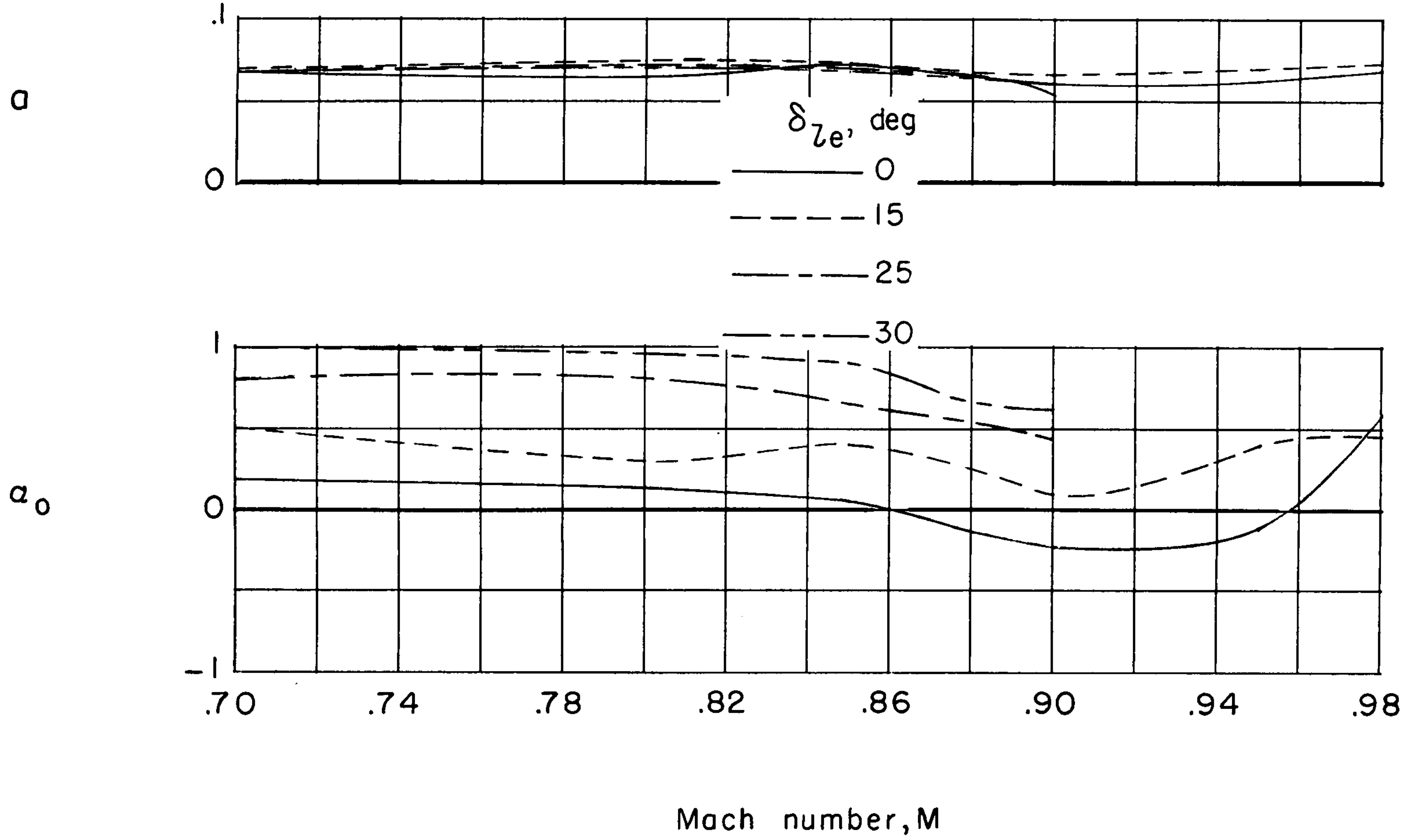

Figure 41.- Effect of leading-edge chord-extension deflection on the variation of lift-curve slope and angle of zero lift with Mach number for model BWE.

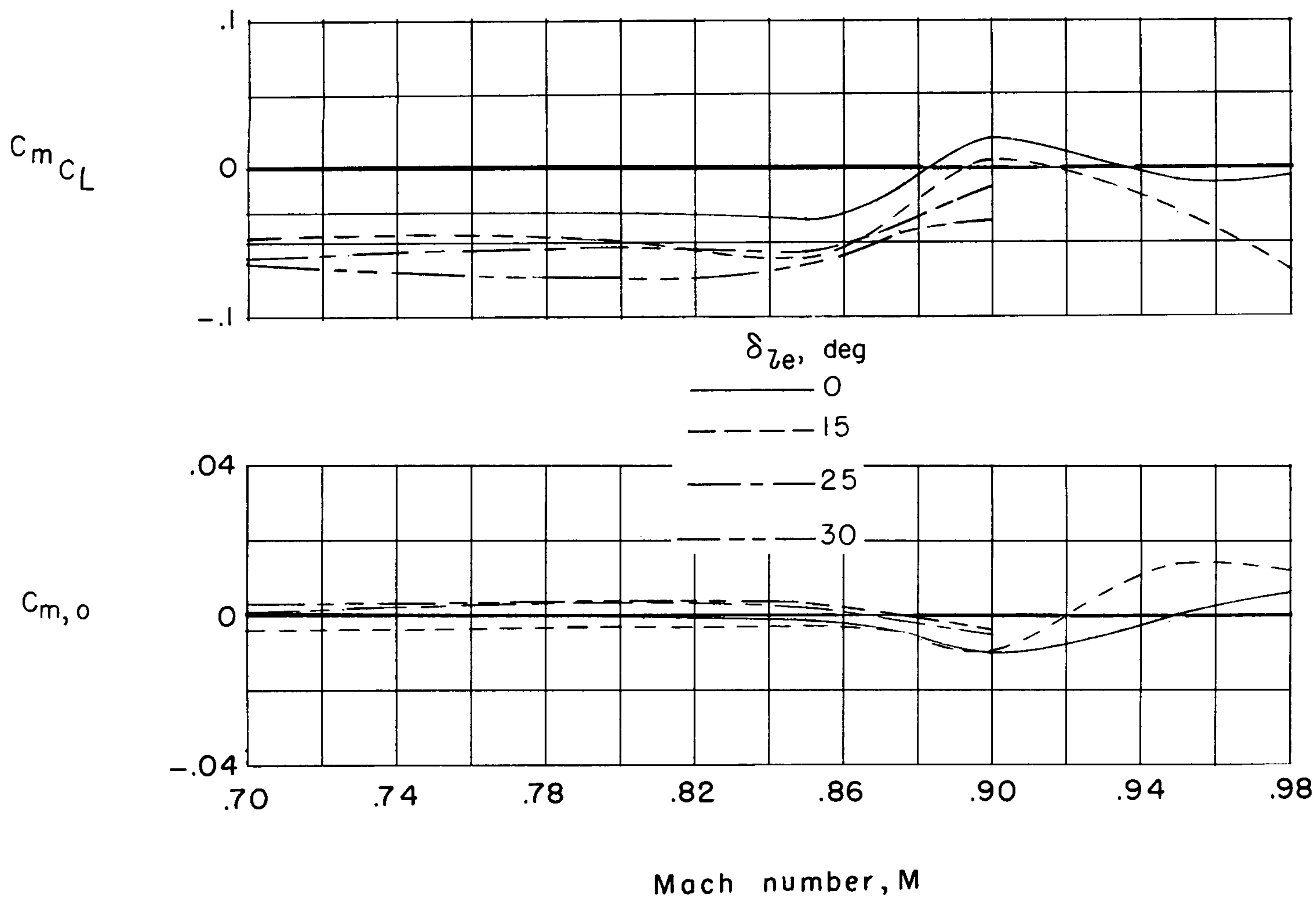

Figure 42.- Effect of leading-edge chord-extension deflection on the variation of $C_{m_{C_L}}$ and $C_{m,o}$ with Mach number for model BWE.

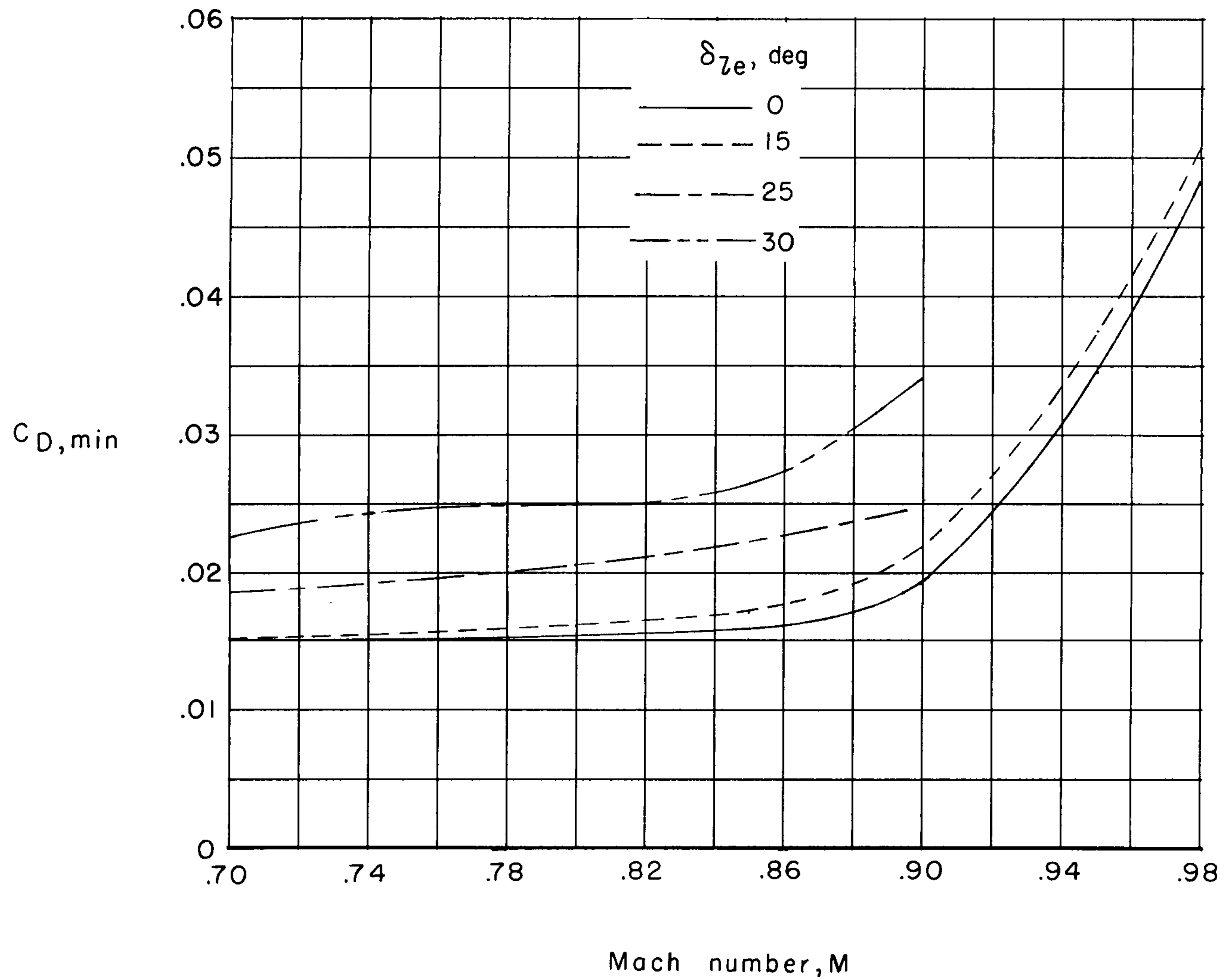

Figure 43.- Effect of leading-edge chord-extension deflection on the variation of $C_{D,min}$ with Mach number for model BWE.

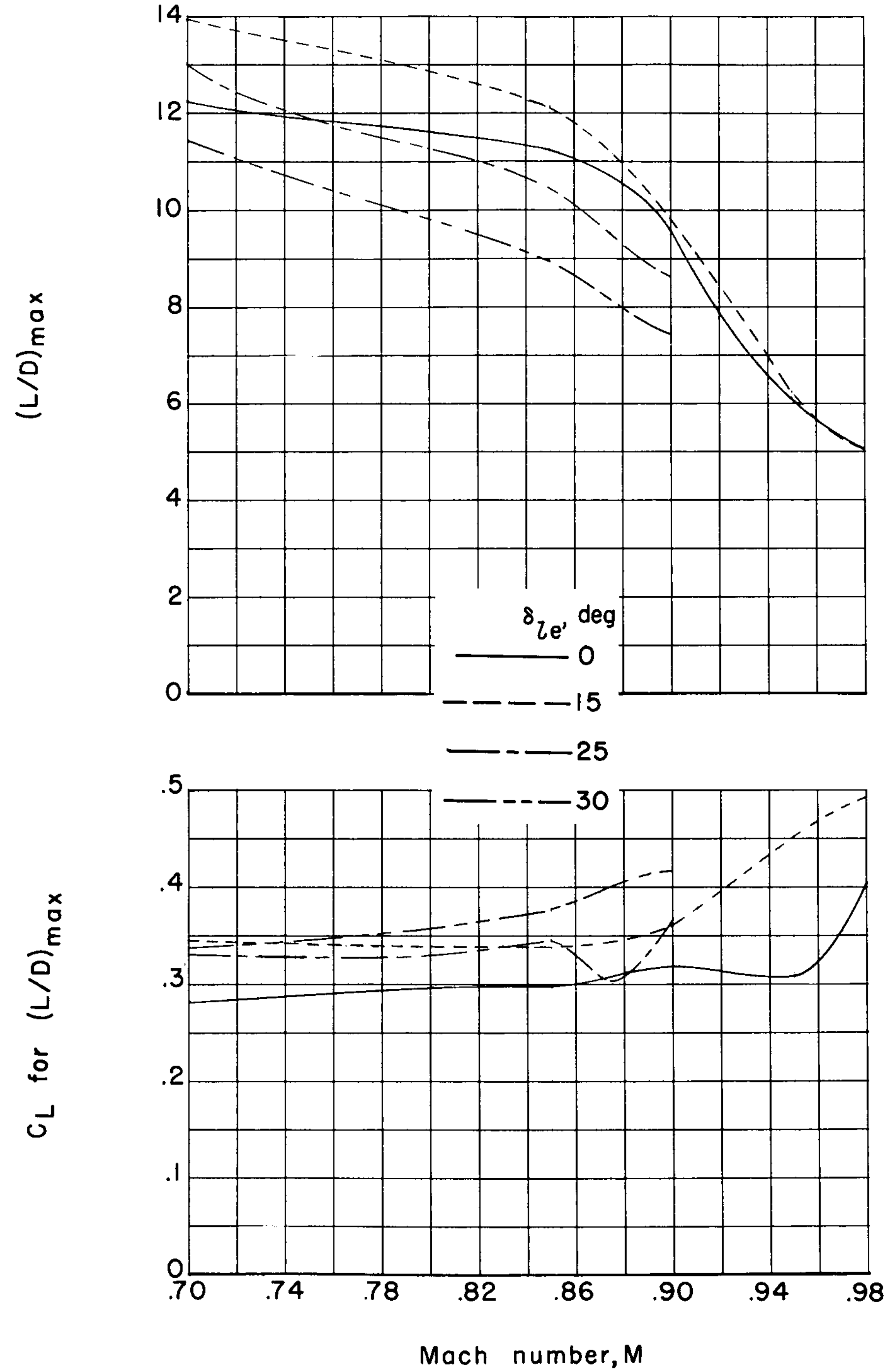

Figure 44.- Effect of leading-edge chord-extension deflection on the variation of $(L/D)_{max}$ and C_L for $(L/D)_{max}$ with Mach number for model BWE.

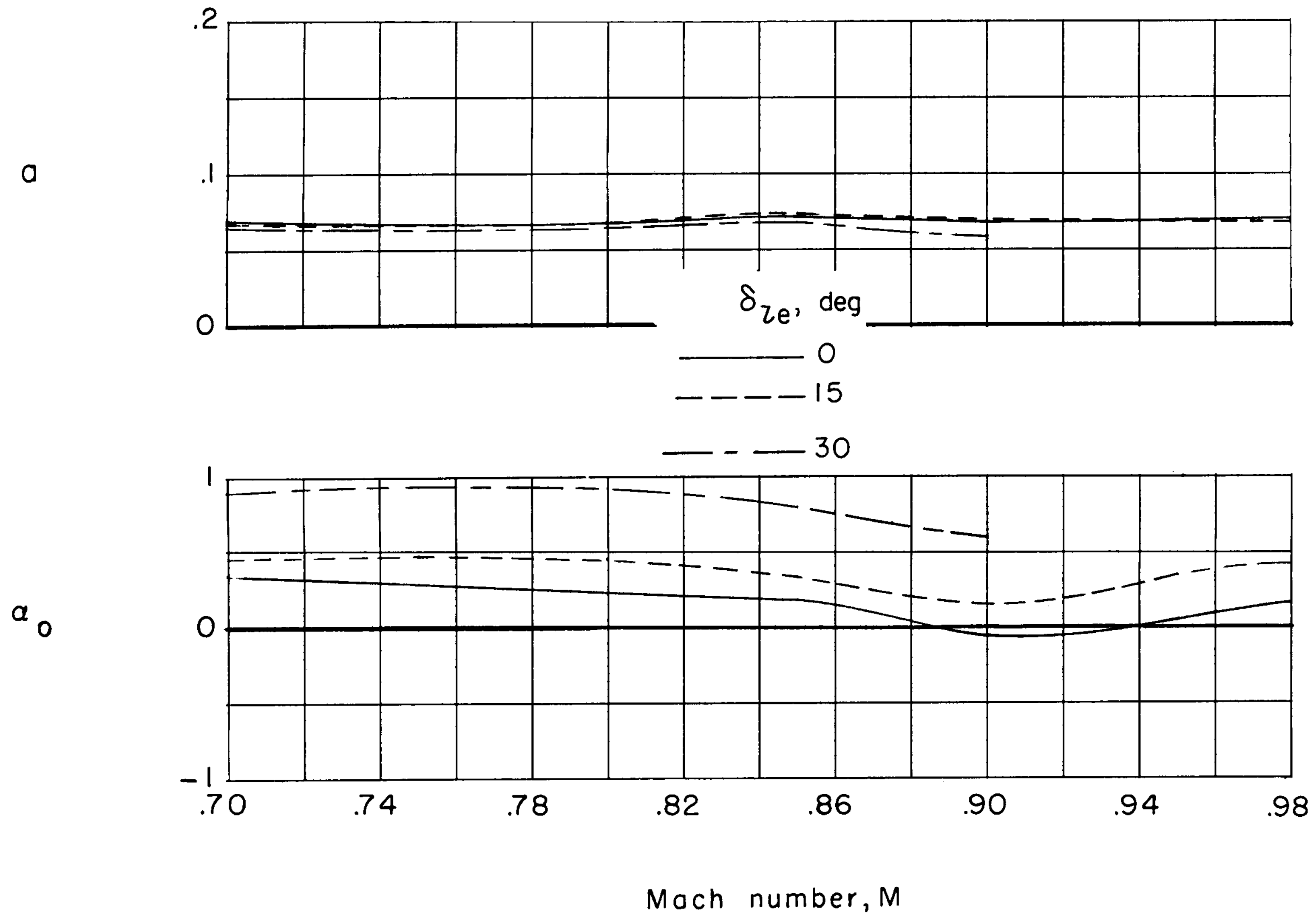

Figure 45.- Effect of leading-edge chord-extension deflection on the variation of lift-curve slope and angle of zero lift with Mach number for model BW_1E.

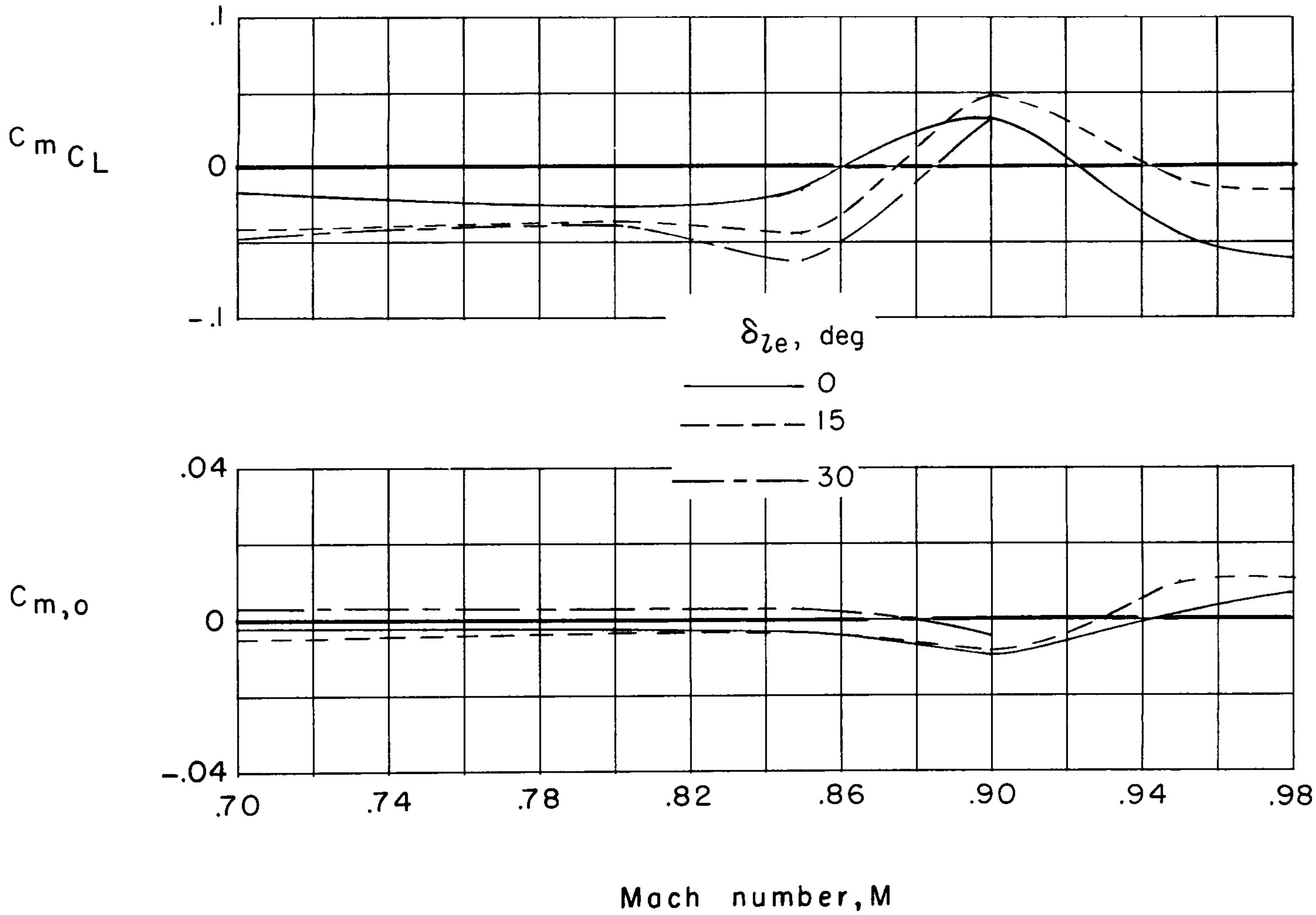

Figure 46.- Effect of leading-edge chord-extension deflection on the variation of $C_{m_{C_L}}$ and $C_{m,o}$ with Mach number for model BW_1E.

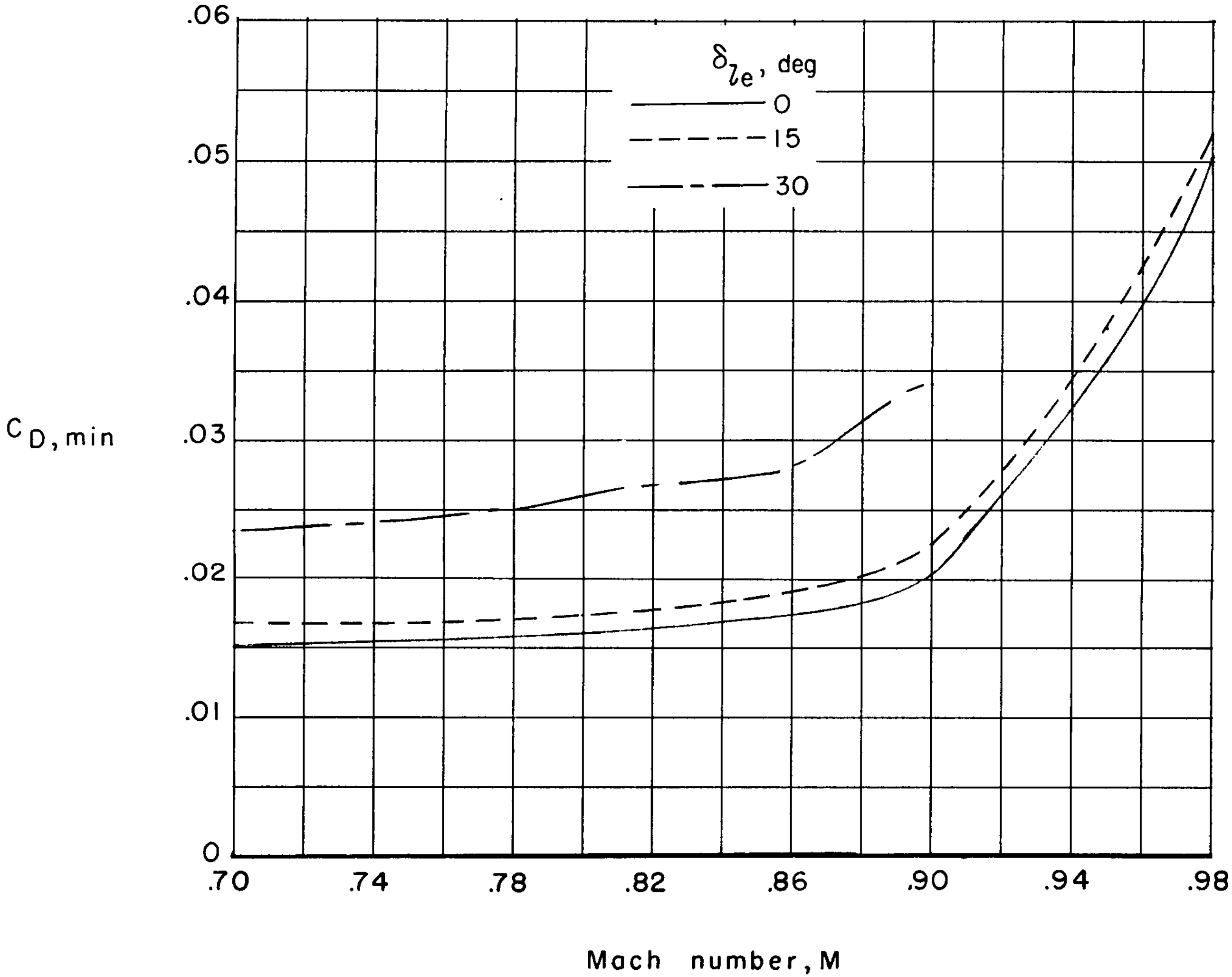

Figure 47.- Effect of leading-edge chord-extension deflection on the variation of $C_{D,min}$ with Mach number for model BW_1E.

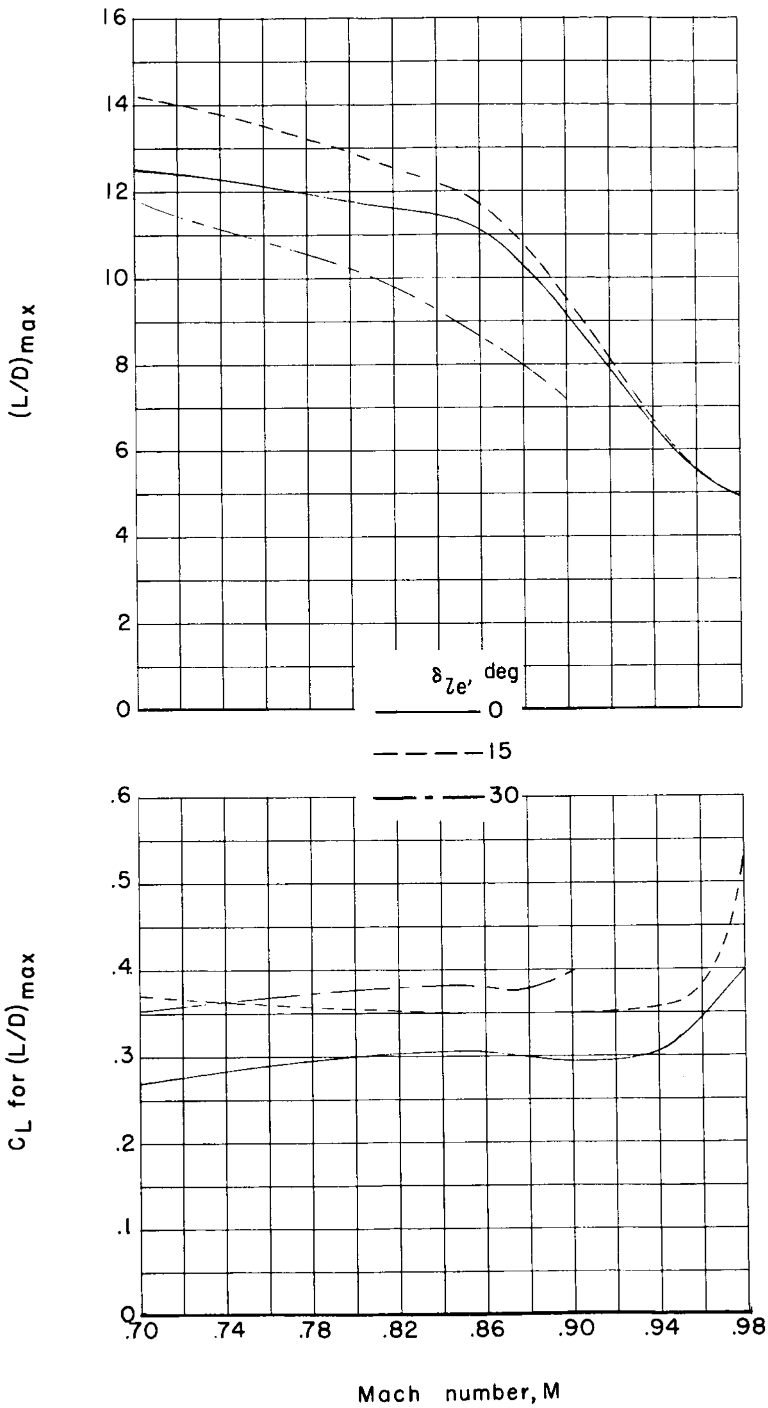

Figure 48.- Effect of leading-edge chord-extension deflection on the variation of $(L/D)_{max}$ and C_L for $(L/D)_{max}$ with Mach number for model BW_1E.

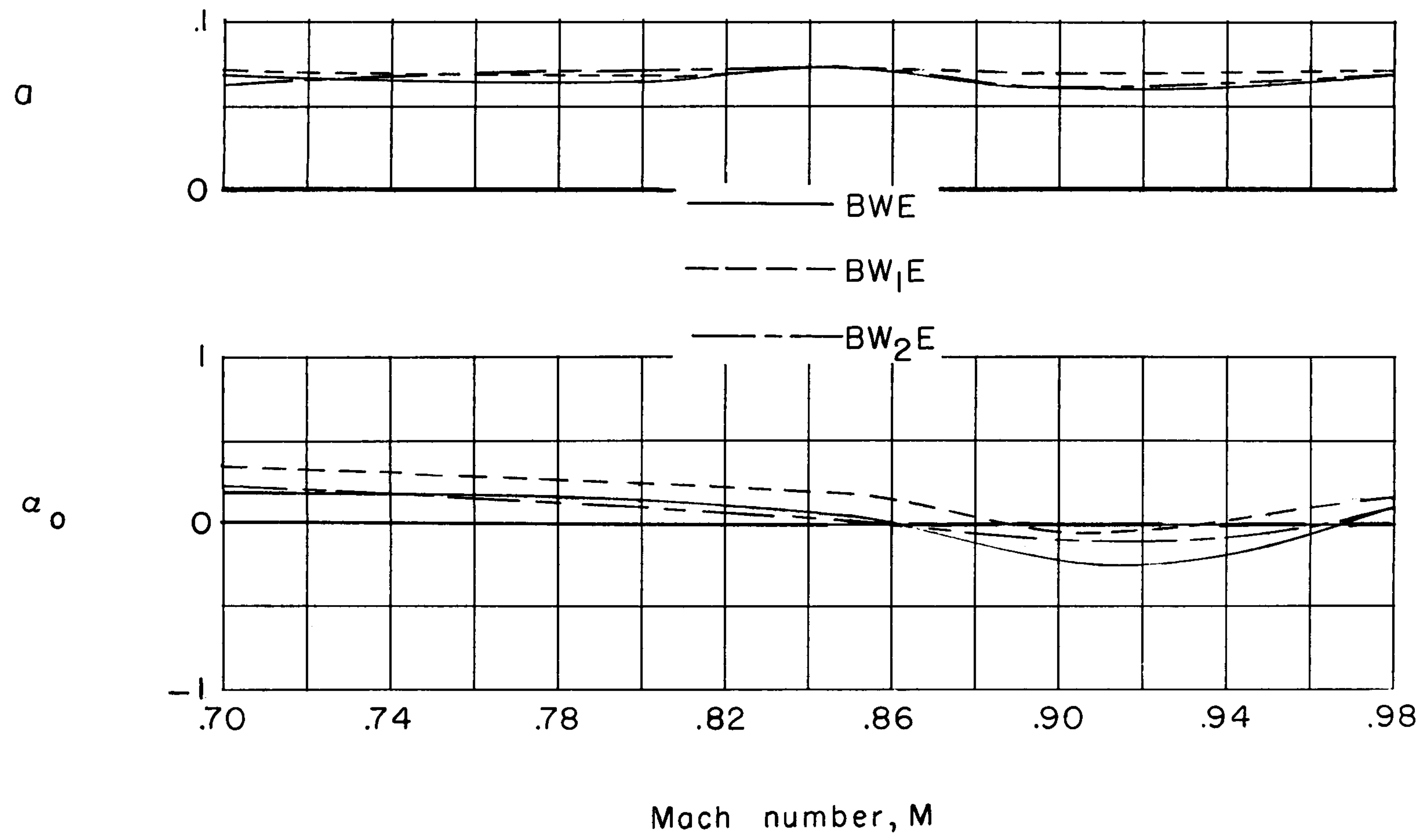

Figure 49.- Effect of leading-edge modifications on the variation of lift-curve slope and angle of zero lift with Mach number. $\delta_{le} = 0^{\circ}$.

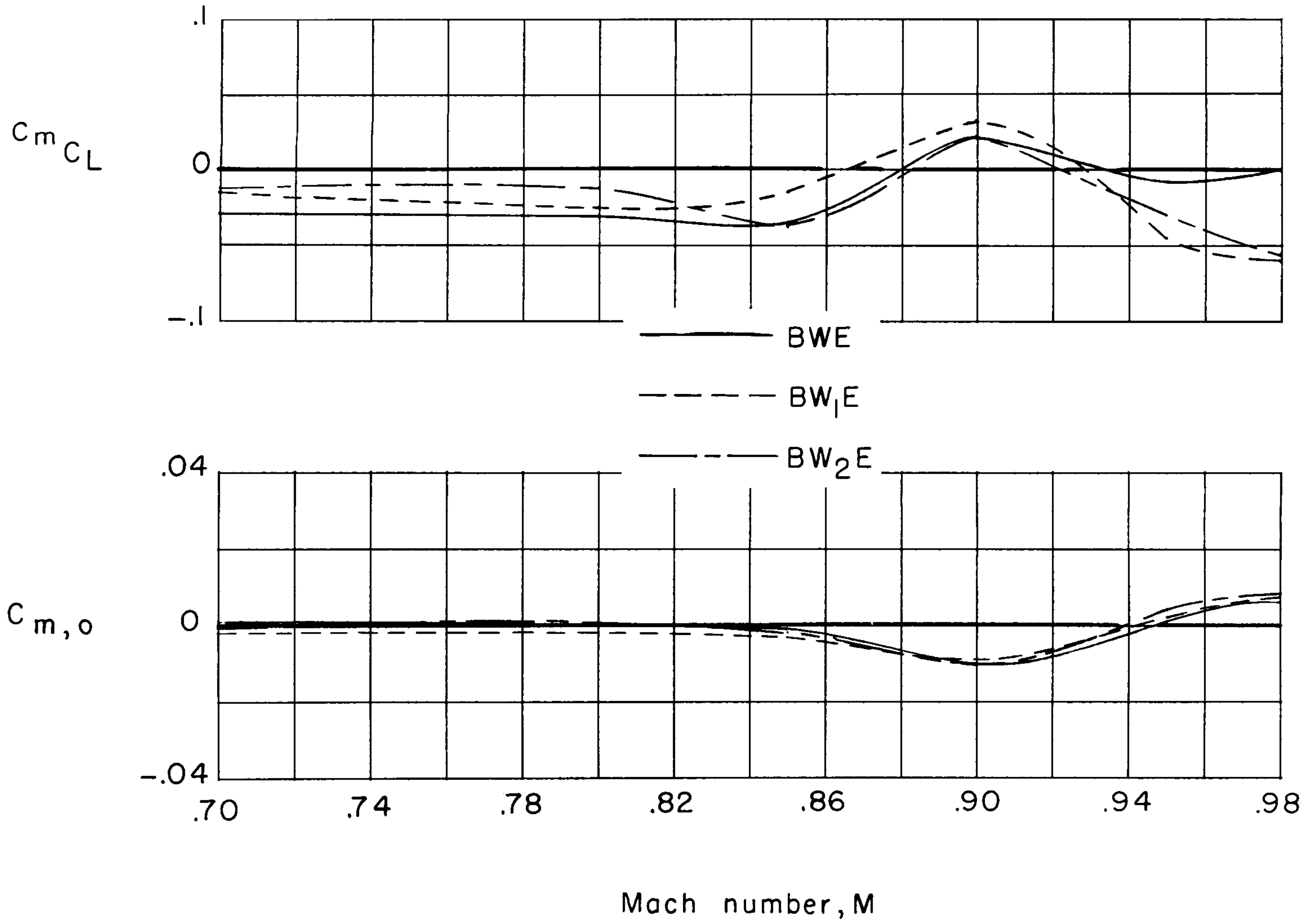

Figure 50.- Effect of leading-edge modifications on the variation of $C_{m_{C_L}}$ and $C_{m,o}$ with Mach number. $\delta_{le} = 0^{\circ}$.

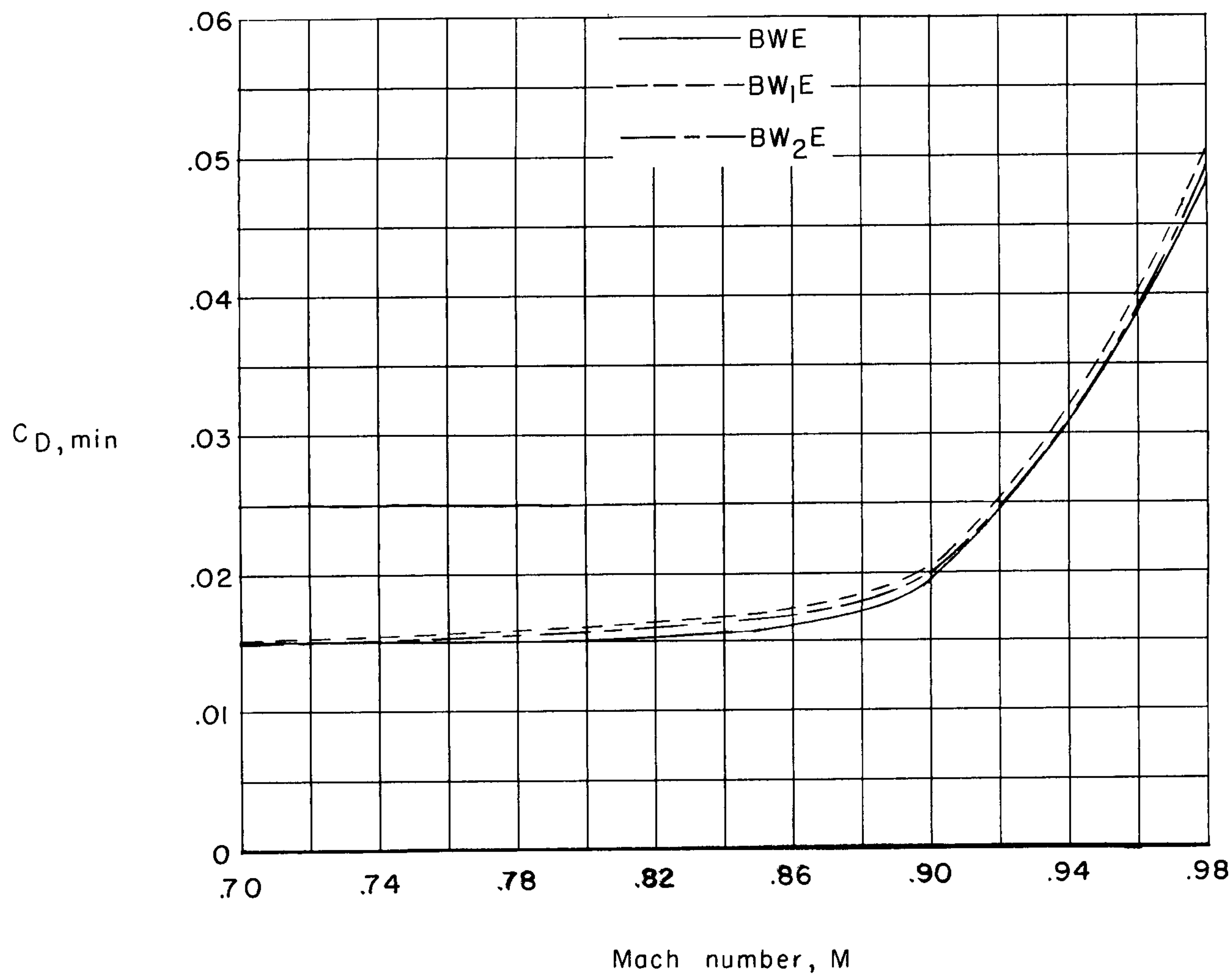

Figure 51.- Effect of leading-edge modifications on the variation of $C_{D,min}$ with Mach number. $\delta_{le} = 0^{\circ}$.

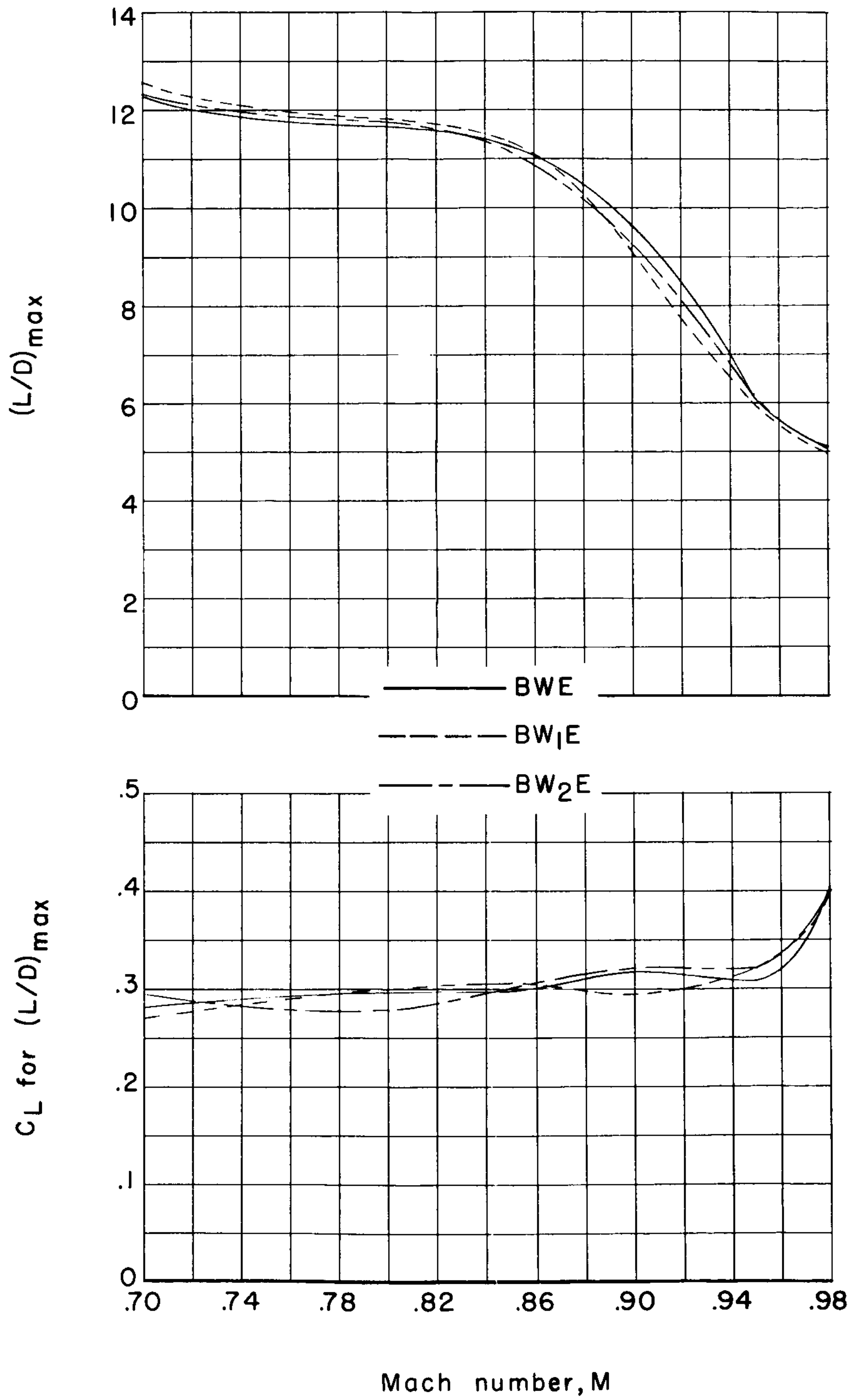

Figure 52.- Effect of leading-edge modifications on the variation of $(L/D)_{max}$ and C_L for $(L/D)_{max}$ with Mach number. $\delta_{le} = 0^{\circ}$.

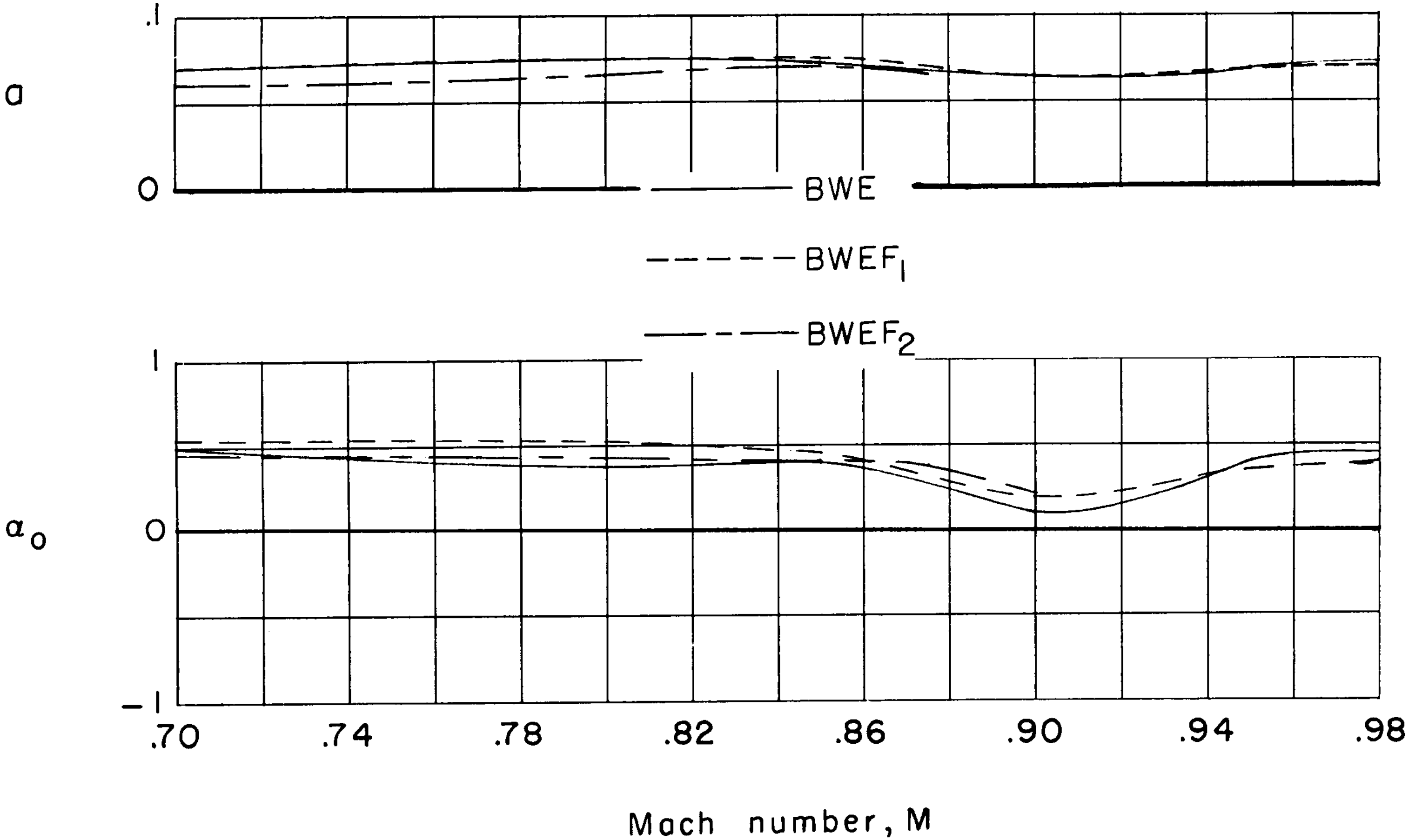

Figure 53.- Effect of wing fences on the variation of lift-curve slope and angle of zero lift with Mach number. $\delta_{le} = 15^o$.

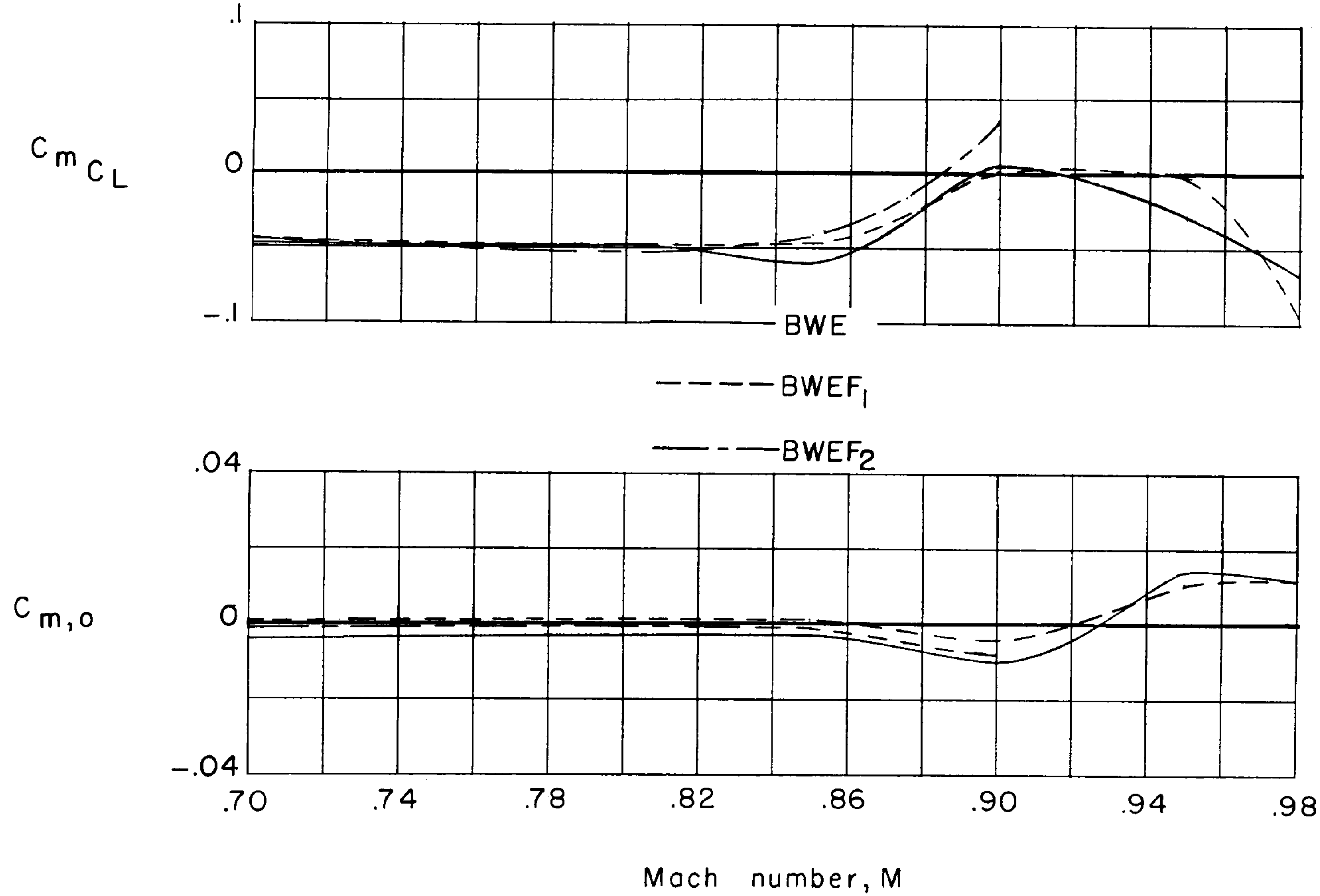

Figure 54.- Effect of wing fences on the variation of $C_{m_{C_L}}$ and $C_{m,o}$ with Mach number. $\delta_{le} = 15^{o}$.

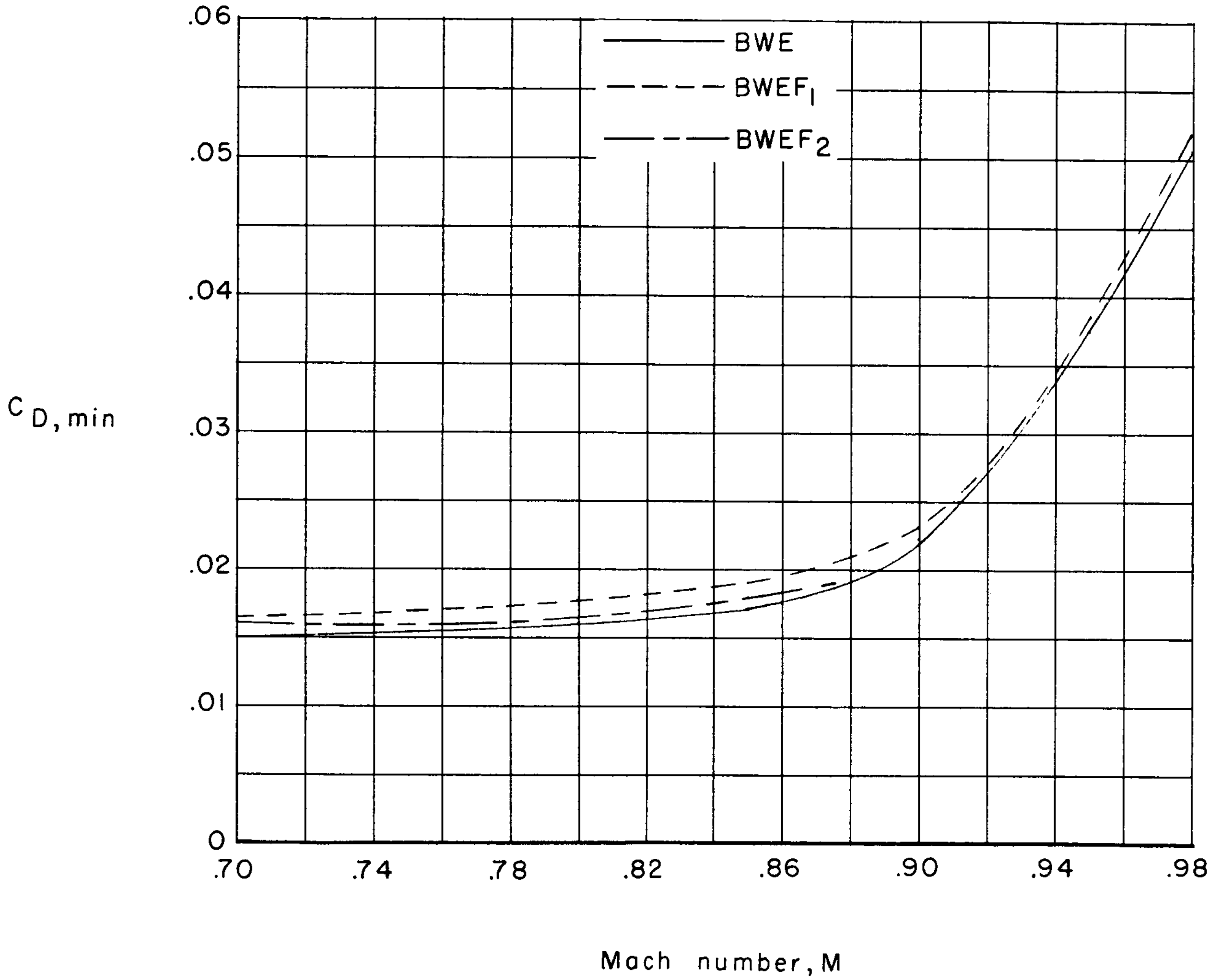

Figure 55.- Effect of wing fences on the variation of $C_{D,min}$ with Mach number. $\delta_{le} = 15^{\circ}$.

[redacted]

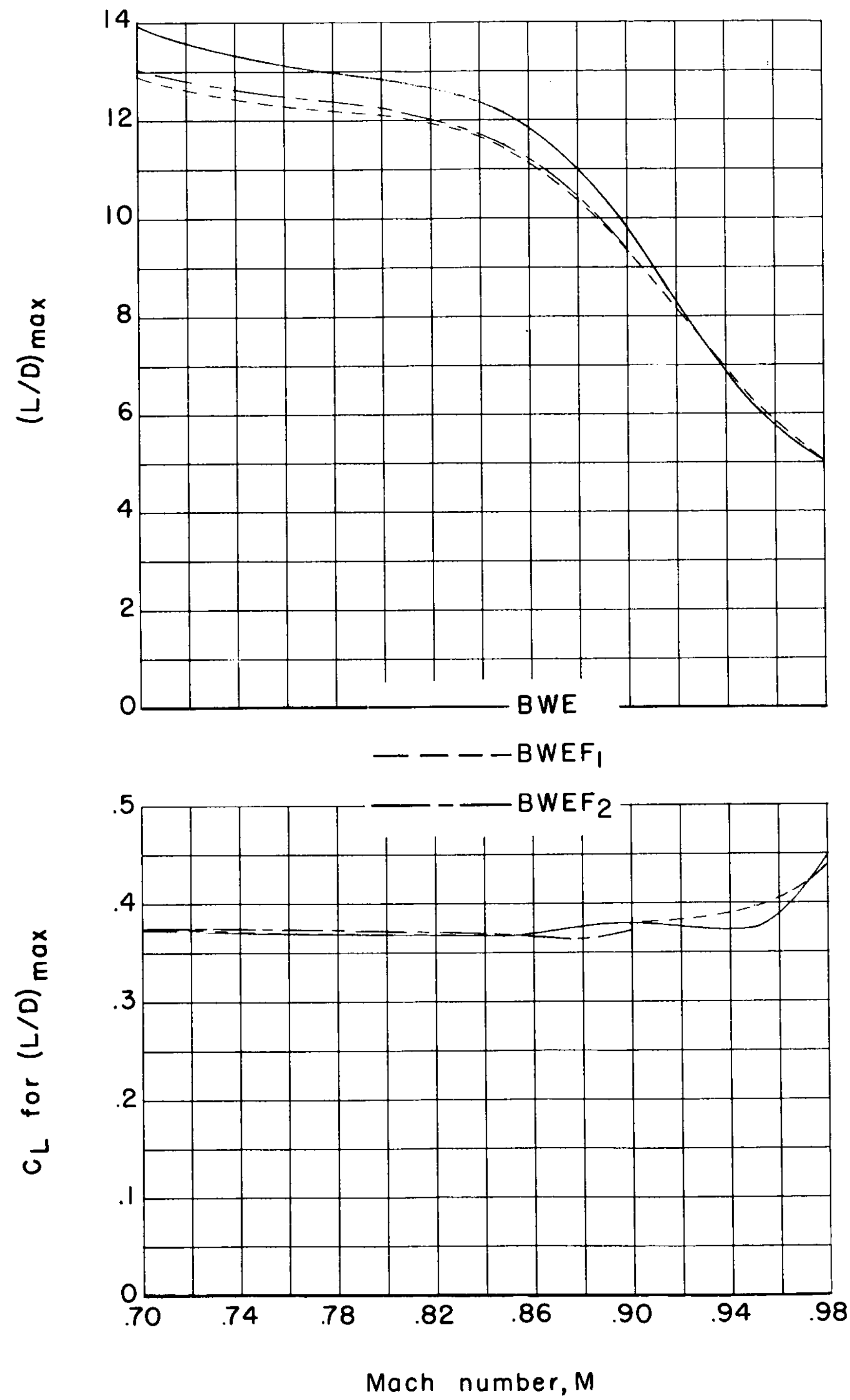

Figure 56.- Effect of wing fences on the variation of $(L/D)_{max}$ and C_L for $(L/D)_{max}$ with Mach number. $\delta_{le} = 15^{\circ}$.

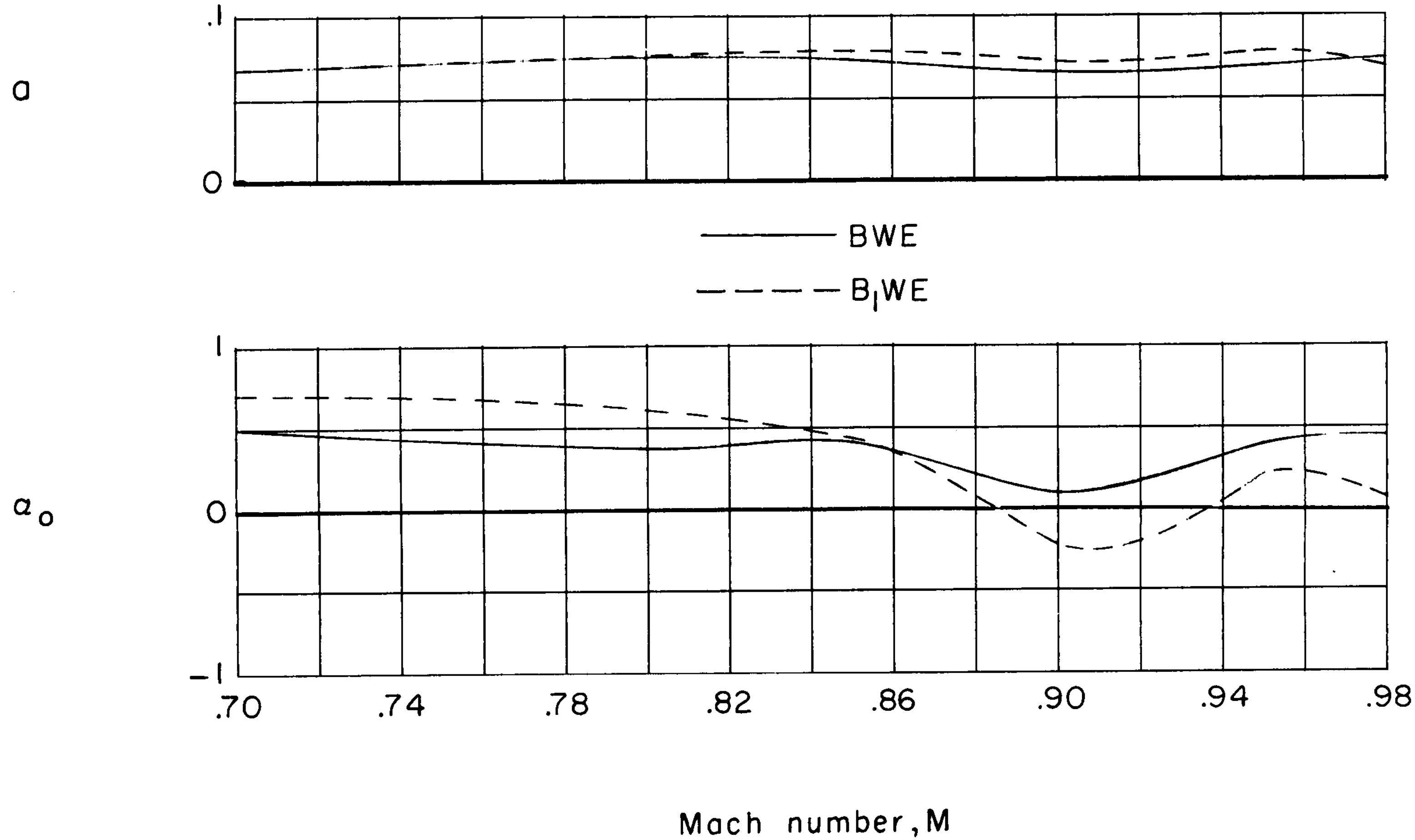

Figure 57.- Effect of body filler on the variation of lift-curve slope and angle of zero lift with Mach number. $\delta_{le} = 15^{\circ}$.

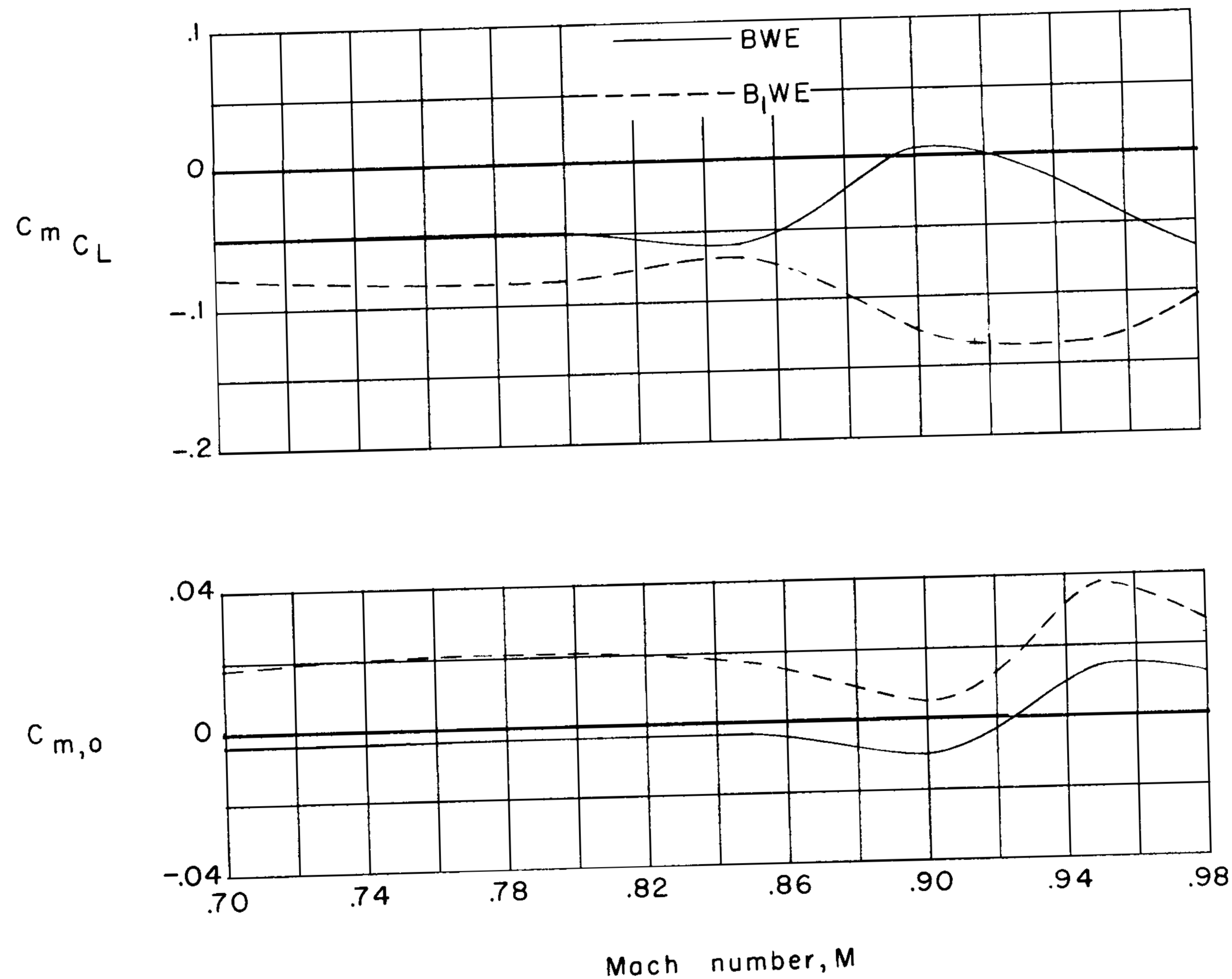

Figure 58.- Effect of body filler on the variation of $C_{m_{C_L}}$ and $C_{m,o}$ with Mach number. $\delta_{le} = 15^\circ$.

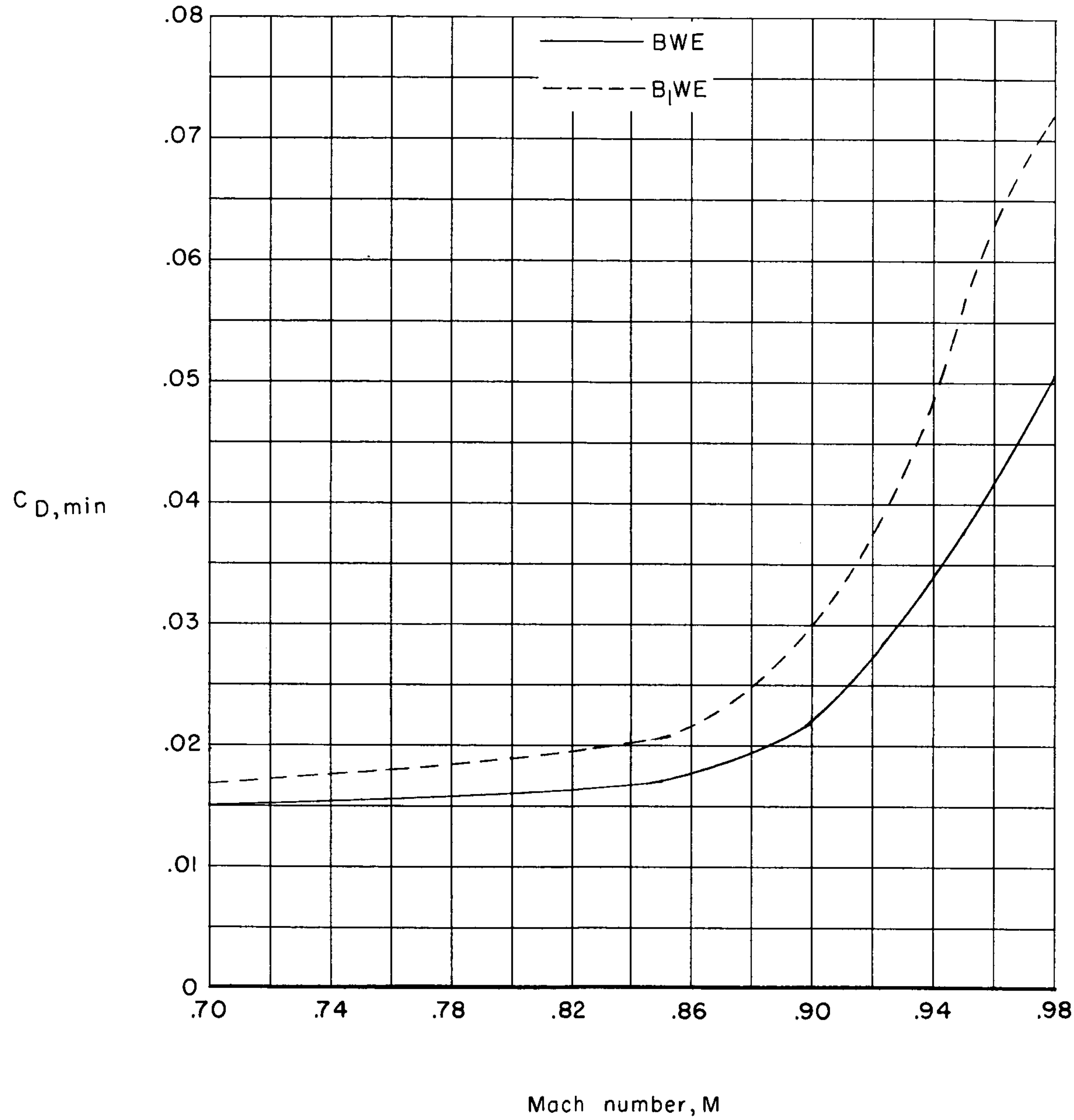

Figure 59.- Effect of body filler on the variation of $C_{D,min}$ with Mach number. $\delta_{le} = 15^{\circ}$.

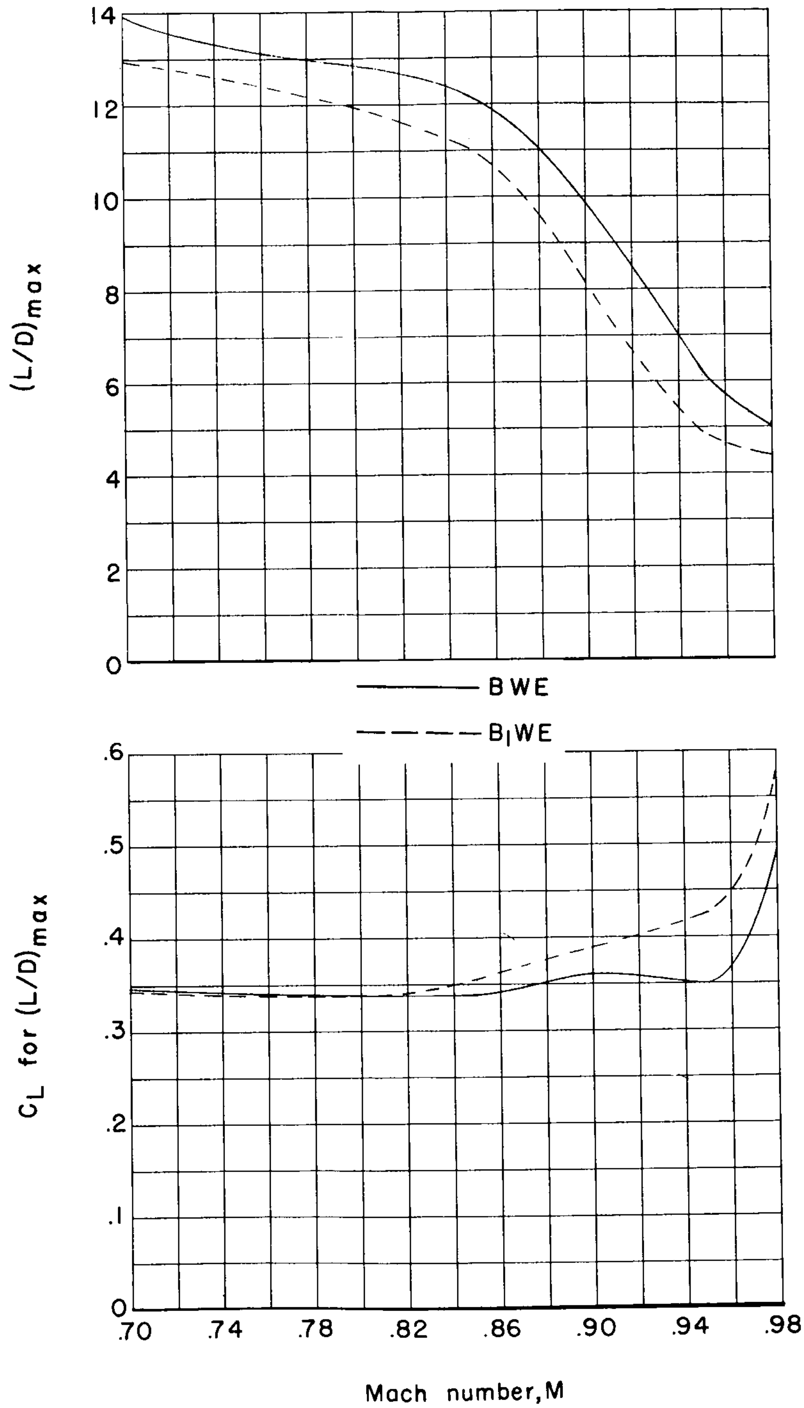

Figure 60.- Effect of body filler on the variation of $(L/D)_{max}$ and C_L for $(L/D)_{max}$ with Mach number. $\delta_{le} = 15^{\circ}$.

L-1014

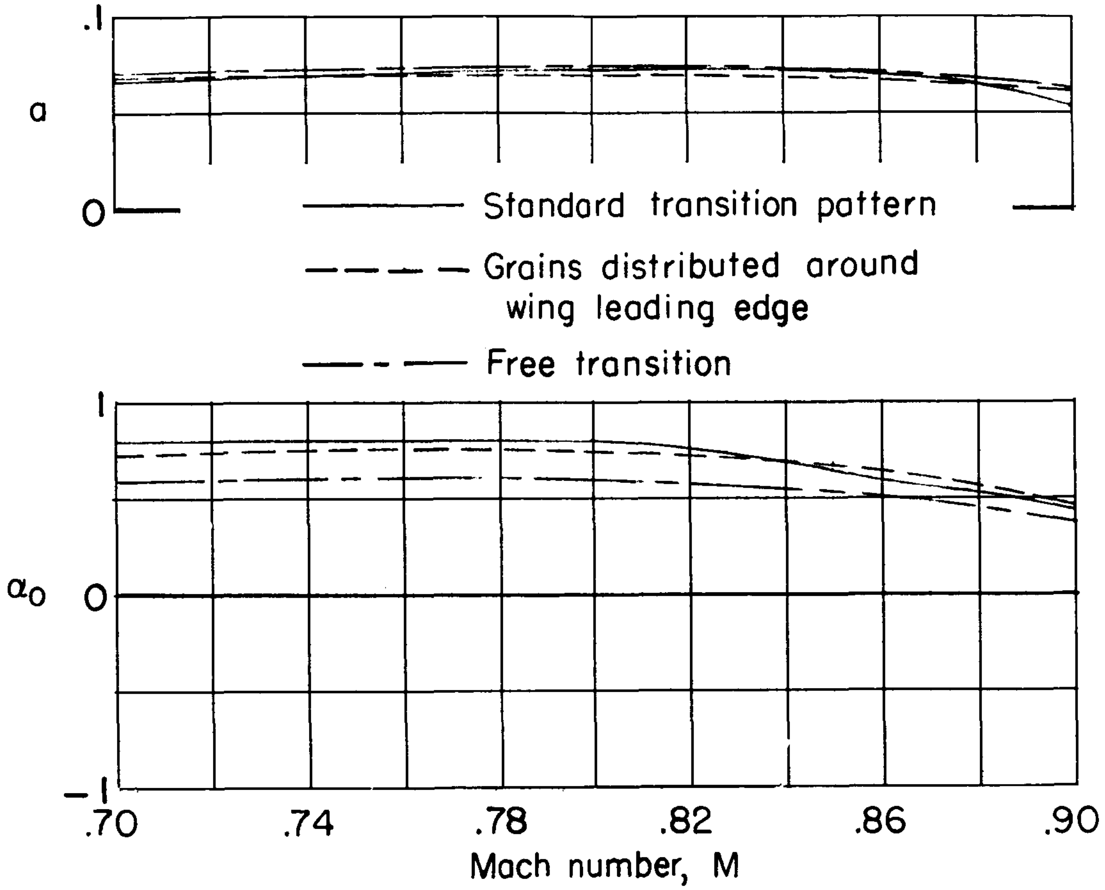

Figure 61.- Effect of boundary-layer transition grains on the variation of lift-curve slope and angle of zero lift with Mach number for configuration BWE with $\delta_{le} = 25^{\circ}$.

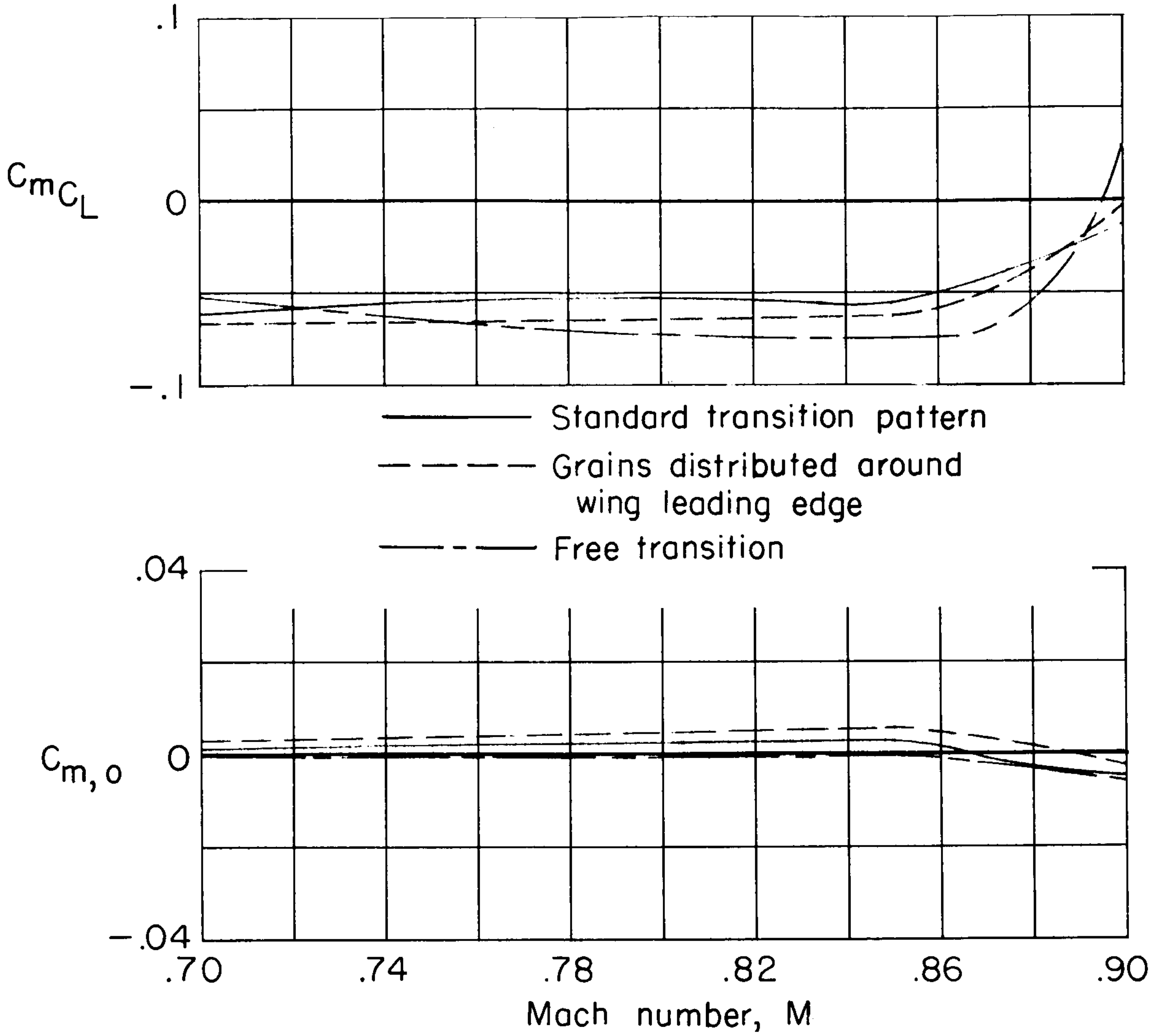

Figure 62.- Effect of boundary-layer transition grains on the variation of $C_{m_{C_L}}$ and $C_{m,o}$ with Mach number for configuration BWE with $\delta_{le} = 25^{\circ}$.

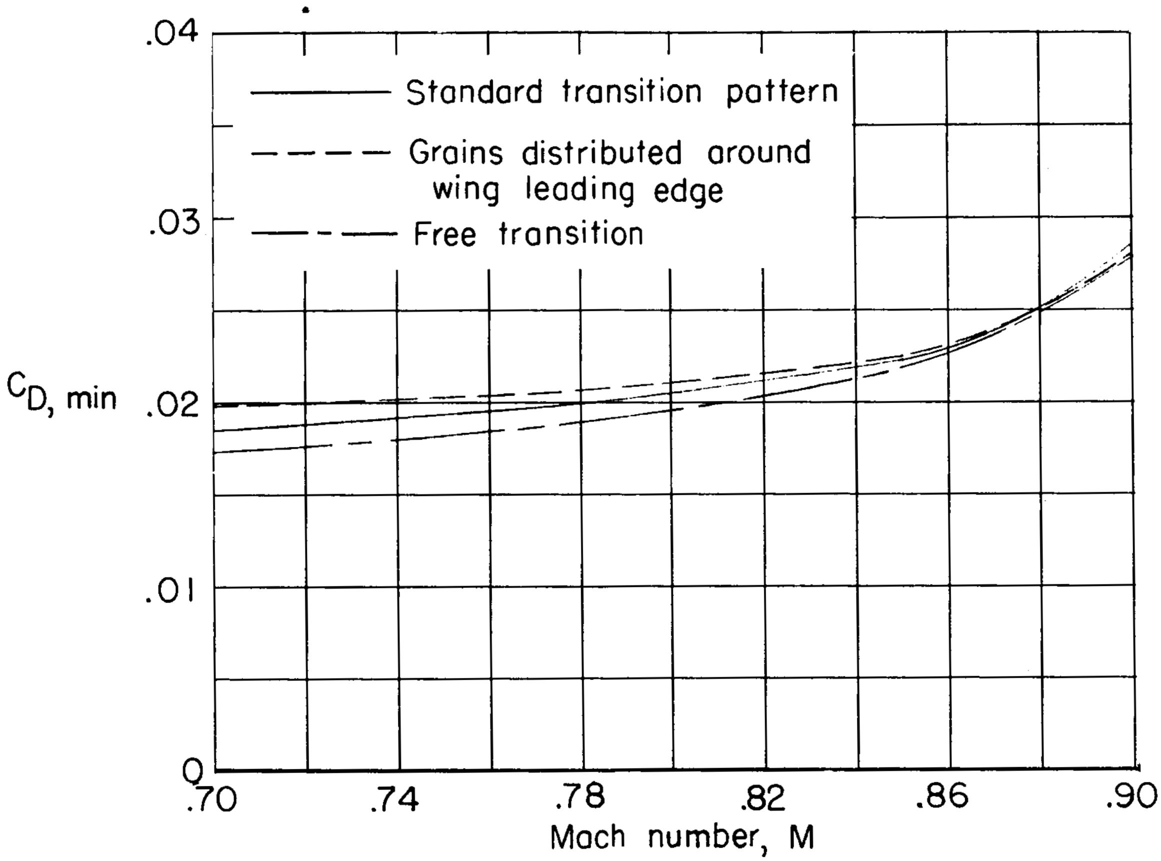

Figure 63.- Effect of boundary-layer transition grains on the variation of $C_{D,min}$ with Mach number for configuration BWE with $\delta_{le} = 25^{\circ}$.

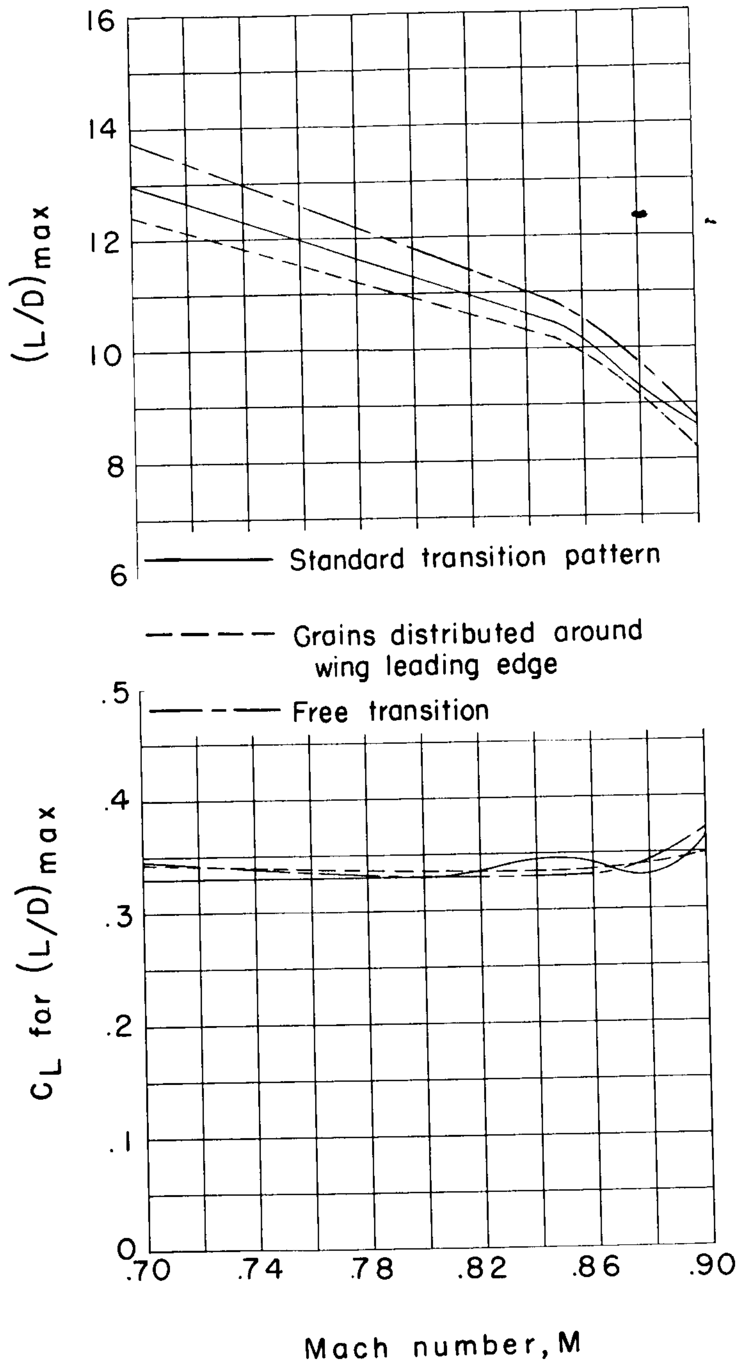

Figure 64.- Effect of boundary-layer transition grains on the variation of $(L/D)_{max}$ and C_L for $(L/D)_{max}$ with Mach number for configuration BWE with $\delta_{le} = 25^{\circ}$.

L-1041

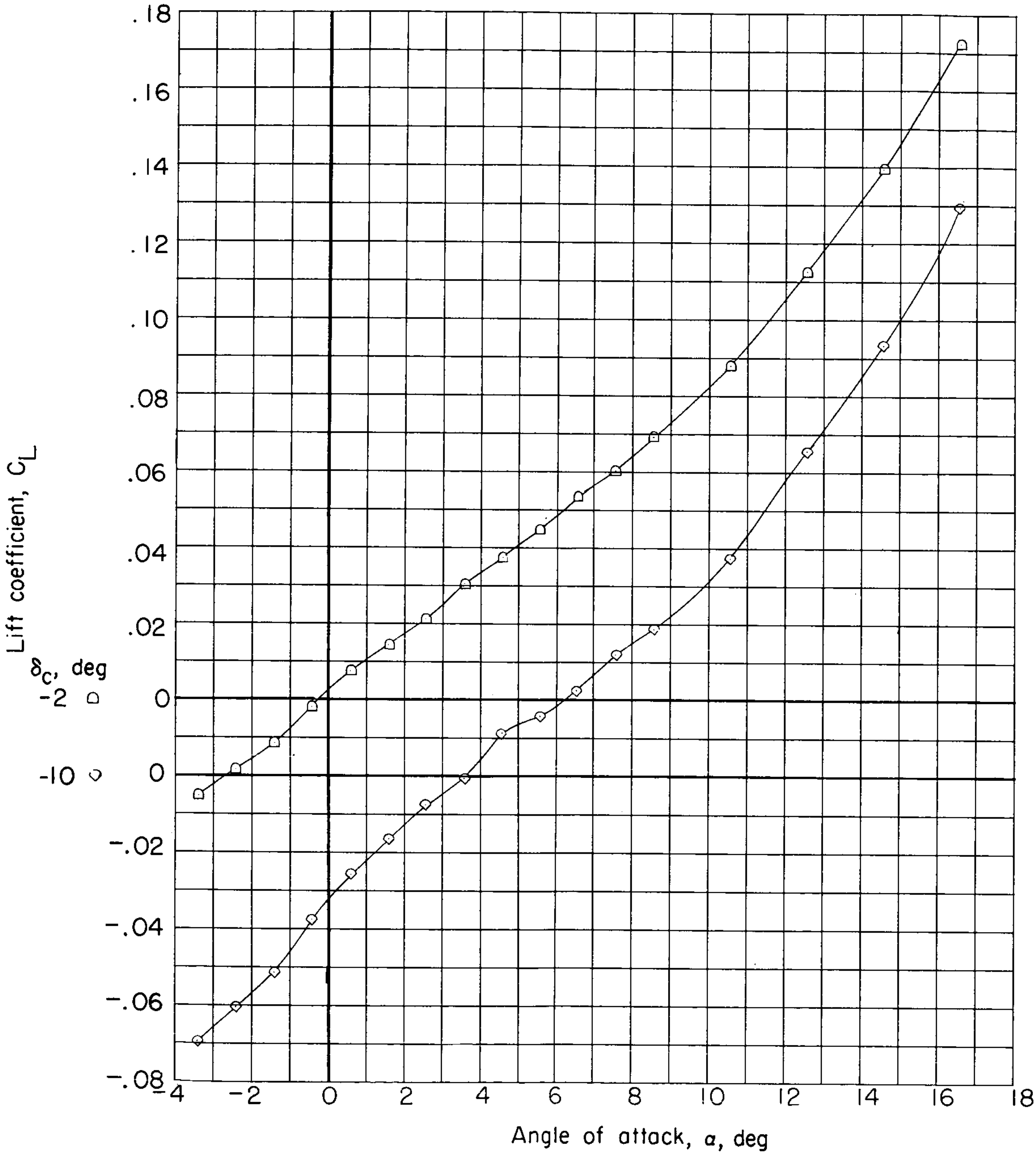

(a) Lift coefficient.

Figure 65.- Aerodynamic characteristics for model BC with $\delta_{tab} = 0^{\circ}$ at $M = 0.80$.

[redacted]

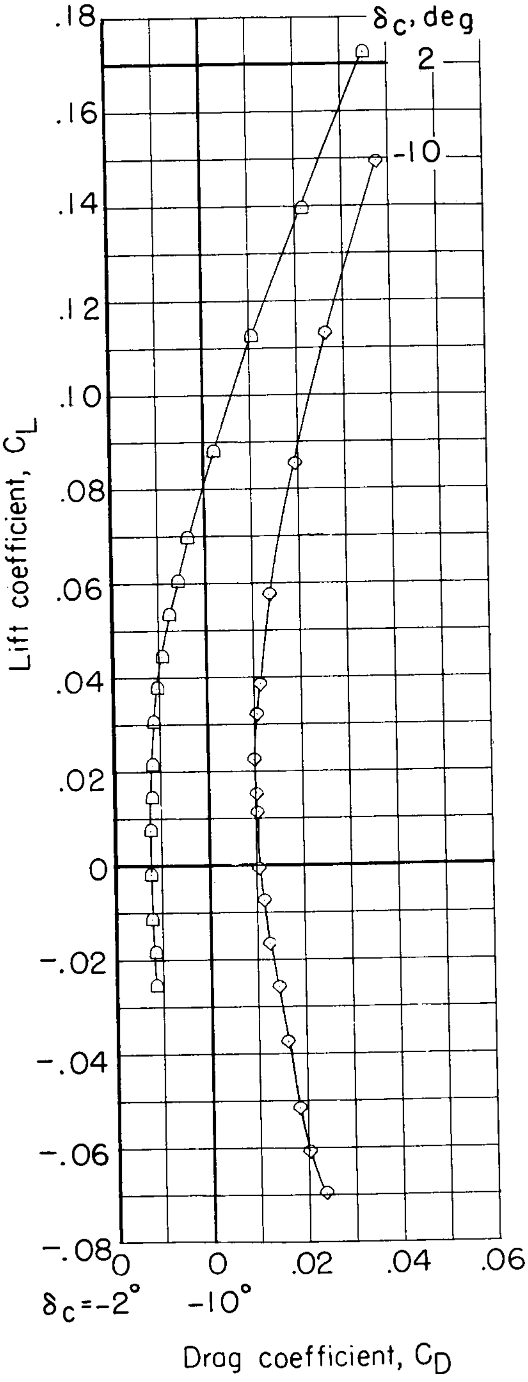

(b) Drag coefficient.

Figure 65.- Continued.

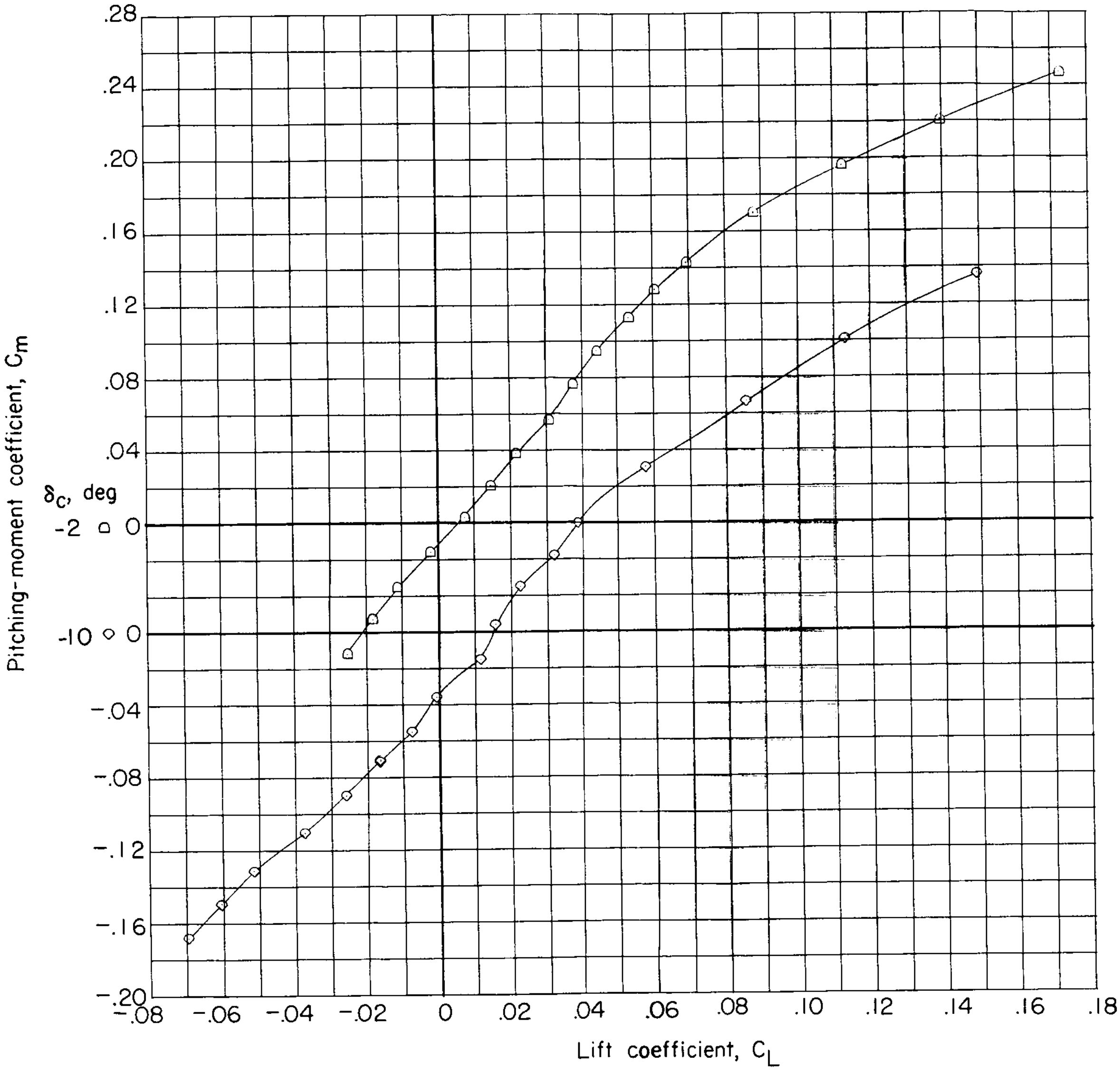

(c) Pitching-moment coefficient.

Figure 65.- Concluded.

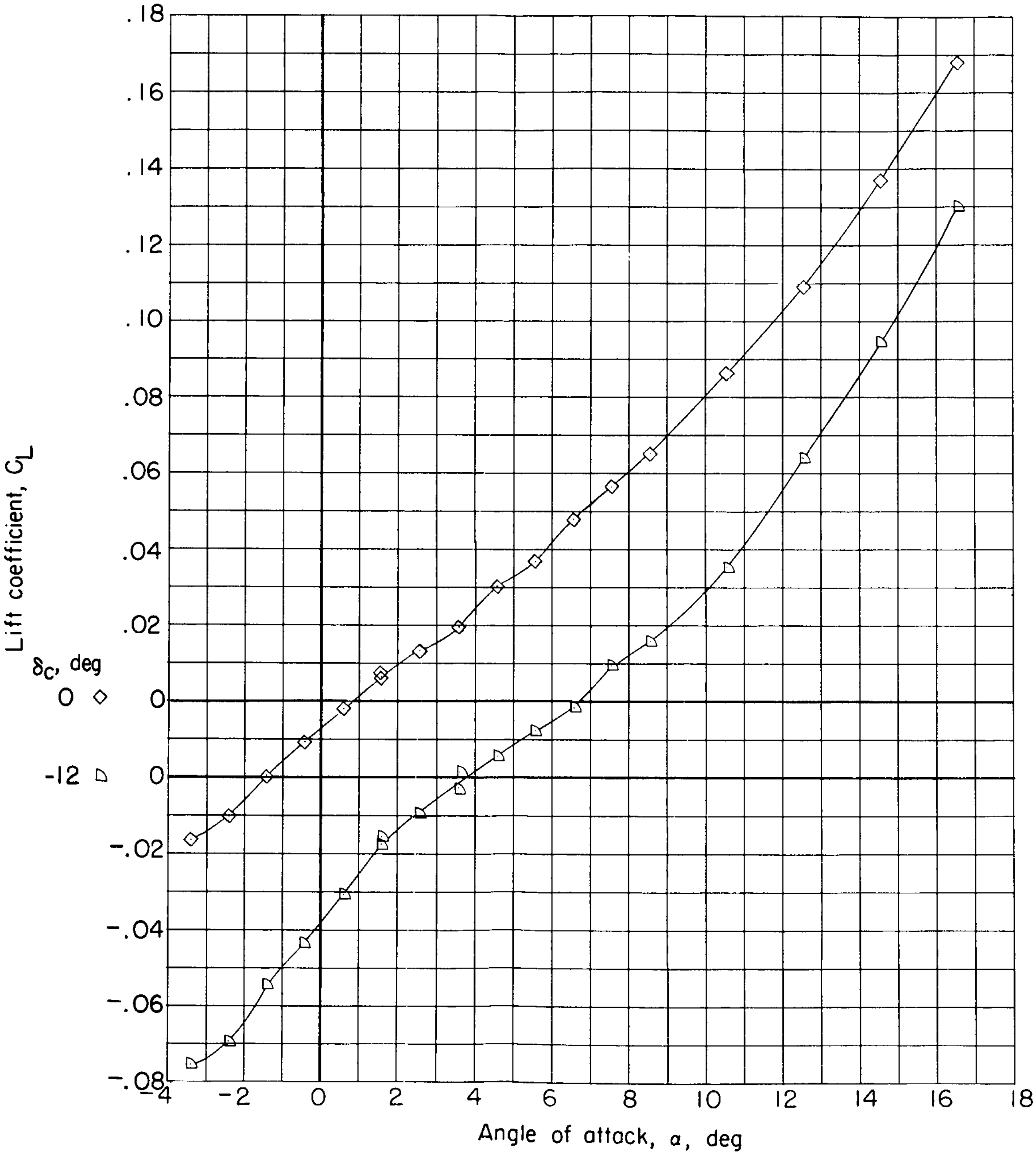

(a) Lift coefficient.

Figure 66.- Aerodynamic characteristics for model BC with $\delta_{tab} = 0^{\circ}$ at $M = 0.85$.

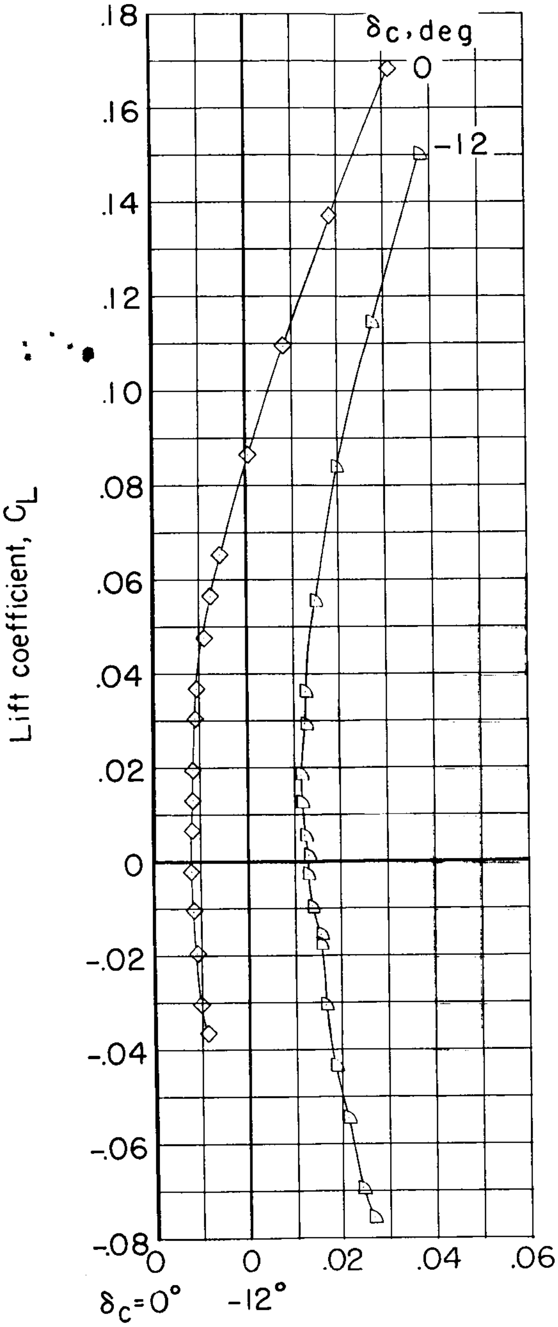

(b) Drag coefficient.

Figure 66.- Continued.

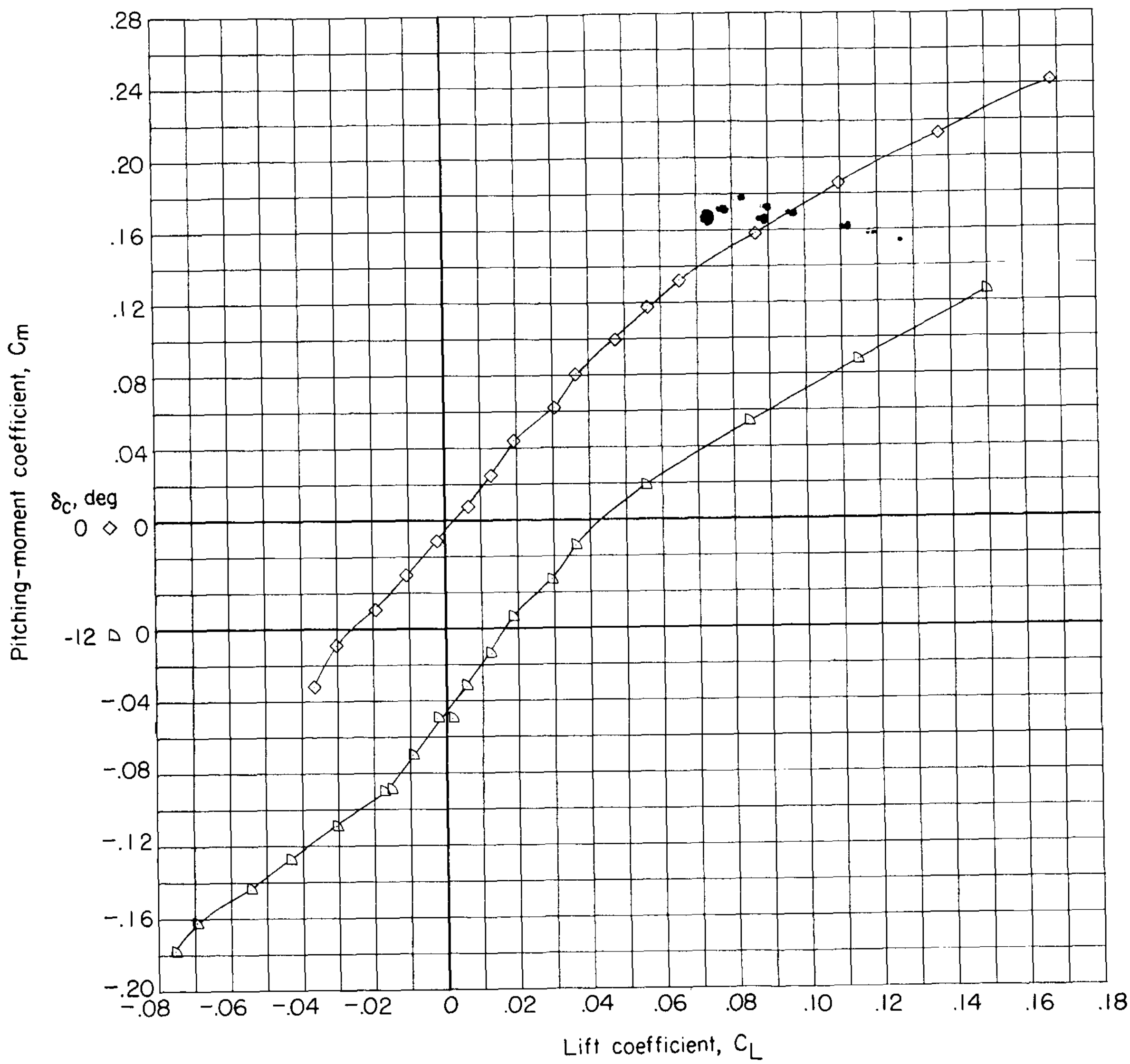

(c) Pitching-moment coefficient.

Figure 66.- Concluded.

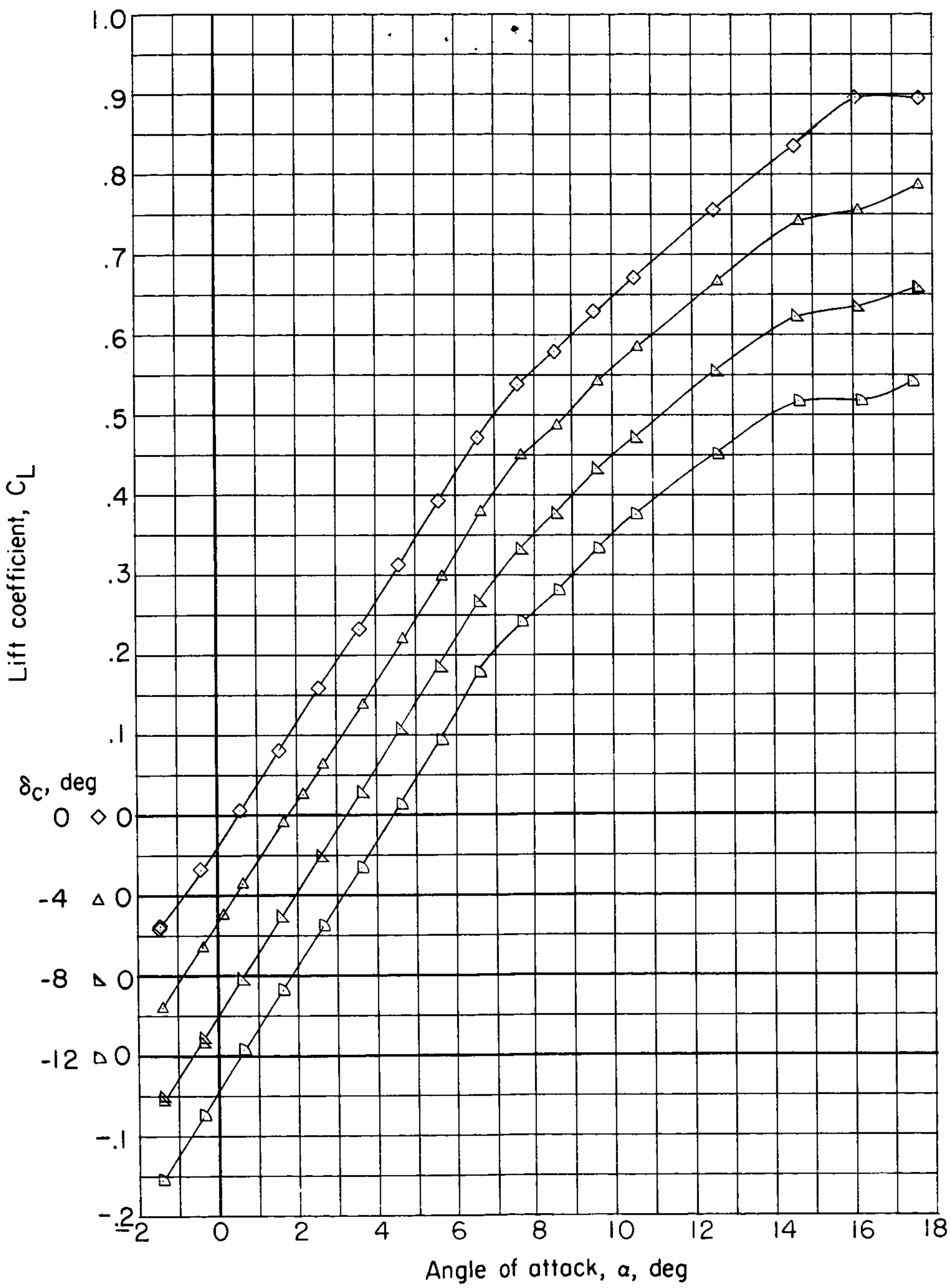

(a) Lift coefficient.

Figure 67.- Aerodynamic characteristics for model BCW_1E with $\delta_{le} = 15^\circ$ and $\delta_{tab} = 0^\circ$ at $M = 0.85$.

[redacted]

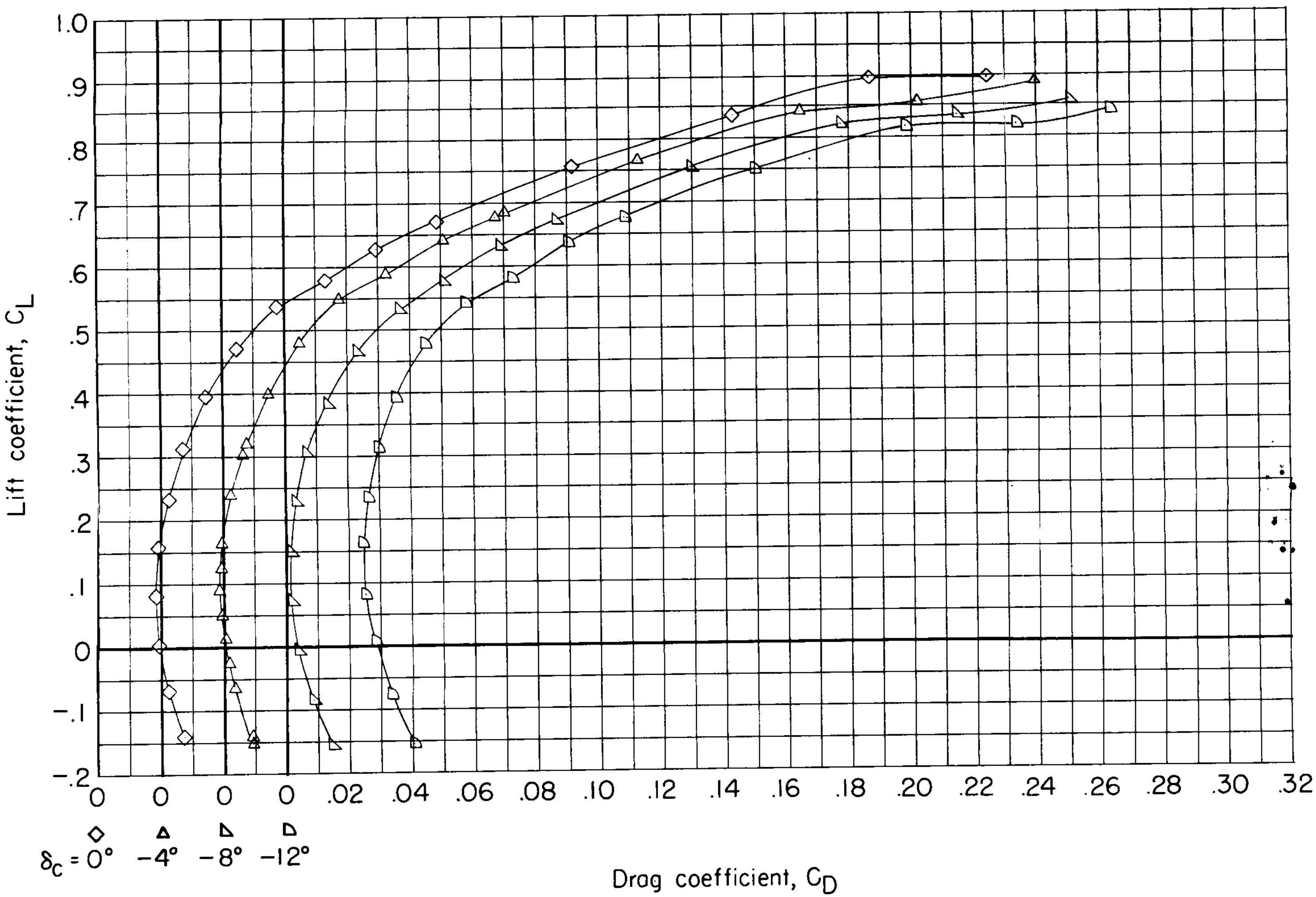

(b) Drag coefficient.

Figure 67.- Continued.

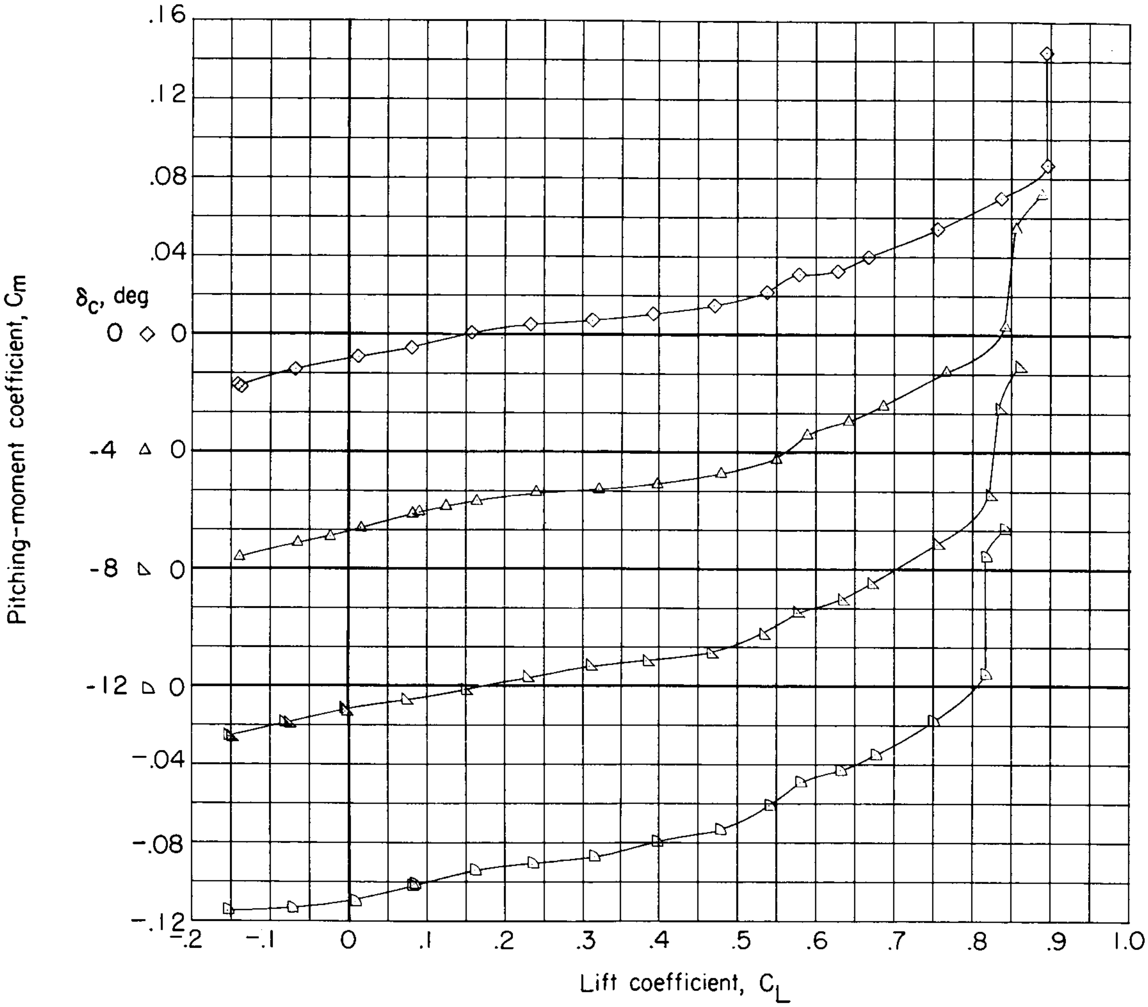

(c) Pitching-moment coefficient.

Figure 67.- Concluded.

[redacted]

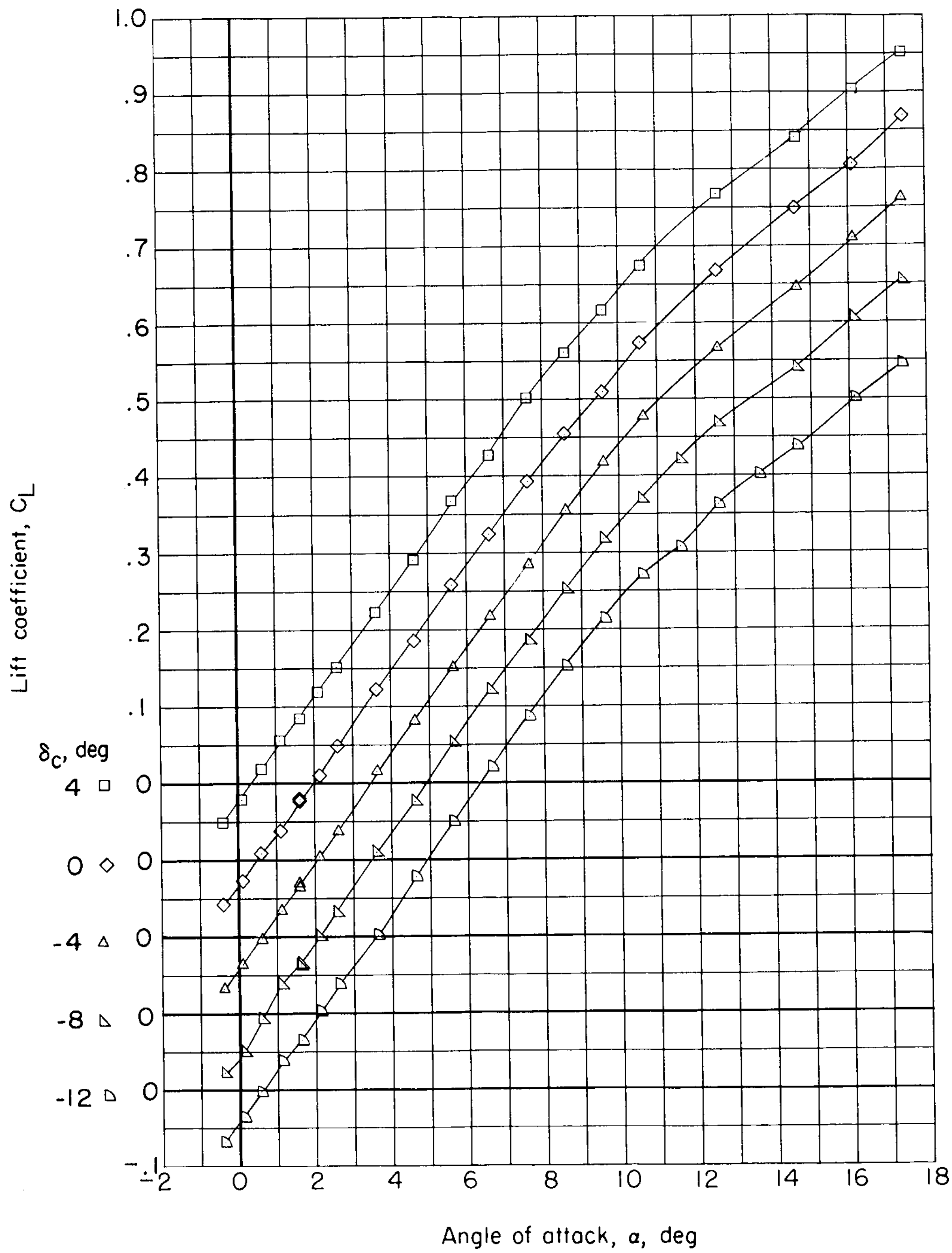

(a) Lift coefficient.

Figure 68.- Aerodynamic characteristics for model BCW_1E with $\delta_{le} = 15^{o}$ and $\delta_{tab} = -4^{o}$ at $M = 0.70$.

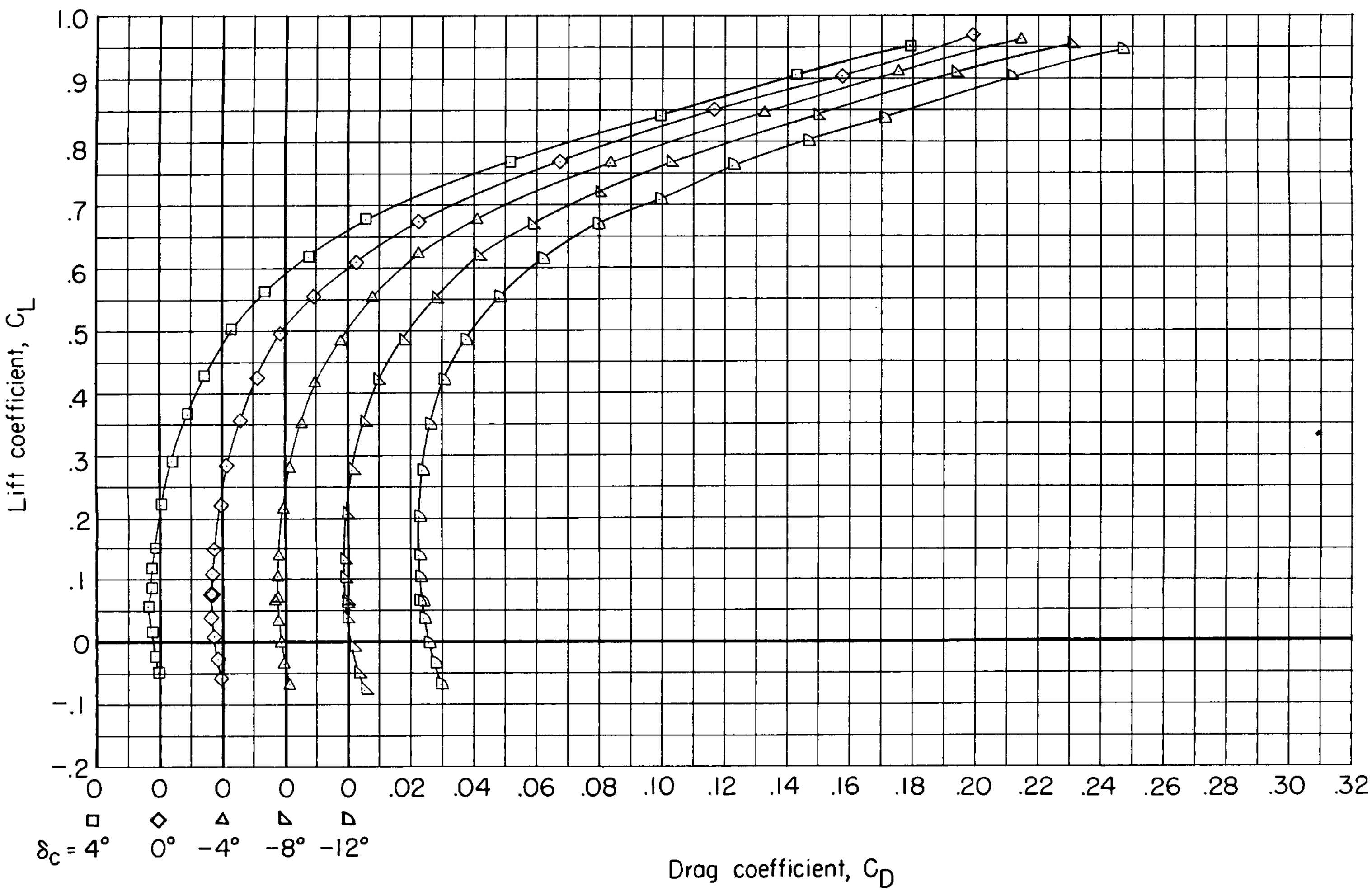

(b) Drag coefficient.

Figure 68.- Continued.

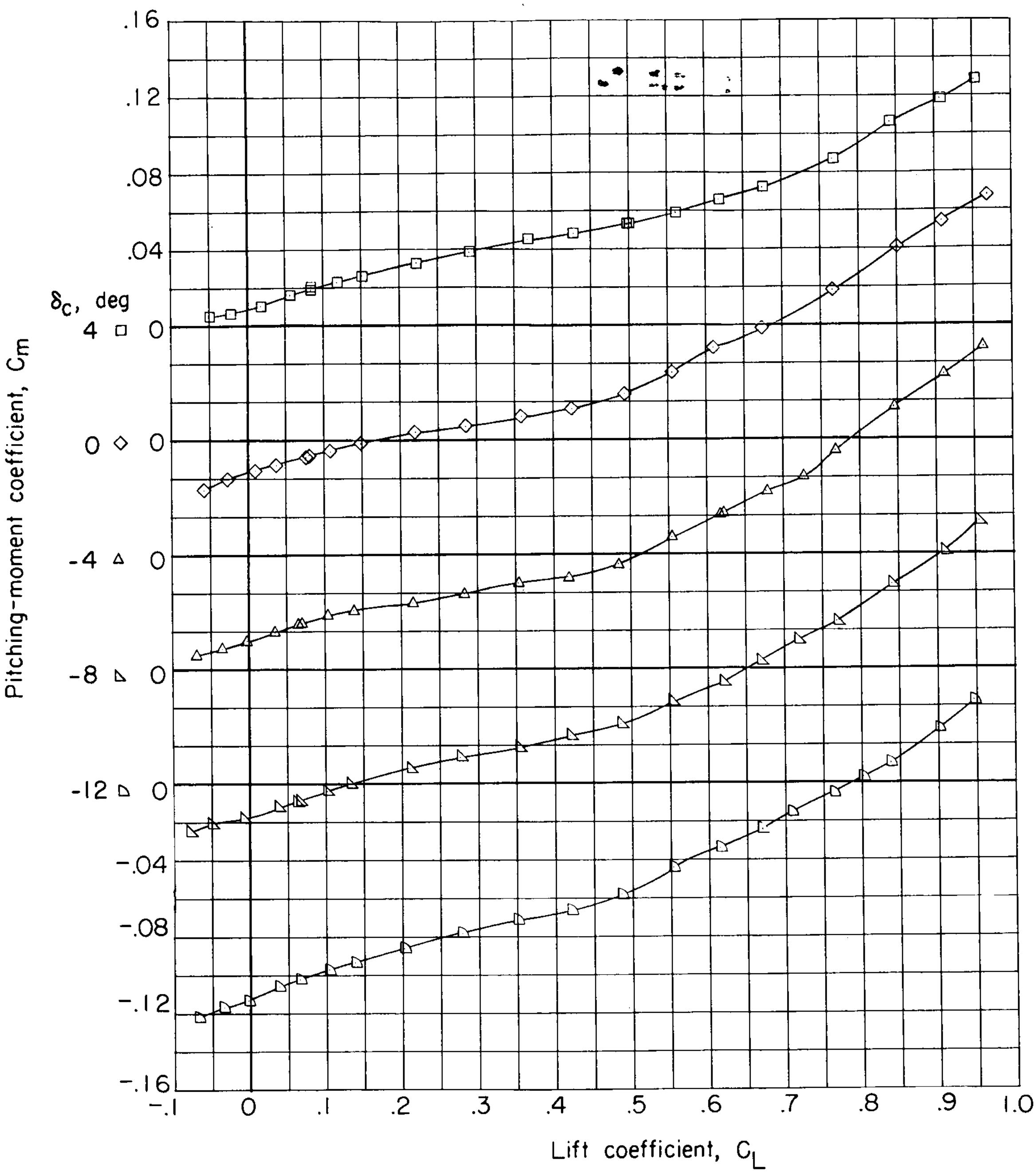

(c) Pitching-moment coefficient.

Figure 68.- Concluded.

L-1041

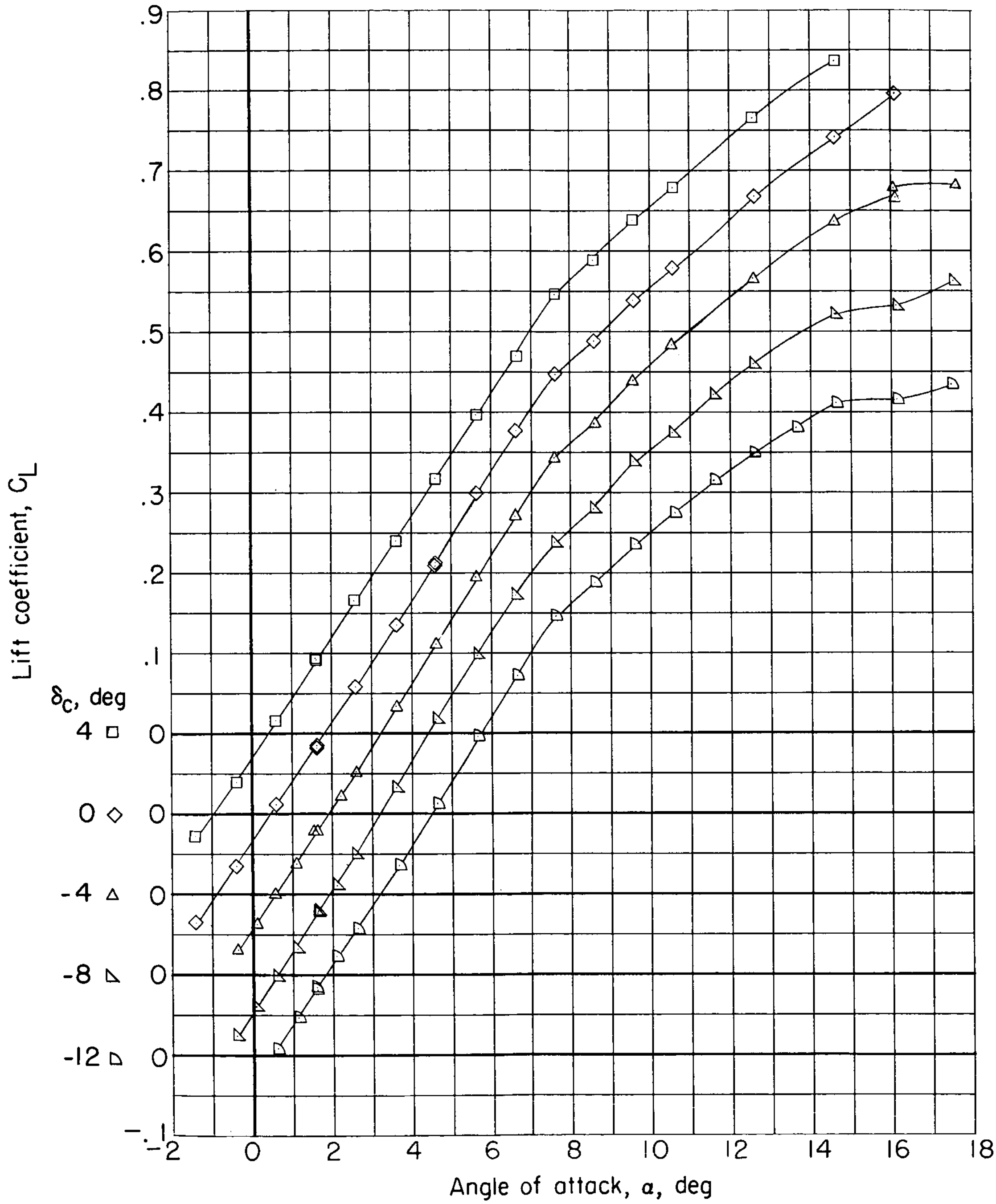

(a) Lift coefficient.

Figure 69.- Aerodynamic characteristics for model BCW_1E with $\delta_{le} = 15^o$ and $\delta_{tab} = -4^o$ at $M = 0.85$.

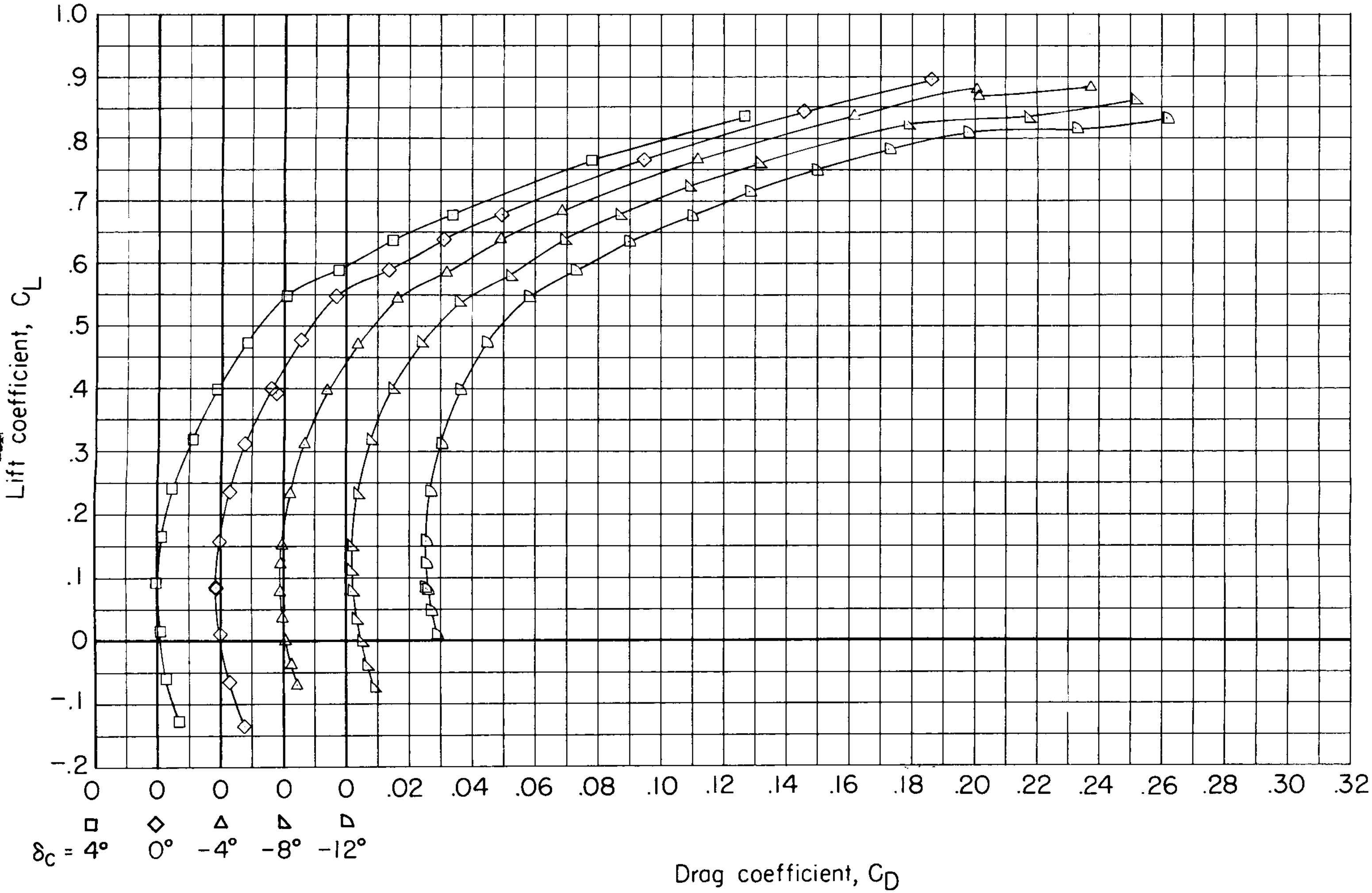

(b) Drag coefficient.

Figure 69.- Continued.

L-1041

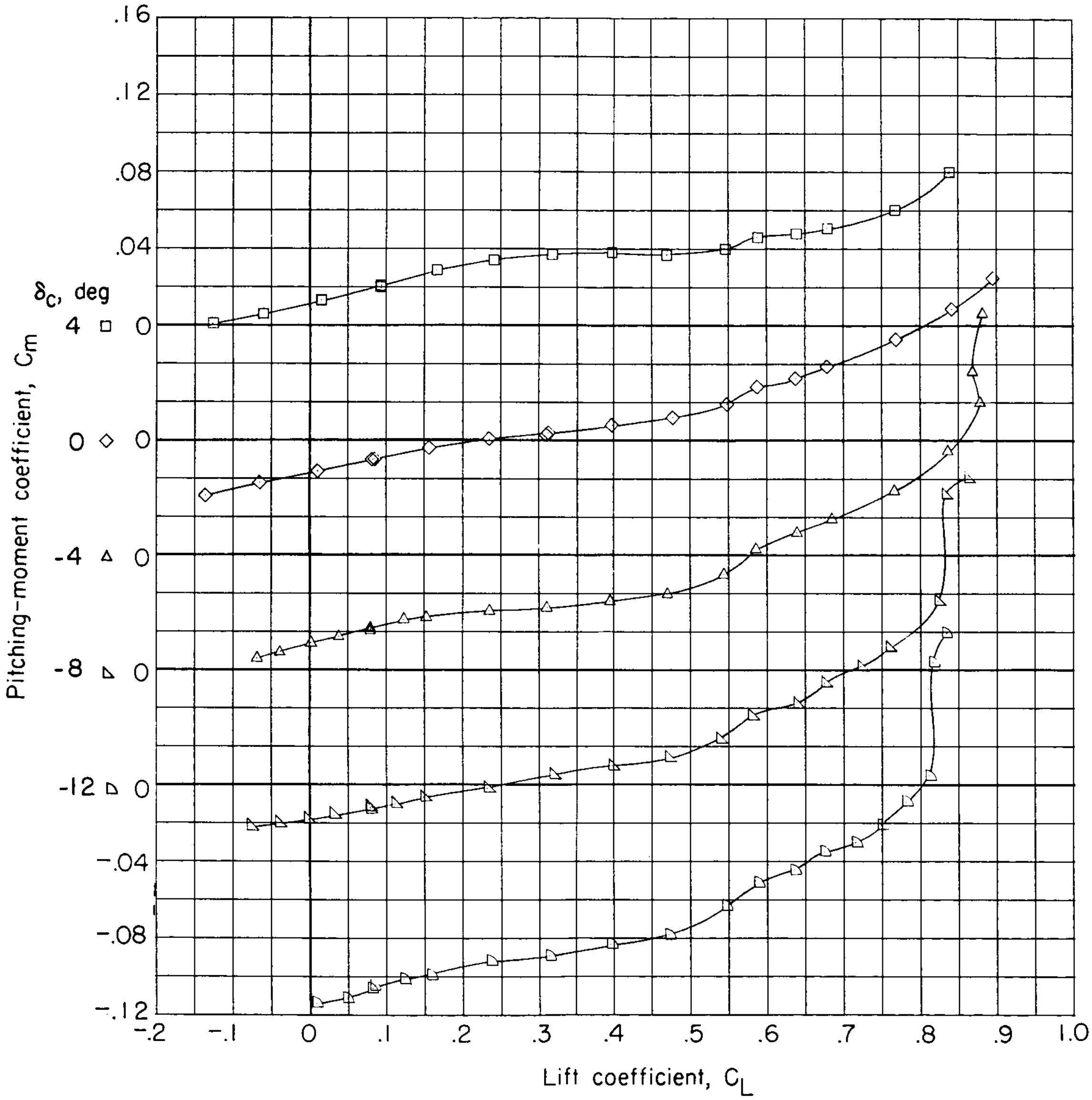

(c) Pitching-moment coefficient.

Figure 69.- Concluded.

[redacted]

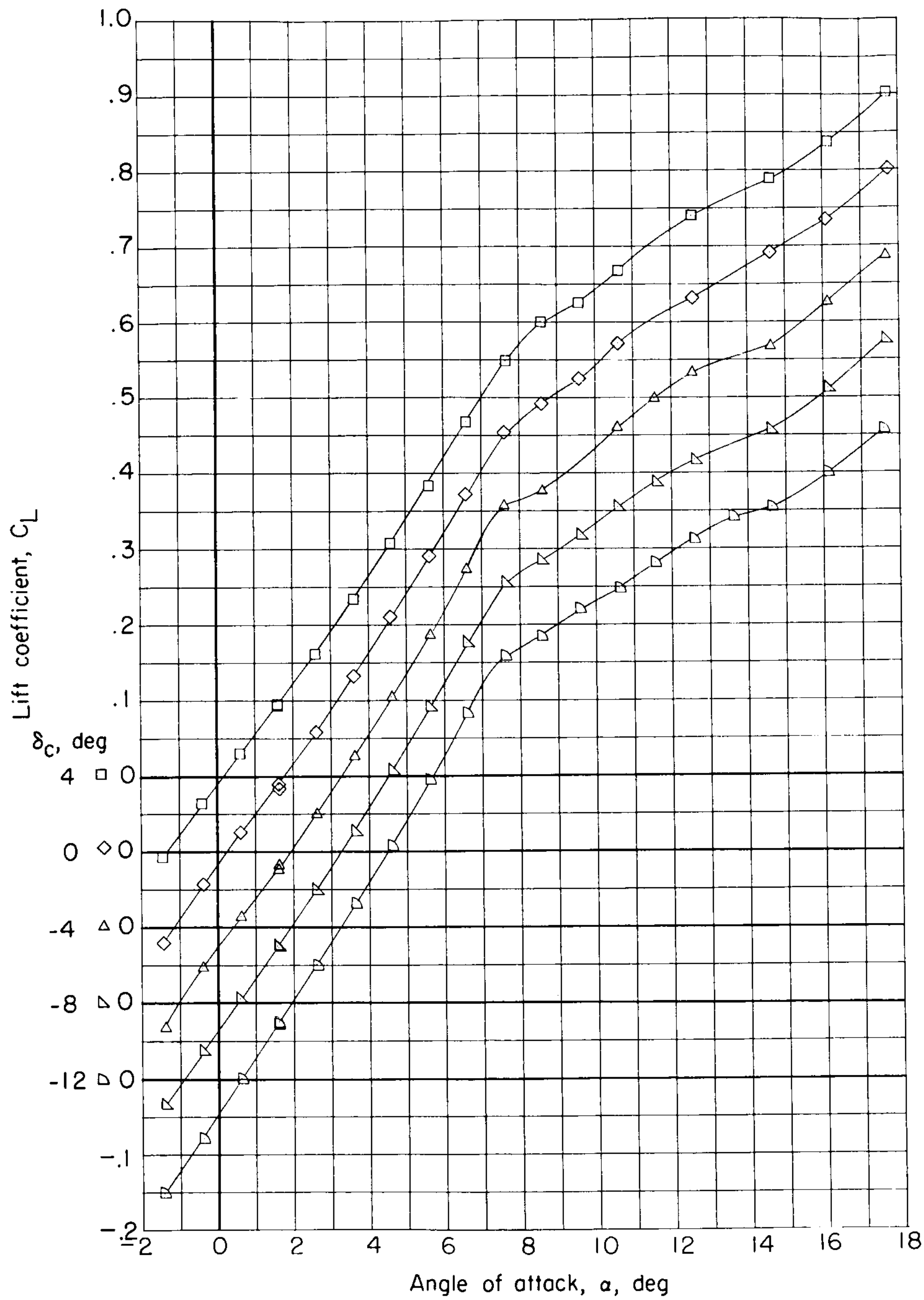

(a) Lift coefficient.

Figure 70.- Aerodynamic characteristics for model BCW_1E with $\delta_{le} = 15^{\circ}$ and $\delta_{tab} = -4^{\circ}$ at $M = 0.90$.

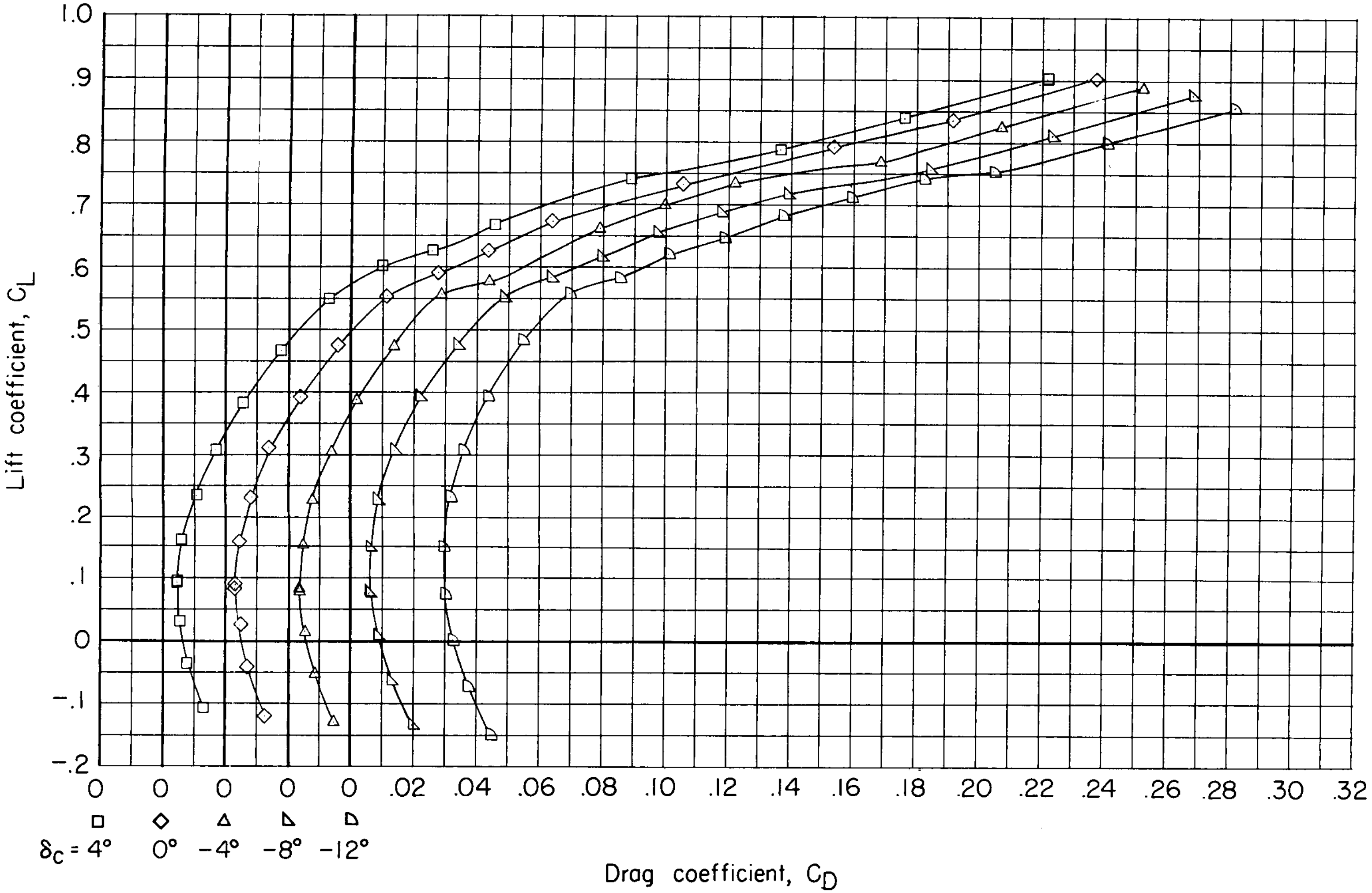

(b) Drag coefficient.

Figure 70.- Continued.

[redacted]

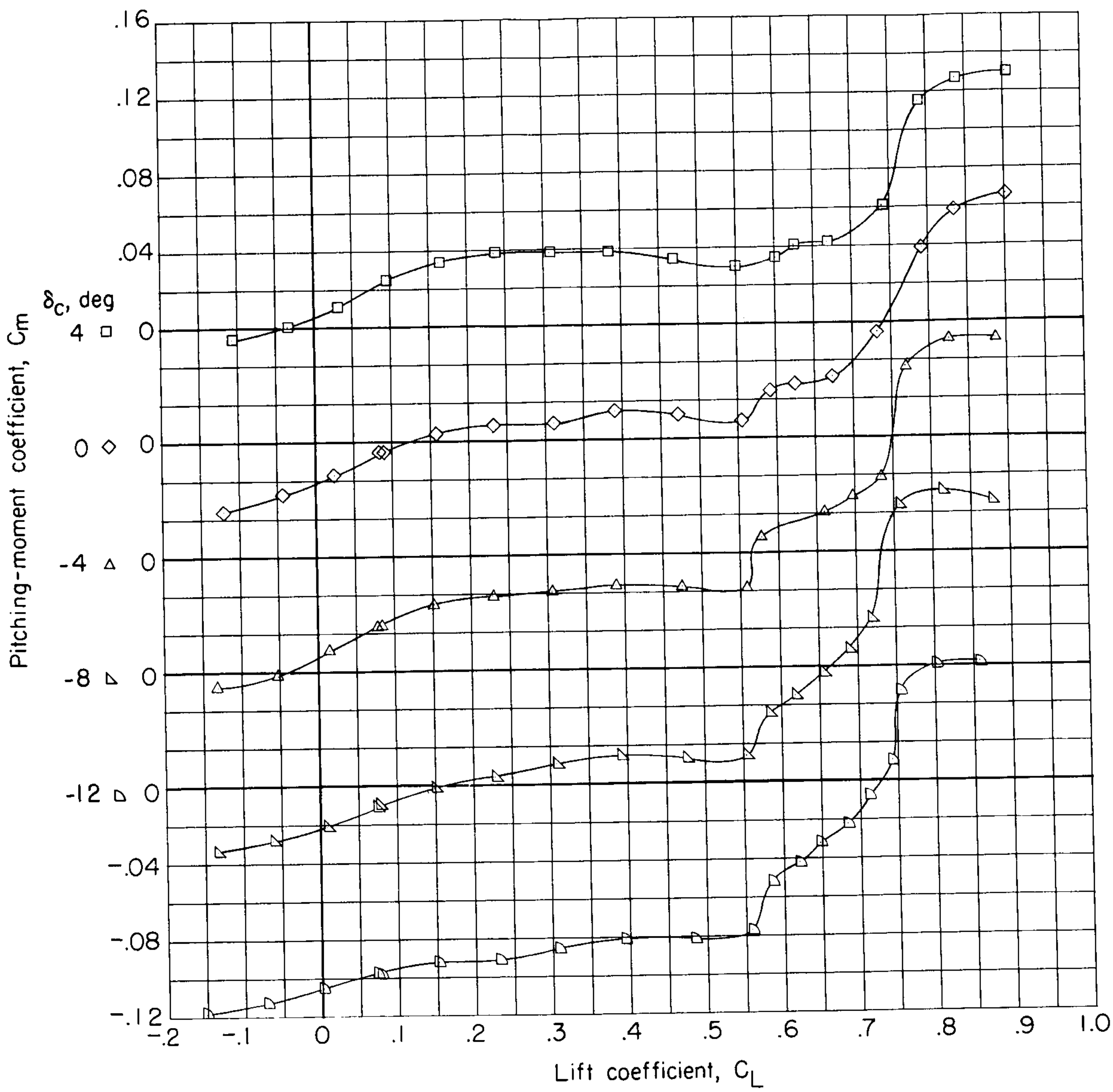

(c) Pitching-moment coefficient.

Figure 70.- Concluded.

[redacted]TIAL

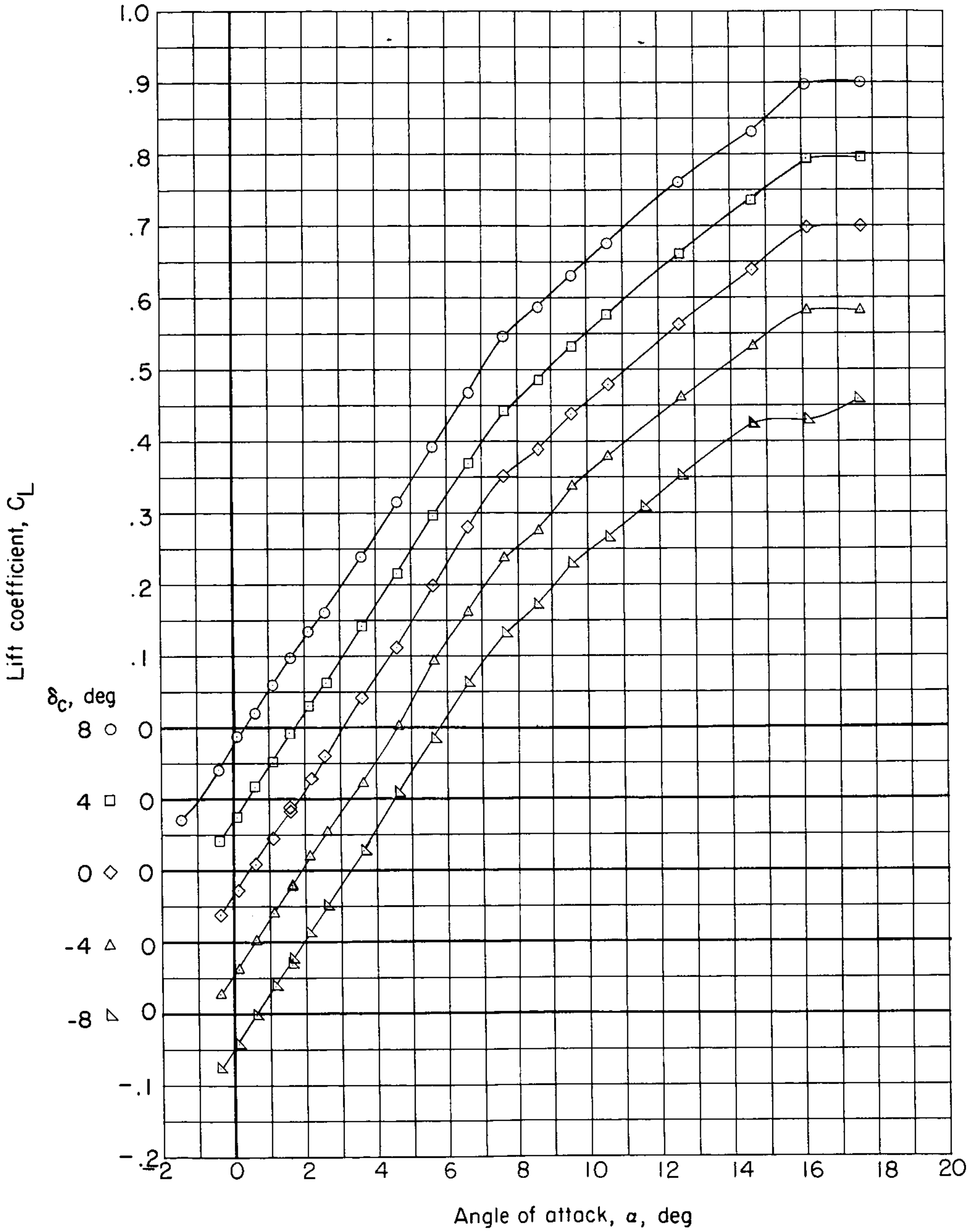

(a) Lift coefficient.

Figure 71.- Aerodynamic characteristics for model BCW_1E with $\delta_{le} = 15^\circ$ and $\delta_{tab} = -8^\circ$ at $M = 0.85$.

DEC[redacted]IED

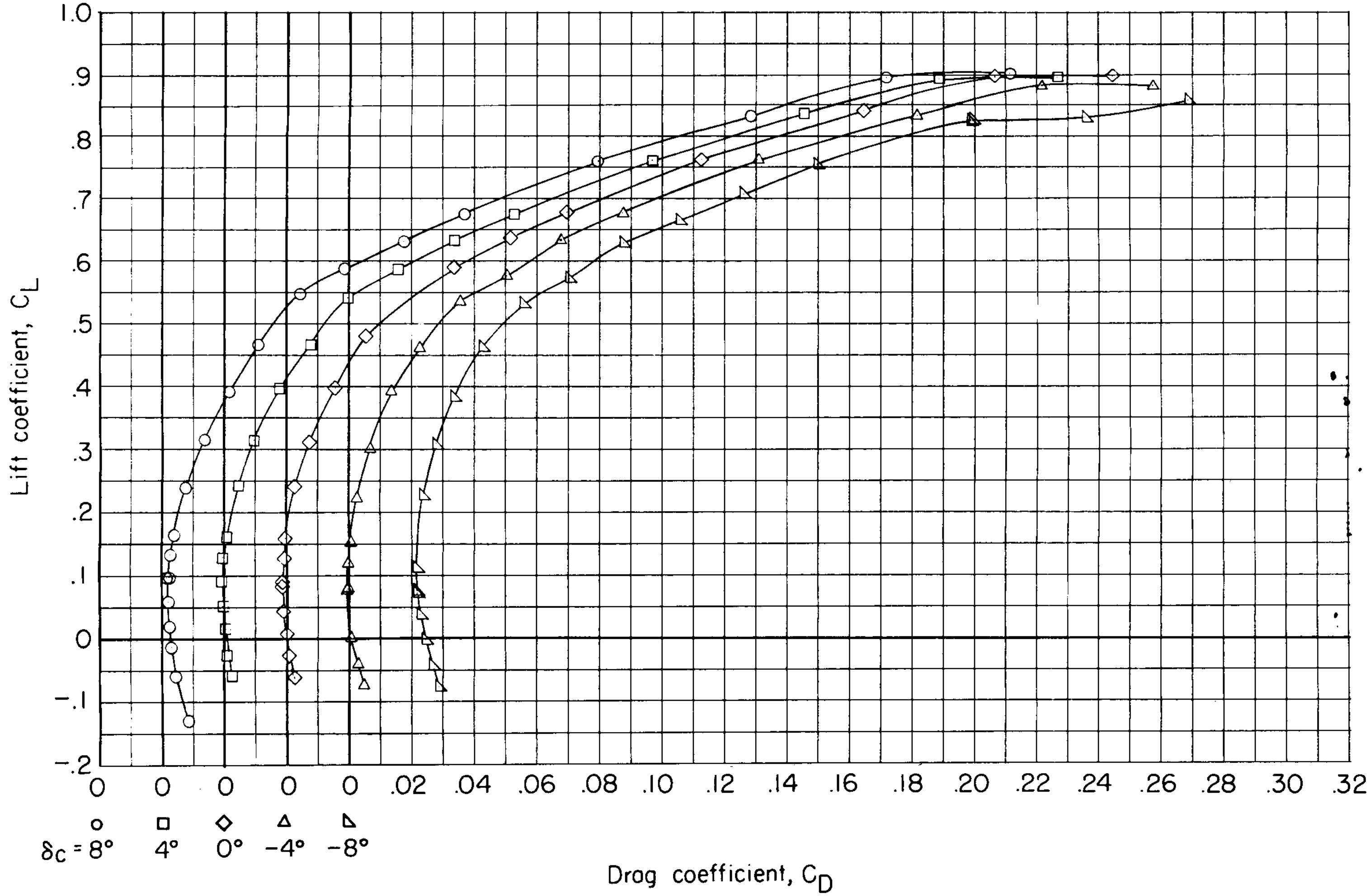

(b) Drag coefficient.

Figure 71.- Continued.

C[redacted]NTIAL

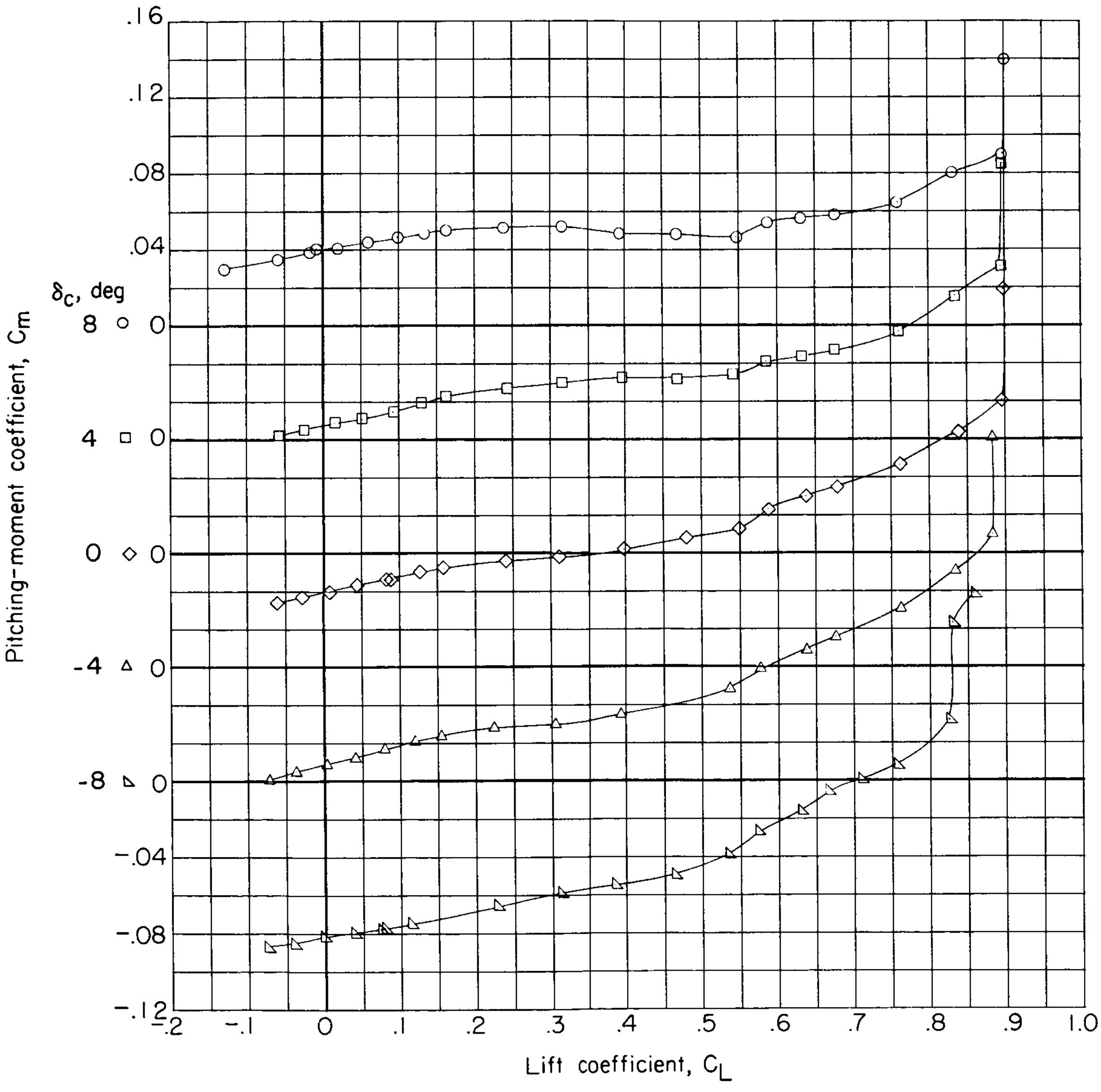

(c) Pitching-moment coefficient.

Figure 71.- Concluded.

[redacted]

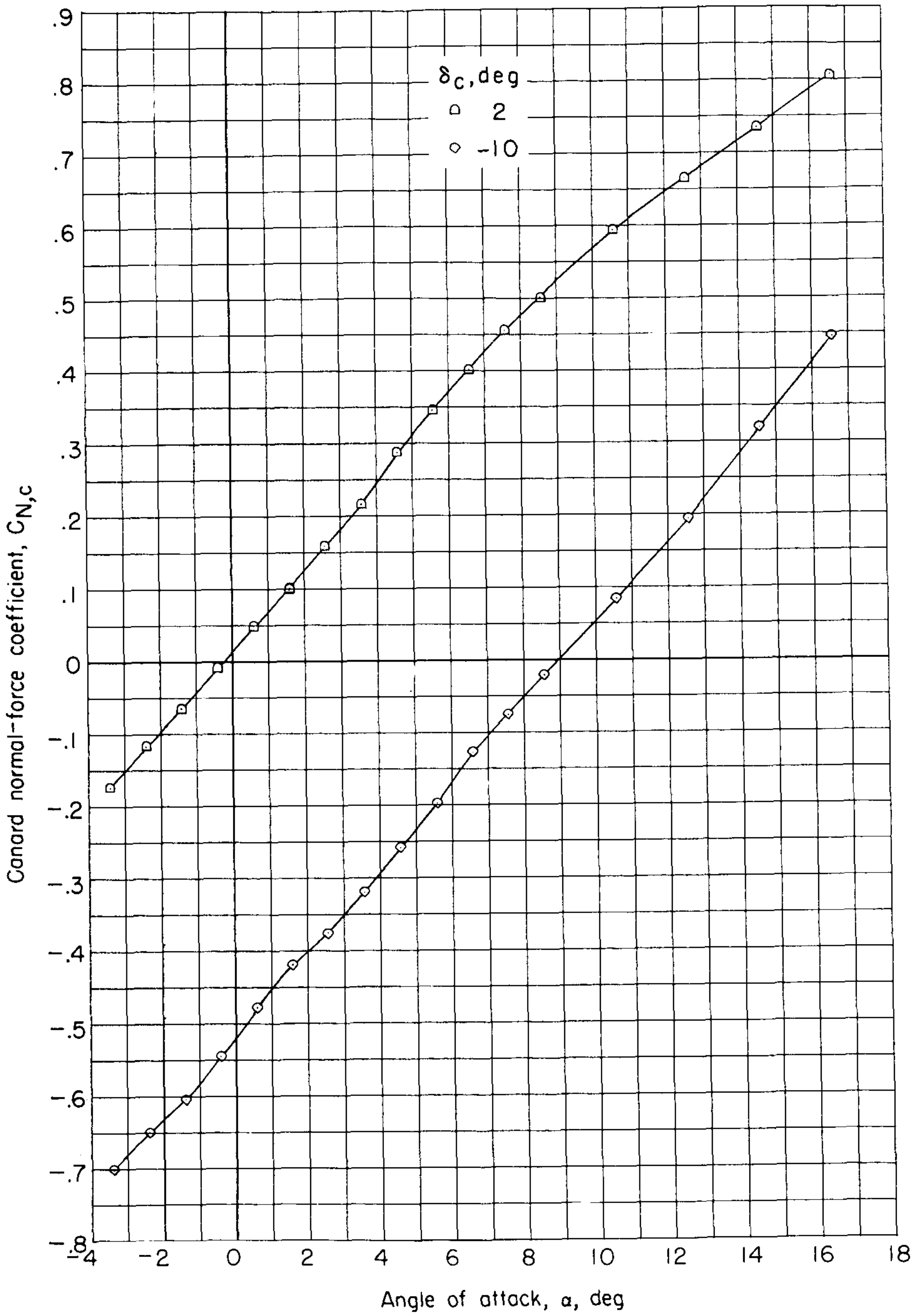

(a) Canard normal-force coefficient.

Figure 72.- Canard normal-force and hinge-moment coefficients for model BC with $\delta_{tab} = 0^{o}$ at $M = 0.80$.

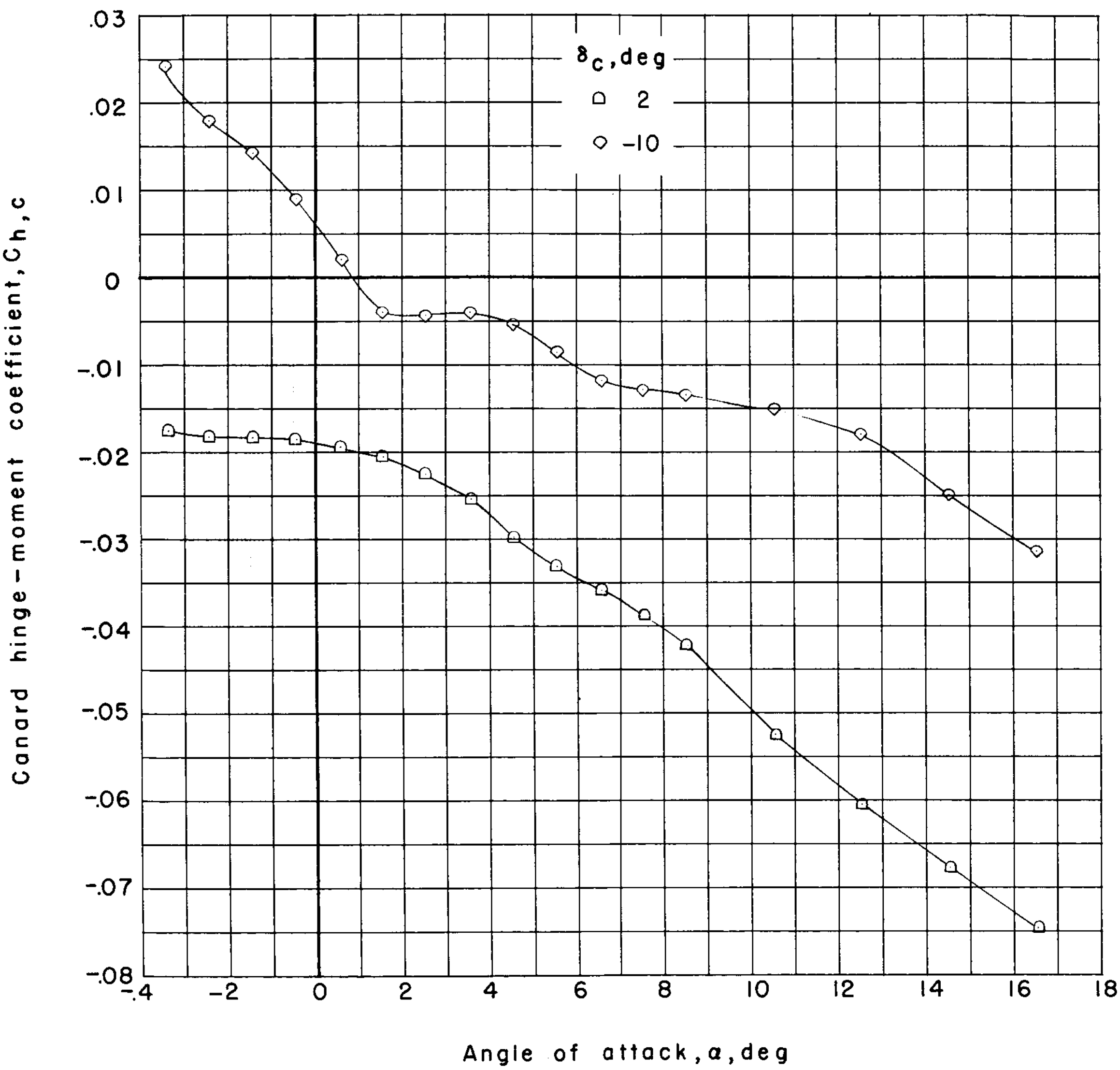

(b) Canard hinge-moment coefficient.

Figure 72.- Concluded.

[redacted]

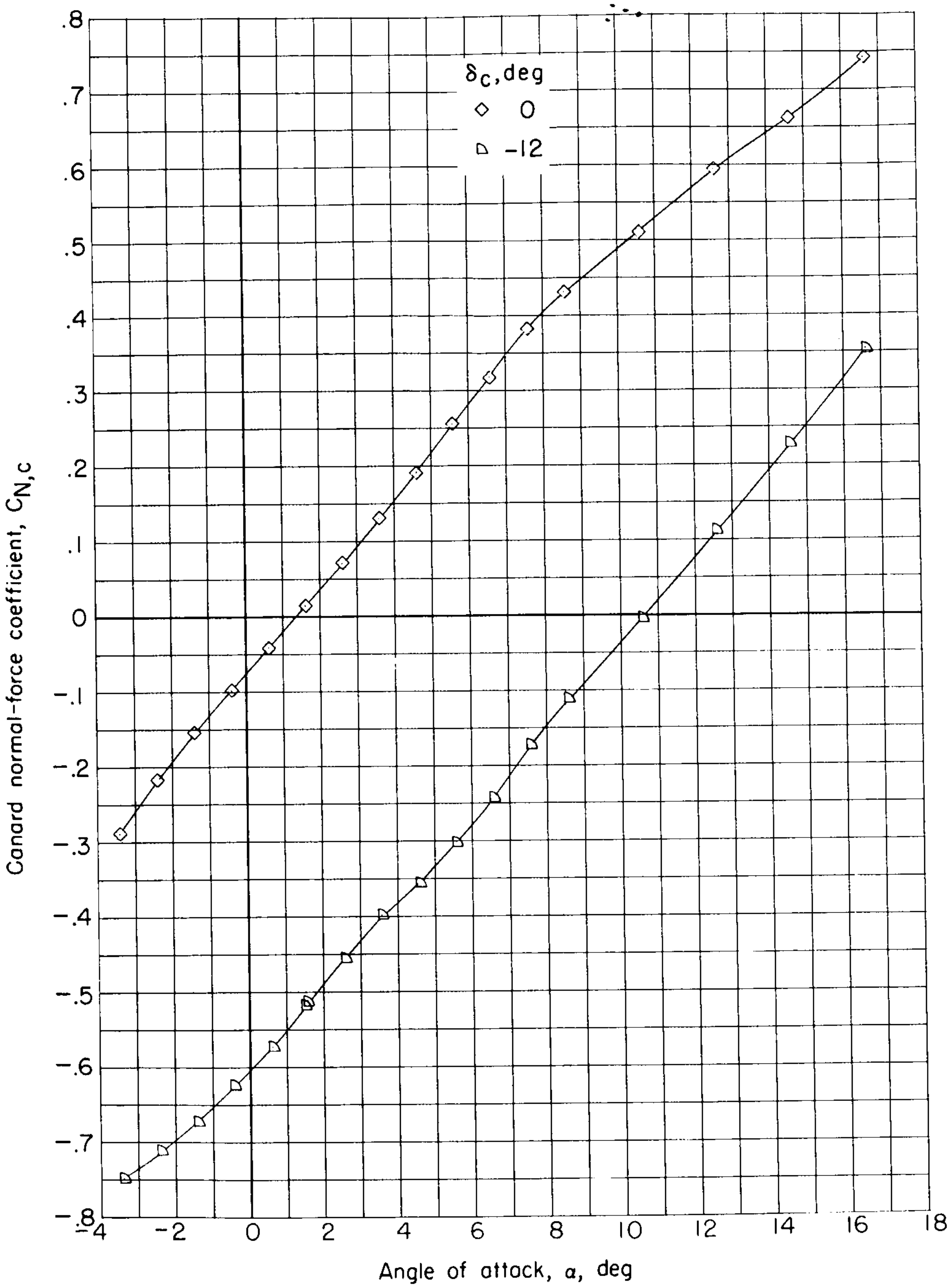

(a) Canard normal-force coefficient.

Figure 73.- Canard normal-force and hinge-moment coefficients for model BC with $\delta_{tab} = 0^{\circ}$ at $M = 0.85$.

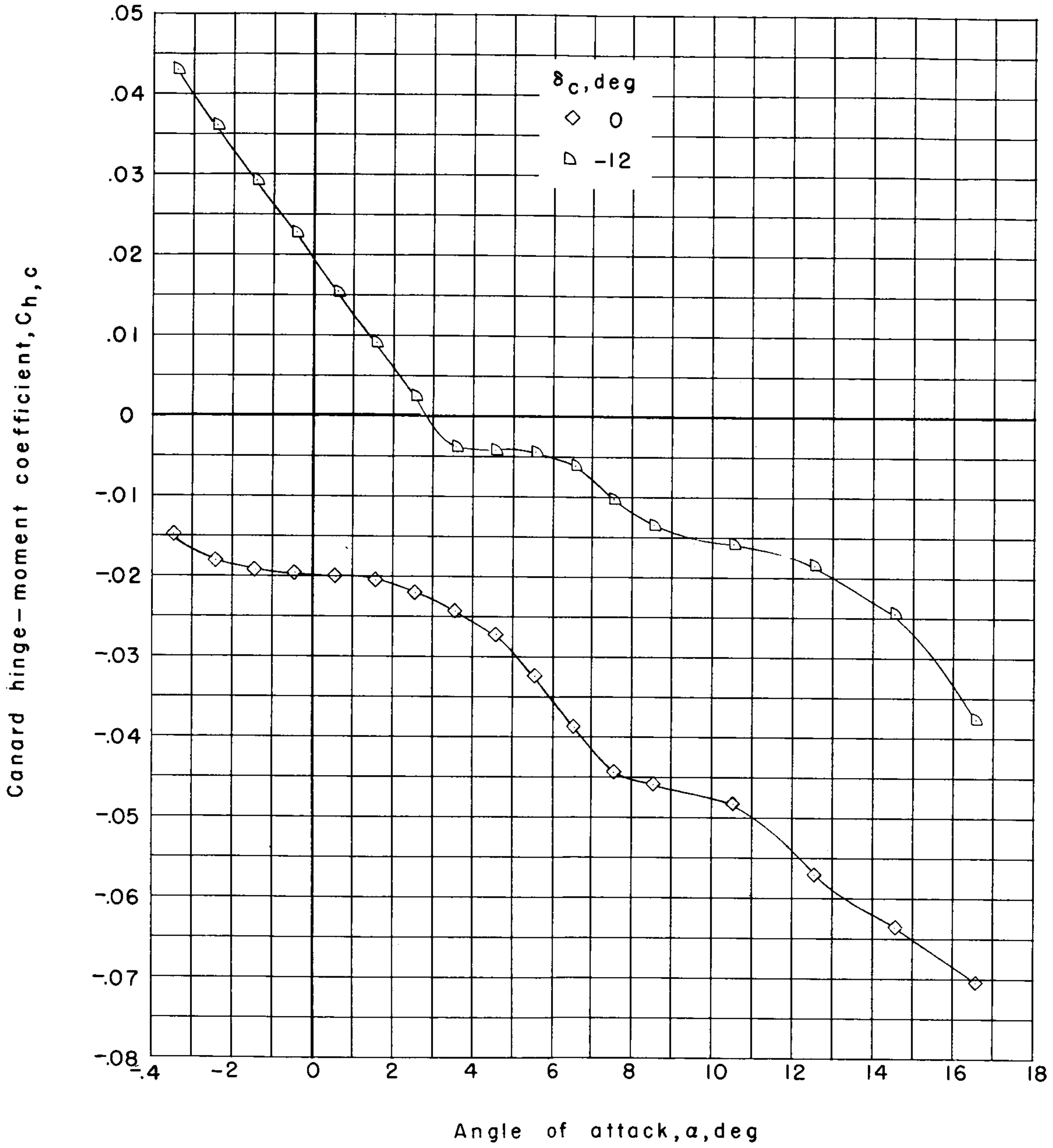

(b) Canard hinge-moment coefficient.

Figure 73.- Concluded.

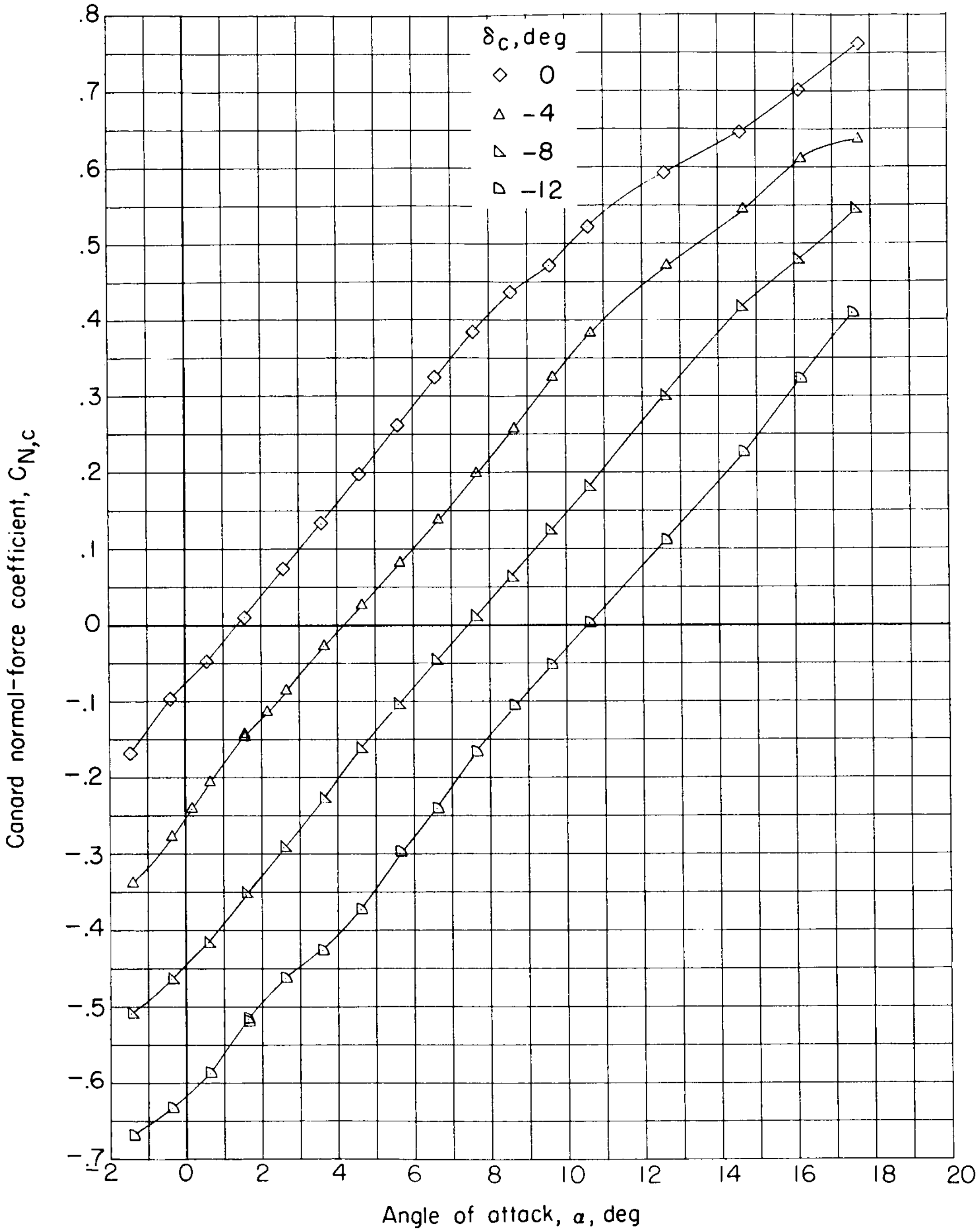

(a) Canard normal-force coefficient.

Figure 74.- Canard normal-force and hinge-moment coefficients for model BCW_1E with $\delta_{le} = 15^o$ and $\delta_{tab} = 0^o$ at $M = 0.85$.

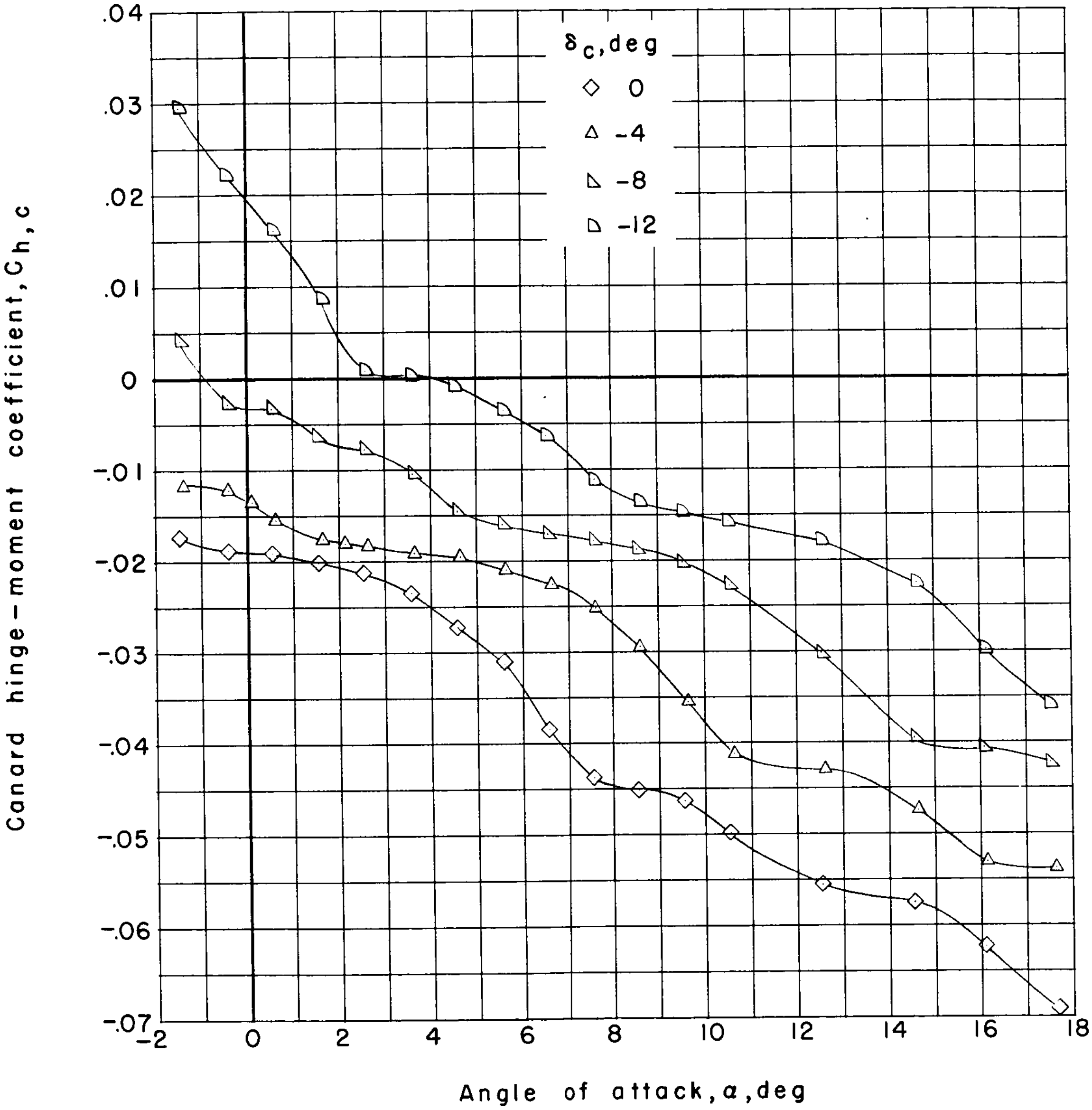

(b) Canard hinge-moment coefficient.

Figure 74.- Concluded.

[redacted]

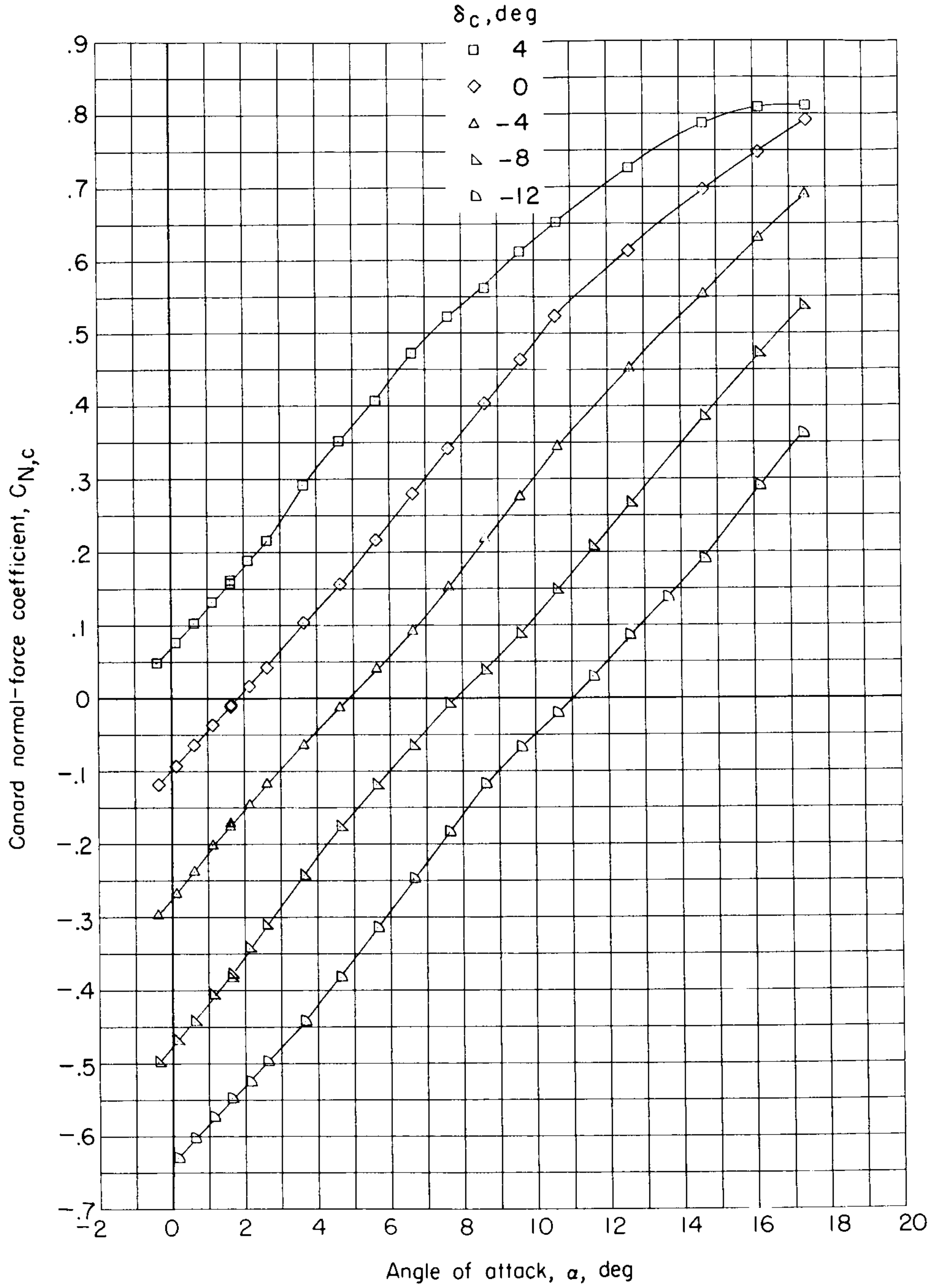

(a) Canard normal-force coefficient.

Figure 75.- Canard normal-force and hinge-moment coefficients for model BCW_1E with $\delta_{le} = 15^\circ$ and $\delta_{tab} = -4^\circ$ at $M = 0.70$.

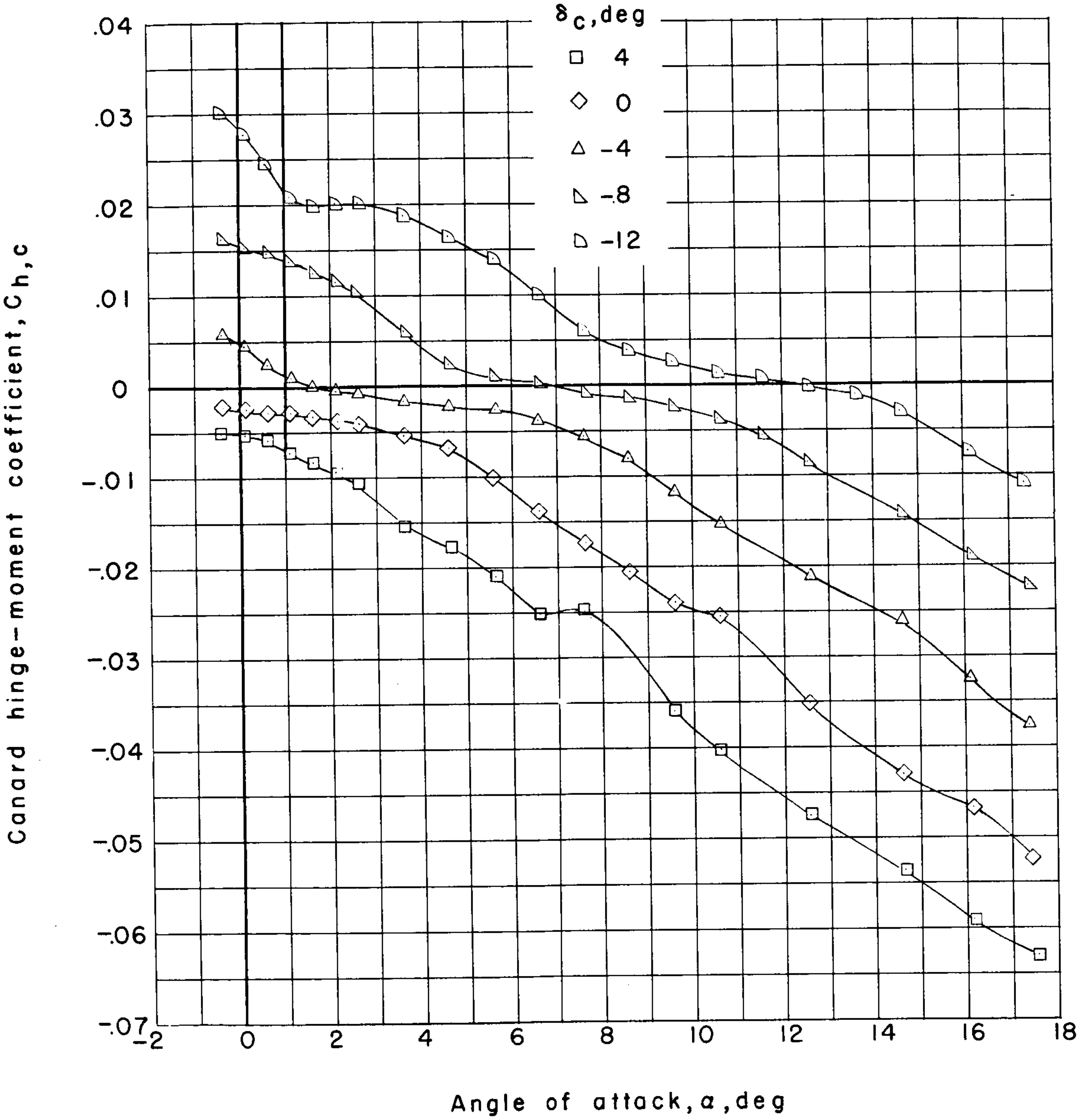

(b) Canard hinge-moment coefficient.

Figure 75.- Concluded.

[redacted]

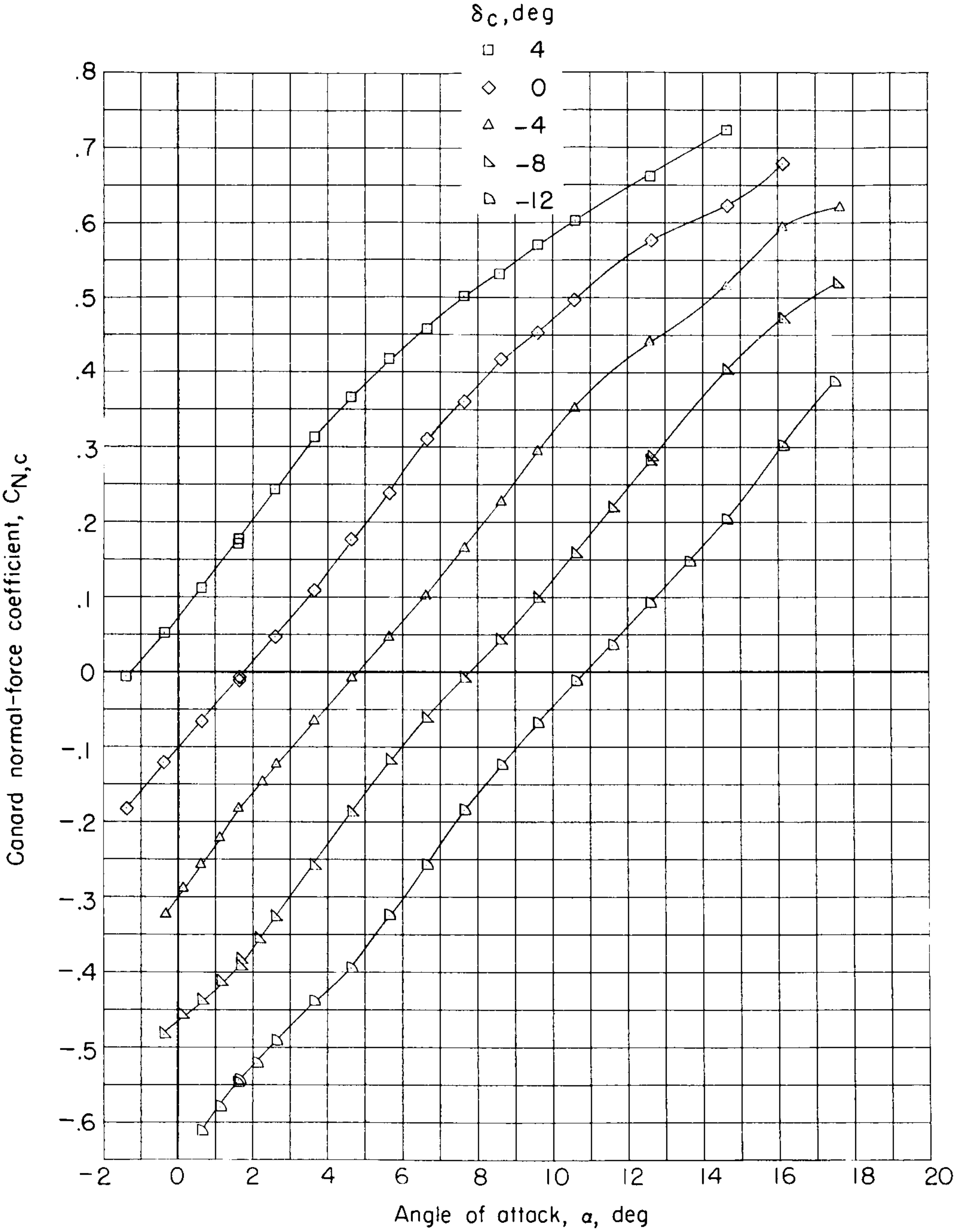

(a) Variation of canard normal-force coefficient with angle of attack.

Figure 76.- Canard normal-force and hinge-moment coefficients for model BCW_1E with $\delta_{le} = 15^{\circ}$ and $\delta_{tab} = -4^{\circ}$ at $M = 0.85$.

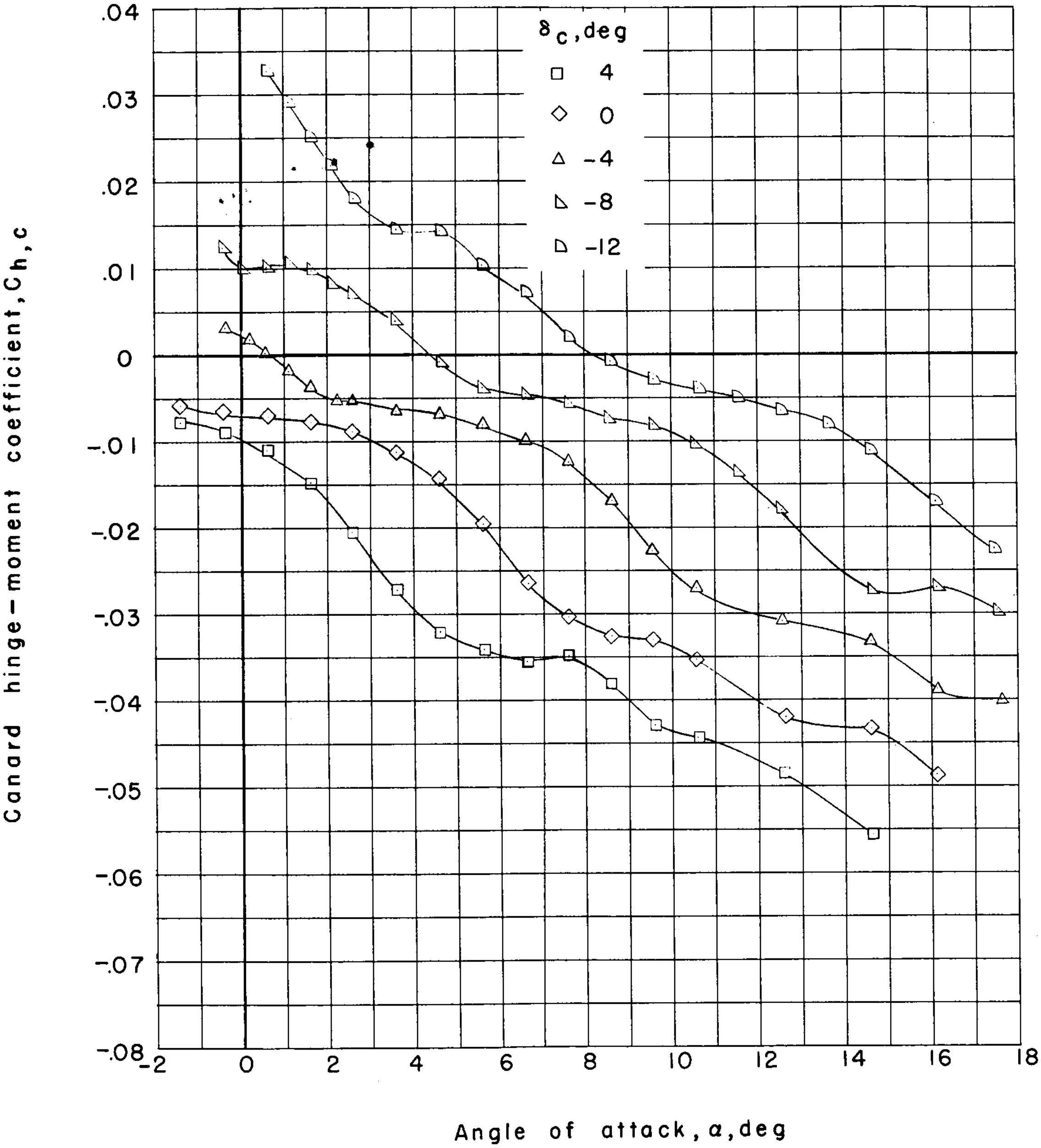

(b) Variation of canard hinge-moment coefficient with angle of attack.

Figure 76.- Continued.

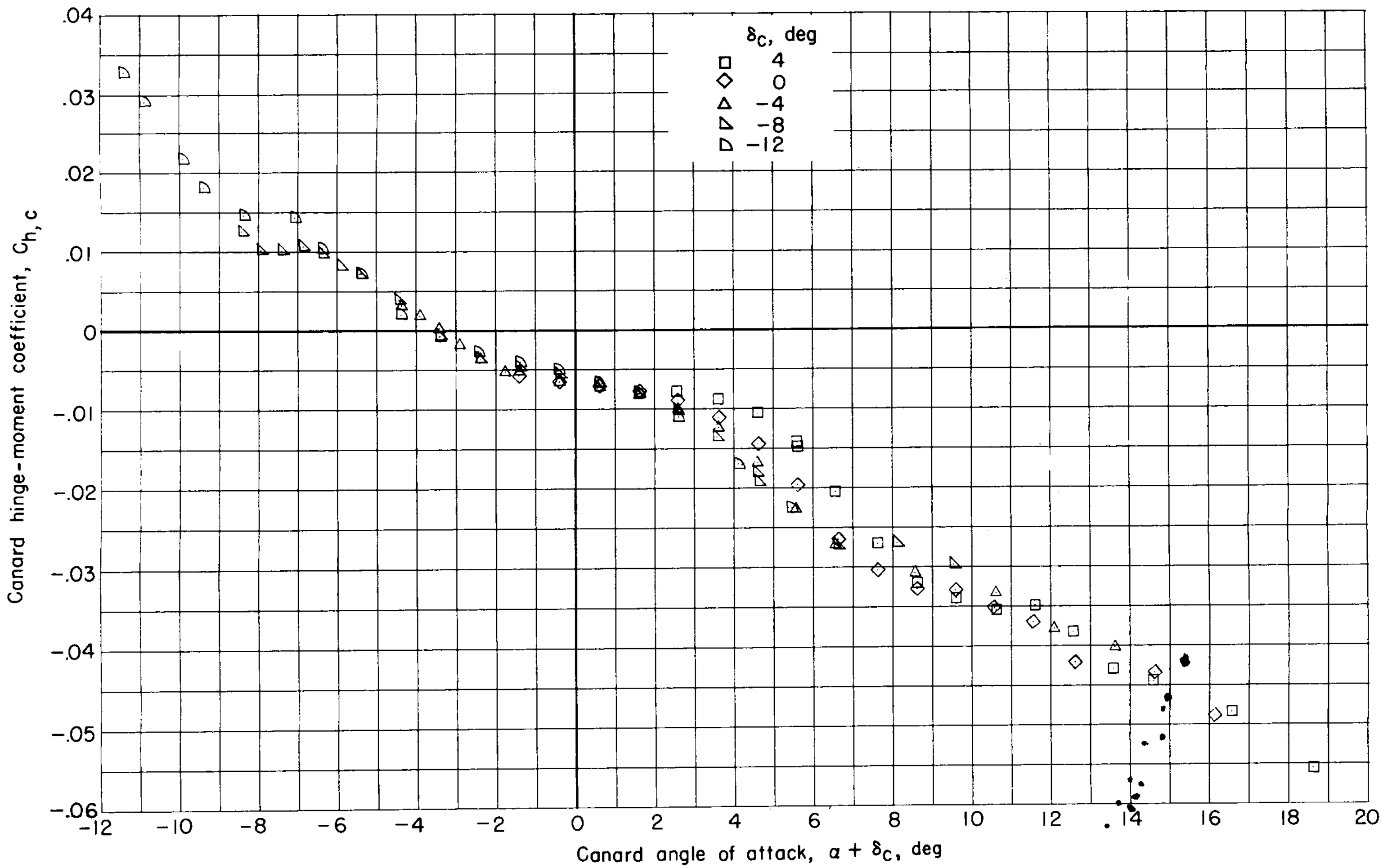

(c) Variation of canard hinge-moment coefficient with canard angle of attack.

Figure 76.- Concluded.

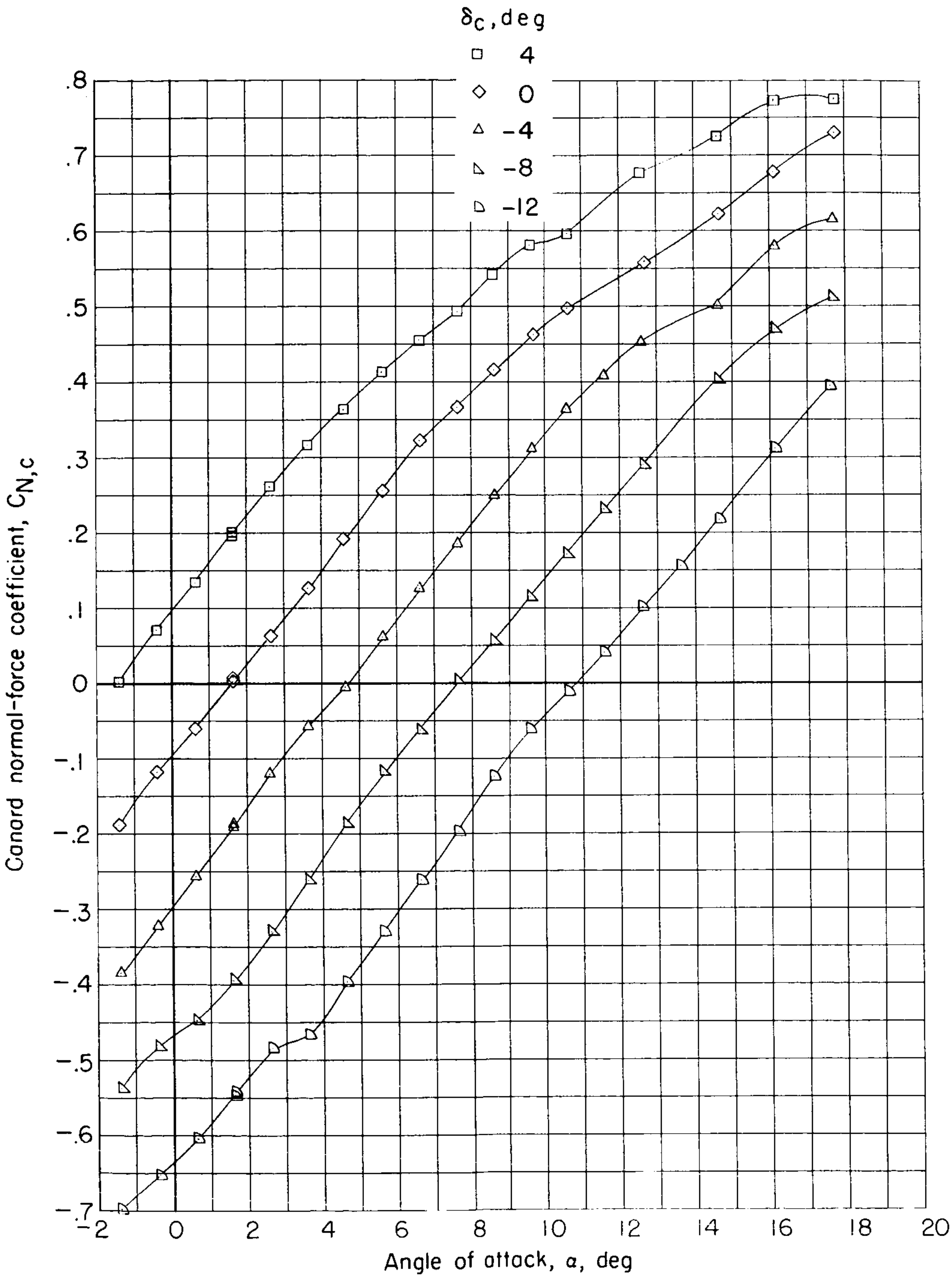

(a) Canard normal-force coefficient.

Figure 77.- Canard normal-force and hinge-moment coefficients for model BCW_1E with $\delta_{le} = 15^{\circ}$ and $\delta_{tab} = -4^{\circ}$ at $M = 0.90$.

L-1041

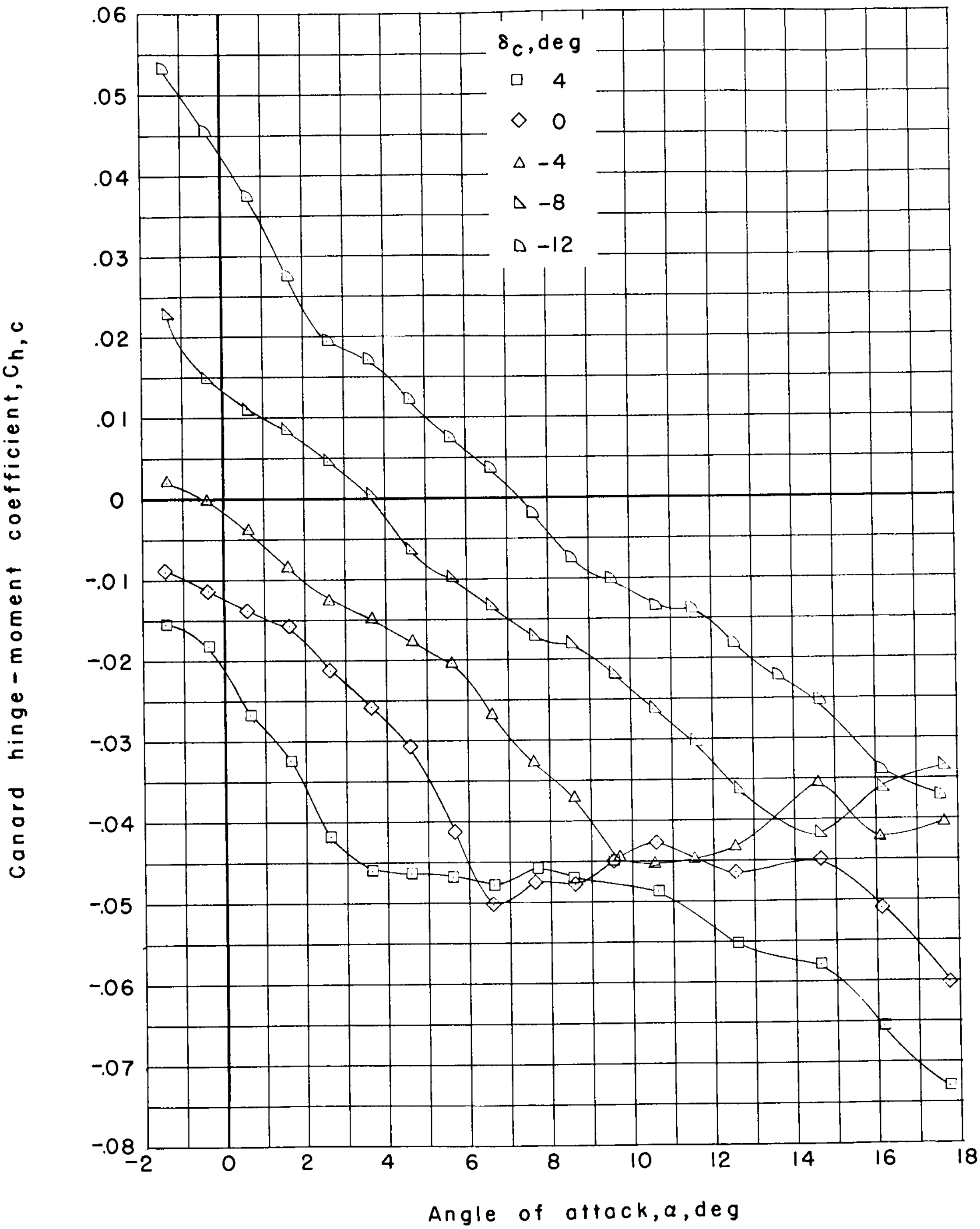

(b) Canard hinge-moment coefficient.

Figure 77.- Concluded.

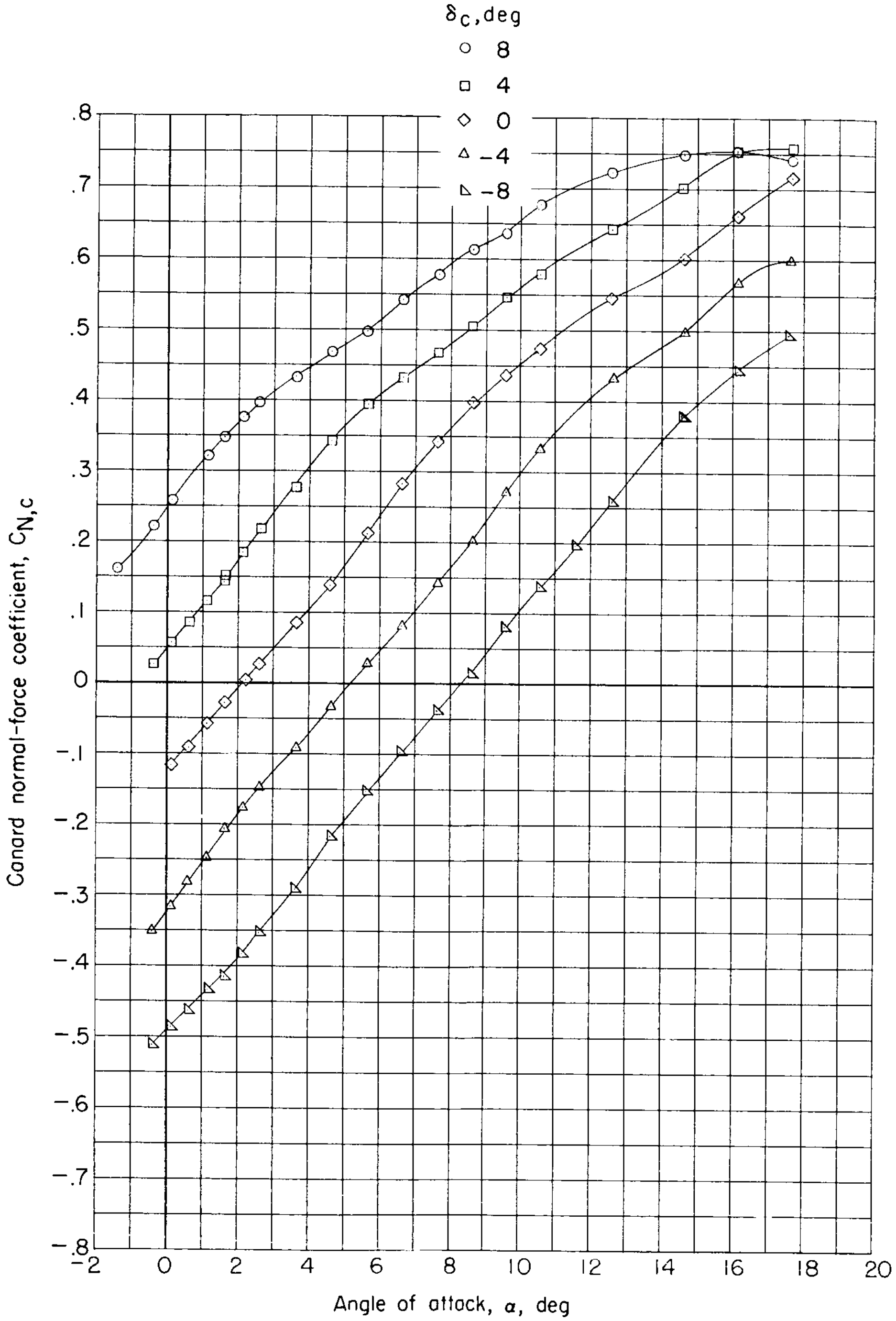

(a) Canard normal-force coefficient.

Figure 78.- Canard normal-force and hinge-moment coefficient for model BCW_1E with $\delta_{le} = 15^{\circ}$ and $\delta_{tab} = -8^{\circ}$ at $M = 0.85$.

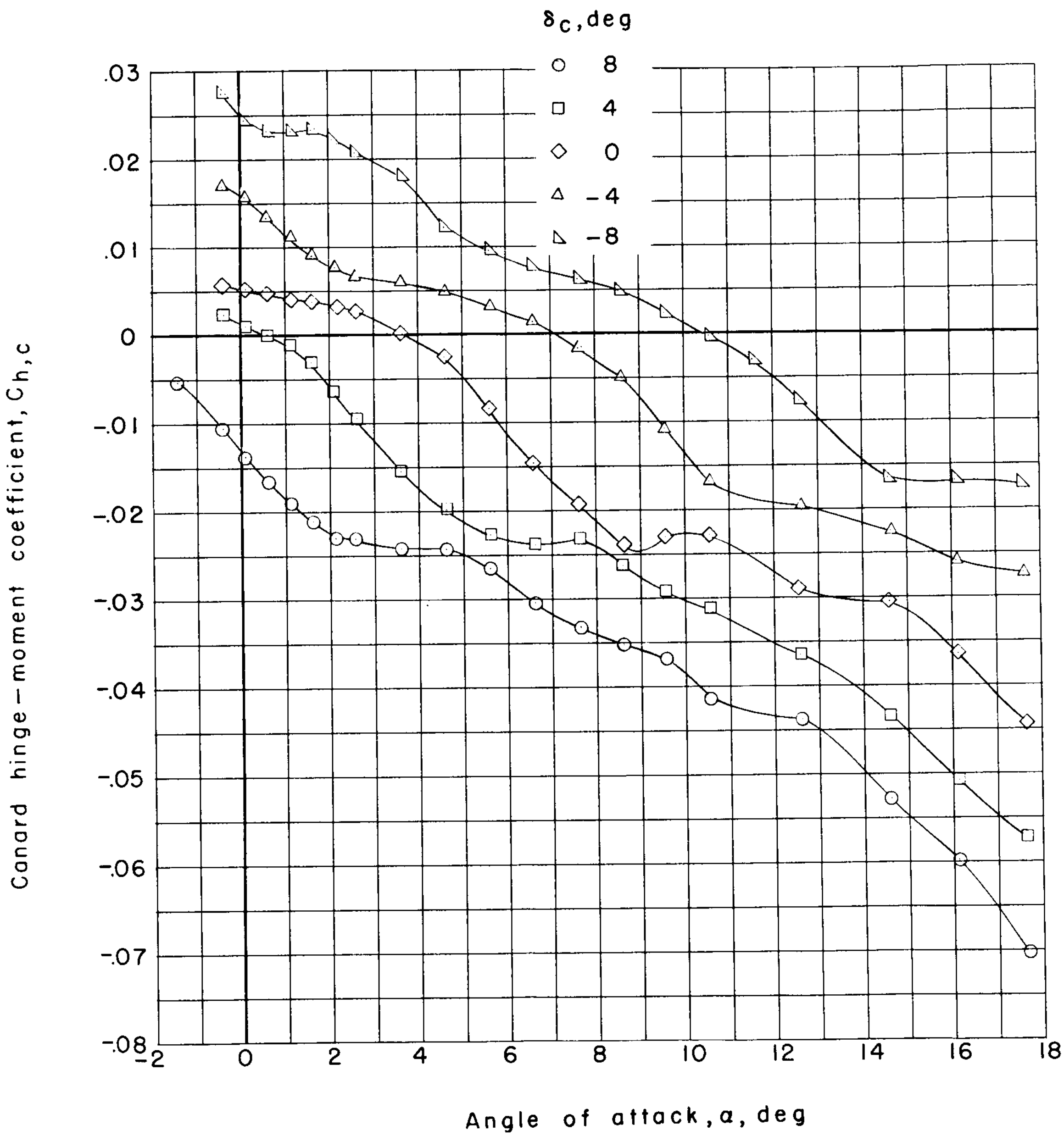

(b) Canard hinge-moment coefficient.

Figure 78.- Concluded.

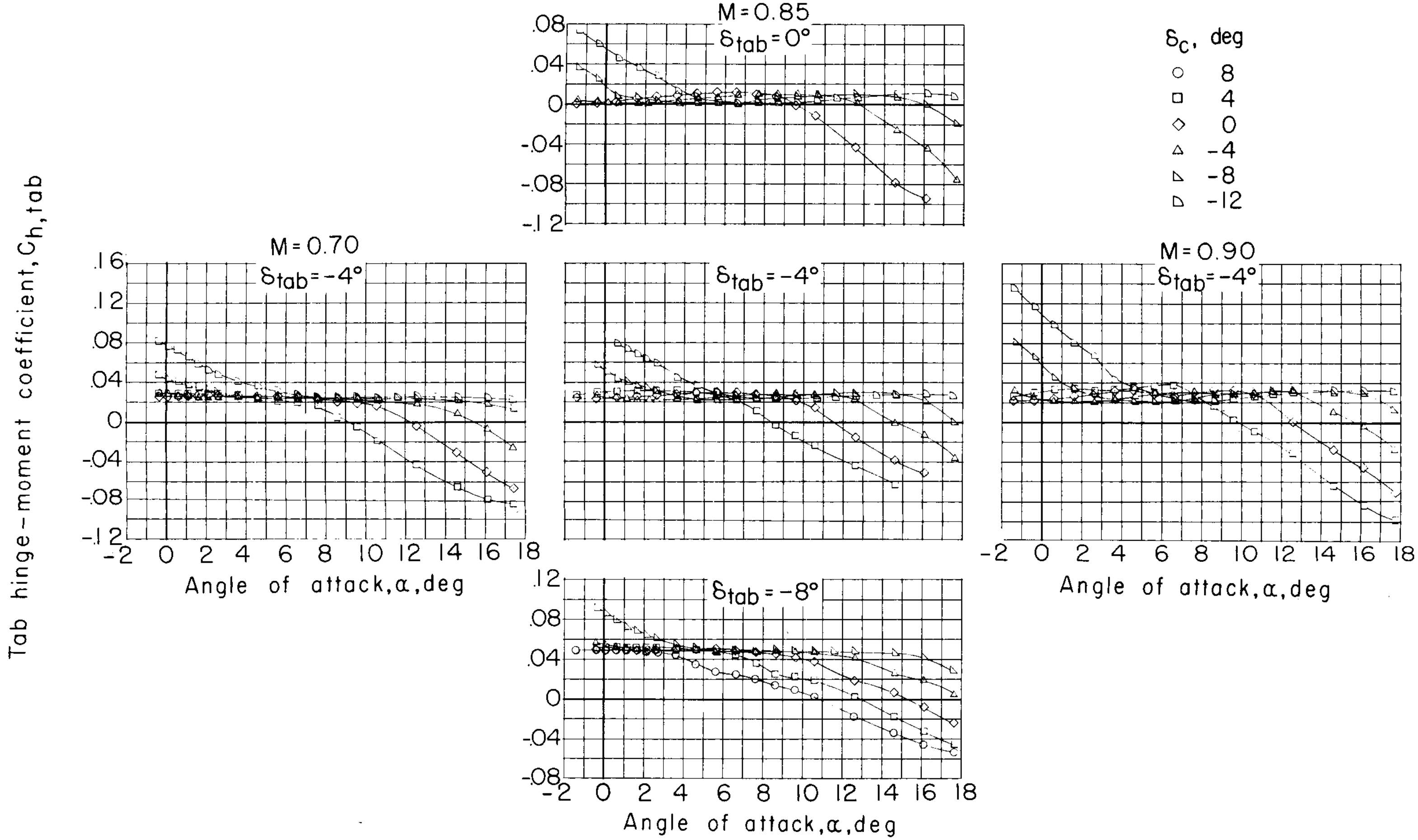

Figure 79.- Tab hinge-moment coefficient for model BCW_1E with $\delta_{le} = 15°$.

[redacted]

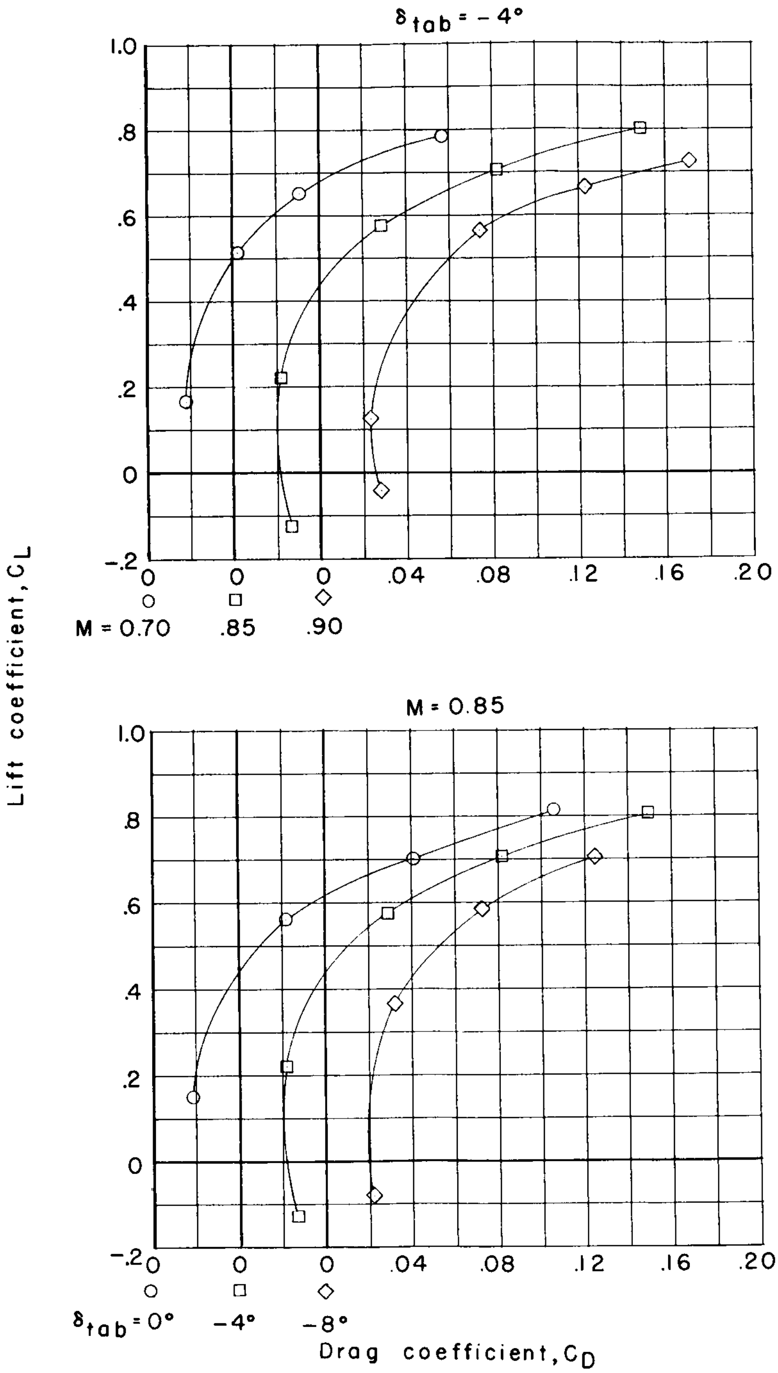

Figure 80.- Effect of canard tab deflection and Mach number on the trimmed drag polars for model BCW_1E with $\delta_{l_e} = 15^{\circ}$. (Symbols represent interpolated points.)